Growth, microstructure and hydrogenation of Pd-catalyzed complex metal hydride thin films

Westerwaal, R.J.

2007

document version
Publisher's PDF, also known as Version of record

citation for published version (APA)
Westerwaal, R. J. (2007). *Growth, microstructure and hydrogenation of Pd-catalyzed complex metal hydride thin films*. [PhD-Thesis - Research and graduation internal, Vrije Universiteit Amsterdam].

Growth, microstructure and hydrogenation of Pd-catalyzed complex metal hydride thin films

Groei, microstructuur en waterstof-absorptie door Pd-gekatalyseerde, complexe metaal hydride dunne films

Ruud Westerwaal

Leescommissie:

prof.dr. P.H.L. Notten, Philips Research en TU Eindhoven
prof.dr.ir. H. Hilgenkamp, TNW UT Twente
prof.dr.dr. H.C. Zabel, Bochum (Duitsland)
dr. H. Geerlings, Shell Amsterdam
prof.dr. A. Züttel, Fribourg (Zwitserland) en VU Amsterdam

Cover: AFM micrograph of a Mg_2Ni thin film deposited by molecular beam epitaxy.

Printed by: Gildeprint Drukkerijen Enschede.

This work is part of the research programme of the 'Stichting voor Fundamenteel Onderzoek der Materie (FOM)', which is financially supported by the 'Nederlandse Organisatie voor Wetenschappelijk Onderzoek (NWO)'. The work was carried out at:

Vrije Universiteit
Faculty of Sciences
Condensed Matter Physics
De Boelelaan 1081
1081 HV Amsterdam
The Netherlands

ISBN-978 90 8659 071 1

VRIJE UNIVERSITEIT

Growth, microstructure and hydrogenation of Pd-catalyzed complex metal hydride thin films

ACADEMISCH PROEFSCHRIFT

ter verkrijging van de graad Doctor aan
de Vrije Universiteit Amsterdam,
op gezag van de rector magnificus
prof.dr. L.M. Bouter,
in het openbaar te verdedigen
ten overstaan van de promotiecommissie
van de faculteit der Exacte Wetenschappen
op dinsdag 20 februari 2007 om 15.45 uur
in de aula van de universiteit,
De Boelelaan 1105

door

Ruud Johannes Westerwaal

geboren te Alkmaar

promotor: prof.dr. R.P. Griessen
copromotor: dr. B. Dam

Contents

Chapter 1

Introduction

1.1 Hydrogen in metals

Not long after the discovery of the element Palladium in 1803 by W. H. Wollaston, it was Graham in 1866 who found that this noble metal can absorb large amounts of hydrogen [1]. Increased research showed that many metals are able to absorb hydrogen resulting in the formation of a metal-hydride phase. Fundamental research and device oriented research increased tremendously by the interesting properties of these metal-hydrogen systems: i) hydrogen has a high diffusion coefficient in metals, as compared to other interstitials, ii) the hydrogen concentration in a metal is in general continuously variable and above the critical point this is possible without crossing phase boundaries in metal-hydride systems like Pd, Nd, Ta and V, iii) unexpected superconducting behavior of some hydrides e.g. PdH_x, $Pd_{1-y}Ag_yH_x$ with T_c's as high as 16 K iv) the hydrogen storage properties of metal-hydride systems can be used as energy storage system where the combustion of hydrogen results only in the production of water. Furthermore, isotope effects can be studied in e.g. diffusion with the use of H, (hydrogen), D (deuterium), T (tritium) with corresponding mass ratios of 1:2:3.

Hydrogenation of a metal host material is quite easy and can be accomplished by hydrogen gas loading or electrolytic charging. However, hydrogenation and the repeated cycling has a negative effect on the microstructure of the bulk metal. The material experiences embrittlement due to expansion upon hydrogen absorption. Eventually this will lead to a pulveration of the host material. As a result it is not always easy to determine the physical properties of the metal hydrides. The problem is circumvented by depositing a thin film of the material. Due to the interaction with the substrate, the film remains intact during hydrogenation. Thin metal hydride films can thus be used as model systems to study the hydrogen storage properties. In addition, these films have very interesting optical properties.

1.2 Metal hydrides as hydrogen storage systems

Global warming and the limited resources of cheap fossil fuels increased the awareness of sustainability. This activate the search for renewable energy sources and energy carriers, to create a whole new energy network. Hydrogen is a very attractive as a energy carrier. To store and transport hydrogen there are several options, each with it's own advantages and problems. Hydrogen - metal systems receive a lot of attention due to the fact that the hydrogen density in a metal-hydride is often higher than in a liquid or even in a solid hydrogen phase. To store hydrogen, the metallic host needs to have certain properties such as a high hydrogen volume and weight density, a good cycling stability, appropriate thermodynamics and low production costs. These requirements limit the number of possible candidates strongly.

In a hydrogen based society, heat and electrical power are primary requests. The stored hydrogen can be used in fuel cells which can provide both by the recombination of electrons, protons and oxygen to water. A fuel cell can power anything that requires electricity like cars, trucks, busses, households, laptops and mobile phones. Heat pumps, hydrogen purification, isotope separation, and moderation in nuclear rectors are some of the other applications of metal-hydrogen systems.

Another important application of hydrogen is in metal-hydride batteries which are used in mobile applications such as laptops and mobile phones. A typical example are the Ni-MH batteries which due to their energy/weight ratio makes them very suitable for mobile applications. These compounds are based on a $LaNi_5$ hydride, which can contain up to 1.4 wt% of hydrogen. Other promisimg metal-hydride systems for future applications are MgH_2, Mg_2TMH_x (TM = transition metals, Ni, Co, Fe, etc.) $NaAlH_4$, $LiAlH_4$ and $LiBH_4$.

1.3 Switchable mirrors

The discovery of the switchable mirror by Huiberts *et al.* at the Vrije Universiteit Amsterdam in 1995 changed the way of looking at metal-hydride systems [2]. They discovered that palladium capped yttrium and lanthanum films switch reversibly and rapidly between a shiny metal and a transparent insulator upon hydrogenation. With this discovery it is possible to study metal-hydrides systems in a complectly different and fundamental way. Also from an device oriented perspective, switchable mirrors are quite interesting. One can think of several applications such as smart windows [3] and hydrogen diffusion indicators [4]. In a fundamental perspective it enables one to study/tuning the Casimir force [5]. Furthermore, switchable mirrors can also serve as hydrogen sensors, which in connection with fiber optics provides a safe way to detect hydrogen [6].

The first generation switchable mirrors consisted of yttrium and lanthanum thin films capped with Pd [2]. Soon it was discovered that al rare earth metals and their alloys showed similar optical behavior upon hydrogenation. The fact that YH_3 is yellowish transparent and YH_2 is bluish in reflection makes their potential use for applications limited, since color neutral is desired. At Philips Research it was discovered that by alloying the rare-earth metals with Mg and Gd, the required optical properties improved considerably due to the fact that they are color neutral and these alloy thin films are indicated as the second generation switchable mirrors [7]. Richardson *et al* have shown that also e.g. Mg_2NiH_x and other complex metal hydride films (third generation) show reversible optical switching at room temperature between a shiny metallic and a transparent semiconducting state [8, 9]. Later, we discovered a third optical state in these complex metal hydrides. This so-called 'black state' is characterized by low reflection < 25 % over the whole visible spectrum when measured from the substrate side, while the transmission, < 0.01 %, is negligible. As a result, the film has an anomalously high absorption of more than 75%. The fact that Mg_2NiH_x can be switched between a reflective metal, an absorbing black and a transparent semiconducting state makes Mg_2NiH_x potentially attractive for smart coating applications [10]. The search for the origin of this unusual hydrogen absorption behavior will be part of the research presented here.

Mg-TM thin films are an interesting example of a complex metal-hydride with potential both as a storage material and as a switchable mirror (smart window application). Though its thermodynamical properties are less favorable than that of e.g. $NaAlH_4$, its hydrogenation properties may hold important clues for the optimization of the hydrogenation properties of complex metal hydrides in general. Secondly, for the use of Mg_2NiH_4 as a storage material, any effect that appears to catalytically enhance the formation of this phase is of interest.

1.4 This thesis

The occurrence of the optical black state and the model to explain this fascinating optical behavior is quite intriguing. In chapter 3 a detailed overview of the hydrogen absorption properties of Mg-Ni thin films is given. In order to judge the applicability of this effect for smart window applications, it is important to understand the origin of this optical behavior.

The main goal of this thesis is to relate microstructure to the optical and cycling properties of complex metal hydride films, e.g. Mg_2TMH_x. This implies that we need to find a connection between the film microstructure and the hydride nucleation.

The preferred hydride nucleation (and thus the optical black state) can have its origin in a chemical gradient throughout the film or in the specific thin film microstructure. Our approach is to first investigate the chemical homogeneity of the film and then the microstructure which is treated in chapter 4. We find no chemical gradient in the Mg-Ni films which is responsible for the preferred hydride nucleation. However AFM, STM, TEM and SEM measurements show a particular thin film microstructure. The first 50 nm of the film consists of a small grained layer. Upon further deposition this layer develops into a more dense columnar microstructure. It is interesting to note that this microstructure is consistent with the double layer model that describes the optical black state. Therefore we propose that the small grained layer close to the substrate induces the preferred hydride nucleation. After this initial nucleation, the more dense columnar structure will transform into the hydride phase.

This leads to the second goal of this thesis. To prove the above proposed model, we need to change the thin film microstructure in order to change the preferred hydride nucleation. There are two possible ways to achieve this. We can adjust the substrate temperature during deposition and in this way change the thin film growth mode. However, we prefer to grow *in-situ* the hydride phase. This new and explorative preparation method will be treated in chapter 5. The *in-situ* grown hydride films consists of a very small grain size microstructure, which is homogenous over the entire film thickness. Most important, these films do not show an optical black state and thus no preferred hydride nucleation at the substrate interface. With this observation we prove the relation between the microstructure and preferred hydride nucleation in Mg-Ni films.

The *in-situ* deposition technique gives also interesting results in the case of simple hydrides. We find that although *in-situ* grown MgH_2 phase is highly resistive, optical spectra indicate that there is still 10 vol.% of metallic Mg present in these films. The high resistivity indicates that these particles are embedded in a MgH_2 matrix of high purity. Furthermore, these Mg grains create an optical absorption edge at 2.0 eV. When re-hydrogenating these Mg films, the absorption edge disappears and the film behaves as an ordinary *ex-situ* hydrogenated Mg film. We will argue that the Mg segregation is induced by the preferential formation of Mg clusters due to their low surface energy.

Remarkably, the *in-situ* grown Mg_2NiH_4 and MgH_2 films appear to be stable both in air and vacuum. Dehydrogenation only occurs when a Pd layer is deposited on top of the *in-situ* grown hydride film. This indicates that the dehydrogenation of the hydride is kinetically blocked. Furthermore, we find that the dehydrogenation induced by the Pd depends very much on the nature of this layer.

In chapter 6 we investigate the catalytical properties of the Pd caplayer. We show that the SMSI (strong-metal support interaction) effect, characterized by a complete encapsulation of the Pd layer clusters by oxidized species originating from the active hydride, plays an very important role on the degradation of the switchability of the film. The SMSI-effect becomes less important when increasing the Pd-layer thickness, and can be partly suppressed by a good wetting of the Pd-clusters on the hydride forming film. This behavior explains the critical thickness for the catalyzed hydrogen-uptake observed in many switchable mirror systems. In addition we show the effect of contaminations and the number of active sites on the catalytic properties of the Pd caplayer. From *in-situ* hydrogenation experiments we conclude that the presence of a small amount of sulphur on the Pd caplayer surface has disastrous consequences for the hydrogen desorption. After sputtering this Pd caplayer with argon ions, the fresh Pd surface regains its original catalytical properties.

Chapter 2

Sample preparation

2.1 Molecular Beam Epitaxy deposition

The thin films used for our research are deposited by molecular beam epitaxy (MBE) (see Fig. 2.1). With this MBE system we can grow both metallic and *in-situ* hydride thin films, the as-grown metallic films are hydrided *ex-situ*. First we will discuss the deposition of metallic films. The thin films are usually deposited on transparent substrates suited for optical measurements. A Pd caplayer is deposited on top of the film to catalyze the hydrogen absorption and desorption and to protect them from oxidation.

For the deposition of Mg_2TM (TM = transition tetals: Ni, Co, Fe, etc.) and Mg films we make use of several electron guns (e-guns) and Knudsen cells (K-cells). E-guns are used to evaporate the transition metals because of the elevated evaporation temperatures required for these metals. Furthermore, our e-guns can contain a large amount of source material which allows us to keep the MBE system under ultra high vacuum (UHV) conditions for a longer period. To deposit an alloy we perform a co-deposition using several sources at the same time. Instead of operating all the sources manually, the e-guns are operated with a P.I.D. algorithm implemented in a HP VEE program. This program is able to read the signal of the quartz-crystal monitor (QCM) and with this information the deposition rate can be held constant and film thickness and composition can be recorded in real-time. High temperature Knudsen cells (up to 2300 K) can also be used to deposit the transition metals. The disadvantage is however that these materials react with the tungsten crucible and one needs to make use of an AlO_2 liner inside the crucible. The combination of a HT Knudsen cell with a tungsten crucible and a AlO_2 liner is very sensitive to abrupt changes in temperature and the repeated heating up and cooling down of the K-cell. This often results in a cracked liner or crucible and since this can damage the Knudsen cell seriously, e-guns are used instead for deposition of the transition metals. To obtain a stable Mg rate we use a Knudsen cell for this material. Also these Knudsen cells are operated with a

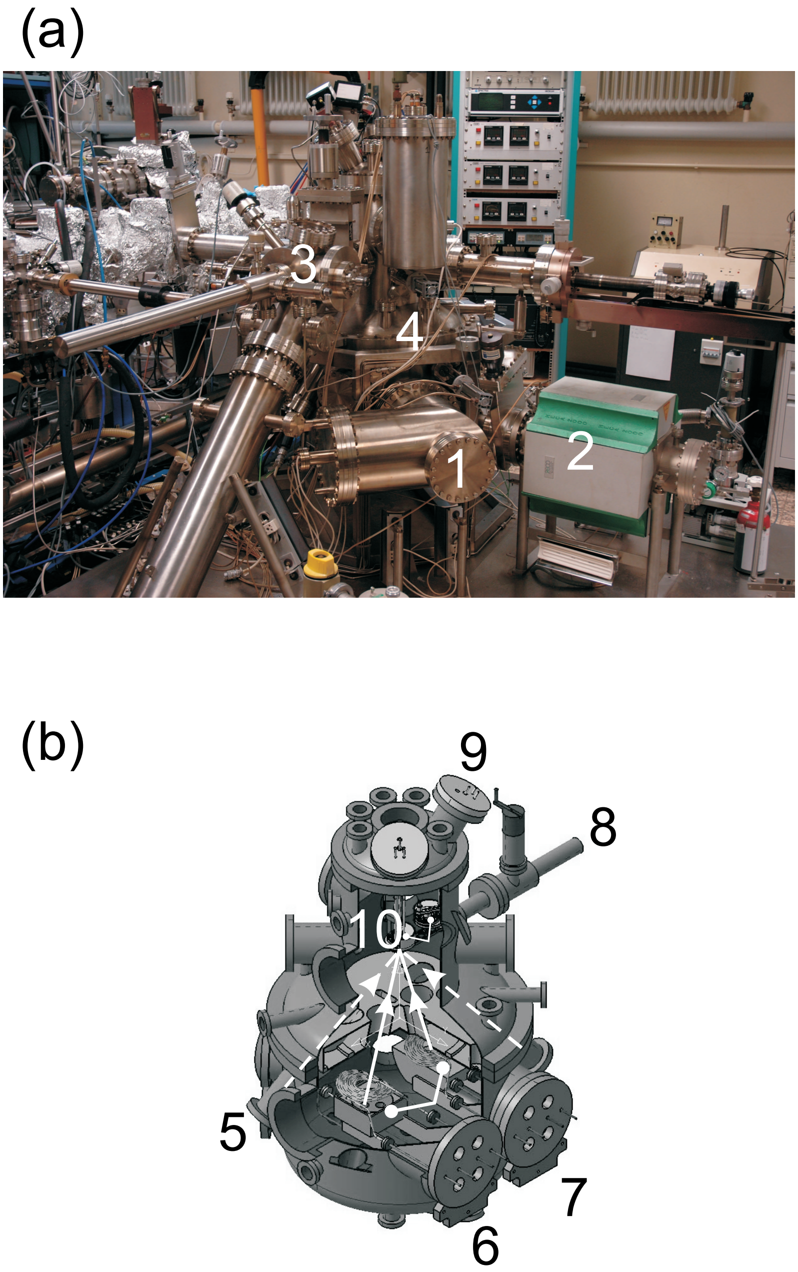

Figure 2.1: (a) Photograph of the UHV-MBE system used in this work and (b) a schematic cross-section of the deposition chamber. (1) Ti sublimation pump, (2) ion getter pump, (3) load lock, (4) evaporation chamber, (5) position K-cell, (6) multi-pocket, (7) e-gun Ni, (8) connection to transport system, (9) quartz crystal monitors (QCM), (10) sample position during evaporation. In the evaporation chamber the e-guns are located at the bottom of the vessel. The two quartz-crystals at the top are oriented in a way that they see different sources.

P.I.D. controller. Typical deposition rates of the Mg and TM are 0.065 nm/s and 0.015 nm/s respectively.

The deposition of the metallic films (in contrast to the *in-situ* growth of hydride films) take place under Ultra High Vacuum (UHV) conditions (1×10^{-8} Pa). Before the actual deposition starts, the source material is pre-heated for half an hour to degas and remove impurities which are adsorbed/absorbed by the material. The ultra high vacuum system creates a very large mean free path λ ($\lambda \sim 10^5$ m at p = 10^{-7} Pa), which minimizes the disturbance and contamination of the created metallic vapor plume before it reaches the substrate surface [11].

Since for this research Mg-TM based switchable mirrors are used, we are interested in alloys of composition $A_{1-z}B_z$, with the individual deposited thicknesses d_A and d_B as measured by two separated quartz crystal monitors (QCM). The fraction z is given by

$$z = \left(1 + \frac{d_A}{d_B}\frac{V_{m,B}}{V_{m,A}}\right) \tag{2.1}$$

The thickness of the alloy is equal to $(1\text{-}z)d_A + zd_B$, while the molar atomic volume $V_{m,alloy}$ of the alloy is the weighted average of the atomic volumes $V_{m,A}$ and $V_{m,B}$ of the pure metals A and B respectively. However in actual films the atomic volume of the alloy $V_{m,alloy}$ is not equal to $(1-z)V_{m,A} + zV_{m,B}$ due to the different density of the actual deposited alloy. This approximation generally over-estimates the real thickness by 10%.

We deposit the thin films on substrates such as, suprasil^{TM} quartz glass, sapphire, CaF_2, and SiO_x. The substrates are cleaned ultrasonically by putting the substrates in an ethanol bath for half an hour and are subsequently dried by spinning. Glassex^{TM} and other cleaning liquids can be used to clean substrates, however intensive experiments showed that chemical liquids can influence the hydrogenation behavior substantially. The best way to keep the substrates clean is to touch them as less as possible. Furthermore a bake-out of the substrate under UHV conditions, inside the deposition system, is generally enough to obtain high quality films. Also cleaning the substrates with an atomic hydrogen flux is very effective in removing any contaminations from the substrate surface. This is done with the same atomic hydrogen source as used for the *in-situ* growth of hydrides. For Secondary Electron Microscopy (SEM) measurements the switchable mirrors are deposited Si wafers. To remove most of the oxide skin on top of the Si wafer, the substrates are etched in 48% Hydrofluoric acid (HF) for approximately 15 minutes. Hereafter the substrates are transported in demineralized water until they are inserted into the UHV system. This still leaves a thin oxide skin of around 3 nm on the substrates, but this does not limit the SEM measurements severely.

The substrate is mounted on a sample holder (stub), which is placed in the load lock. In the load lock we can bake out the stub with the substrate to remove the adsorbed gasses and water. After pumping down the load lock to 10^{-7} Pa, the stub is transported to the main deposition chamber with a linear rack and pineon bar (LRP). Perpendicular to the LRP bar there is a high precision linear transfer bar (HPLT) which can pick-up the stub from the LRP bar. In this way the substrate can now be turned over 180 degrees to face the various deposition sources. This configuration provides the possibility to mount a mask on the LRP to partly cover the substrate from the sources. This makes it possible to grow staircase or matrix films in which the deposited film thickness or composition varies in one or two directions respectively. Furthermore, during deposition it is possible to heat up the stub and so increase the temperature of the substrate. In this way we can grow crystalline films or change the thin film microstructure grow mode.

2.1.1 *In-situ* resistivity measurements

During deposition we can perform resistivity measurements if we have equipped the substrate with the necessary electrical contacts. The measured resistivity provides us with information about the nature of the as-grown phase and its quality. We can determine wether a film grows in the metallic or (hydride) semiconducting state. Also the growth mode in the initial stages of growth can be determined.

To measure the resistivity, ρ, accurate and independent of the sample shape, we use the Van der Pauw method [12]. To measure the intrinsic resistivity, four contacts are made to the sample (see Fig. 2.2). When a current i_{ab} is send through contacts a and b, the voltage drop $\triangle V_{dc}$ between the other two contacts d and c is measured. The resistivity $R_{ab,cd}$ is then defined as,

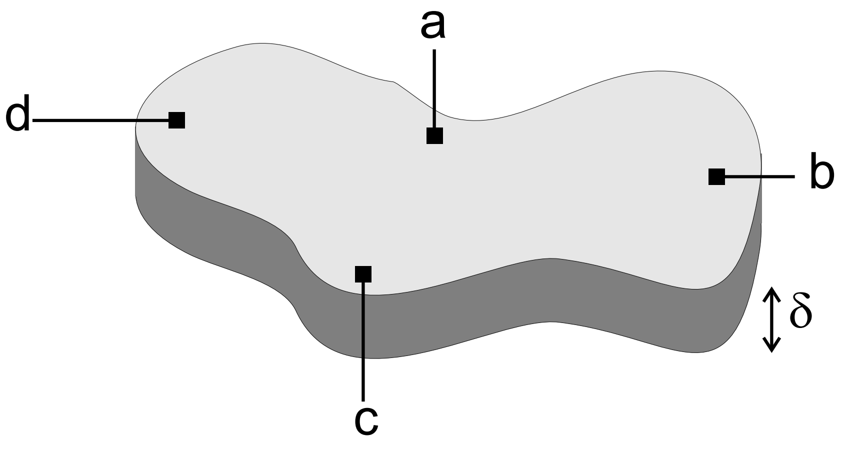

Figure 2.2: For Van der Pauw resistivity measurements four contacts must be placed on the edge of the sample. With this method the resistivity can be measured accurately, independent of the sample shape.

$$R_{ab,cd} = \frac{\triangle V_{dc}}{i_{ab}} \tag{2.2}$$

By sending a current though contacts b and c and measuring the voltage drop $\triangle \mathrm{V}_{ad}$ the resistivity is found by

$$R_{bc,da} = \frac{\triangle V_{ad}}{i_{bc}} \tag{2.3}$$

The resistivity of the sample can be found by

$$\rho = \frac{\pi\delta}{ln2} \frac{R_{ab,cd} + R_{bc,da}}{2} f \tag{2.4}$$

In this equation is δ the film thickness and $f(R_{ab,cd}+R_{bc,da})$ can be given in the implicit form

$$cosh\left(\frac{R_{ab,cd}/R_{bc,da} - 1}{R_{ab,cd}/R_{bc,da} + 1}\frac{1}{f}\right) = exp\left(\frac{1}{f}\right) \tag{2.5}$$

The resistivity of the sample is continuously calculated with a HP VEE program by making use of a polynomial fitting of $f(R_{ab,cd}/R_{bc,da}$. This results in a 3^{th} order polynomial fit for $1 \leq R_{ab,cd}/R_{bc,da} \leq 3$ and $3 \leq R_{ab,cd}/R_{bc,da} \leq 10$ and a 5^{th} order polynomial for $10 \leq R_{ab,cd}/R_{bc,da} \leq 100$.

2.1.2 *In-situ* optical reflection measurements

Instead of the resistivity we can also measure the optical reflection spectra during deposition, using a high temperature (HT) fiber as a substrate (see Fig. 2.3). These types of fibers have a low degassing of the fiber jacket. The core diameter of the fiber is 200 μm and the cladding is 15 μm thick. The fiber end is cleaved by using a Vytran LDC-200 auto cleaver. Cleaving the fiber results in a flat and clean substrate surface. The probe fiber is clamped in a holder so that it is in line of sight with the various sources. The other end of the fiber is glued with a UHV epoxy in a fiber-optic SMA (SubMiniature version A) connector that is mounted in a feedthrough of the load lock. A bifurcator in combination with a splice bushing is used to guide the light from a tungsten-halogen source to the end of the fiber (see Fig. 2.3). Reflected light is guided via the second path of the bifurcator to an Ocean Optics USB 2000 CCD spectrometer. This spectrometer covers the range from 1.2 to 3.1 eV and records periodically the spectra of the reflected light during the deposition from the end of the fiber. The spectra are normalized to the corresponding calculated thin film spectrum. This technique is tested for several metallic thin

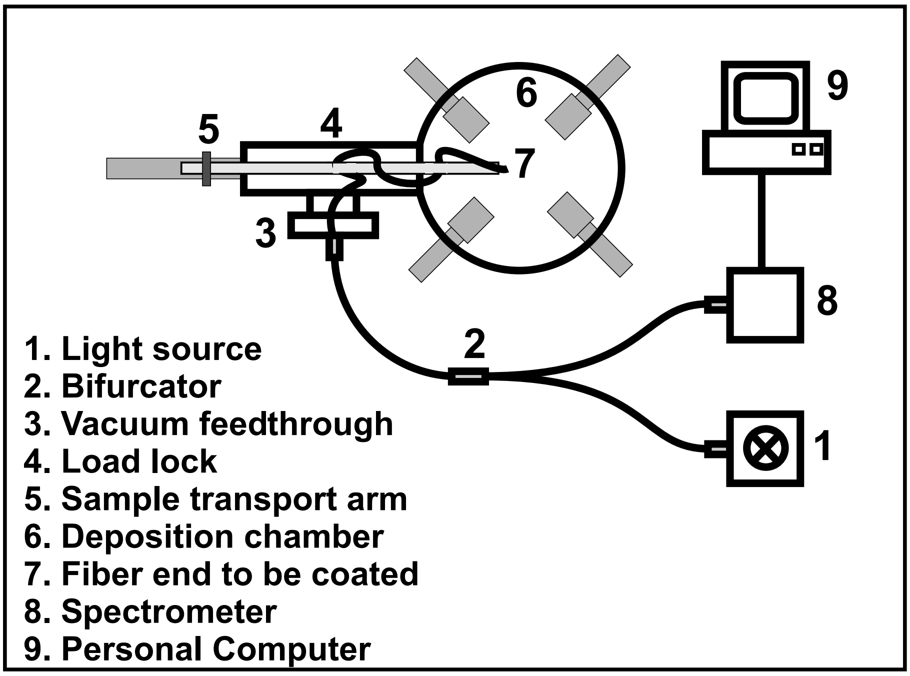

Figure 2.3: Schematic representation of the thin film deposition chamber together with the fiber set-up to measure *in-situ* the reflection. The film is deposited onto the freshly cleaved fiber surface.

films and results in a good agreement between the calculated and the *in-situ* measured spectrum.

The reflection and transmission spectra of the complete optical system (fiber, fiber-film interface, film, film-vacuum interface, etc.) is calculated using a transfer matrix method that considers the Fresnel reflection and transmission coefficients at each interface and the absorption in each material [13, 14]. For this calculation the values of n and k of the involved materials are taken from Palik's book of optical constants [15].

The optimization of the deposition conditions for *in-situ* growth of Mg_2NiH_4 and the tuning of the atomic hydrogen source will be discussed in the next section.

2.1.3 Fiber spectroscopy of thin metal films during growth

The reflection at an energy of 1.95 eV as a function of the film thickness (measured with a quartz crystal monitor) is shown for Ni, Pd, Mg, Y and Mg_2Ni in Fig. 2.4. The reflection starts with a decrease in reflection within the first deposited 10 nm for all the elements except Mg, resulting in a temporary minimum. Upon further deposition the thin film becomes optically closed and

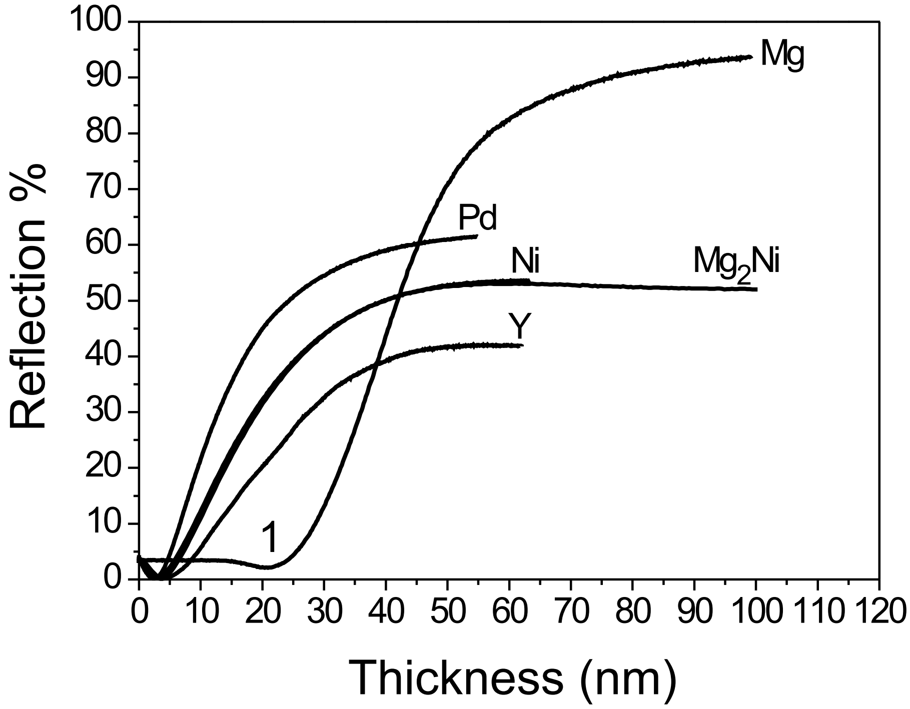

Figure 2.4: Reflection of Ni, Pd, Mg, Y and Mg_2Ni films at an energy of 1.95 eV as a function of thickness as measured by a QCM. The beginning of the spectra is characterized by a minimum in reflection for all the measured elements at a certain thickness. Above a certain thickness the reflection reaches a constant value and the films become optically closed.

the reflection reaches a constant value. The reason for the anomalous behavior of Mg is probably the low sticking of Mg atoms on a bare substrate/fiber compared to the measured thickness by the QCM [16].

Caranto *et al.* also observe this reflection minimum in their measurements but they do not give a proper explanation of the formation of the minimum in reflection [17]. Emmerson *et al.* argue that this effect can result from a change in electronic structure of both the growing layer and the substrate [18]. Furthermore, a decrease in the free carrier density will also result in a decrease in reflection [19]. Butler *et al.* assume that the minimum of the reflection is typical for noble metals [20, 21]. Heavens *et al.* point out that the minimum in reflection is precisely in accordance with the theory of a thin homogeneous film and is observed for many metallic layers. Although they describe thin film optics quite extensively for several kinds of films, the origin of this effect is not explained explicitly. Furthermore, they state that the position of the minimum is wavelength dependent for gold, silver and iron but not for platinum

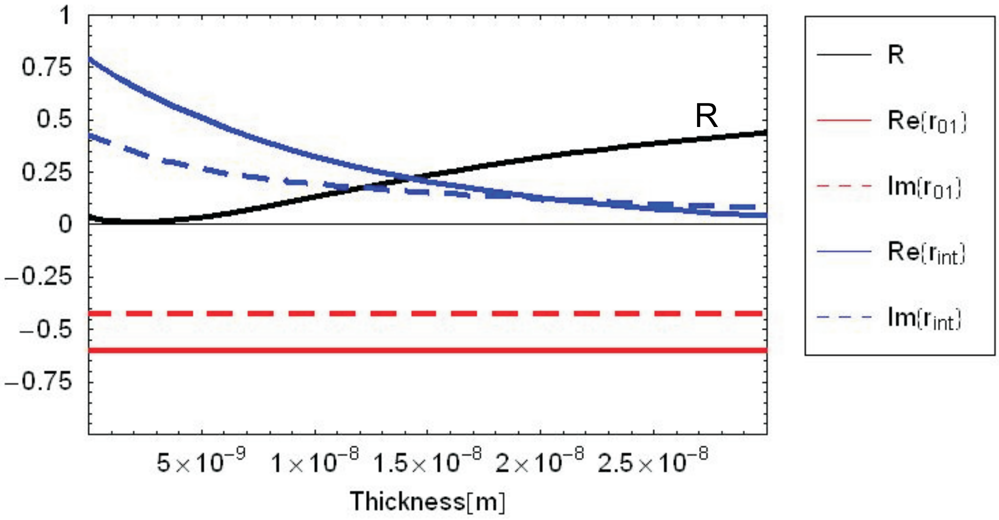

Figure 2.5: Reflection (R) as calculated by equation 1. The imaginary part of r_{01} and r_{int} (Im(r_{01}), Im(r_{int})) and the real part of r_{01} and r_{int} (Re(r_{01}), Re(r_{int})) are shown. It is clear that r_{01} is constant and negative (this is due to the phase change when reflecting at an interface). r_{int} Is positive and decreases monotonically (as one expects due to the higher absorption in the layer with increasing thickness). The interference of r_{01} and r_{int} is destructive for all d because the 2 contributions are out of phase. The destructive interference is obviously largest when $|r_{01}+r_{int}|$ has a minimum value.

and that there is a discrepancy between the theoretical calculated reflection and experiment due to the thin film microstructure, which influences the n and k values of thin films.

To establish the the physical origin of this behavior, we calculate the reflection for a single film with equation 2.6 [13, 14],

$$R(\omega) = \left| \frac{r_{01}exp[-i\delta(d)(n_1+ik_1)] + r_{12}exp[i\delta(d)(n_1+ik_1)]}{exp[-i\delta(d)(n_1+ik_1)] + r_{01}r_{12}exp(i\delta(d)(n_1+ik_1)} \right|^2 \tag{2.6}$$

in which r_{ij} is the reflection at the interface ij. The film thickness enters equation 2.6 implicitly through the dimensionless parameter $\delta(d)$ that governs the phase shift and the damping of the wave upon crossing the entire film, n_i is the refractive index and k_i the extinction coefficient. Equation 2.6 predicts a reflection minimum at a thickness of 2.1 nm for a fiber/Ni/vacuum system (we find similar values for the other metals/alloys Pd, Mg_2Ni, Y, etc.). This means that the characteristic minimum we observe is a direct consequence of equation 2.6. Since this calculation does not make use of a variation of n and k as function of deposited thickness or film microstructure, this implies that the minimum is due to the thickness dependence of the reflection described by this equation [13, 14]. Equation 2.6 can be rewritten as equation 2.7.

$$R(\omega) = \left| r_{01} + \frac{r_{12}(1 - r_{01}^2) exp[2i\delta(d)(n_1 + ik_1)]}{1 + r_{01}r_{12} exp[2i\delta(d)(n_1 + ik_1)]} \right|^2 \qquad (2.7)$$

There are two terms, r_{01} is the reflection from the fiber/film interface and the second term, here indicated as r_{int}, is the contribution from multiple internal reflections inside the growing film. In Fig. 2.5 the magnitude of the real and imaginary part of r_{01} and r_{int} are plotted versus film thickness. The real and imaginary part of r_{01} (Rer_{01} and Imr_{01}, respectively) are constant and negative (which is due to the phase change accompanying the reflection at the fiber-film interface). The real part and imaginary part of r_{int} (Rer_{int} and Imr_{int} respectively) are positive and decrease monotonically. This is what one expects for the absorption of a layer which increases in thickness. The interference of r_{01} and r_{int} is destructive for all d because the two contributions are out of phase. As the contribution of r_{int} is larger than that of r_{01} for thicknesses < 2.1 nm, the sum of r_{01} and r_{int} is positive. Since r_{int} is decreasing as function of thickness, the destructive interference is obviously largest when $|r_{01}+r_{int}|$ is minimal (R is minimal and in this case at d = 2.1 nm). As r_{int} dies out, the sum of r_{01} and r_{int} become more negative. However due to the fact that R is defined as $R = |r_{01} + r_{int}|^2$, R becomes more and more positive as r_{int} dies out. This means that the dip in reflection originates from the destructive interference due to the phase change upon reflection from the surface of the growing layer combined with an increase of absorption due to the growing film thickness.

Thus the minimum in reflection is caused by a two-step process. First, due to a destructive interference which has its origin in a phase change when the light is reflected from the growing layer. Second the increase in film thickness causes an increase in absorption. The combination of these two effects result in the observed minimum. Our calculations show that we can explain the minimum in reflection by a complete theoretical description without assuming changes in n and k values as function of thickness or microstructure. Hence, we can use the optical reflection data as a measure to identify the phases formed during growth.

To find the optimal metal-hydrogen ratio we use both *in-situ* resistivity and optical reflection measurements.

2.2 Activated reactive evaporation

As mentioned before, the Pd caplayer catalyzes the hydrogen absorption and desorption. However this Pd layer, which remains metallic under hydrogenation, limits a precise determination of the physical properties of the hydrogenated film. Furthermore, diffusion of the Pd layer into the film can have serious influence on the hydrogenation properties. Together with the observed preferred hydride nucleation in Mg-Ni thin films, led us to the idea of the *in-situ* growth of hydrides by activated reactive evaporation (ARE). Since the MBE deposition chamber is subjected to restrictions on the maximum applied pressure, it is not possible by just an increase in the applied hydrogen pressure during deposition. In addition it is expected that the reaction of Mg with a *molecular* hydrogen flux is negligible. Therefore, to grow a specific hydride phase from the constituent elements, we make use of an atomic hydrogen source (see Fig. 2.6, 2.7 and 2.8). With this deposition technique we are able to *in-situ* grow clean hydride phases. The partial pressure of contaminating elements in the deposition chamber, e.g. O_2, CH_4, and S combinations are below 10^{-8} Pa and no contamination of the thin films is expected, which is confirmed by RBS measurements. The partial water pressure during *in-situ* growth is 10^{-6} Pa, however RBS measurements show no oxygen contamination of the *in-situ* grown Mg_2NiH_4 phase.

In the hydrogen source, molecular hydrogen of purity 5N from a H_2 gas bottle is dissociated at a hot tungsten capillary, 64 mm long, 1 mm in diameter which is inserted in a water cooled socket (see Fig. 2.6 and Fig. 2.8). Here it is sealed by a gold wire gasket. The capillary is heated by electrons that are emitted from a tungsten filament and impacting on the capillary. To change the temperature of the capillary, and thus the dissociation rate of the molecular hydrogen, the electron emission current is adjusted. The atomic hydrogen beam leaves the capillary with an angular distribution peaked along the capillary axis. The flux of the atomic hydrogen beam can be controlled by both the molecular hydrogen gas flow and the temperature of the capillary. The fraction of the hydrogen that is dissociated depends on the temperature of the capillary and on the hydrogen pressure. The source was kindly provided to us by Forschungszentrum Jülich (Institut für Schichten und Grenzflächen) and quantitative data are given in Ref. [22, 23].

In our experiments the gas flow rate is usually held constant and results in a hydrogen pressure at the source inlet and in the deposition chamber of 2.2×10^3 Pa and 2×10^{-2} Pa, respectively. Before the molecular hydrogen gas enters the hydrogen source it is pumped with a turbo pump to remove most of the gas contaminations (see Fig. 2.7). In reactive deposition conditions, the heating power is around 130 W corresponding to a capillary temperature of about 2100 K. The distance from the capillary orifice to the substrate is around 15 cm. From data on the atomic hydrogen flux, measured 8 cm from the capillary orifice at the substrate position, we estimate an atomic hydrogen flux of 2×10^{15} atoms/cm^{2}s at the actual substrate distance of 15 cm by assuming a hemi-spherical distribution. When we grow a Mg hydride or Mg_2NiH_4 complex metal hydride from the constituents Mg, Ni and H, we generally use an over-stoichiometric flux of atomic hydrogen for hydride formation. As an example of

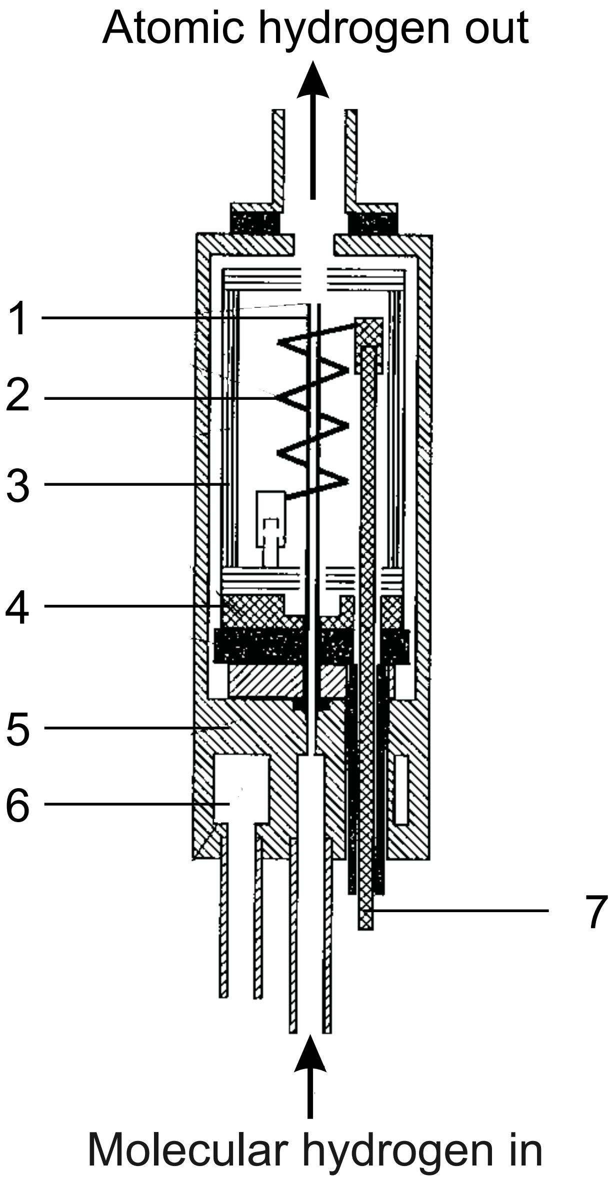

Figure 2.6: The atomic hydrogen source incorporates a capillary held by a water-cooled socket. The capillary is heated by electron impact and is surrounded by radiation shields. Condenser plates at both ends of the source eliminate escaping electrons. (1) W capillary, (2) W filament, (3) Mo radiation shields, (4) Mo condenser plates, (5) Cu housing, (6) water cooling system, (7) electrical contact.

the conditions of growth, the parameters of *in-situ* deposition of the Mg_2NiH_4 hydride is given next. The gas flow rate through the source is given by $Q = p_{appl.} \times C_g$ with C_g the flow conductance of the source. For molecular flow C_g is found to be 7 cm^3/s which gives Q = 0.15 mbarl/s [22, 23]. From the atomic

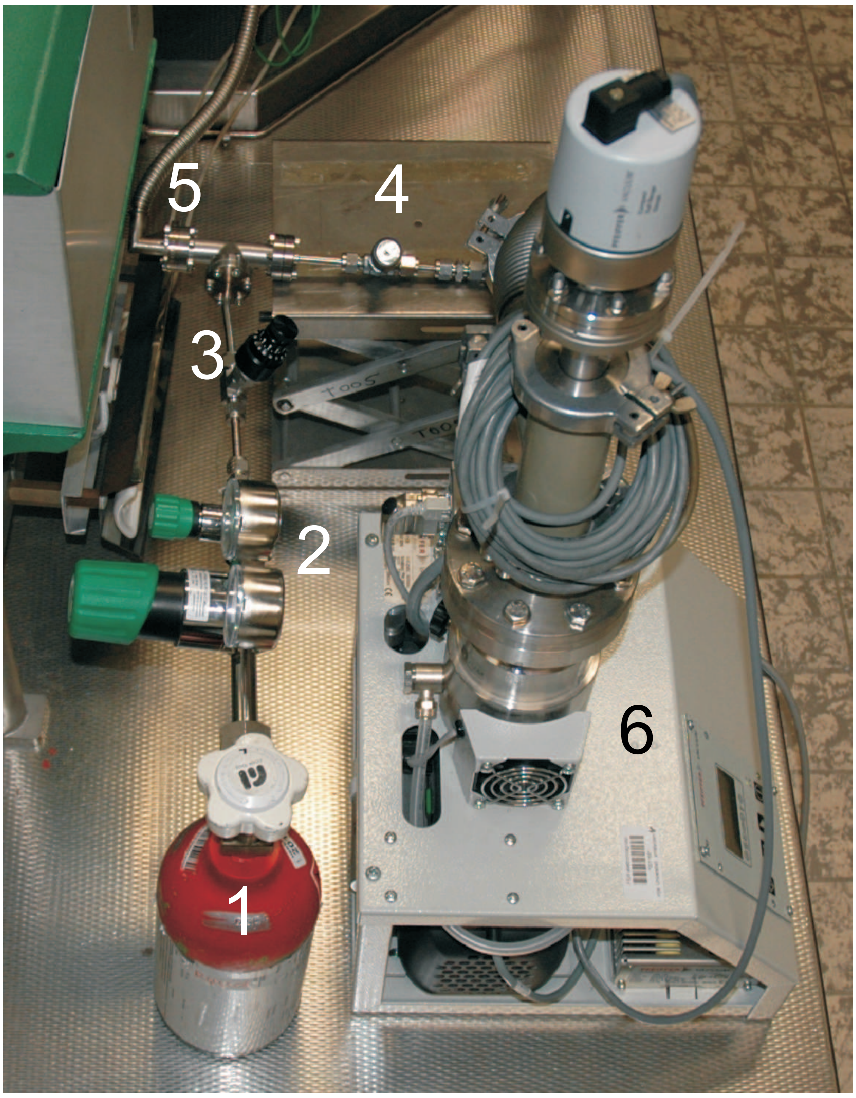

Figure 2.7: Photograph of the molecular hydrogen gas treatment before it enters the atomic hydrogen source. (1) Hydrogen gas bottle (of purity 5N), (2) pressure reducing valve, (3) valve to change the inlet pressure of the atomic hydrogen source, (4) valve to turbo pump, (5) tube to the atomic hydrogen source, (6) turbo pump.

flux data: 2100 K, 0.15 mbarl/s, distance to the substrate 8 cm, the number of hydrogen atoms arriving at the substrate is around 2×10^{15} atoms/cm^{2}s. However the distance between our source and substrate is 15 cm so we have to correct this value by $8^2/15^2$ resulting in 5.7×10^{14} atoms/cm^{2}s arriving at the substrate. The rate of the Mg and Ni atoms of 0.023×10^{-7} cm/s and 0.005×10^{-7} cm/s respectively results in $N_M = 15 \times 10^{13}$ atoms/cm^{2}s

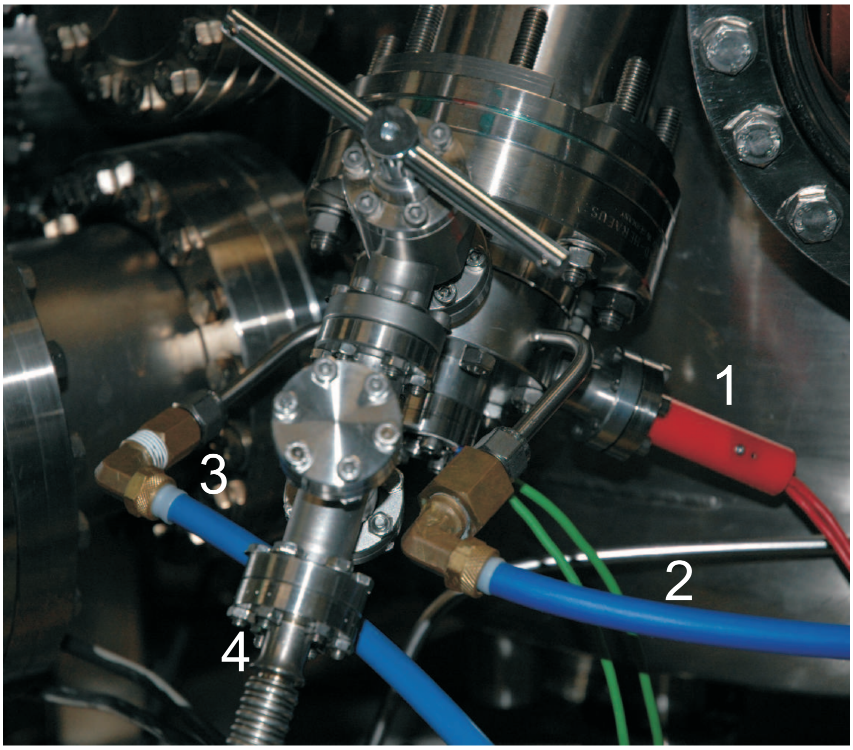

Figure 2.8: Photograph of the connections of the atomic hydrogen source. 1) Electrical contact, (2) water cooling inlet, (3) water cooling outlet, (4) molecular hydrogen gas inlet.

and thus is the ratio $N_H/N_M = 4$. This is higher than the hydrogen to metal ratio for stoichiometric Mg_2NiH_4 (1.3), so every 3^{rd} incoming H atom will be incorporated in the growing film. During the MgH_2 thin film growth this ratio is $H/Mg = 25$.

Chapter 3

Mg-TM-H thin films, an overview

We give here an overview of the structural, thermodynamic and optical properties of Mg_2Ni thin films covered with Pd exposed to hydrogen. Similarly to bulk, thin films of metallic Mg_2Ni take up 4 hydrogen per formula unit and semiconducting transparent $Mg_2NiH_{4-\delta}$ is formed. The dielectric function $\tilde{\epsilon}$ of Mg_2Ni and fully loaded $Mg_2NiH_{4-\delta}$ is determined from reflection and transmission measurements using a Drude-Lorentz parametrization. Besides the two 'normal' optical states of a switchable mirror - metallic reflecting and semiconducting transparent - Mg_2NiH_x exhibit a third 'black' state at intermediate hydrogen concentrations with low reflection and essentially zero transmission. This state originates from a subtle interplay of the optical properties of the constituent materials and a self-organized double layering of the film during loading. $Mg_2NiH_{4-\delta}$ preferentially nucleates at the film/substrate interface and not - as intuitively expected - close to the catalytic Pd capping layer. Using $\tilde{\epsilon}_{Mg_2Ni}$ and $\tilde{\epsilon}_{Mg_2NiH_4}$ and this loading sequence, the optical response at all hydrogen concentrations can be described quantitatively. The uncommon hydrogen loading sequence is confirmed by X-ray diffraction and hydrogen profiling using the resonant nuclear reaction $^1H(^{15}N,\ \alpha\gamma)^{12}C$. Pressure-composition isotherms suggest that the formation of $Mg_2NiH_{4-\delta}$ at the film/substrate interface is mainly due to a locally enhanced kinetics. A hydrogen diffusion model for Mg_2Ni thin films is given. This model, which is based on a lower enthalpy of formation close to the substrate, shows that it is very well possible to have an increased hydrogen concentration close to the film/substrate interface and thus a preferred hydride nucleation. Furthermore, the possibility to use these thin films in devices is discussed.

3.1 General introduction into the structural properties of the Mg-TM-H system

Mg_2NiH_4 is an interesting example of a complex metal hydride with potential both as a storage material and as a switchable mirror. Though its thermodynamical properties are less favorable than that of $NaAlH_4$, its hydrogenation properties may hold important clues for the optimization of complex metal hydrides in general. Mg_2Ni reacts with hydrogen at 1.38×10^5 Pa, at temperatures above 473 K and forms a hydride with 3.6 wt% of hydrogen [24]. However to achieve a desorption pressure of 10^5 Pa or more, as requested for practical applications, the Mg_2NiH_4 hydride has to be heated above 500 K.

Although the only possible stable ternary hydride compound in the Mg-Ni-H phase diagram is Mg_2NiH_4, this compound has still some unresolved properties. The hydrogen solubility range of the hexagonal Mg_2Ni is limited to $Mg_2NiH_{0.3}$ [24, 25]. Bulk Mg_2Ni has a hexagonal symmetry with $a = 5.216$ Å and $c = 13.20$ Å and the lattice mainly expands along the c-axis when hydrogen is dissolved in solid solution ($a = 5.23$ Å and $c = 13.43$ Å) [26]. Stoichiometric Mg_2NiH_4 crystallizes in two phases: a low temperature (LT) phase and a high temperature (HT) phase. Below 510 K the structure is monoclinic with a slightly distorted antifluorite lattice [27]. Heating Mg_2NiH_4 above 510 K, at a hydrogen pressure of one atmosphere, a transition occurs to a cubic HT-phase with the metal atoms in an antifluorite structure [28, 29, 26]. In the HT as well as in the LT phase the hydrogen atoms are covalently bounded to the Ni atoms. The resulting complex $[NiH_4]^{4-}$ is ionically bound to the positively charged Mg^{2+} ion. The charge distribution in the HT Mg_2NiH_4 phase strongly resembles that of the family of Mg_2IVB compounds. Hume-Rothery [30] reported a well-defined antifluorite-type of compounds with composition Mg_2IVB with IVB representing an element of the group (Si, Ge Sn, Pb), for which the antifluorite phase Mg_2IVB is the only stable intermediate phase present in the respective phase diagram [31]. Calculations by Corkill *et al.* [32] and Baranek *et al.* [33] on the electronic structure of these compounds shows that there is a weak Mg-Mg and IVB-IVB bonding and a predominantly ionic bonding between the Mg and IVB atoms. This observation confirms the idea of a $[NiH_4]^{4-}$ entity which is similar to the IVB^{4-} ions. This group of compounds is a subgroup of Mg_2X which is a family of compounds with the antifluorite structure with the Mg ions defining the simple cubic sublattice. The lattice parameters for these antifluorite compounds Mg_2X (with X = Si, Ge, Sn, Pd, FeH_6, CoH_5, and NiH_4) [34] are almost the same. This points to an equivalence between the tetravalent entities Ge^{4-} and $[NiH_4]^{4-}$, $[CoH_5]^{4-}$, and $[FeH_6]^{4-}$. The charge transfer of the Mg atoms towards the IVB atom results in essentially closed s-p electron shells and the IVB atoms tend to complete their octet of valence electrons. Due to these properties, band gaps and nonmetallic behavior is expected [35, 36].

In this light the complexes $[NiH_4]^{4-}$, $[CoH_5]^{4-}$, and $[FeH_6]^{4-}$ can be seen as a sort of pseudo-Ge^{4-} anions. Alternatively they could be considered as quite different valence state arrangements of 18 electrons in closed-shell configurations around the transition-metal atom. Both points of view go along with an inert gas description of the transition metal-hydrogen cluster, and in fact this has its semi-empirical counterpart in the well-known 18-valence electron rule [37]. The main difference between Ge^{4-}, $[NiH_4]^{4-}$, $[CoH_5]^{4-}$, and $[FeH_6]^{4-}$ clusters is the energy ordering of the nine occupied electron levels. This implies that the energy band gap depends on the particular transition metal. Gupta *et al.* [38] reported that nine-band-filling effects appear to be a most important factor when considering the stability of the hydrides Mg_2NiH_4, Mg_2CoH_5 and Mg_2FeH_6 and that the corresponding tetravalent complexes all obey the 18 valence electron rule. Even more generally, Gupta *et al.* [39] reported that the hydrides Mg_2NiH_4, Mg_2CoH_5 and Mg_2FeH_6 belong to a family of antifluorite ternary metal hydrides M_2TMH_x, where M is a divalent simple metal (M = Mg, Ca, Sr) and TM a transition metal (TM = Fe, Co, Ni, Rh, Ir, Ru, Os). For these compounds, x has such a value that the 18 valence electron rule is always satisfied.

Myers *et al.* [40] calculated using an energy minimization that for the LT Mg_2NiH_4 phase the hydrogen atoms are in an almost perfect tetrahedron. However for the high temperature cubic phase Garcia *et al.* determined the hydrogen positions from total energy minimization and found a tetrahedrally distorted square-planar distribution, which is in agreement with neutron diffraction data [34, 41]. Furthermore it is reported that the electronic band structure around the Fermi level of this compound in the HT phase strongly depends on the hydrogen surrounding of the Ni atom. A square planar configuration of $[NiH_4]^{4-}$ results in metallic behavior, a tetrahedrally distorted square planar configuration in a pseudogap, and a regular tetrahedral configuration a semiconducting behavior (which is comparable to the LT phase). Garcia *et al.* also investigated the movement of the hydrogen atoms around the atoms in the high temperature cubic Mg_2NiH_4 form. They found the typical in-plane and out of plane jump frequencies to be $4 \times 10^{13} e^{-1.29eV/kT}$ s^{-1} and $3 \times 10^{13} e^{-0.67eV/kT}$ s^{-1} respectively. It is this movement which makes the exact determination of the hydrogen positions difficult.

Several other complex metal hydride compounds containing Mg and a first row transition metal are reported. These include Mg_2CoH_5 [42], $Mg_6Co_2H_{11}$ [43], Mg_2FeH_6 [44] and Mg_3MnH_7 [45] The ternary hydrides Mg_2CoH_5 and Mg_2FeH_6 do not undergo a structural phase transition at 510 K and resemble the structure of the HT cubic form of Mg_2NiH_4. Cubic Mg_2FeH_6 has ${FeH_6}^{4-}$ octahedra units and Mg_2CoH_5 has square-pyramidal ${CoH_5}^{4-}$ units. These square-pyramidal units also appear in the compounds $Mg_6Co_2H_{11}$, along with saddle-like ${CoH_5}^{4-}$ complexes. Mg_3MnH_7 contains nearly octahedral ${MnH_6}^{5-}$ units bridged by Mg in trigonal prismatic coordination, along with an isolated hydride ion bonded only to Mg [8, 9]. Band structure calculations for Mg_2CoH_5 (E_g = 1.92 eV) Mg_2FeH_6 (E_g = 1.8 eV) [38] support experimental evidence for semiconductor behavior in these materials. Mg_3MnH_7 (with calculated E_g = 2.56 eV) [46] has an orange color and is presumably semiconducting. The enthalpies of formation of Mg_2CoH_5 and Mg_2FeH_6 are -86 and -98 kJ/mol H_2 respectively [42]. Dissociation pressures at 298 K are estimated to be 5.07×10^{-4} Pa for Mg_2CoH_5, 4.05×10^{-6} Pa for Mg_2FeH_6, and 0.10 Pa for MgH_2.

3.2 Hydrogenation of Mg-Ni thin films

3.2.1 Structural investigation XRD

Schefer *et al.* measured for bulk Mg_2Ni a hexagonal symmetry with a = 5.216 Å and c = 13.20 Å and found that the lattice mainly expands along the c-axis when hydrogen is dissolved to form a solid solution (a = 5.23 Å and c = 13.43 Å) [26]. As reported by Richardson *et al.* as-prepared Mg-Ni thin films where amorphous by X-ray diffraction and annealing these films at 398 K resulted in reflections of Mg_2Ni, Mg and Mg_6Pd for Mg rich samples [8, 9]. Post-annealing rendered these samples to become inert to hydrogenation. Song *et al.* investigated phase separation due to hydrogenation cycles of bulk Mg_2Ni with X-ray diffraction measurements [47]. They found that a small contamination with O_2 of the H_2 gas reacts with Mg_2Ni to form MgO. This reaction is accompanied by a Ni segregation which results eventually in the formation of the $MgNi_2$ phase. These two examples indicate a few important properties of the Mg-Ni system as encountered by X-ray measurements. First, the preparation of crystalline (LT) Mg_2Ni thin films is very difficult. Second, a possible contamination of the Mg_2Ni phase by e.g. O_2, C, S etc. can have large influences on the crystalline structure and increases the amorphousness of the original phase. Furthermore, the crystallinity decreases upon hydrogenation and annealed Mg_2Ni thin films to improve the crystallinity are almost inert to hydrogenation.

Lohstroh *et al.* measured with X-ray diffraction the structural changes upon hydrogenation of Mg_2Ni thin films. Figure 3.1 shows the X-ray diffraction spectra in a θ-2θ configuration of a 200 nm thick Mg_2Ni film capped with 3 nm Pd. The two peaks correspond to the (003) and (006) reflection of hexagonal Mg_2Ni. The c-axis lattice parameter deduced from the peak positions 2θ (003) = 20.13°, 2θ (006) = 40.94° amounts to c = 13.23 Å which is comparable with the bulk value as found by Schefer *et al.* [26]. The absence of other reflections in these thin films indicates textured growth with the c-axis of the hexagonal lattice in the direction of the layer normal. However it is found that the crystallinity also for these samples is poor, which is confirmed by the width of the rocking curve around the (003) reflection (larger than 8°).

The structural changes due to the hydrogenation process on the structure

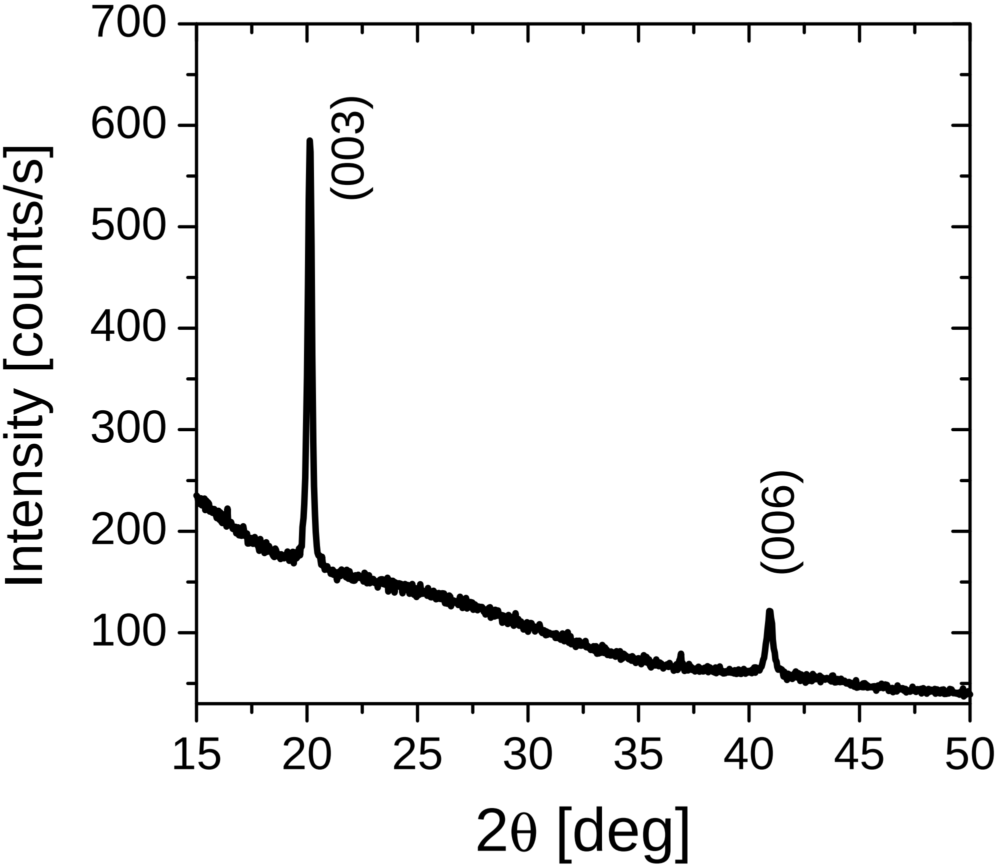

Figure 3.1: X-ray diffraction spectra of a 200 nm thick as deposited sample of Mg_2Ni capped with 3 nm Pd. The Mg_2Ni (003) and (006) reflections point to textured growth of the hexagonal lattice with the c-axis out of plane. The c-axis lattice parameter (c = 13.23 Å) is close to the bulk value (c_{bulk} = 13.20 Å). The background intensity originates from the glass substrate.

of Mg_2Ni is monitored around the (003)-Bragg reflection. In figure 3.2 the lattice parameter and the peak intensity are shown as the hydrogen pressure is increased stepwise up to 0.95×10^5 Pa. The data are plotted as a function of resistivity which is a measure of the hydrogen concentration in the sample.

In the solid solution regime $\log\rho \sim x$ and a linear increase of the c-axis is observed until a lattice spacing of c = 13.41 Å is reached at ~0.065 mΩcm. The peak intensity and width remain constant during the expansion, hence hydrogen dissolves in the host lattice without changing the crystal symmetry. A comparison with the bulk value for $Mg_2NiH_{0.3}$ (c = 13.43 Å) [26] and with the electrochemical loading experiments confirms that the solubility range $0 \leq x \leq 0.3$ is only marginally affected by the thin film geometry or the clamping to the substrate. Usually, the adhesion to the substrate strongly influences

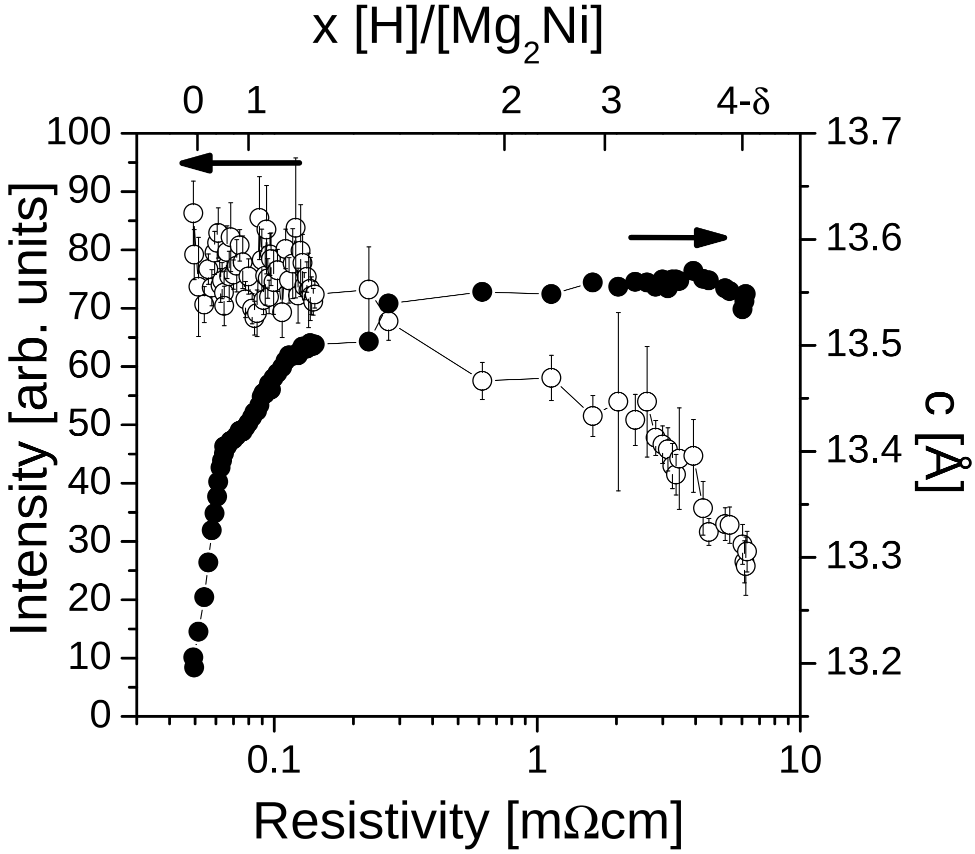

Figure 3.2: c-axis lattice parameter (•) and amplitude (◦) of the (003) reflection during hydrogen loading. At low hydrogen concentration (i.e., at low resistivity) a linear increase of c is observed. Eventually, c remains constant and the peak intensity starts to diminish around $\rho \approx 0.25$ mΩcm. The hydrogen concentration (upper scale) is estimated from electrochemical loading experiments.

the hydrogen uptake in thin films and superlattices [48, 49, 50]. In the case of Mg_2NiH_x ($0 \leq x \leq 0.3$) the expansion is mainly along the c-axis which - in the textured films - can almost freely expand along the layer normal.

Noréus *et al.* and Soubeyroux *et al.* showed that a $Mg_2NiH_{0.3}$ could be obtained by a conventional hydrogenation process [25, 51]. Mintz *et al.* determined the solid solution in Mg_2NiH_x by means of X-ray measurements and found that the solubility limit of hydrogen is around $Mg_2NiH_{0.27}$ [52]. Several investigations showed that upon hydrogenating $Mg_{2+\epsilon}Ni$ above this solid solution limit, the first hydride formed is MgH_2 rather than Mg_2NiH_4 [24, 53, 54]. Post *et al.* investigated the hydriding of a $Mg_{2.42}Ni$ sample and found that $Mg_2NiH_{0.2}$ was formed first (which corresponds to the solid solution in $Mg_2NiH_{0.3}$) and subsequently the excess of Mg was hydrided to form MgH_2 whereafter the Mg_2NiH_x further loaded to the fully hydrided phase, Mg_2NiH_4 [55]. The possible reason for this loading sequence is that the chemical potential of hydrogen in MgH_2 is much more negative than in Mg_2NiH_4. This hydrogenation sequence is theoretically confirmed by Zeng *et al.* [56].

For hydrogen concentrations above $x \approx 0.3$ Lohstroh *et al.* showed that deviations from the linear expansion of the c - axis occur as shown in Fig. 3.2 and Fig. 3.3. Furthermore, the diminishing intensity of the (003) reflection points to a decreasing of the $Mg_2NiH_{0.3}$ volume fraction as the two phase region $Mg_2NiH_{0.3}$-$Mg_2NiH_{4-\delta}$ is entered. However, Lohstroh *et al.* could not follow the whole hydrogenation cycle by X-ray measurements and the crystal structure of semiconducting $Mg_2NiH_{4-\delta}$ thin films could not be resolved. It is concluded that the crystal structure is either nanocrystalline or amorphous. The $Mg_2NiH_{0.3}$ to $Mg_2NiH_{4-\delta}$ phase transition involves a 32 % volume expansion and a thorough rearrangement of the atomic positions, it is not surprising that the initially poor crystallinity further deteriorates. Similar results have been reported earlier for the crystal structure of $Mg_2NiH_{4-\delta}$ thin films [57, 58].

Farangis *et al.* [59] found by investigating the direct environment of the Mg - atoms by Extended X-ray Absorption Fine Structure (EXAFS) that these samples (which were X-ray amorphous after deposition) exhibit order on a microscopic scale up to the second shell neighbors with reduced coordination numbers. The degree of local order decreases with increasing Ni content. After hydrogenation, no EXAFS oscillations could be detected suggesting weak scatterers with a low coordination number located around Mg, and a further deterioration of the crystalline order. Furthermore, the hydrogenation process (in a helium atmosphere with 4% hydrogen) was incomplete in stoichiometric Mg_2Ni thin films i.e. the signature of metallic Mg_2Ni was still present in the EXAFS spectra [59]. Di Vece *et al.* showed that EAXFS at the Ni absorption edge of $Mg_2NiH_{4-\delta}$ films suggests that H is situated in the vicinity to the Ni-atoms and $[NiH_4]^{4-}$ clusters are formed [58]. After unloading, the Mg_2Ni - Bragg reflection is partially regained which is presumably due to the heat treatment used in the unloading procedure. These findings make clear that the crystallinity of thin Mg_2Ni films is very low and cannot easily be improved by means of annealing or deposition techniques.

For bulk powder samples Blomqvist *et al.* showed that Mg_2NiH_4 is thermodynamically stabilized by stacking faults at unit cell level in the lattice [60, 61]. This effect, called microtwinning, depends on the thermal history of the sample and on the excess of Mg. It is reported that the excess of Mg stabilizes the Mg_2NiH_4 phase. Furthermore, microtwinning could be induced by mechanical pressure and oxygen contamination [51, 62]. When the LT Mg_2NiH_4 phase is heated up to the phase transition at 510 K, microtwinning is induced by the reorientational motion of the tetrahedral $[NiH_4]$ complexes. Microtwinning counteracts Mg doping, and the hydride becomes non-conducting. The microtwinning is, however, sensitive to mechanical pressure. By compressing the hydride the microtwinning is reduced and the hydride becomes conducting again, and also loses its stability. Since the Mg_2NiH_4 phase can be formed during hydrogenation in Pd capped thin Mg-Ni films at room temperature and at moderate pressures (up to 10^5 Pa H_2), it is not subjected to the high-to-low temperature phase transition at which microtwinning is introduced. Therefore it is expected that this mechanism is not present in thin films at these pressure and temperatures [60, 61].

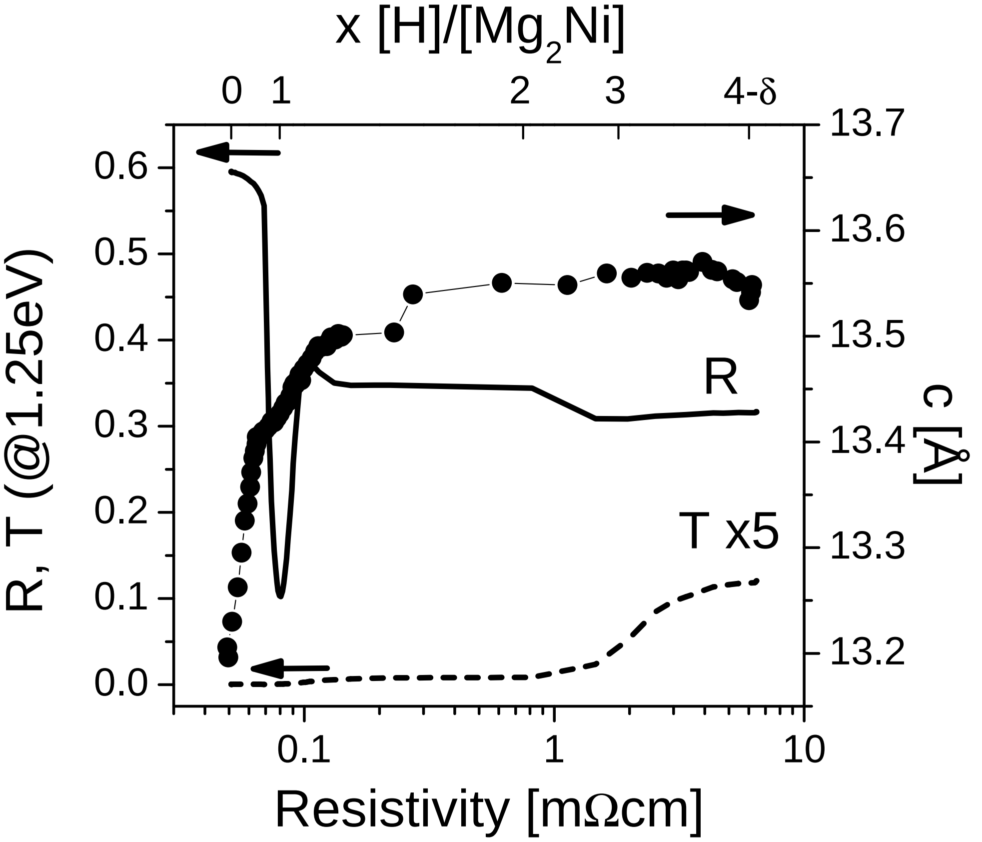

Figure 3.3: Comparison of c-axis expansion (●) with reflection R and transmission T (at 1.25 eV) for a sample 200 nm Mg_2Ni capped with 3 nm Pd. In solid solution (for $x \leq 0.3$), R shows metallic reflectivity. At the beginning of the two phase regime $Mg_2NiH_{0.3}$ -$Mg_2NiH_{4-\delta}$ the c-axis expansion exhibits a kink and simultaneously R decreases dramatically. Transmission is only observed for $x \geq 3.0$. For reasons of clarity T is multiplied be a factor 5. The hydrogen concentration (upper scale) is estimated from electrochemical loading experiments.

3.2.2 Electrical properties

The temperature (between 2 K and 280 K) and concentration (for $0 < x < 4$) dependencies of the electrical resistivity, charge carrier density and magnetoresistance of Mg_2NiH_x thin films were investigated by Enache *et al.* [63]. They showed that the charge carrier density n_{dc} (obtained form Hall-effect measurements) decreases linearly with increasing hydrogen concentration x. Although the electrical resistivity increases by almost three orders of magnitude during the hydrogenation from metallic Mg_2Ni to Mg_2NiH_4, the charge carrier concentration n decreases only gradually from typically 10^{23} cm^{-3} to 10^{21} cm^{-3}. These metallic-like features indicate that $Mg_2NiH_{4-\delta}$ prepared at room temperature under 1.3×10^5 Pa H_2 behaves as heavily doped semiconductor and that the estimated non-stoichiometry is $\delta = 0.05$ [63]. By combining Hall effect, electrical resistivity and electrochemical data, it is found that the charge carrier density n varies like (4-x) with x indicating the hydrogen concentration. This behavior shows that the hydrogen atom behaves as a negatively charged H- ion, in agreement with the anionic hydrogen model where each hydrogen removes one electron from the conduction band to form the negatively charged $[NiH_4]^{4-}$ complexes in groups I, II and III of the periodic table [64]. When the Mg_2NiH_4 thin film is completely loaded it behaves like a semiconductor, which is in agreement with the electronic ground state of the low-temperature Mg_2NiH_4 phase as calculated by Myers *et al.* [40] Enache *et al.* did not know that there was a double layer in these type of films. The linear decrease of n with increasing x is thus only a manifestation of the double layer. However the end state data of $Mg_2NiH_{3.95}$ are still valid [63].

3.2.3 Optical properties Mg-TM-H systems

That Mg-Ni alloys change their optical appearance upon hydrogenation is already known for decades. Reilly *et al.* found already in 1968 that metallic Mg_2Ni changes optically to a reddish Mg_2NiH_4 compound upon hydrogenation [24]. Lupu *et al.* (1987) found a band gap of 1.68 eV for the low temperature [LT] as well for the high temperature [HT] Mg_2NiH_4 phases from resistivity data and reflection measurements on powder samples [65]. Selvam *et al.* measured two gaps, 2.0 eV and 2.4 eV, the direct respectively the indirect gap of Mg_2NiH_4 [66]. A gap of 1.3 eV for a film of unknown composition was found by Fujita *et al.* from resistivity data and optical measurements for both the LT and HT phases [67]. Isidorsson *et al.* [57] estimated from transmission edge measurements a gap of 1.6 eV for Mg_2NiH_4 thin films, which is in reasonable agreement with the band structure calculations of Myers *et al.* and Häussermann *et al.* [40, 68]. The large spread in values of the optical data indicates that a well defined characterization of the samples is very important and the preparation with a well defined composition and morphology must be accurately controlled.

In 2001 Richardson *et al.* showed that Mg-Ni films can be hydrogenated at room temperature and low pressures when they are capped with a thin Pd caplayer [8, 9]. This is in sharp contrast with bulk Mg-Ni samples for which high temperatures up to 600 K and high hydrogenation pressures of 10^5 to 10^6 Pa are usually needed [24]. So far all the alloys of Mg with transition metals Ni, Co, Fe ,Mn, V have been found to switch upon hydrogenation [8, 9]. However not all the alloys form a stoichiometric phase Mg-TM before hydrogenation. In case of nickel a stoichiometric alloy phase, Mg_2Ni, with the same Mg-Ni ratio as the hydride, can be prepared from the elements. This is the reason why a Mg_2Ni film is used in many experiments as a model system. The unloading of these Pd capped thin films is usually done in air.

During measurements of reflection, transmission and the electrical resistivity during hydrogenation of a $Mg_{2.1}NiH_x$ thin film, Isidorsson *et al.* found that an unexpected behavior of the reflection occurs [57]. Above the solid solution, $x = 0.3$, the reflection drops markedly and reaches a minimum ($R \leq 10\%$) at $x \simeq 0.8$. During this decrease the optical transmission remains very low (typically 0.001) until x is almost 4. The electrical resistivity at this minimum in reflection is still relatively low and is in the order of 100 $\mu\Omega$cm. In a simple Drude model a decreasing reflection R is due to a decreasing plasma energy $\omega_p^2 = n_e e^2/\epsilon_0 m$ (n_e: effective charge carrier density, ϵ_0: vacuum permittivity, e: electron charge and m: electron mass). Such a simple analysis would give a decrease of the charge carrier density by a factor 25 % [57]. Enache *et al.* reported that the Hall effect measurements do not confirm such an abrupt decrease of n_e. This seems to be mutually incompatible since metals always have a large reflection. The low reflection and transmission imply a high absorption of $\geq 75\%$ of the incoming light.

3.3 Optical black state

3.3.1 Properties of the black state

The results described above stimulated an extended research to unravel the origin of this peculiar optical behavior. Lohstroh *et al.* performed a detailed investigation of the hydrogenation behavior of Mg_2Ni thin films. The effect is illustrated in figure 3.4, where the reflection R and transmission T are shown at various hydrogen concentrations for a 250 nm thick Mg_2NiH_x sample covered by 7 nm Pd. The resistivity increases from 0.061 mΩcm in the metallic Mg_2Ni state (corresponds to Fig. 3.4 (a)) to 1.37 mΩcm for semiconducting, transparent Mg_2NiH_4 (corresponds to Fig. 3.4 (c)), the later value being mainly limited by the metallic Pd layer on top. At intermediate hydrogen concentrations, R decreases dramatically over the entire visible spectrum whereas T remains extremely low as shown in Fig. 3.4(b). Around 1.5 eV a broad

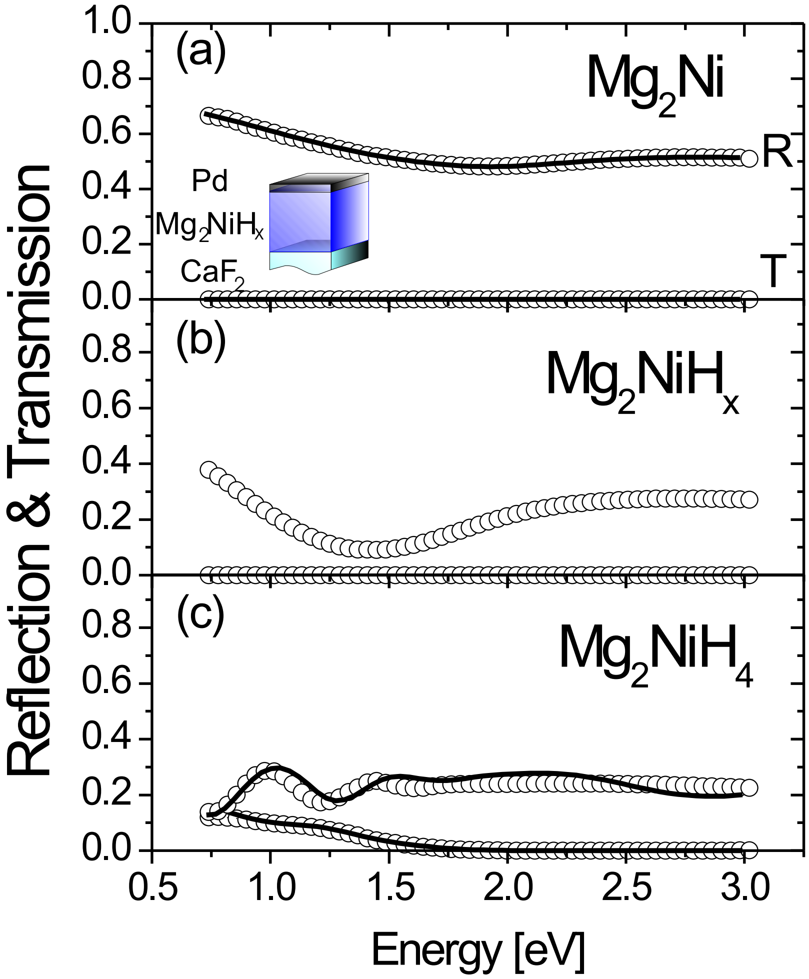

Figure 3.4: Reflection R and transmission T of a 250 nm Mg_2Ni / 7 nm Pd film on CaF_2. (a) as deposited Mg_2Ni, (b) black Mg_2NiH_x and (c) fully loaded Mg_2NiH_4. The reflection is measured through the substrate. At intermediate hydrogen concentrations, R exhibits a deep minimum around 1.5 eV and stays below 25 % over the entire visible range while is T very low ($T < 10^{-4}$). The solid lines are calculations (see text) using known dielectric functions for Mg_2Ni and Mg_2NiH_4. The curves in (b), corresponding to the black state, cannot be fitted with any choice of the refraction index n and extinction coefficient k for the Mg_2NiH_x layer.

minimum ($R \leq 10\%$) is observed.

The peculiarity of the optical black state is obvious when one tries to fit the reflection and transmission spectra with an effective medium approximation for a homogeneous Mg_2NiH_x layer. For this one calculates R and T for the entire sample by means of a transfer matrix method that considers reflection

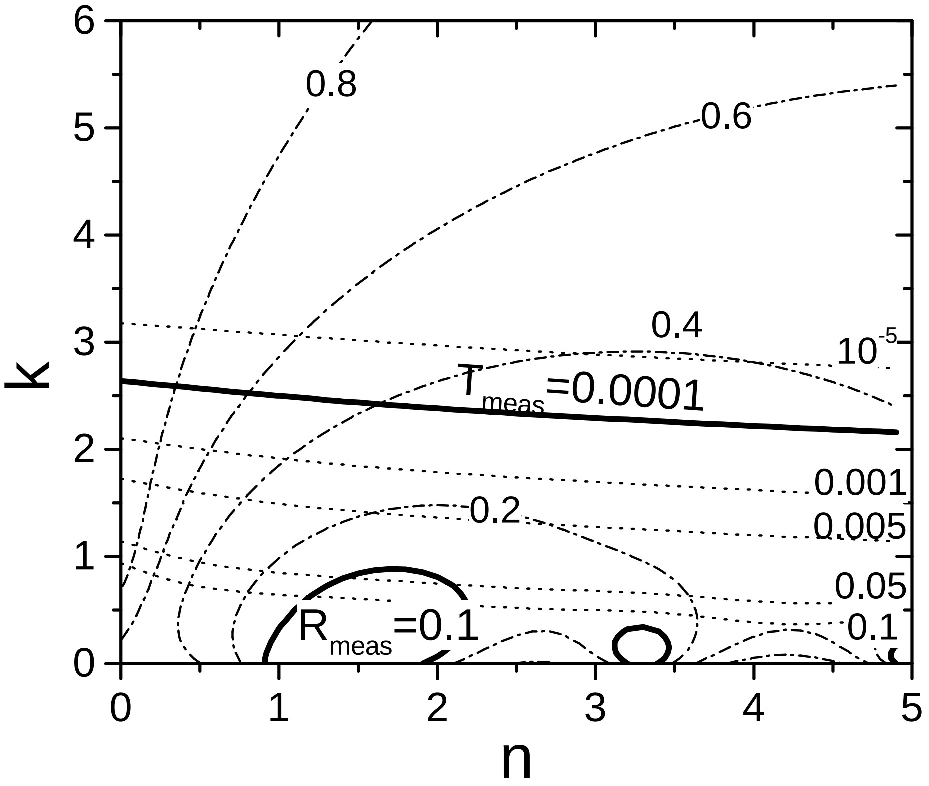

Figure 3.5: Contour maps of the reflection (- ·) and transmission (···) calculated for a sample 250 nm Mg_2NiH_x / 7 nm Pd on a CaF_2 substrate. The incoming beam ($\hbar\omega$ = 1.5 eV) reached the layer through the substrate and (n,k) are those of the Mg_2NiH_x layer. The contours of the experimentally obtained values R_{meas} and T_{meas} are indicated (thick lines). There exists no couple (n,k) that describes simultaneously the experimentally observed reflection R_{meas} and transmission T_{meas}, i.e. these contours never cross.

and transmission at each interface and absorption in each layer (i.e. 7 nm Pd - 250 nm Mg_2NiH_x on Ca_2F). The refraction indices for Ca_2F and Pd are known (Ref. [15]) and R and T are then calculated for a dense grid of (n,k) values for the Mg_2NiH_x layer [69]. Possible solutions for (n,k) are found when R and T coincide with the experimental values.

Figure 3.5 gives the results of such a calculation for incoming light with an energy of $\hbar\omega = 1.5$ eV. There is no couple (n,k) that simultaneously describes the measured values R_{meas} and T_{meas} (indicated by thick lines). The discrepancy is quite serious since a 10^3 larger transmission would be necessary for the lines to cross and it persists for all energies between 0.8 eV and 2.5 eV. Although the particle size D ranges from $\approx$ 30 nm for the metallic sample to nanocrystalline (too small to be detected with x-rays) in the fully loaded state and hence $D << \lambda$ (λ: wavelength of light) effective medium theories

[70] fail to explain the optical properties. Measurements of the total reflection and transmission coincide within experimental errors with the measured specular reflection and transmission hence confirm that the diffuse scattering is negligible and can be excluded as a reason for low reflection.

Lohstroh *et al.* demonstrated that the highly absorbing state in Mg_2NiH_x can be explained by a subtle interplay of the effective dielectric function $\tilde{\epsilon} = \epsilon_1 + i\epsilon_2$ (which is related to the refractive index n and extinction coefficient k by $\epsilon_1 = n^2 - k^2$ and $\epsilon_2 = 2nk$) and a self - organized double layering of the Mg_2NiH_x film during hydrogenation[71, 72, 73]. It is shown that although the hydrogen is physisorbed, chemisorbed and absorbed by the Pd layer and subsequently diffuses into the Mg_2Ni film, the nucleation of the hydrogen-rich phase starts deep in the sample near the film-substrate interface. This preferred hydride nucleation is obvious when the sample is observed simultaneously from both sides: once through the transparent substrate and once through the Pd cap layer side. Figure 3.6 displays photographs taken from two pieces of the same sample (a) in the metallic Mg_2Ni state and (b) black Mg_2NiH_x, respectively. On the left hand side the view is through the substrate and on the right hand side the Pd cap layer faces the front. Without hydrogen, both sides are shiny reflecting, and the small difference in appearance is mainly due to the different media for the incoming light (sapphire, which is optically thick and air). After hydrogen is introduced at a pressure of 1.6×10^3 Pa, it takes a couple of minutes for Mg_2NiH_x to become black when viewed through the substrate. Surprisingly, at the same time Mg_2NiH_x keeps a metallic appearance when observed from the Pd side. Note, that the Pd cap layer (5 nm) has a rather high transparency ($T > 40\%$) and hence the Mg_2NiH_x layer underneath contributes significantly to the observed reflection. These photographs demonstrate vividly that the originally homogenous film starts to react with hydrogen at the substrate-film interface. It is indicated that further H-uptake causes the hydrogen-rich layer to grow at the expense of the metallic part until eventually the entire film has switched to Mg_2NiH_4.

Due to the double-layering and the transparency of Mg_2NiH_4, the reflection exhibits typical interference fringes when the optical path of the light reflected between the two interfaces fits a multiple of the wavelength (see Fig. 3.7). With increasing hydrogen concentration the increasing thickness of the layer Mg_2NiH_4 yields to a shift of the interference fringes towards lower energies as well as to a smaller difference between adjacent maxima.

The increasing thickness of the evolving Mg_2NiH_4 layer can be directly determined from the experimental reflection data as shown in Fig. 3.8. The solid lines are model calculations of R in accordance with the above described scenario. The dielectric function of Mg_2Ni, $Mg_2NiH_{0.3}$ and Mg_2NiH_4 has been determined independently [72]. In Figs. 3.8 (b) and (c) a self-organized double layer $Mg_2NiH_{0.3}$ / Mg_2NiH_4 is assumed for the transfer matrix calculation (see sketch in Fig. 3.8).

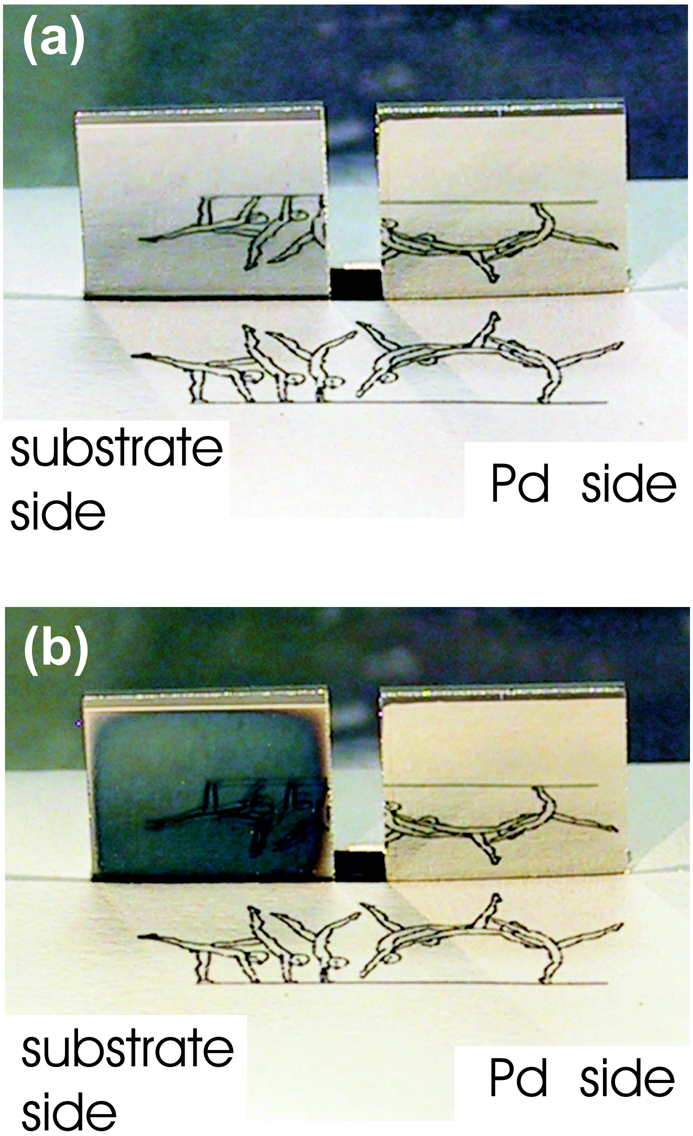

Figure 3.6: Photographs of two identical films 200 nm Mg_2Ni / 5 nm Pd on sapphire. On the left hand side we look at the film through the substrate and on the right hand side from the Pd layer side. (a) As deposited: both sides appear metallic as can be seen from the reflection of the test pattern in front of the samples (b) Upon exposure to hydrogen (1.6×10^3 Pa at room temperature) the "substrate" side of the sample becomes black while the "Pd" side stays metallic. The difference in appearance is not due to the thin metallic Pd cap layer but to the nucleation of the hydrogen-rich phase Mg_2NiH_4 at the film-substrate interface.

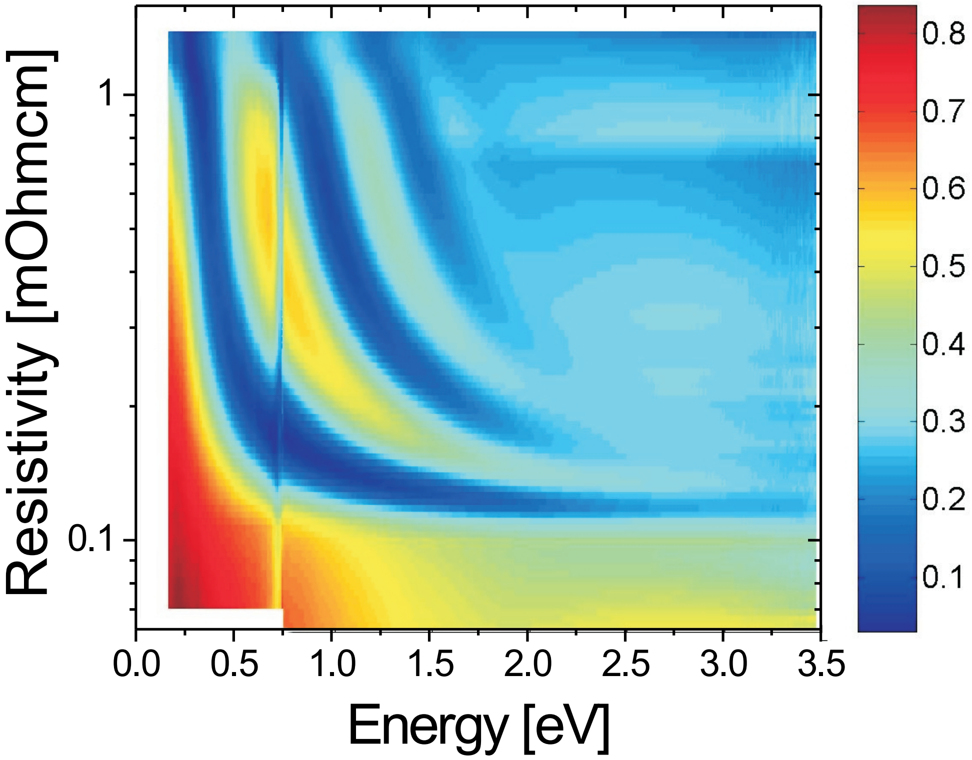

Figure 3.7: Intensity map of the reflection R (measured through the substrate) during hydrogen uptake of a sample 250 nm Mg_2Ni / 7 nm Pd. The resistivity is a measure for the hydrogen concentration, upon loading ρ increases from 0.061 mΩcm (metallic Mg_2Ni) to 1.37 mΩcm (semiconducting Mg_2NiH_4). At low resistivity (that is in the metallic state) R is high. At around $\rho = 0.13$ mΩcm R exhibits a deep minimum over the entire visible wavelength regime. A double layer system $Mg_2NiH_{0.3}$-Mg_2NiH_4 is formed and subsequently interference minima and maxima appear. As the transparent layer increases in thickness these interference fringes shift to lower energies. Around 0.75 eV is an artifact of the measurement due to an absorption line in the background.

The only free parameter is the thickness of Mg_2NiH_4 which varies from $d \approx 30$ nm to the total thickness 250 nm. In Fig. 3.8(a) (in the black state), the bottom layer close to the substrate ($\sim$ 30 nm) is presumed to consist of a mixture $Mg_2NiH_{0.3}$ and Mg_2NiH_4. This mixture of metallic and semiconducting particles ($D << \lambda$) can be described within the effective medium Bruggeman approximation for spherical particles [70] and an effective dielectric function for a volume ratio 20 vol% $Mg_2NiH_{0.3}$ - 80 vol% Mg_2NiH_4 was assumed in the 30 nm layer close to the substrate with 220 nm metallic $Mg_2NiH_{0.3}$ on top. The agreement of the calculated curves with the experimental data confirm that black Mg_2NiH_x can be understood as the result of the interplay of the

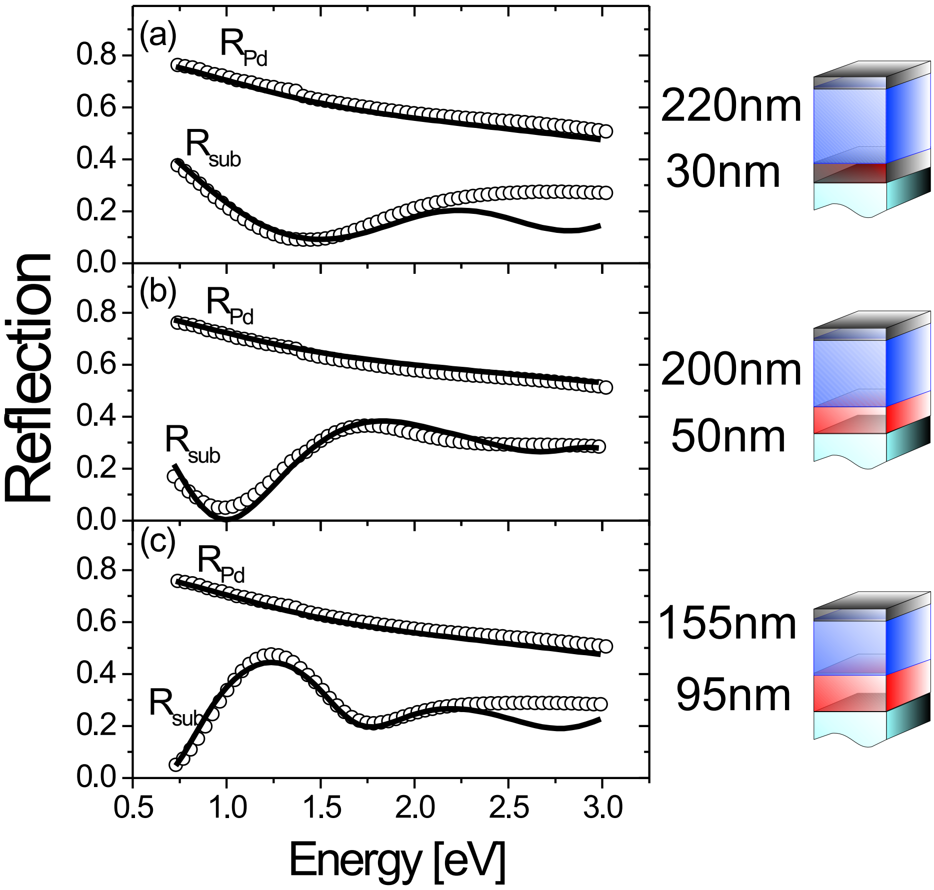

Figure 3.8: Reflection spectra R (○) of a 250 nm Mg_2NiH_x / 7 nm Pd on CaF_2 sample measured through the substrate (R_{sub}) and from the Pd side (R_{Pd}) at various H concentrations (at $\rho = 0.13$, 0.14 and 0.18 mΩcm, compare Fig. 3.7). The solid lines are model calculations that assume a self-organized double layer, as sketched schematically on the right. The thickness used in the calculations for the evolving bottom layer Mg_2NiH_4 is 30, 50 and 95 nm. The remaining part of the film (220, 200 and 155 nm) is assumed to be $Mg_2NiH_{0.3}$.

composition dependent effective dielectric function of the mixed layer and the self-organized layering of the system. The composite layer near the substrate effectively suppresses the reflection whereas the metallic $Mg_2NiH_{0.3}$ on top inhibits any transmission and ensures a metallic conductivity. The discrepancy between the experimental data and theory at higher energies is most likely due to non-ideally flat interfaces of the self-organized double layer. The assumption of a volume ratio 20 vol% $Mg_2NiH_{0.3}$ - 80 vol% Mg_2NiH_4 for the first 30 nm close to the substrate is not essential as Borsa *et al.* have shown [74]. It is also possible with a 30 nm layer of Mg_2NiH_4 hydride phase to obtain a perfect fitting of the optical spectra.

As indicated by Lohstroh *et al.* this self-organized layering process is fully reversible. During hydrogen unloading reflection, transmission and resistivity go through the same stages as during loading but in reversed order. In Fig. 3.9 the difference between hydrogen loading and unloading is indicated. Upon absorption hydrogen enters at the Pd and unexpectedly diffuses directly towards the substrate side. There it starts to form the hydride and this phase grows in the direction of the film surface (see Fig. 3.9a). In Fig. 3.9b the unloading process of the Mg_2Ni film is indicated. The dehydrogenation now starts at the film surface, which is fully understandable from a standard diffusion point of view.

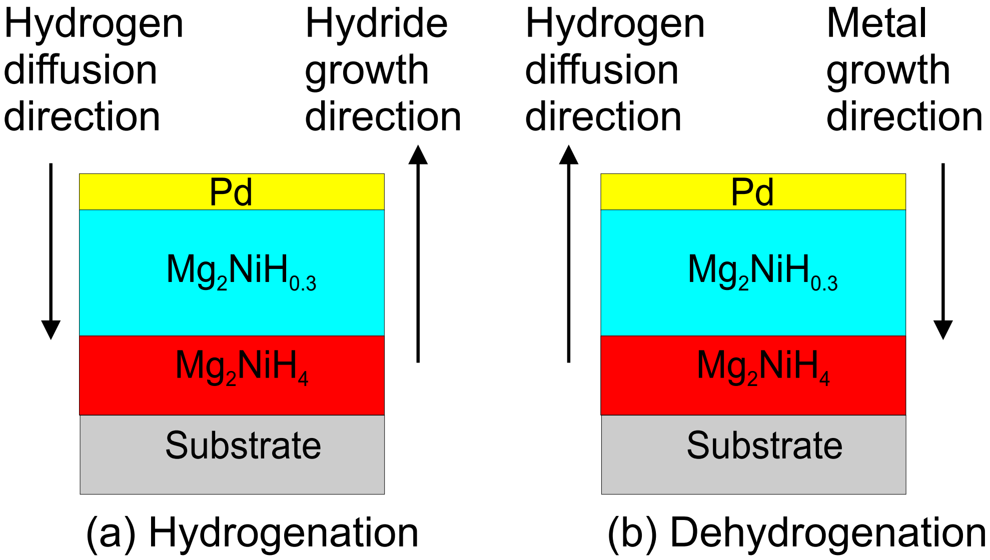

Figure 3.9: (a) Schematic model of the hydrogen absorption by a Mg-Ni thin film. Hydrogen enters at the Pd side and the Mg_2NiH_4 hydride starts to form at the substrate side. (b) Hydrogen desorption by the same film. Now the hydrogen leaves the film at the Pd side and this is also where the hydride to metal transition starts.

As found by Isidorsson *et al.* and Van Mechelen *et al.* [10, **?**] the Mg/Ni ratio influences the nucleation of the Mg_2NiH_4 hydride phase throughout the film. In slightly Mg-rich films (with $2.0 < y < 2.4$) only the first minimum and maximum are observed, pointing to the formation of a double layer with ill-defined interfaces. Borsa *et al.* investigated this composition dependent effect in detail by combining optical and electrical measurements with calculations of the expected reflection, transmission and electrical resistivity using a transfer matrix method and a mean-field model (Bruggeman). They found that during the first stages of the hydrogenation process, the $Mg_{2\pm\delta}NiH_y$ films consist of a self-organized double layer structure with at the substrate/film interface a transparent Mg_2NiH_4 layer and a $Mg_2NiH_{0.3}$ top-layer. This prefered hydride nucleation and concomitant optical black state does not depend on composition. The hydrogenation process of the rest of the film depends critically on the composition of the Mg-Ni alloy. Hydrogenation of Mg_yNi films with $2 < y < 2.5$ takes place by a random nucleation and growth of the Mg_2NiH_4 phase within the remaining metallic $Mg_2NiH_{0.3}$ top layer. For thin films of composition Mg_yNi films with $1.7 < y < 2$ the already formed Mg_2NiH_4 layer at the substrate increases in thickness at the expense of the $Mg_2NiH_{0.3}$ top layer, resulting in a more extended interference pattern.

An optical black state related to a preferred hydride nucleation is also observed in other Mg-TM systems (e.g. like Mg-Co, Mg-Fe and Mg-Co-Ni [75]). However the hydride nucleation in these thin films depends on the hydrogenation history of the film. The spatial separation of the hydrogen uptake at the catalytic Pd layer and subsequent nucleation of the hydride (Mg_2NiH_4, Mg_2CoH_5 and Mg_2FeH_6) at the film-substrate interface seem to be inherent to these systems. A preferred hydride nucleation near the substrate occurs in sputtered films as well as in UHV thermal deposited thin films and is little influenced by the used deposition technique. It is also independent of the kind of substrates used (Si, SiO_2, CaF_2, sapphire, quartz, ITO covered glass) [16]. The initial hydride nucleation at the substrate interface does not depend on composition for Mg/Ni-ratios between 1.5 and 6 [76].

The optical black state observed for Mg_2TMH_x thin films has a different origin as compared to Mg-RE thin films (RE: rare-earth). Giebels *et al.* showed that in these Mg-RE thin films the black state results from a spatial disproportionation in Mg and REH_2 grains upon hydrogenation. The optical black state in these Mg-RE-H systems is caused by the coexistence of nanograins of metallic Mg and insulating (dielectric) MgH_2 [77]. The same effect is observed for Mg-Gd [78, 79], Mg-La [77, 80] and Mg-Sc [81] films.

Since these films absorb hydrogen quite easily at room temperature and at reduced hydrogen pressures as compared to bulk samples (pressures well below 10^5 Pa) indicates the importance of the small grain size for the hydrogenation process and the use of a Pd caplayer (typical for these thin films). The preferred hydrogenation at the film/substrate interface, suggests a tunability of the preferred hydride nucleation. This suggests new strategies for the optimization of catalysts in, for example, nanostructured hydrogen storage materials.

3.3.2 Hydrogen depth profiling

To prove the coexistence of two phases in separate layers and preferred hydride nucleation at the interface, Lohstroh *et al.* measured the hydrogen depth profile at two stages of the hydrogenation process, for a thin film in the black state and in the fully loaded $Mg_2NiH_{4-\delta}$ state.

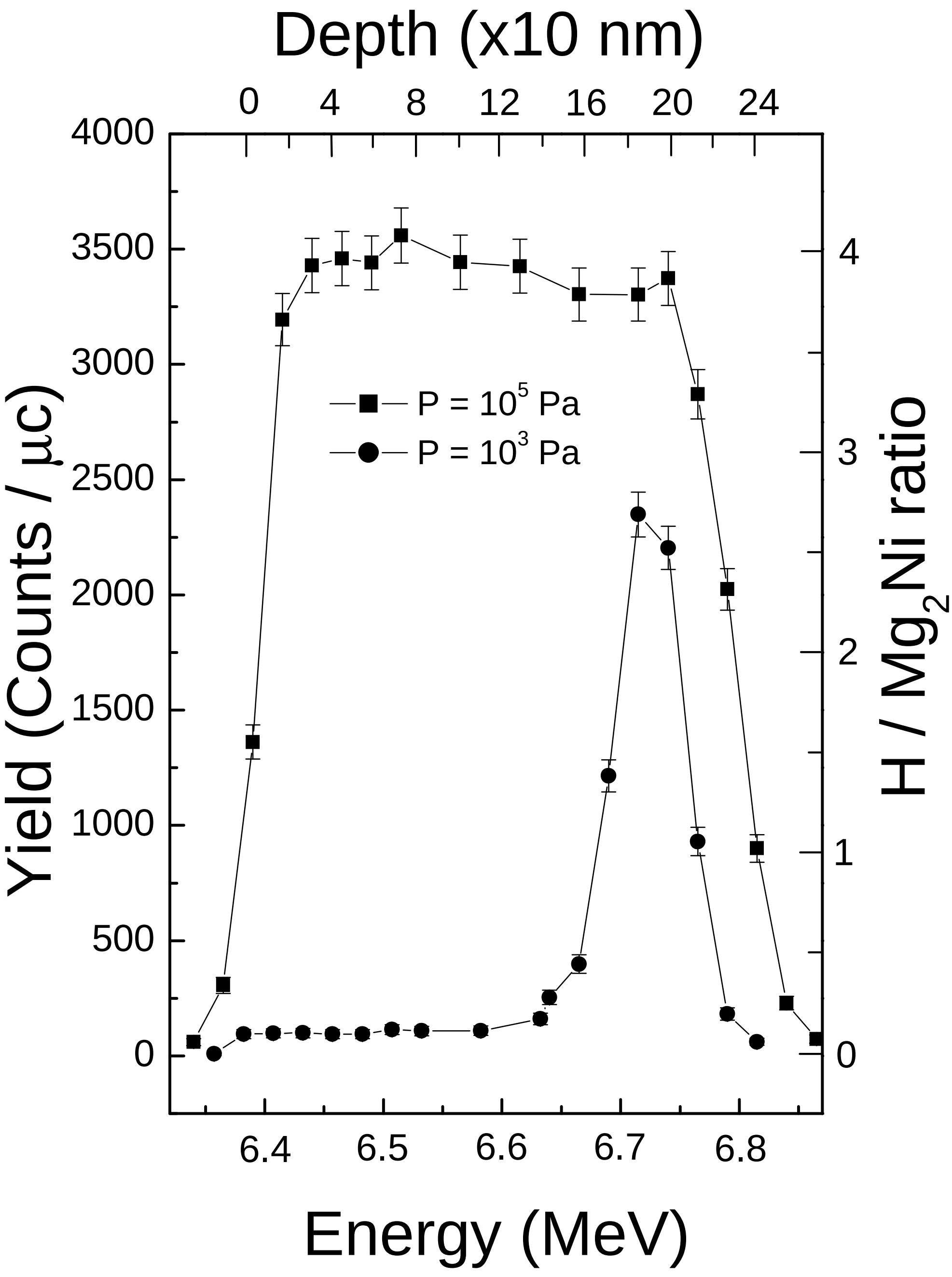

Figure 3.10: Hydrogen depth profiling of a 200 nm thick Mg_2Ni film capped with 5 nm Pd. The sample is first hydrogenated at 10^3 Pa to generate the black state (circles) and subsequently exposed to 10^5 Pa to measure the fully loaded sample (squares).

After loading a Mg_2Ni film to the black state the sample is introduced in the analysis chamber and cooled down to 77 K in order to prevent hydrogen desorption before and during the measurements. Figure 3.10 shows the results for a 200 nm thick Mg_2Ni sample capped with 5 nm Pd. The hydrogen concentration is plotted as a function of the sample depth, i.e. 0 nm corresponds to the Pd surface. In the black state, the hydrogen concentration has a maximum around 180 nm i.e., close the film/substrate interface while the rest of the sample only exhibits a very small H content. The hydrogen rich layer extends approximately over 50 nm and the concentration (per Mg_2Ni) is $x \approx 2.7$ at its maximum. A second measurement is taken after the sample is exposed to 10^5 Pa of hydrogen in the H-reaction cell during one week and the results are also plotted in Fig. 3.10 (squares). The hydrogen concentration of the fully loaded sample is indeed homogeneous over the entire film thickness and close to $x \approx 4$. The expansion of the hydrogen profile to higher energies (i.e. larger depth) reflects the increasing layer thickness (by approximately 15 %) during hydrogen uptake. This measurement indeed confirms the prefered hydride nucleation upon hydrogenation and subsequently the double layer formation within the Mg_2NiH_xfilm.

3.3.3 Electrochemical loading of Mg_2Ni thin films

Electrochemical loading is either done in galvanostatic mode with a constant current $I = -50\ \mu A/cm^2$ or by means of the galvanostatic intermittent titration technique (GITT). In GITT measurements the equilibrium potential U_{eq} is measured as a function of hydrogen concentration. A constant current is applied during a time τ_{p_i}, and subsequently the working electrode (i.e. the Mg_2NiH_x film) is allowed to relax in an open circuit configuration to its equilibrium potential $U_{eq}(x_i)$ at the hydrogen concentration x_i. These steps are repeated until the sample is fully loaded. Typical current pulse times are $\tau_{p_i} = 40$ s with current densities of $j \approx 0.05$ mA/cm^2 and relaxation times $\tau_{r_i} = 180$ s. In a proton donating electrolyte the reaction at the working electrode is

$$H_2O + e^- \rightarrow H_{ad} + OH^- \tag{3.1}$$

hence for each transferred electron one H - atom is produced that is adsorbed on the Pd surface and subsequently diffuses into the film. From U_{eq} and the Nernst equation (with p_{H_2} in Pa, U_{eq} in volts)

$$\ln p_{H_2} = \left(-\frac{2F}{RT}(U_{eq} + 0.926) \right) + 11.51 \tag{3.2}$$

the pressure-composition isotherms can be measured. $F = 96485.3$ C/mol and $R = 8.315$ J/mol K denote the Faraday and molar gas constant, respectively. The 0.926 term is a correction for the used electrode and electrolyte. The 11.51 term is due to the conversion from bar to Pa.

Figure 3.11 shows the pressure-composition isotherms of a 190 nm $Mg_{1.8}Ni$ sample covered with 13 nm Pd at temperatures T between 20 and 50 °C. The

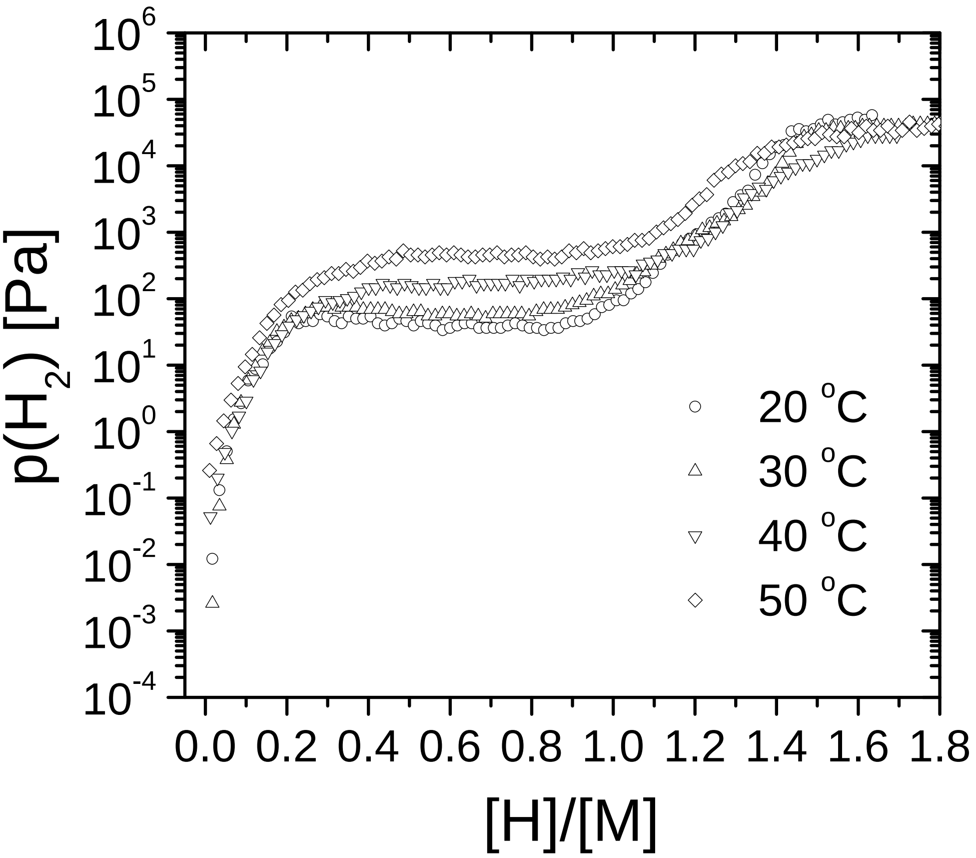

Figure 3.11: Pressure composition isotherms of a 200 nm thick $Mg_{1.8}Ni$ film covered with 13 nm Pd at temperatures $T = 20$, 30, 40 and 50°C determined from elctrochemical GITT measurements. With increasing temperature the equilibrium plateau for the $Mg_2NiH_{0.3}$-$Mg_2NiH_{4-\delta}$ phase transition increases from 40 Pa to 460 Pa. [H]/[M] denotes the number of hydrogen atoms per metal atom. (Note that in contrast, the hydrogen concentration x in Mg_2NiH_x refers to the number of hydrogen atoms per formula unit Mg_2Ni.)

plateau pressure of the $Mg_2NiH_{0.3}$ -$Mg_2NiH_{4-\delta}$ phase transition increases with increasing temperature from ≈ 40 Pa at 20 °C to 460 Pa at 50 °C. From the plateau dissociation pressure p_{dis} the heat of formation can be estimated using the van't Hoff equation: [82]

$$\frac{1}{2}\ln p_{dis} = \frac{\Delta H}{RT} - \frac{\Delta S}{R} + 5.75 \tag{3.3}$$

where ΔH is the heat of formation and p_{dis} is given in Pa. For metal hydrides, ΔS mainly stems from the entropy loss of gaseous hydrogen. ΔH is obtained from a plot of $\ln p_{dis}$ vs. 1/T. ΔH amounts to $\Delta H = -31.7$ kJ/mol H which agrees well with the value reported for hydrogen absorption in bulk

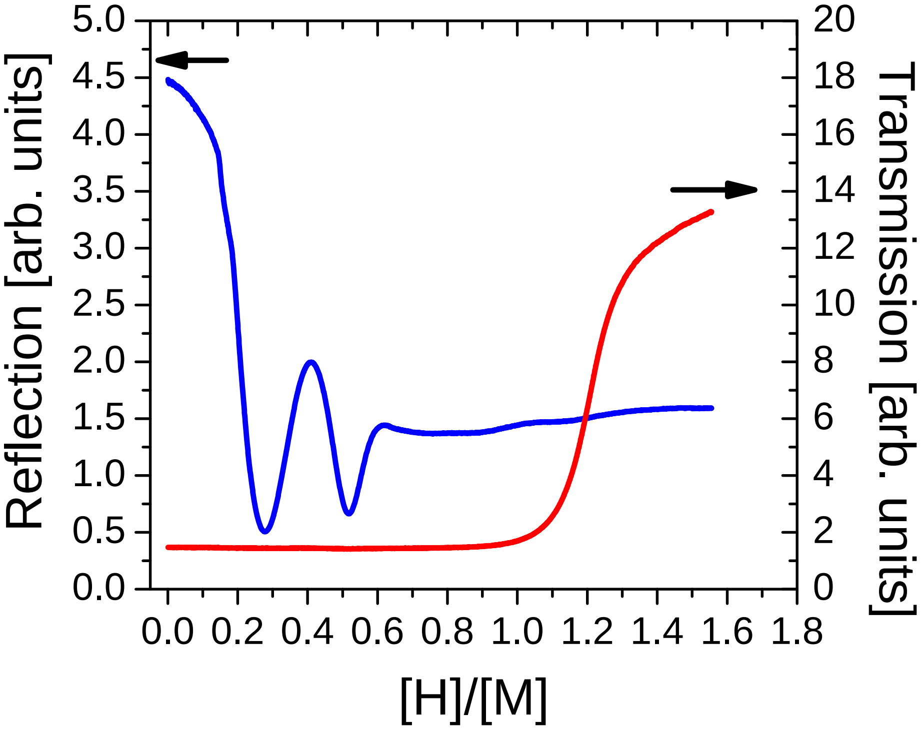

Figure 3.12: Reflection R and transmission T of 300 nm $Mg_{1.8}Ni$ covered with 24 nm Pd measured *in-situ* during galvanostatic loading. [H]/[M] denotes the number of hydrogen atoms per metal atom. The oscillating behavior of the reflection is due to interferences of the growing $Mg_2NiH_{4-\delta}$ layer thickness.

Mg_2Ni ($\Delta H = -32.3$ kJ/mol H) [24, 83]. The solid solution limit is [H]/[M] ≈ 0.16 at 20°C. Here, [H]/[M] denotes the number of hydrogen atoms referred to the total number of metal atoms (whereas the hydrogen concentration x gives the hydrogen content per formula unit Mg_2Ni). The observed solid solution limit is slightly higher than the value in bulk [H]/[M]=0.1 ($x = 0.3$ in $Mg_2NiH_{0.3}$). Above [H]/[M] ≈ 1.0 the isotherms increase considerably while single phase $Mg_2NiH_{4-\delta}$ is further loaded with hydrogen. The plateau observed at 10^5 Pa is an artifact of the measurement due to hydrogen gas developing at atmospheric pressure.

During electrochemical loading, reflection and transmission exhibit the same features as in gasochromic loading, i.e. a large decrease of R at low hydrogen concentrations followed by an oscillating behavior and a subsequent onset of transmission. R and T (at $\hbar\omega = 1.95$ eV) of a 300 nm thick $Mg_{1.8}Ni$ film covered with 24 nm Pd obtained during galvanostatic loading are shown in Fig. 3.12. Comparison of these data with those shown in Fig. 3.3 allows to relate the hydrogen concentration, optical appearance and resistivity values for characteristic points in the loading cycle. In the solid solution regime R is high and the sample is metallic reflecting. The rapid decrease of R coincides with the beginning of the two - phase region (compare Fig. 3.11). The minimum of R is associated with an average hydrogen concentration [H]/[M] $\approx$ 0.27. At larger hydrogen contents R recovers and even shows a second oscillation which stems from interference of light that is reflected at the two interfaces of the evolving transparent $Mg_2NiH_{4-\delta}$ layer (compare Fig. 3.8c). This points to an ordered double layering with flat interfaces. In the black state each additional H-atom above the solid solution limit is in fact located in a $\approx$ 30 nm layer close to the substrate interface (see section 3.3.2). If one considers this double layering and re-calculates the hydrogen content for the nucleating layer, the concentration amounts to [H]/[M] $\approx$ 1.12. This implies that in the black state, the hydrogen concentration close to the film / substrate interface amounts to $x \approx 3.14$ per formula unit $Mg_{1.8}NiH_x$ pointing indeed to a mixture of $Mg_2NiH_{0.3}$ and $Mg_2NiH_{4-\delta}$ (and presumably a small amount of amorphous Mg-Ni of unknown composition) with an approximate atomic ratio of 25:75. The average H-concentration in the black state mainly depends on the ratio between the thickness of the composite layer and the metallic layer $Mg_2NiH_{0.3}$ on top. Above [H]/[M] $\approx$ 1.0, Mg_2NiH_x becomes transparent.

3.3.4 Hydrogen diffusion model for Mg_2Ni thin films

The unusual hydrogenation process in Mg_2Ni films requires an increased hydrogen concentration close to the film/substrate interface. This is not trivial since the hydrogen enters the film at the Pd layer and one expects a hydrogen gradient towards the interface with the highest concentration at the Pd side. Borsa *et al.* investigated the peculiar time dependence of the hydrogen concentration in these kind of thin films and a diffusion model is proposed to explain the increased hydrogen concentration at the film/substrate interface [74]. To model the peculiar hydrogen absorption it is assumed that the thin Mg_2Ni films consist of a double layer made of layer C (with columnar grains) and layer N (with nanograins), see chapter 4 [16]. The enthalpy of hydride formation ΔH_N is assumed to be more negative than ΔH_C, the enthalpy of hydride formation in the columnar region. By solving numerically the diffusion equation with: (i) at equilibrium the chemical potential is the same everywhere, (ii) the current of hydrogen in a material is proportional to the gradient of the chemical potential μ_H of hydrogen, i.e. $J_H = -L\nabla\mu_H$ [84], iii) the chemical potential is a continuous function of space, iv) the H particle current is also a continuous function and v) at the film/substrate interface $d\mu/dx = 0$. one can obtain the evolution in time of the chemical potential and the hydrogen concentration profiles in this double layer system. The results are shown in figure 3.13, for a 50 units thick two layer model. For the N-layer (10 units thick) $\Delta H_N/kT = -15$ (ΔH = enthalpy) and for the C-layer $\Delta H_C/kT = -10$. The chemical potential

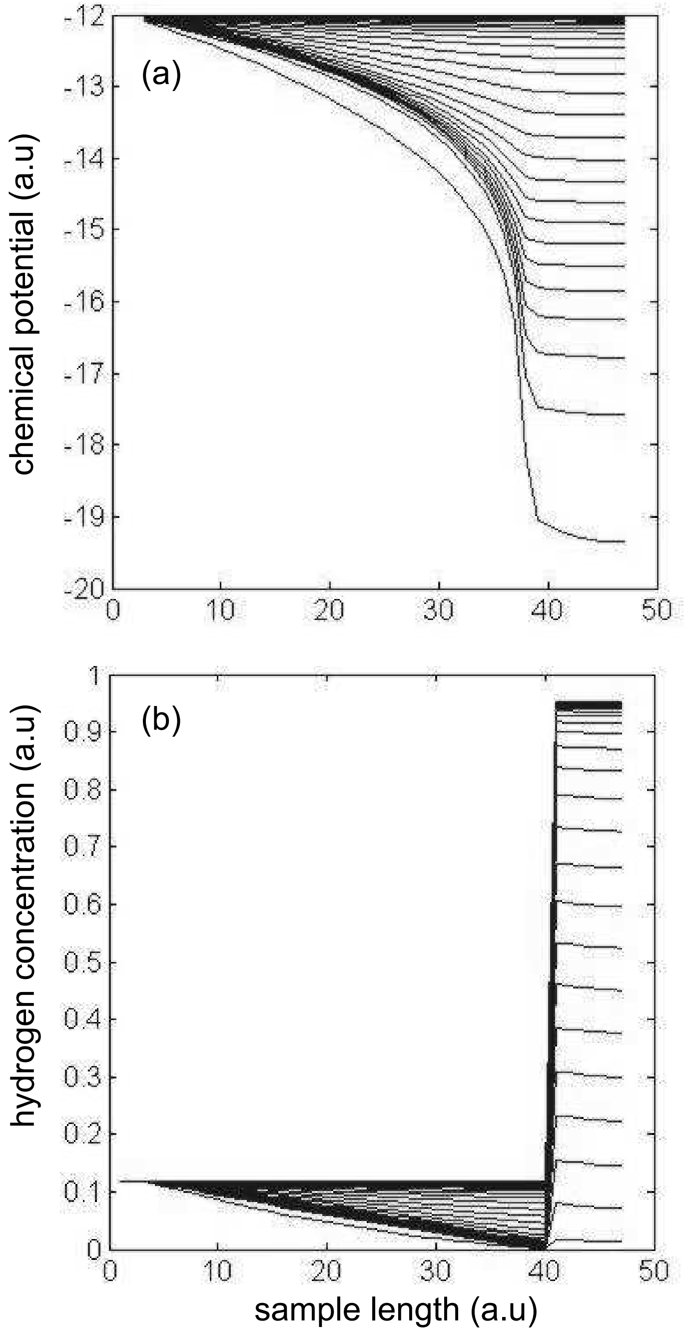

Figure 3.13: (a) Profiles of the chemical potential of hydrogen as a function of time and sample depth. (b) hydrogen concentration c profile in the sample. Clearly visible is the high concentration in the thin layer near the 'substrate' on the right. The lowest profile corresponds to t=1 time step; the top one to 12 time steps.

of the H_2 gas is assumed to be μ/kT = -12; The parameter L is related to the diffusion coefficient D through the relation L = Dcc$_o$/kT (c = concentration, c$_0$ = maxim concentration in the system); the diffusion coefficient D is chosen as 5×10^{-6} cm^2/s. It is found that for a system where hydrogen diffuses from the C-layer (i.e. from the Pd side in the real sample) to the N-layer (i.e. to the substrate side), the chemical potential in the C-layer decreases steadily from the Pd side to the substrate side (Fig. 3.13(a)) whereas the concentration of hydrogen in the N-layer (i.e. near the substrate) is clearly larger than in the rest of the film (Fig. 3.13(b)). This model shows that it is very well possible to have a higher concentration near the substrate than in the rest of the sample.

3.4 Applications Mg-TM-H thin films

3.4.1 Mg-Ni smart windows

Smart coated windows can have a considerable influence on the heat consumption of for buildings. To achieve a smart coating which regulates the solar heat input and while maintaining transparency requires that the optical properties of the visible spectrum should be different from those of the thermal long wavelength range. The heat dissipation is controlled by the emissivity around 0.1 eV (8 μm; 373 K black-body radiation). To obtain a smart window that is transparent in the visible and reflects at energies below 0.5 eV (2.5 μm), one can make use of a switchable mirror. The fact that Mg-Ni-H thin films display three optical states during hydrogenation makes them very attractive for applications such as in solar heat collectors, hydrogen sensors, smart windows etc. Since the quality of solar heat collectors depends on a high absorption of the solar spectrum (at photon energies between $0.5 < E < 4$ eV) and a low emission of thermal radiation (at $E < 0.5$ eV, for 372 K) [85], Van Mechelen *et al.* investigated the infrared optical behavior of Mg-Ni films upon hydrogenation [10]. The observed black state (high absorption) for Mg_2NiH_x films in the visible spectrum is also found for infrared energies [57, 63, 71, 72, 74].

To control the temperature of solar collectors, these Mg_2Ni thin films can be quite well suited. When the temperature of the device is reaching undesirably high temperatures, the film can be switched to a reflecting metallic state. On the contrary, to increase the thermal load of the system, the switchable mirror can be switched into the optical black state. The most important point of this temperature regulation is that it becomes possible to use lighter and cheaper materials for solar collectors (plastics), which are sensitive to high temperatures.

In figure 3.14 Van Mechelen *et al.* shows contour-plots of the reflection R for a Mg-Ni film (as measured from the substrate side), as a function of photon energy, E, and resistivity (which is a measure of the hydrogen concentration x [63]), during loading. This is done for films of several thicknesses d. Figure

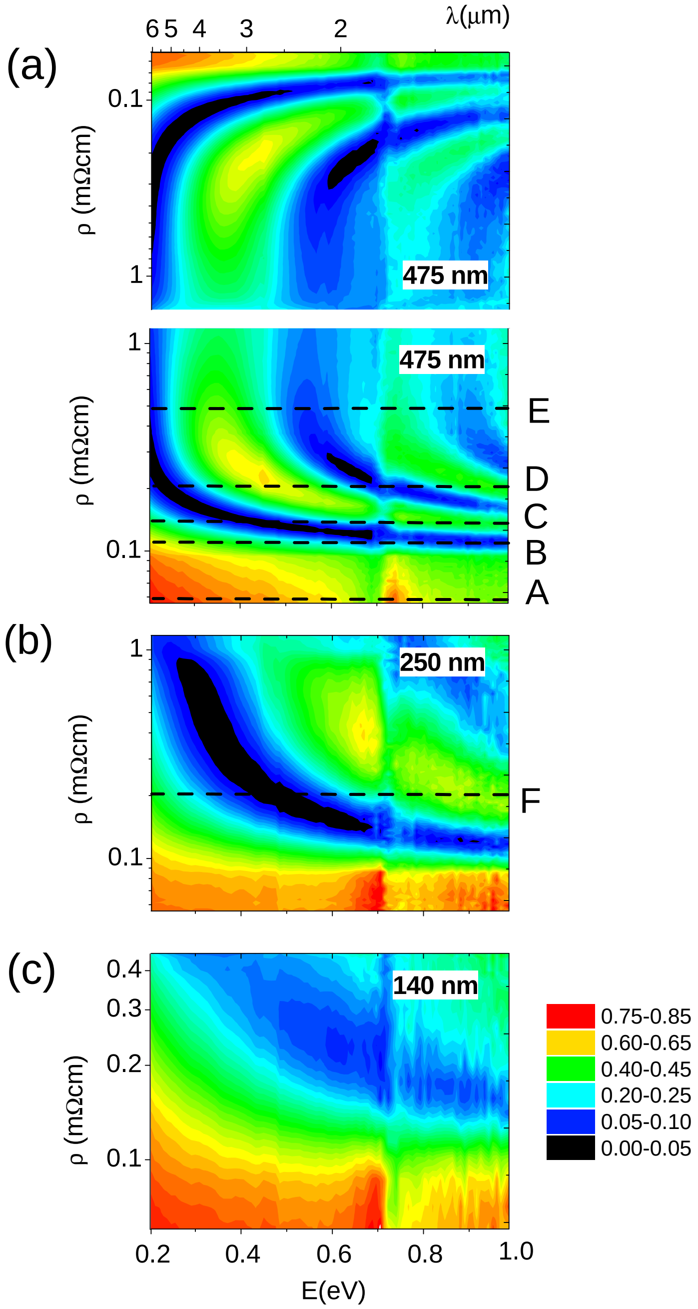

Figure 3.14: Contour plots of reflection vs. photon energy and electrical resistivity ρ for a (a) 475 nm Mg$_{1.96}$Ni, (b) 250 nm Mg$_{1.70}$Ni, and (c) 140 nm Mg$_{1.43}$Ni film. The hydrogen concentration is very roughly proportional to ρ.

3.14a shows also the unloading process which indicates that the hydrogenation process is completely reversible. This makes these systems very attractive for future applications. The hyperbolic-like bending of the minima and maxima as a function of the energy, and the increment of the number of reflection oscillations with increasing thickness, are consistent with the two-layer model as shown by Lohstroh *et al.* [71, 72]. This interference pattern can be qualitatively understood from the interference condition $2t(x)n = N\lambda \propto N/E$, where n and N are the refraction index and interference order, respectively [86] and $t(x)$ is the thickness of the hydrided layer.

Van Mechelen *et al.* show that one can tune the reflection as a function of energy for different loading stages as shown in figure 3.15a (A to E in figure 3.14a) for a $d = 475$ nm thick film. The film changes optically from the metallic unloaded film (stage A) in figure 3.15a, to the optical black state upon absorbing a small amount of hydrogen (the average H content depending on d [71, 72]), the film becomes black. The reflection decreases drastically for $E > 0.5$ eV ($\lambda < 2.5$ μm), and varies between 0.05 and 0.3 for $0.5 < E < 4$ eV (see Fig. 3.15b and Ref. [57, 71, 72]), while it is still reflecting ($R > 0.6$) in the thermal range. It is shown that by linearly extrapolating the reflection of 3.15b to low energies and convoluting $A = 1 - R$ with the blackbody radiation at 373 K, the thermal emittance in this state (Fig. 3.15b) is 0.16. Similarly, a solar absorption of about 0.84 is estimated by using the data at $E > 0.5$ eV in the same figure together with those obtained for similar films at energies up to 4 eV [57, 71, 72]. These relatively high solar absorption and low thermal emittance are comparable to those recently reported for films of a-Si:H/Ti on Al substrates [87]. The main advantage of the Mg_2Ni films is that their behavior is switchable. Moreover, the small amount of H needed, which involves minimal morphology changes and thus little aging, makes the switching between A and B very attractive from an applications point of view.

Van Mechelen *et al.* showed that upon increasing the H content (stage C) a very different reflection pattern is measured with a narrow highly absorbing state at ~ 0.4 eV ($\lambda \simeq 3.1$ μm), whose energy and width can be tuned by varying the film thickness. Due to the layered loading mechanism, the reflection spectrum at this state of the loading process is identical to that of a later loading stage in a thinner 250 nm film (F), as shown in Fig. 3.15c. A larger H content in a thick enough film gives raise to more than one R minima (D).

Since optical appearance of these Mg-Ni thin films can now be changed by either thickness [10], hydrogen concentration [10] on composition [74] makes them very interesting as selective coating.

3.4.2 Mg-Ni hydrogen sensors

The use of hydrogen as an energy carrier in a hydrogen oriented economy demands hydrogen sensors for all kind of applications. These sensors must

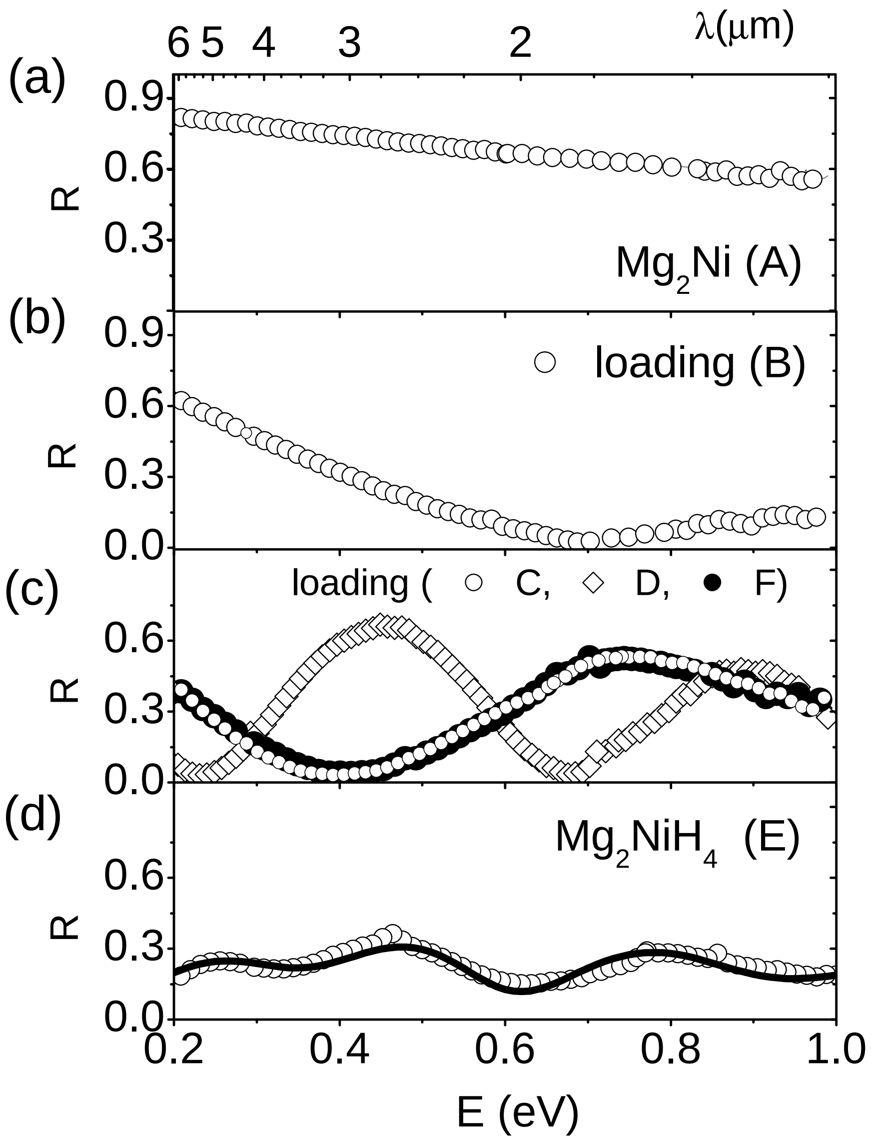

Figure 3.15: Reflection spectra for the 475 nm $Mg_{1.96}Ni$ film shown in Fig. 2(a) at different stages (A to E) of H loading. The letters refer to those in Fig. 2(a). The solid circles in (c) correspond to the 250 nm $Mg_{1.7}Ni$ film. The line in (d) is the fit to the data with $n \approx 3.7$ and $k \approx 0.5$, both weakly depending on energy in the studied range.

be selective for hydrogen, sensitive, reliable, re-usable and not too expensive. Furthermore, since hydrogen is highly explosive electrical contacts for the detector in the presence of hydrogen is not desired. Hydrogen is mainly detected by a catalytic resistor detectors or electrochemical devices. Problem of these systems is that they are too large and too expensive to be used in large quantities. This problem can be avoided by using an optical fiber which is coated on one side with an hydrogen sensitive switchable mirror. The optical changes of this layer due to hydrogen absorption can be detected optically at the other end of the fiber, since optical fiber sensors are very sensitive to a hydrogen concentration [21, 88, 89]. Moreover they are cheap to produce, insensitive to electromagnetic noise, and explosion safe. By combining several optical fibers and a central detecting system one can perform multiple sensing on hydrogen. When considering the hydrogen sensitive layer on top of the fiber, the Mg-TM-H systems are very interesting. The reflection of these layers is very sensitive on the pressure of hydrogen and changes already at low hydrogen concentrations.

Slaman *et al.* [6] report about the implementation of Pd-capped chemochromic metal hydrides as a sensing layer in fiber optic hydrogen detectors. A drop in absolute reflection by a factor of 10 on hydrogenation for Mg based alloys on is demonstrated for hydrogen levels down to 15% of the lower explosion limit. These Mg-Ni and Mg-Ti based coated fibers are tested for sensitivity of hydrogen in argon and oxygen and temperature dependence of the detectors. Although the Mg-Ni system has a good response to a hydrogen atmosphere, the sensors based on a Mg-Ti compound have even more superior optical and switching properties.

Chapter 4

The microstructure of Mg_2TM thin films

4.1 Abstract

Hydrogen absorption by a thin Mg_2Ni film capped with Pd, results in the nucleation of the Mg_2NiH_4 phase at the film/substrate interface. On further hydrogenation a self-organized two-layer system consisting of a mixed $Mg_2NiH_{0.3}$/Mg_2NiH_4 bottom-layer and a $Mg_2NiH_{0.3}$ top-layer is formed. This leads to an intermediate optical black state in Mg_2Ni thin films, which transform from metallic/reflective to semiconducting/transparent upon hydrogenation. This hydrogen absorption behavior is completely unexpected, since hydrogen enters the film through the top Pd-capped film surface. To explain the preferential nucleation of Mg_2NiH_4 at the film/substrate interface we determine the chemical homogeneity of these thin films by RBS and SIMS. Furthermore by STM, TEM and SEM we analyze the microstructure. We find that up to a film thickness of 50 nm, the film consists of small grains and clusters of small grains. On further growth a columnar structure develops. We propose that the nucleation barrier for the formation of the Mg_2NiH_4 phase is lowest for the small loosely packed grains at the interface while the columnar grain boundaries promote hydrogen diffusion to the substrate.

4.2 Introduction

As shown in the previous chapter, a third optical state in the Mg-TM system is found upon hydrogenation. In films thicker than 50 nm we observe a highly absorbing optical state at intermediate hydrogen concentration. The fact that Mg_2NiH_x can be switched between a reflective metal, an absorbing black and a transparent semiconducting state makes Mg_2NiH_x potentially attractive for smart coating applications [10]. The black state originates from a self-organized double layering of the Mg_2Ni film during hydrogen absorption [71, 72]. We have shown by optical modelling that the black state is due to a highly absorbing initial 30 nm layer (of mixed $Mg_2NiH_{0.3}/Mg_2NiH_4$ particles) which produces an interference effect with the reflective $Mg_2NiH_{0.3}$ top-layer. The black state is found irrespective of the substrate used so far (Si, SiO_2, CaF_2, sapphire, quartz, ITO covered glass). Furthermore, it does not depend on composition for Mg/Ni-ratios between 1.5 and 6 and remains visible also after many switching cycles [76]. To identify the origin of the preferred hydride nucleation and to evaluate its applicability for smart window applications, it is important to address the origin and mechanism of the self-organized double layering [21, 88, 89]. Also, for the use of Mg_2NiH_4 as a storage material, any effect that enhances the formation of this phase is of interest.

As evidenced by electrochemical loading experiments, the thermodynamic behavior of these thin films is similar to that of bulk samples and similar plateau pressures were found [72]. Kinetically however, thin films behave differently from bulk samples. Hydrogen absorption of Pd-capped thin Mg_2Ni films already takes place at room temperature (RT) and hydrogen gas pressures below 100 Pa. In bulk samples, elevated temperatures (598 K) and high hydrogen pressures (2×10^6 Pa) are needed to form a hydride phase [24]. There are two possible explanations for this preferred nucleation behavior: i) a lowered enthalpy of formation at the interface (thermodynamic origin) or ii) a lowered nucleation barrier resulting from a local change in the strain state of the film, a different thin film microstructure or a local change in composition. Even the presence of the substrate itself may affect the nucleation process as it could provide the nucleating hydride phase with a lower interface free energy. It is noteworthy to point out that the *dehydrogenation* process is *not* anomalous: the metallic phase nucleates at the film surface upon dehydrogenation.

To address the origin of this unusual hydrogenation behavior, we investigate the homogeneity of the as-grown film. The possibility of a chemical gradient throughout the as-grown films is considered in section 4.4.1. The thin film microstructure as a possible reason for the peculiar hydrogenation behavior is examined in sections 4.4.2 and 4.4.2. While the Mg/Ni ratio and chemical composition turns out to be uniform throughout the layer thickness, we find that the grain size of the as-grown films at the interface is extremely small as compared to that of the ensuing columnar growth. We argue that the microstructure generated in the deposition process is responsible for the self-organized layering upon hydrogen absorption.

4.3 Experiment

4.3.1 Experimental setup

The Mg_2Ni thin films are prepared in a Ultra High Vacuum (UHV) system with a base pressure of $< 10^{-8}$ Pa by co-evaporation from a Knudsen cell (Mg, purity 99.98%) and an electron gun (Ni, purity 99.98%). The deposition rate during evaporation is monitored using two separate quartz-crystal monitors. For *ex-situ* experiments the samples are protected from oxidation by a Pd caplayer (purity 99.98%). This layer also promotes hydrogen dissociation and absorption. During deposition, the resistance is continuously measured to find the electrical percolation thickness of the nucleating phases. The chemical composition and the thickness of the as-deposited films, is measured by Rutherford Backscattering Spectrometry (RBS). The chemical composition depth profile is investigated by Secondary Ion Mass Spectroscopy (SIMS) Depth Profiling. The ToF-SIMS depth profiling is performed with a dual beam in interlaced mode (alternating sputtering and analysis) on an IONTOF IV instrument using Time-of-Flight detection of secondary ions. The instrument is equipped with a high-current sputter gun and a 3-Lens Ga gun. For Scanning Tunnelling Microscopy (STM) measurements the Mg_2Ni samples are transported *in-situ* from the UHV chamber to the STM chamber consisting of an Omicron UHV scanning probe microscope. For topographical images of the surface the constant current mode is used. Atomic Force Microscopy (AFM) measurements are done *ex-situ* with a Digital Instruments Nanoscope III AFM. A Philips FEG XL series xl30s apparatus working in TLD mode at a background pressure of 10^{-4} Pa is used for Secondary Electron Microscopy (SEM). The cross-section TEM images are made with a JEOL 4000 EX/II working at 400 kV, which has a point-resolution of 0.17 nm. The cross-section samples are cut, polished and ion milled with 4 kV Ar-ions with an Gatan PIPS. The plane-view images are made with a JEOL 2010F working at 200 kV (point-resolution 0.23 nm and an information limit of 0.11 nm). This TEM also contains a Gatan Imaging Filter (GIF) model 2000.

4.4 Experimental Results

4.4.1 Compositional homogeneity

RBS and SIMS measurements

The homogeneity of the chemical composition is determined from RBS and SIMS. For RBS measurements we use carbon substrates. We find a Mg:Ni ratio close to 2 and no perceptible depth gradients. The relative amount of oxygen [O]/[Mg] is less than 0.006, and is mainly concentrated at the film/substrate

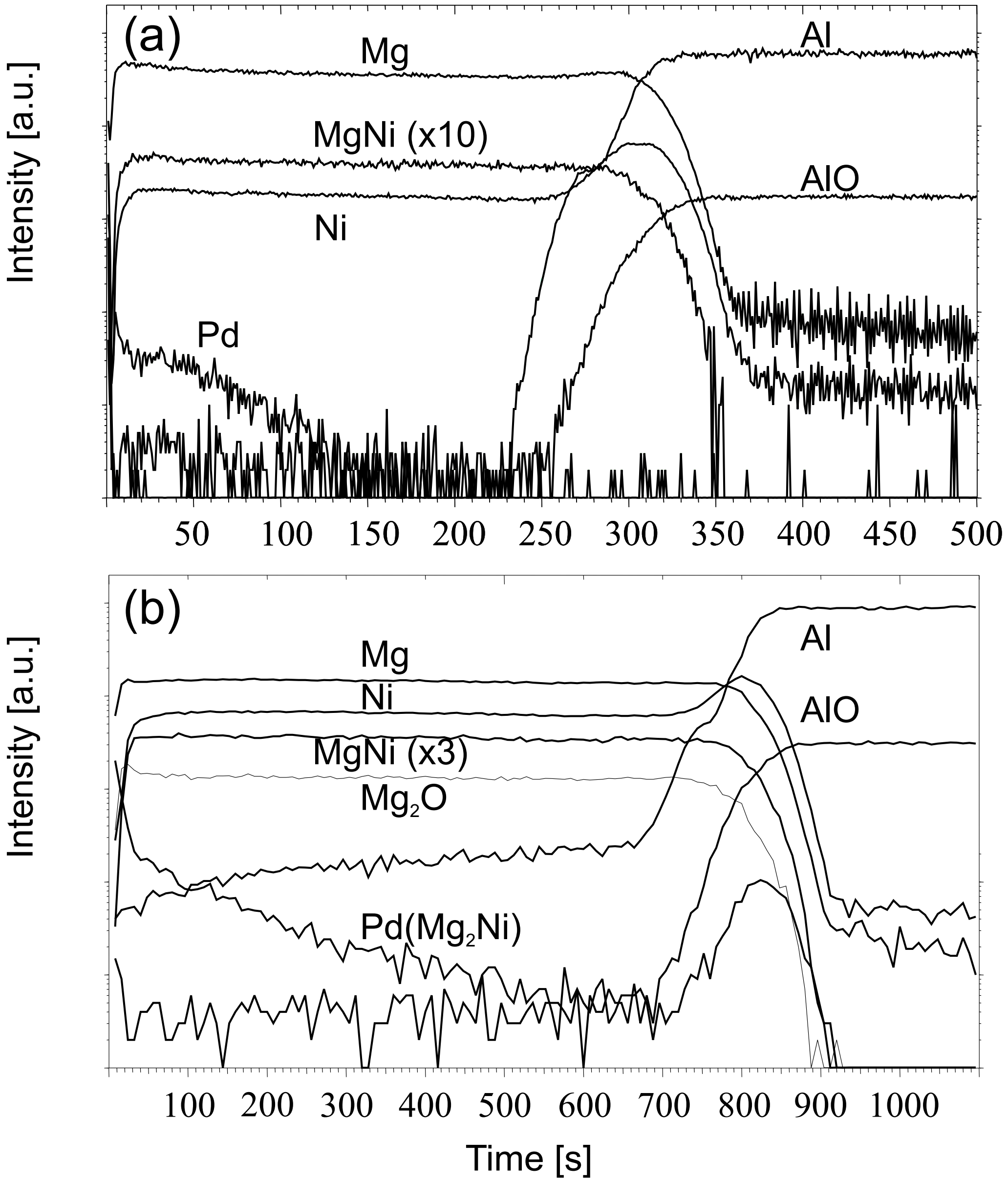

Figure 4.1: (a) ToFSIMS depth profile $Pd/Mg_2Ni/Al_2O_3$ (positive mode) of a 200 nm Mg_2Ni thin film covered by 5 nm Pd in the as-prepared state. Pd, Ni, Mg and Mg_2Ni intensities are shown together with Al and AlO. (b) ToFSIMS depth profile $Pd/Mg_2Ni/Al_2O_3$ (positive mode) of the same film hydrogenated to Mg_2NiH_4 and then unloaded back to the black state. The MgNi signal is multiplied by 10 and 3 in figure a and figure b, respectively.

interface and at the film surface. Inside the Mg_2Ni film no contamination with other elements could be detected.

Using SIMS we investigate the composition depth profile and the influence

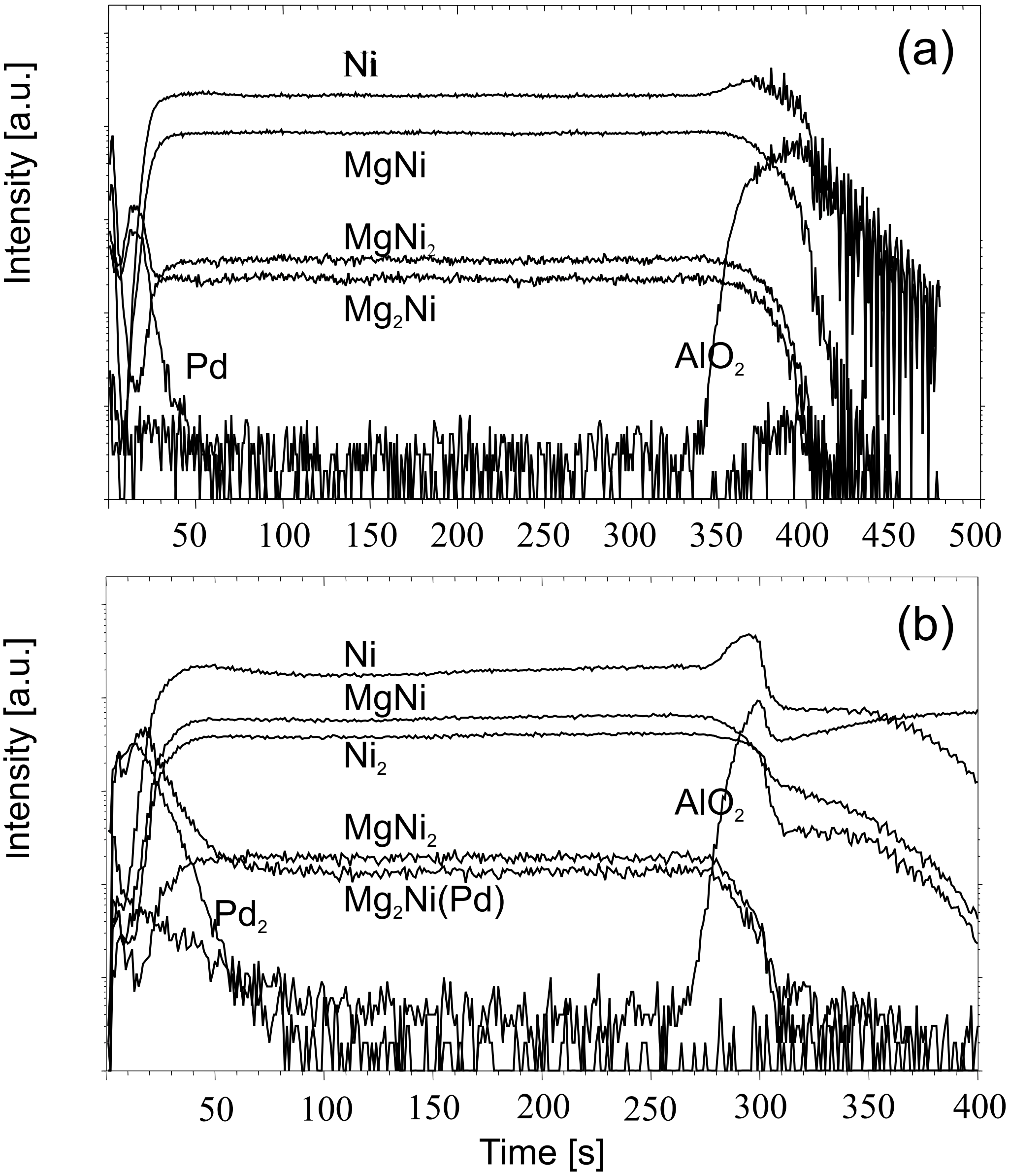

Figure 4.2: (a) ToFSIMS depth profile Pd/Mg_2Ni/Al_2O_3 (negative mode) of an 200 nm Mg_2Ni thin film covered by 5 nm Pd in the as-prepared state. Pd, Ni, Mg and Mg_2Ni intensities are shown together with Al and AlO. (b) ToFSIMS depth profile Pd/Mg_2Ni/Al_2O_3 (negative mode) hydrogenated to Mg_2NiH_4 and then unloaded back to the black state.

of hydriding in more detail. We compare films in different hydrogen loading states. To obtain depth information the film is bombarded with 2 keV O_2^+ ions in the positive mode or 1 keV Cs+ ions in the negative mode, to remove the surface layer step by step. Between each sputter step, the chemical composition is probed by using a 15 keV Ga^+ ion beam. Therefore, the x-axes (representing

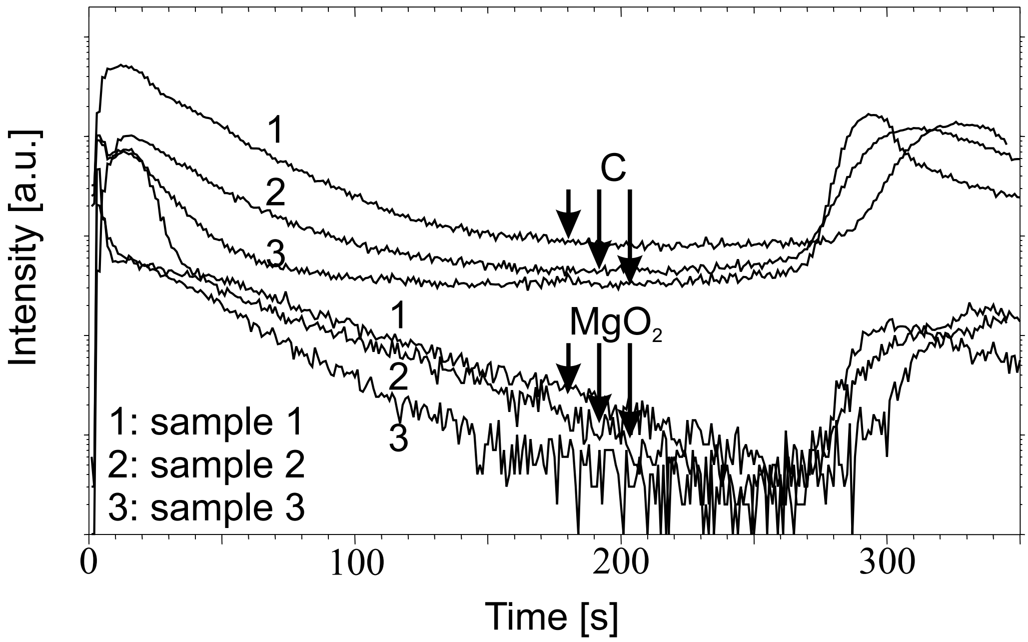

Figure 4.3: C and MgO_2 contaminations for different Mg_2Ni films: sample 1 is often exposed to air. Sample 2 and 3 were kept under argon and have been cycled once.

sputter and analyzing time) in Fig. 4.1, 4.2 and 4.3 corresponds to the depth in the sample, starting from 0 seconds at the Pd caplayer.

Results for the as-prepared Mg_2Ni film are shown in Fig. 4.1a and Fig. 4.2a for the positive and negative mode, respectively. The Mg, Ni and MgNi profiles are constant over the whole layer thickness with some decay towards the sapphire (Al_2O_3 (1102)) substrate. The latter is possibly caused by ion-beam induced roughening of the metallic layers. The increased Ni-intensity at the Mg_2Ni/Al_2O_3 interface is attributed to matrix effects due to the presence of oxygen. The low intensity of the Mg and Ni profiles at the surface indicates that the 5 nm Pd cap-layer is closed. The tail in the Pd profile is most likely an artefact due to roughening, induced by sputter bombardment. RBS measurements do not show diffusion of the Pd caplayer into the Mg_2Ni film. Fig. 4.1b and 4.2b show the profiles for the sample that has been loaded up to Mg_2NiH_4 and subsequently unloaded back to the black state. It is obvious that the Mg, Ni and MgNi profiles remain constant throughout the sample. No indication is found for a hydrogenation induced phase segregation within the metallic phase.

The contamination level (e.g. C, O) is generally low (in agreement with RBS measurements) and depends on the storage conditions. Sample 1, Fig. 4.3, which was exposed to ambient air several times, shows enhanced impurity levels at the surface. At the film/substrate interface always some oxygen contamination is observed. Since we have impurities at both the Pd surface and the substrate interface, we do not consider them to be related to the preferential nucleation of the hydride near the substrate/film interface, otherwise we would also expect the preferred hydride nucleation at the Pd/film interface.

We conclude that the Mg/Ni ratio is roughly constant throughout the Mg_2Ni film for the as-prepared film as well as for the films that have absorbed and desorbed hydrogen. However, as depth profiling by ion sputtering always causes a certain intermixing, SIMS cannot exclude the presence of a chemical gradient *within* the first 30 nm.

4.4.2 Structural homogeneity

Resistance percolation measurements

The nature of the first stages of growth may be the cause for local deviations in stoichiometry. The sticking of impinging adatoms to the substrate may be different from the sticking to a growing Mg_2Ni film. Thus, as long as we do not have a closed layer, sticking differences could result in compositional deviations near the substrate. To investigate the nature of the initial growth stages of Mg, Ni and Mg_2Ni, we measure *in-situ* the electrical resistance during growth of the respective layer. Before evaporation two electrical contacts are made to the non-conducting sapphire substrate. After a certain deposition time of Mg, Ni or Mg_2Ni the thin film becomes electrically connected, resulting in a drastic decrease of the electrical resistance. Extrapolating the resistivity to zero at the steepest slope defines the so-called percolation thickness, see Figs. 4.4d, 4.4e and 4.4f.

The growth of a Ni thin film results in an electrical percolation thickness of 0.54 nm, Fig. 4.4d. This small value (approximately 3-5 monolayers) is related to the high density of small nuclei as indicated in Fig. 4.4a. For Mg, however, we observe a low density of large nuclei. We find an electrical percolation thickness of 20 nm (see Fig. 4.4e), in agreement with the pronounced island growth in Fig. 4.4b. Remarkably, when Mg and Ni are co-deposited in a 2 to 1 ratio, a much smaller percolation thickness of 2.5 nm is obtained (see Fig. 4.4f). The percolation thickness is thus strongly reduced with respect to the percolation thickness of pure Mg. This is also evident from Fig. 4.4c. It appears that the nucleation and growth behavior scales roughly with the melting temperature of Ni, Mg_2Ni and Mg (2073 K, 1033 K and 923 K), respectively. We conclude that a difference in chemical composition as a result of different sticking of the Mg, Ni and Mg_2Ni on the substrate is likely to occur only during the first 2.5 nm of Mg_2Ni growth. Since the preferred hydride phase formation responsible for the black state takes place in a 30 - 50 nm thick layer adjacent to the substrate, it is not plausible that this is due to a chemical gradient in the first 2.5 nm.

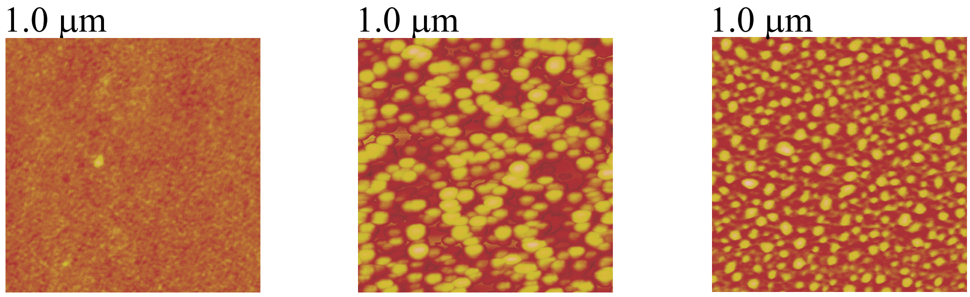

(a) 5 nm Ni
$\Delta z = 5$ nm

(b) 5 nm Mg
$\Delta z = 30$ nm

(c) 5 nm Mg_2Ni
$\Delta z = 10$ nm

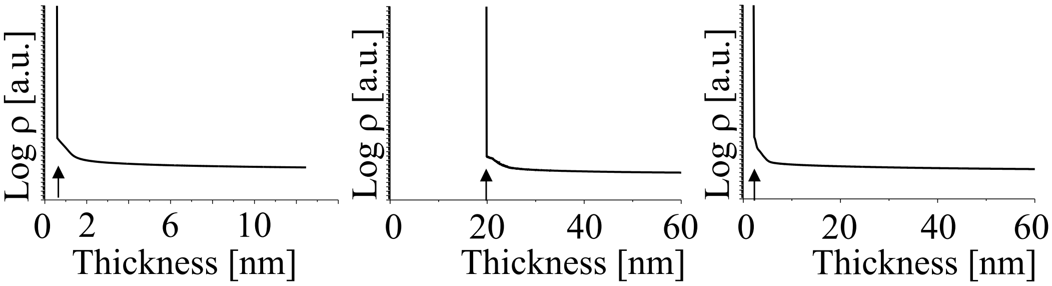

(d) Percolation Ni

(e) Percolation Mg

(f) Percolation Mg_2Ni

Figure 4.4: The AFM images a, b, and c show the surface morphology for a 5 nm layer of Ni, Mg, and Mg_2Ni, respectively. In d, e, and f logarithmic resistance is plotted versus thickness for Ni, Mg and Mg_2Ni, resulting in a percolation thickness for Ni = 0.54 nm, Mg = 20 nm, and Mg_2Ni = 2.5 nm.

STM investigation of the growth of Mg_2Ni

To investigate how the microstructure of a thin Mg_2Ni film evolves as a function of deposited thickness, we study the surface morphology of as-deposited films in various stages of growth by UHV-STM. Since the optical black state is observed for a variety of substrates, we assume that the results obtained on silicon substrates are representative for the microstructural development of thin Mg_2Ni films in general. Therefore we study the microstructure development during different stages of deposition of thin Mg_2Ni films. Here we assume that the grown film microstructure is stable and bulk diffusion is negligible. STM micrographs of Mg_2Ni films with a thicknesses of 20, 50 and 150 nm, are shown in Fig. 4.5. For 20 nm films (see Fig. 4.5a + 4.5d) islands with a grain size of ~30 nm are observed. These grains are dispersed over the substrate surface and on top of the islands the onset of a vague substructure of smaller grains can be seen. When the film thickness is increased to 50 nm (see Fig. 4.5b + 4.5e) the diameter of the grains increases to approximately 50 nm. Moreover, it is

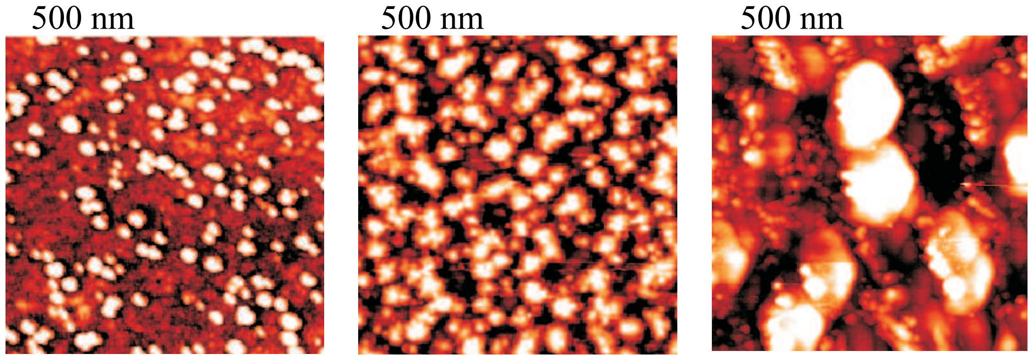

(a) 20 nm, $\Delta z = 1.92$ nm (b) 50 nm, $\Delta z = 4.44$ nm (c) 150 nm, $\Delta z = 10$ nm

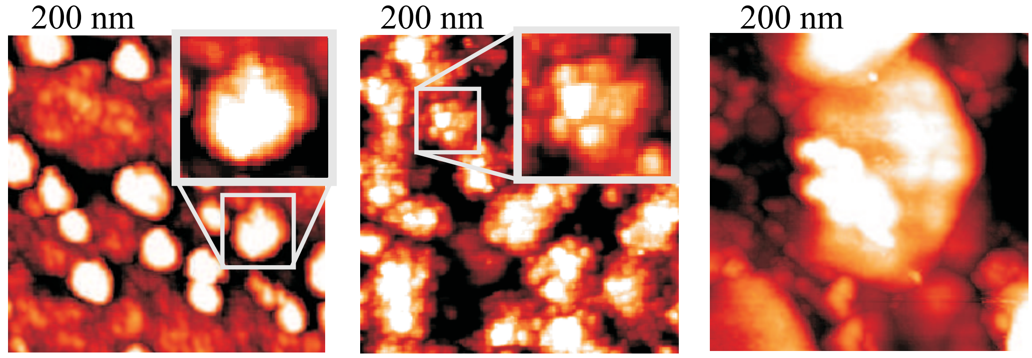

(d) 20 nm, $\Delta z = 1.92$ nm (e) 50 nm, $\Delta z = 4.44$ nm (f) 150 nm, $\Delta z = 10$ nm

Figure 4.5: STM micrographs of *in-situ* grown thin Mg_2Ni films with thicknesses of 20, 50 and 150 nm. Panels (a)-(c) depict a scan range of 500 nm while panels (d)-(f) show a 200 by 200 nm area of the same samples. The maximum height difference from low (dark color) to high (white) is given by $\triangle$z. For a thickness of 20 nm (a, d) the islands are well dispersed over the substrate and at d = 50 nm (b, e) clusters of small grains are observed. At d = 150 nm (c, f) the grains have coalesced into crystallites.

clear now that the grains consist of a cluster of smaller grains. These subgrains are approximately 10 nm size. Increasing the film thickness leads to extensive grain growth. The most striking microstructure transition occurs on further deposition up to a thickness of 150 nm. The initial growth clusters develop into large grains with a diameter of over 100 nm on 150 nm Mg_2Ni (see Fig. 4.5c + 4.5f). The hexagonal shape of these large grains reflects the hexagonal unit cell of Mg_2Ni and indicates a preferential orientation of the c-axis normal to the substrate. Smaller grains are often observed with a typical size between 10 - 30 nm between the large grains. This implies that the microstructure close to the substrate has a very porous (like) character with many grain boundaries and interfaces. The 30 - 50 nm thickness of this porous layer corresponds very well to the 30 - 50 nm layer close to the substrate, which was found to show a

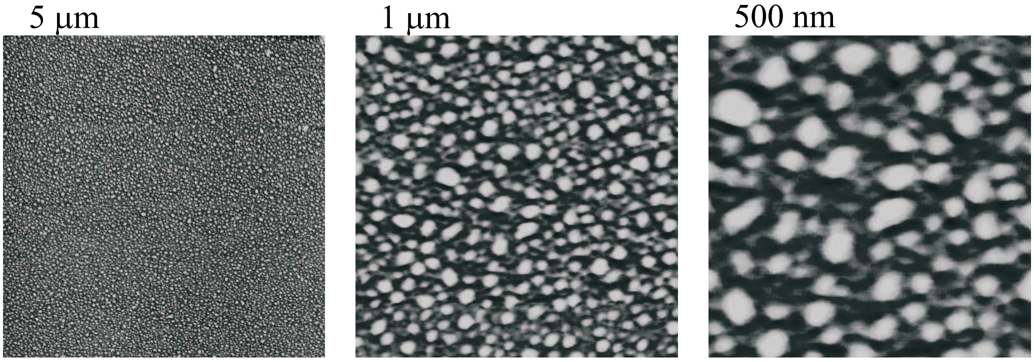

(a) 5 nm, Δz = 10 nm (b) 5 nm, Δz = 10 nm (c) 5 nm, Δz = 10 nm

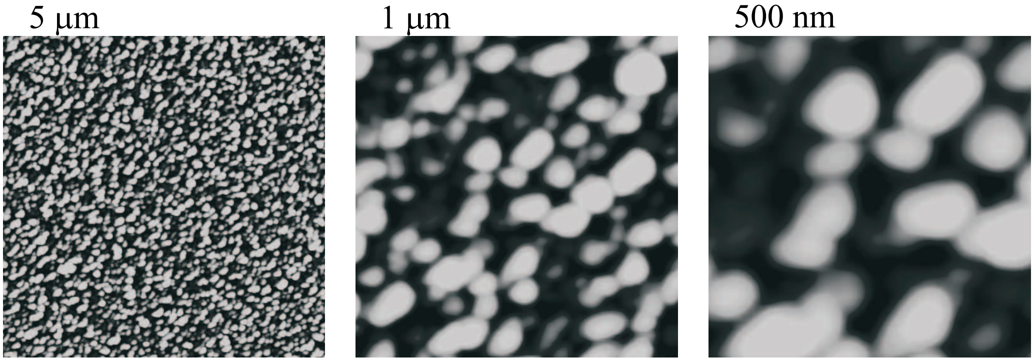

(d) 200 nm, Δz = 60 nm (e) 200 nm, Δz = 60 nm (f) 200 nm, Δz = 60 nm

Figure 4.6: AFM micrographs of Pd capped Mg_2Ni films of d = 5 and d = 200 nm thickness for different scan sizes and height scale $\triangle z$. At a thickness of 5 nm the film consists of finely dispersed small grains while at d = 200 nm large grains of 100 nm diameter are observed.

preferential nucleation of the Mg_2NiH_4 phase and hence to be responsible for the optical black state. The initially grown islands develop into large grains with a diameter of 100 nm. The development from small island growth (observed at a thickness of 20 nm) to large and dense grain development (at a thickness of 150 nm) is typical for a columnar growth mode.

AFM surface structure investigation of Mg_2Ni

To investigate the surface morphology of Mg_2Ni thin films on a larger scale, we perform AFM measurements. *Ex-situ* AFM micrographs of Mg_2Ni films with a thicknesses of 5 and 200 nm are shown in Figs. 4.6a - 4.6c and 4.6d - 4.6f, respectively. These thin films are capped with a 5 nm Pd caplayer to prevent oxidation effects. The 5 nm thick Mg_2Ni film (Figs. 4.6a - 4.6c) consists of equally dispersed small grains of 30 nm in diameter. A 200 nm thick Mg_2Ni film (Figs. 4.6d - 4.6f), shows extensive grain growth up to 100 nm i.e., the same

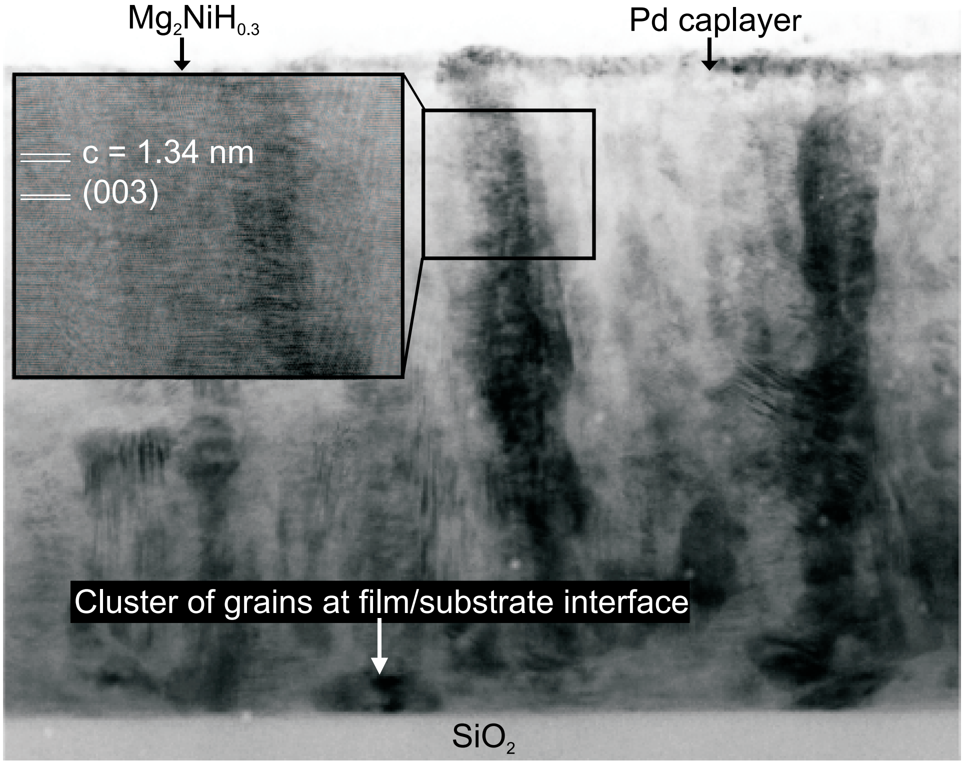

Figure 4.7: TEM cross-section micrographs of 10 nm Pd capped 330 nm Mg_2Ni film. This film was hydrogenated and unloaded again to the $Mg_2NiH_{0.3}$ phase. Clear dark columnar structures indicate a distinct local microstructure. Some of these columnar structures develop from a cluster of grains at the film/substrate interface. The inset shows a High-Resolution image of a column with the $Mg_2NiH_{0.3}$ lattice planes along the c-axis (c = 1.34 nm).

characteristic grain growth as observed in the STM measurements in Figs. 4.5. The structural evolution of the initial grown grains to large structures, is an important indication for a columnar growth mode.

TEM measurements on Mg_2Ni

The microstructural development observed by STM is further investigated by TEM measurements. Fig. 4.7 shows a TEM cross-section of a 330 nm Mg_2Ni thin film covered by 10 nm Pd. The image clearly shows vertical columnar structures. Note, that a difference in brightness indicates a difference in intensity diffracted outside the objective aperture (i.e. dark grains are in strongly diffracting condition). On top of this predominant diffraction contrast, a slight increase in brightness occurs from bottom to top of the Mg_2Ni film due to a locally decreasing thickness of the TEM sample. These columns extend from the substrate to the top of the film, where they end with

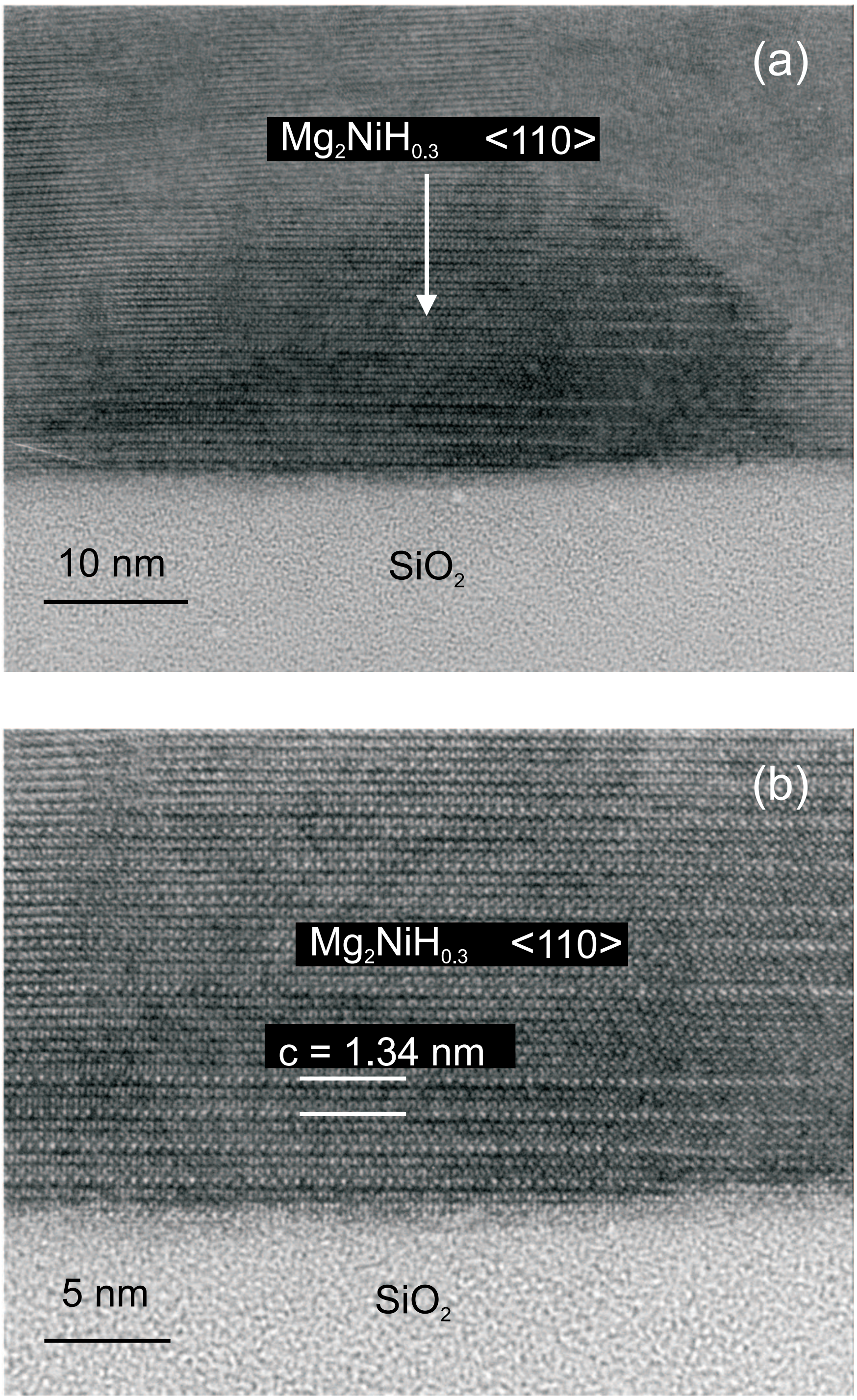

Figure 4.8: HR-TEM micrographs of a larger grain close to the substrate interface, which shows the characteristic layering of the $Mg_2NiH_{0.3}$ structure along <110> with c = 1.34 nm.

local protrusions at the film surface. Close to the Si substrate a more irregular structure can be seen, consisting of grains or clusters of grains. Some of these larger interfacial grains appear to act as a pedestal or seed for columnar growth. After a certain film thickness these clusters disappear into the columnar structures. High-Resolution images (see Figs. 4.8 a-b) both within the columns and the interfacial grains, allow the identification of the (003)-lattice planes of $Mg_2NiH_{0.3}$ with a c-lattice parameter of 1.34 nm, which is almost the same value as obtained from X - ray measurements in chapter 3 [72]. A TEM plane-view measurement of the film surface on the same Mg_2Ni sample is shown in Fig. 4.9. A pattern of diffuse black lines delineates areas with an average diameter of 50 - 100 nm. We identify this pattern to be the columnar grain boundaries resulting from the columnar growth observed in the cross-section measurements.

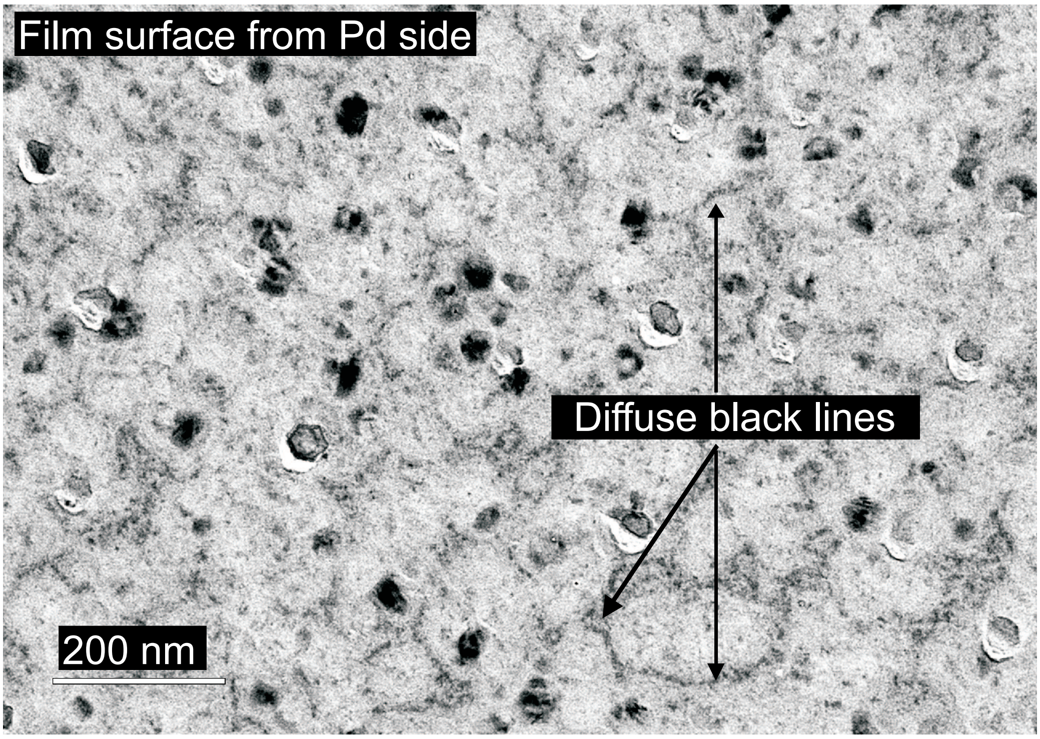

Figure 4.9: TEM plane view measurement of the film surface showing a network of diffuse black lines indicating the boundaries of the columns, with an average diameter of 50 - 100 nm.

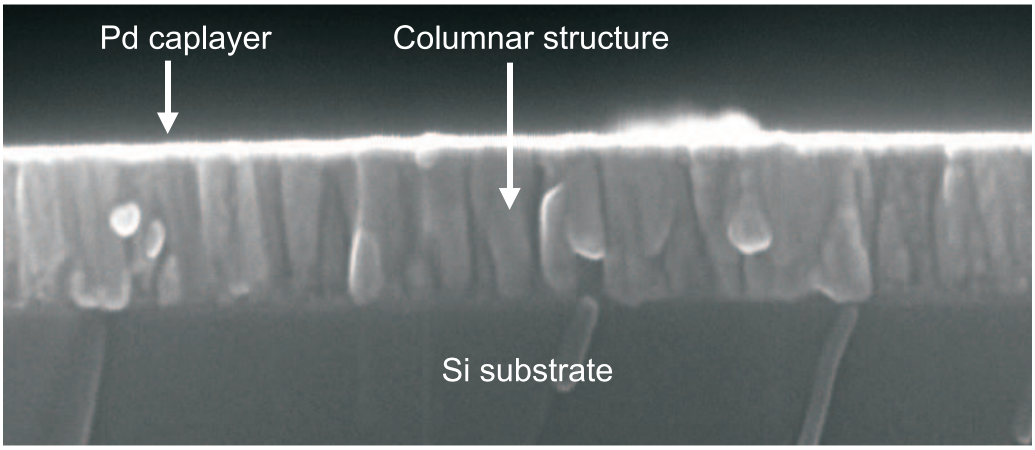

Figure 4.10: SEM micrograph of the cross section of an as-prepared 200 nm Mg_2Ni film capped by 5 nm Pd. A columnar structure with columns perpendicular to the substrate is observed.

All these observations are in agreement with the textured growth observed by X-ray measurements, with the c-axis of the hexagonal lattice perpendicular to the substrate and a coherence length in the growth direction of around 30 nm [72]. This implies that the columnar structures are not single crystalline but consist of densely packed grains with aligned c-axes.

SEM measurements on Mg_2Ni

To obtain a more direct image of the granular nature of the film, we use SEM on cleaved 200 nm Mg_2Ni films deposited on etched (HF) Si substrates. The micrographs in Fig. 4.10, show again a pronounced columnar microstructure.

The columns are very similar and the diameter of the columns increases with increasing distance from the substrate. The orientation of the columns is almost perpendicular to the substrate surface. Adjacent columns are separated by what seems to be 'open' channels as indicated in Fig. 4.11. Close to the film/substrate interface there is a 40 nm layer with a distinct microstructure. This layer consists of a more irregular structure of grains and clusters of grains, resulting in an increased grain boundary density and more disorder at the substrate interface. Some of these grains seem to serve as seed point for the growth of a column. The top of the columns corresponds to a local protrusion at the film surface. From a comparison of this structure with the STM results in Fig. 4.5, we conclude that the crystallites in Fig. 4.5c en 4.5f are in fact the protrusions as observed in Fig. 4.11.

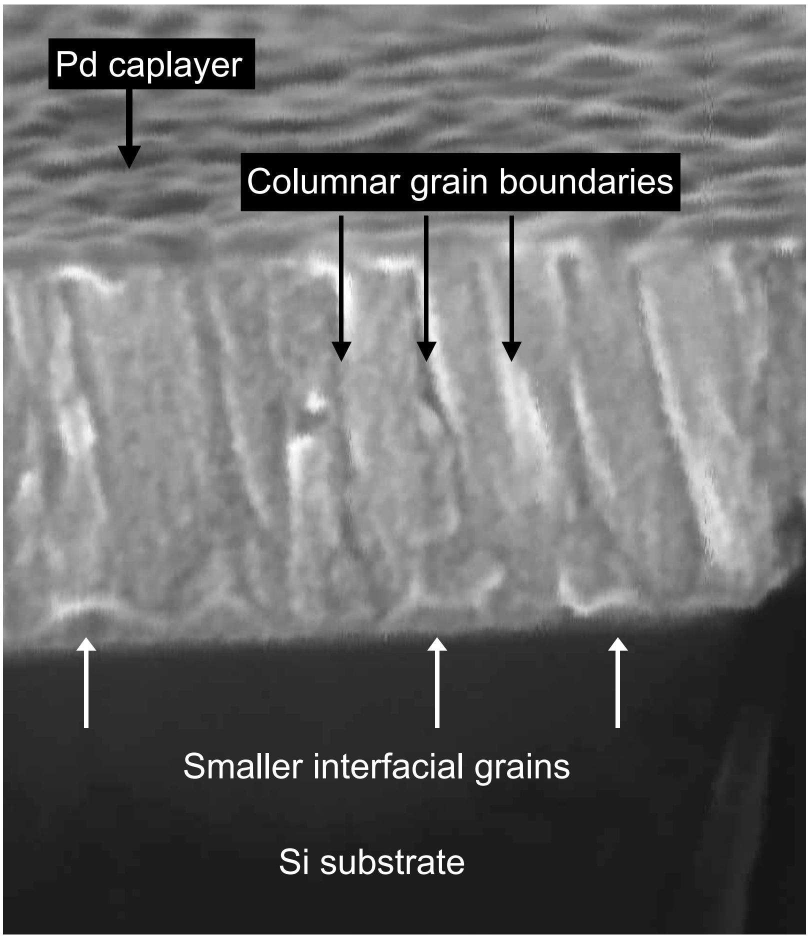

Figure 4.11: SEM micrograph of the same film as in figure 10, showing the columnar grain boundaries as 'open' channels.

4.5 Microstructure of Mg-Co and Mg-Fe thin films

4.5.1 *In-situ* STM on as-deposited 2Mg-Co and 2Mg-Fe thin films

The structural investigation of thin Mg_2Ni films revealed that the microstructure of these thin films consists of a small-grained layer close to the film/substrate interface. This porous layer develops into a columnar microstructure upon further deposition. This specific microstructure is at the origin of the self-organized double layering of these thin Mg_2Ni films. However, as Lokhorst *et al.* have shown [75] in contrast to Mg_2Ni thin films, the optical properties of Mg-Co and Mg-Fe thin films change with the number of hydrogenation

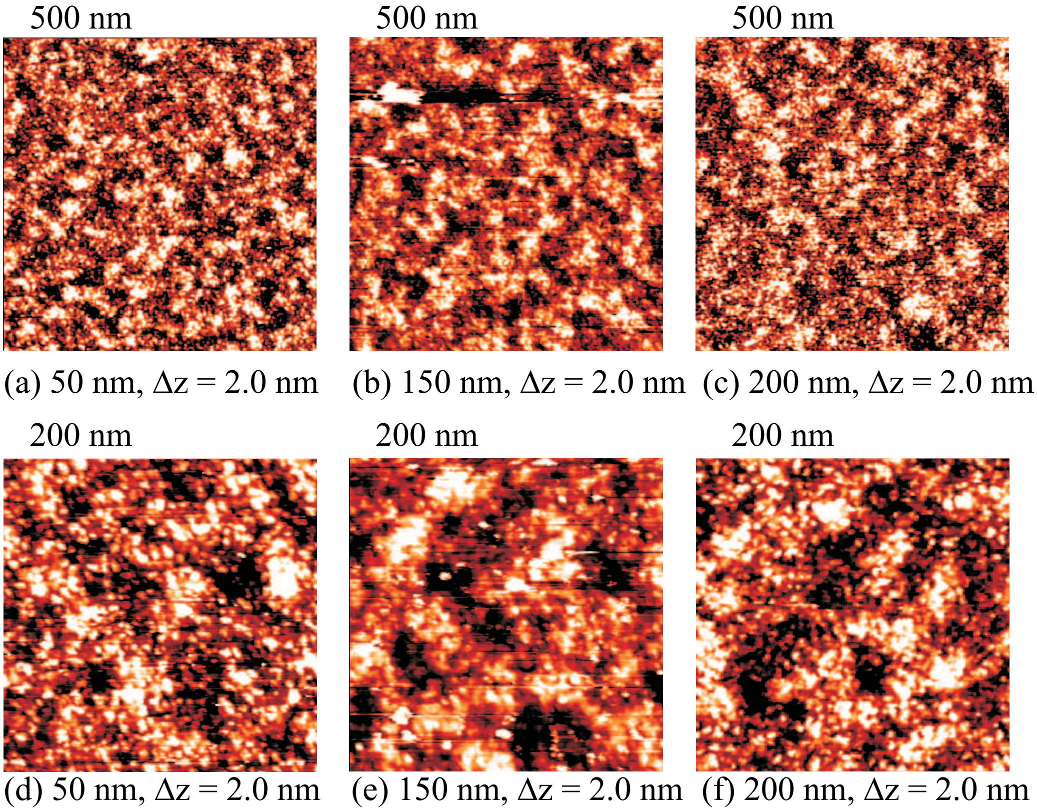

(a) 50 nm, Δz = 2.0 nm (b) 150 nm, Δz = 2.0 nm (c) 200 nm, Δz = 2.0 nm

(d) 50 nm, Δz = 2.0 nm (e) 150 nm, Δz = 2.0 nm (f) 200 nm, Δz = 2.0 nm

Figure 4.12: STM micrographs of *in-situ* grown thin 2Mg-Co films with thicknesses 50, 150 and 200 nm. The scan range in panels (a)-(c) is 500 nm and in panels (d)-(f) 200 nm. The maximum height difference from low (dark color) to high (white) is 2.0 nm. For a thickness of 50 nm (a, d) small grains with a diameter of 5 nm are observed that coalesce into larger structures of 25 nm. At d = 150 nm (b, e) and at d = 200 (c, f) the same kind of small grain clusters of small grains is observed. This indicates almost no microstructural development throughout the film

cycles. Upon subsequent loading cycles the hydrogenation behavior changes from a homogeneous dispersed hydride nucleation throughout the whole film to a double layer behavior. It is also reported that this effect is more pronounced for Fe than for Co based films and that it increases with increasing Mg concentration in Mg rich thin films. For Mg_yCoH_x, with y = 4 and 6, the transmission increases with the number of hydrogenation cycles. This means that the amount of residual metallic Mg decreases. This is likely to happen in large Mg grains whose center part remain metallic during hydrogenation.

Since Mg and Co do not form an alloy at deposition ratio Mg/Co = 2, we will indicate this composition by 2Mg-Co. To compare the Mg_2Ni thin film microstructure with that of 2Mg-Co and 2Mg-Fe and investigate how

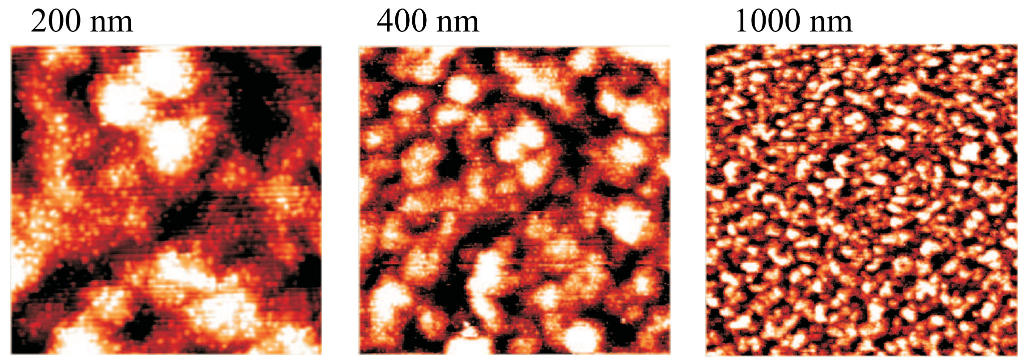

(a) 50 nm, Δz = 2.1 nm (b) 150 nm, Δz = 2.1 nm (c) 200 nm, Δz = 2.1 nm

Figure 4.13: STM micrographs of *in-situ* grown thin 2Mg-Fe film with a thicknesses of 200 nm. Panel (a) depict a scan range of 200 nm while panel (b) show a 400 by 400 nm area of the same sample and in panel (c) an 1000 nm by 1000 nm area is shown. The maximum height difference from low (dark color) to high (white) is 2.1 nm. These films consist of very small grains which are in the order of 1 nm. These small grains coalesce into larger structures.

the double layer can evolve as function of the number of cycles, *in-situ* STM measurements are performed on 2Mg-Co and 2Mg-Fe thin films of various thicknesses. In Fig. 4.12 STM measurements of 2Mg-Co films with thicknesses of 50, 150 and 200 nm respectively are shown.

The 50 nm films (see Figs. 4.12a + 4.12d) show that the grains have a size of ∼5 nm. They are inhomogeneously dispersed over the substrate surface and seem to accumulate in larger grains/structures of 25 nm. When we increase the film thickness to 150 nm (see Fig. 4.12b + 4.12e) the surface microstructure does not change, as is the case for Mg_2Ni thin films. This is even more clear when the film thickness is increased to 200 nm (see Fig. 4.12c + 4.12f) no structural development within the film is observed. It is intriguing that there is no structural development at all, since the temperature zone model at this temperature predicts a change in structure as a function of film thickness [90]. Most probably this is due to the fact that 2Mg-Co and 2Mg-Fe do not form an alloy but consist of a two phase system, Mg grains coexisting with Co or Fe grains.

In Fig. 4.13 STM measurements of a 200 nm 2Mg-Fe film are shown. The microstructure is quite similar to the microstructure of a 200 nm 2Mg-Co film. The 2Mg-Fe film shows even smaller grains which are in the order of a few nm (see Fig. 4.13a + 4.13b). Again these small grains are accumulated into larger structures (see Fig. 4.13c). These larger structures are more pronounced than in the case of 2Mg-Co. These observations suggest a distinct difference in the thin film microstructure of as-prepared Mg_2Ni versus 2Mg-Co and 2Mg-Fe thin films.

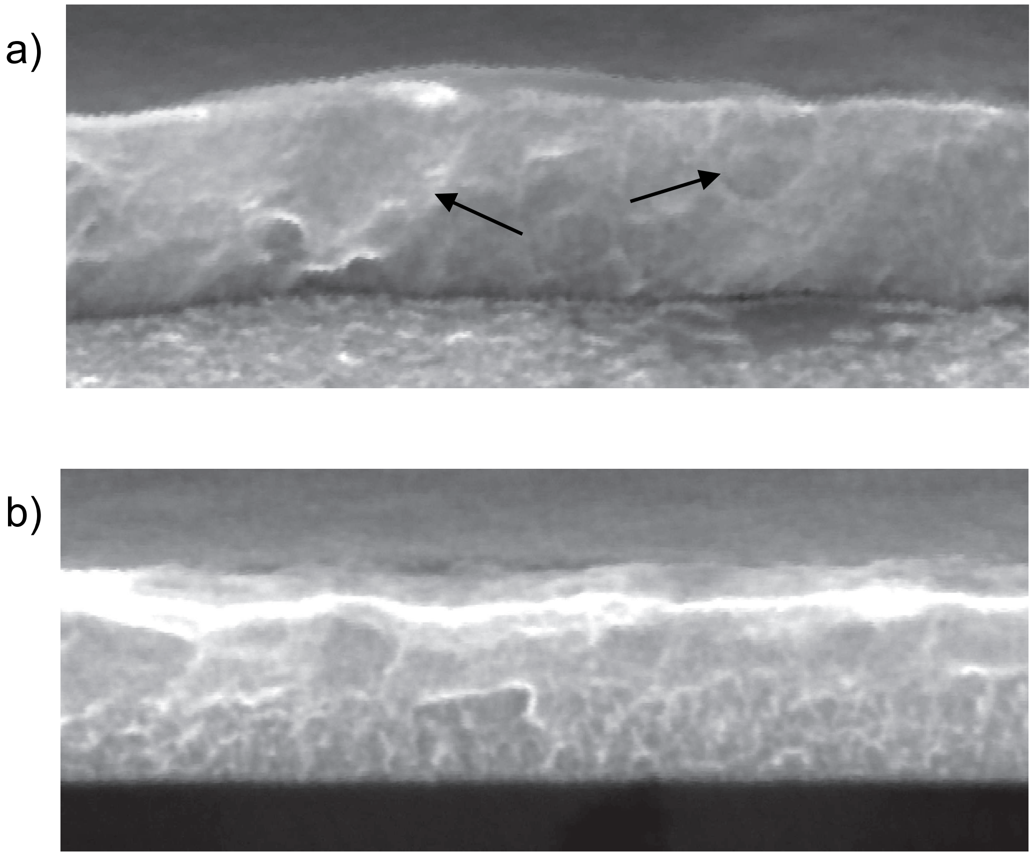

Figure 4.14: (a) SEM image of the cross-section of an as deposited 200 nm 2Mg-Co. The film does not show a clear microstructure throughout the film.(b) SEM cross-sectional image of a 200 nm 2Mg-Co which has been cycled for several times. A clear net of white line has developed throughout the thin film indicating grain or structure boundaries.

4.5.2 SEM measurements on as-deposited and hydrided 2Mg-Co thin films

The thin film microstructure of 2Mg-Co is further investigated by SEM measurements on cleaved 200 nm 2Mg-Co films deposited on etched Si substrates. The SEM micrographs of an as-prepared 2Mg-Co film and a 2Mg-Co thin film that is cycled several times are shown in Fig. 4.14a and 4.14b, respectively.

The as-prepared film, Fig. 4.14a, shows that the individual grains, as observed by STM, are too small to distinguish inside the film cross-section. Although the previously observed small grained microstructure can not be seen by SEM, it is obvious that the cross-section of the film is not completely homogeneous as indicated by arrows in Fig. 4.14. These structures correspond probably to the boundaries of grains of different density, structure etc. When this 2Mg-Co film is hydrogenated, a change in microstructure can be observed, Fig. 4.14b. After a few hydrogenation cycles a network of white lines (strong scattering of the electrons) can be observed. This network of grain boundaries is inhomogeneous distributed over the cross-section of the film with more and thinner lines close to the film substrate interface.

4.6 Discussion

We have found no evidence for a compositional change at the substrate interface. However, in the microstructure two sub-layers can be distinguished. First, we discuss the origin of this microstructure. Then we describe a scenario leading to the preferential nucleation of the complex hydride.

4.6.1 Microstructural growth of Mg_2Ni

The columnar microstructure (see Fig. 4.15) of Mg_2Ni thin films is consistent with the predictions of structure zone models, which categorize self-organized structural evolution during physical vapor deposition as a function of film growth parameters [90]. The most important parameter is the reduced temperature T_R defined as the ratio of the substrate temperature (T_S) and the melting temperature of the deposited film (T_M), $T_R = T_S/T_M$. The thin Mg_2Ni films are deposited at room temperature, while the incongruent melting point is at 1063 K, hence $T_R \sim 0.3$. Indeed, the observed columns are expected only for $T_R > 0.3$. At this temperature, small nuclei are formed randomly on the substrate. The temperature is high enough for a partial coalescence of the grains, but too low to achieve complete epitaxy. Due to the low mobility of the ad-atoms the grown grains increase in size. The competition in growth rate between neighboring grains induces the columnar growth. In addition, geometrical shadowing plays an important role in the formation of these columns [90, 91, 92, 93, 94, 95, 96, 97, 98, 99]. As a result, the columns are usually tilted towards the deposition source. Since our Mg_2Ni films are deposited using two separated sources, tilted by an angle of +/- 15° with respect to the substrate normal, we expect the geometrical shadowing to be negligible and the deposition geometry cancels the shadowing effect. On the other hand, as the melting point of Ni (1726.15 K) is much higher than the melting point of Mg (923.15 K) the mobility of the Mg adatoms on the substrate surface is higher than that of the Ni atoms, a source dependent growth of the columnar structure is expected. In these films no preferred columnar growth direction is observed. This suggests that the adatoms mobility is not the growth rate determining factor for this columnar growth.

4.6.2 Preferred nucleation of Mg_2NiH_4

We show now that the peculiar Mg_2Ni microstructure, can lead to the preferred nucleation of the Mg_2NiH_4 phase near the interface with the substrate.

As argued above, we assume that the preferential nucleation of the hydride phase near the interface (see Fig. 4.15b) is connected to the thin film microstructure, Fig. 4.15a. From experimental research on Mg_2Ni powder samples it is known that the hydrogenation kinetics is very sensitive to imperfections (lattice defects, porosity) in the sample and to stress development during hydrogen uptake [100]. Alloys consisting of nanocrystalline and/or amorphous phases absorb and desorb hydrogen more readily at the same hydrogenation temperature, H_2 - pressure and sample composition than their crystalline coun-

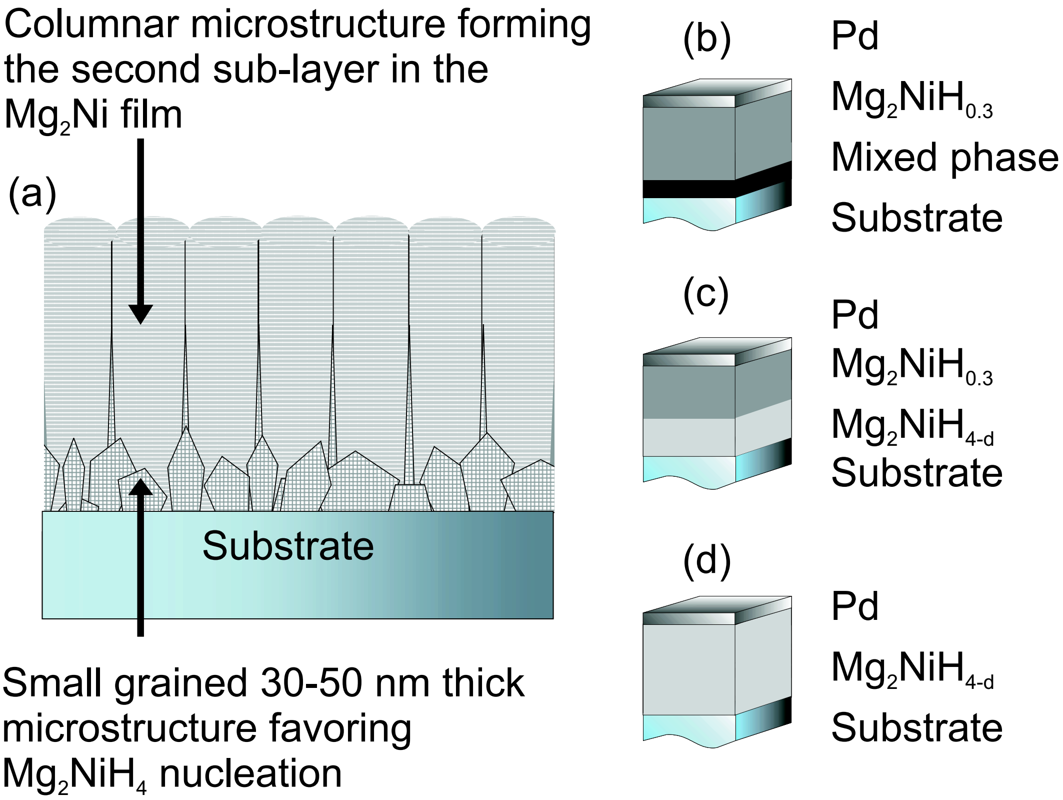

Figure 4.15: (a) Schematic representation of the Mg_2Ni thin film microstructure. The first 30 - 50 nm thick layer consists of small grains favoring nucleation of Mg_2NiH_4. From this layer a columnar microstructure develops. Nucleation of the Mg_2NiH_4 phase starts in this 30 - 50 nm sub-layer (b) resulting in the optical black state. This layer hydrogenates to Mg_2NiH_4 and increases in thickness upon further hydrogenation (c), resulting in a bi-layer system. This continues until the whole film is loaded to semiconducting, transparent Mg_2NiH_4, (d).

terparts [83, 101, 102, 103]. It has been suggested that the larger surface to bulk ratio represents an increased density of nucleation sites [104, 105, 106].

Similarly, we assume that the porous, small-grained microstructure observed in thin films near the substrate interface represents a higher density of nucleation sites [60, 61, 68, 107]. In addition, the small grains have the advantage to transform as a whole, preventing the formation of a metal-insulator phase boundary. Indeed, we find that the layering persists upon further loading [72], which suggests that the interface energy between the metal and hydride phase plays an important role. The interface energy for a closed bilayer is of course much lower than for hydrides nucleating randomly within columns. Note, that the persistent layering is only visible in sub-stoichiometric Mg_2Ni films [74].

The nucleation of the hydride at the substrate assumes a supersaturated $Mg_2NiH_{0.3}$ metal phase with a sufficiently high diffusivity. The columnar grain boundaries provide additional pathways for the necessary fast hydrogen diffusion.

The dehydrogenation of a fully loaded film starts at the *top* of the film. However, our kinetic hydrogenation scenario implies that the nucleation of the metallic phase should also start at the *substrate* interface, since the nucleation of the hydride in a metal should be similar to that of a metal in a hydride matrix. However, the diffusivity through the hydride phase is much smaller than that in the pure metal, thus the desorption starts at the Pd side. The asymmetry between H loading and unloading is thus partly due to different kinetics [108, 109].

4.6.3 Preferred nucleation in 2Mg-Co and 2Mg-Fe thin films

In this section we discuss the results on the microstructural growth of 2Mg-Co and 2Mg-Fe thin films with the experimental results obtained by Lokhorst *et al.* [75], who investigated the change in optical properties of Mg-Co and Mg-Fe films as a function of the number of hydrogenation cycles. They found that as a consequence of the repeated hydrogenation process, the Mg and Co/Fe grains become better mixed. This structural reorganization is identified as a transition from a grain-like to a defect-oriented microstructure and involves large changes in the respective microstructure. Furthermore, this development of microstructure upon hydrogenation, is accompanied by a change in optical properties and the appearance of an optical black state. This implies that as a function of the hydrogenation cycles a preferred hydride nucleation starts to develop at the film/substrate interface like in the Mg_2Ni thin films.

Lokhorst *et al.* explained the origin of this hydride formation in terms of a difference in the amount of high surface energy sites for nucleation. To overcome the hydride nucleation barrier, the hydride formation preferably starts at heterogenous incongruent grain boundaries, because these already have a high surface energy. In this process the substrate acts as a nucleation site. The heterogeneous incongruent boundaries between these grains have a large surface energy and promote hydride formation. The grain boundaries between grains of the same material have less surface energy and are therefore not favorable for nucleation. Therefore, in the less well mixed films a competition between nucleation at the substrate and at the grain boundaries between the Mg and TM grains homogeneously dispersed throughout the film is observed. When the film becomes more and more homogeneous, the only grain boundary is at the substrate side which subsequently induces a preferred local hydride nucleation. This results in the black state in the Mg-Co-H and Mg-Fe-H systems.

Since the number of hydrogenation cycles change the optical appearance of these films, it is important to indicate the origin of this mechanism. Hydrogen absorption and desorption change the film microstructure from a grain-like structure to a more homogeneous film and induce a defect network throughout these films. This change from a grain to a defect oriented structure has a large influence on the hydrogenation behavior of these films. Thus the as-deposited microstructure of the film is of significant importance for the measured physical properties of the film and the development of the properties upon repeated hydrogenation. This indicates that there is a strong relation between the hydrogenation behavior and the structure of the thin film.

4.7 Conclusion

From RBS, SIMS and electrical resistivity measurements we find that Mg_2Ni films have a homogeneous chemical composition from the surface to the substrate interface. Only in the first 2.5 nm unequal sticking of Mg and Ni on the bare substrate *might* induce some stoichiometry fluctuation. However, the preferred nucleation of the Mg_2NiH_4 phase takes place in a 30 nm layer close to the substrate. We propose therefore that the origin of the bilayer formation (and hence of the peculiar optical black state in Mg_2NiH_4) is due not to chemical but rather to microstructural effects.

By comparing the surface morphology of samples with various thicknesses ranging from 20 to 150 nm, we find in the first stages of growth an island growth mode. The islands transform into clusters of small grains resulting in a porous sub-layer with many grains and grain boundaries. Further deposition results in an increasing grain size and a subsequent columnar microstructure in the upper part of the film.

This two-layer microstructure is most probably the origin of the unusual hydrogen uptake and corresponding optical black state. The small grained layer close to the substrate lowers the activation energy for hydrogenation, resulting in a preferred nucleation of Mg_2NiH_4. This double layer formation is responsible for the the optical characteristics of the black state. Hence, it appears that this particular optical property is closely related to the growth induced microstructure of the thin film.

Our result shows that the simple diffusion models for hydrogenation often used in the hydrogen storage literature is not necessarily applicable to thin films or to nanosized metal-hydrides. Depending on the microstructure the hydride may nucleate from the inside of a grain. Apart from grain size engineering it might therefore also be worthwhile to try to engineer the defect structure to enhance the hydrogen absorption rate.

In 2Mg-Co and 2Mg-Fe thin films the defect (micro)structure seems to play a very important role in the hydrogenation behavior of these type of films. However further research has to be done to determine the origin of this behavior.

Chapter 5

Optical, structural, and electrical properties of *in-situ* grown thin films by activated reactive evaporation

5.1 Abstract

Mg_2NiH_4 and MgH_2 thin films have been prepared successfully by activated reactive evaporation (ARE) in a Molecular Beam Epitaxy (MBE) system equipped with an atomic hydrogen source. The optical reflection spectra and the resistivity of the films are measured *in-situ* during deposition. Both *in-situ* grown Mg_2NiH_4 and MgH_2 films appear to be stable in vacuum due to the fact that the dehydrogenation of the hydride phase is kinetically blocked. Hydrogen desorption only takes place when a Pd caplayer is added. The optical band gap of the *in-situ* deposited Mg_2NiH_4 hydride, 1.75 eV, is in good agreement with that of Mg_2NiH_4 formed by *ex-situ* hydrogenation of as-prepared metallic Pd capped Mg_2Ni films.

The microstructure of *in-situ* grown Mg_2NiH_4 is homogeneous with very small grains throughout the layer. As a result, on re-hydrogenation, the Mg_2NiH_4 phase nucleates randomly throughout the film and does not induce the optical black state.

The *in-situ* grown MgH_2 phase is highly resistive, although the optical spectra indicate the presence of 10 vol.% metallic Mg. The high resistivity indicates that these particles are embedded in a MgH_2 matrix. It is found that the fraction of metallic Mg grains is almost independent of the Mg and atomic H deposition rates. This excess of metallic Mg grains creates an absorption band at 2.0 eV, which is not observed for *ex-situ* hydrogenated MgH_2 films. The observed optical spectra can be modelled accurately using a Maxwell-Garnett or Bruggeman effective medium approximation. The *in-situ* deposition tech-

nique enables us to grow thick MgH_2 thin films and avoids the formation of a blocking layer which limits the formation of MgH_2 films as is the case for *ex-situ* hydrogenation of Mg-films. The absorption band observed for *in-situ* grown films disappears upon re-hydrogenation and the films behaves like an *ex-situ* hydrogenated film.

5.2 Introduction activated reactive evaporation

As shown in chapters 3 and 4, the optical black state in as-prepared Mg_2Ni thin films originates from the nucleation of the Mg_2NiH_4 phase at the film/substrate interface upon hydrogenation [71, 72]. This results from the peculiar double layer microstructure of these Mg-Ni thin films [16]. To confirm this model, we decided to change the thin film microstructure by growing *in-situ* hydride films. In all previous studies the hydride phase is formed by *ex-situ* hydrogenation using Pd as a catalytic caplayer. Here, we present a new method to prepare (complex) metal hydride films *in-situ* using activated reactive evaporation (ARE). So far only a few studies have been done on the *in-situ* growth of hydrides. Schoenes *et al.* report on the optical properties of single-crystalline YH_x thin films prepared by molecular beam epitaxy in the presence of atomic hydrogen [110]. Hayoz *et al.* also report the *in-situ* growth of Y dihydride by Y evaporation under a H_2 partial pressure of 5×10^{-4} Pa [111]. So far, the activated reactive evaporation technique has not been applied for the formation of complex Mg_2NiH_4 and binary MgH_2 films. We demonstrate that it is indeed possible to deposit also these films from the atomic constituents using an atomic hydrogen source, a Knudsen source for Mg and an electron gun for Ni.

The reliable growth of a hydride phase requires *in-situ* monitoring of the growth process. For this, we measure the optical properties and the resistivity during deposition. We find that an atomic hydrogen source is essential to grow a (complex) hydride phase. During the deposition, the molecular hydrogen pressure in the deposition chamber rises to about 2×10^{-2} Pa. This pressure is far below the equilibrium molecular hydrogen pressure of Mg_2NiH_4 (50 Pa) and MgH_2 (1.9×10^{-1} Pa). These phases can only form due to a sufficient flux of atomic hydrogen. The hydride phase both in vacuum and in air are remarkably stable. This shows that the dehydrogenation process has a high activation barrier.

The ARE technique makes it possible to study the electrical and optical properties without the interference of the catalytic Pd caplayer. The *in-situ* growth technique opens also the way for controlled doping and for constructing multilayered films of different hydride phases during deposition. In addition, it is a tool to change the thin film microstructure. Indeed, we find that the *in-situ* grown films display a totally different microstructure. The self-organized bilayer segregation and the associated optically black state are absent for *in-situ* grown Mg_2NiH_4 films, while the *in-situ* MgH_2 films excel by a remarkable high resistivity. In the first part of this chapter the results on the *in-situ* growth of Mg_2NiH_4 will be discussed which is followed by a discussion of the *in-situ* growth of MgH_2 thin films. As starting point, we measure the resistivity during *in-situ* deposition of Mg_2NiH_4 films to determine the quality of the grown hydride phase.

5.3 Resistivity measurements during *in-situ* growth of Mg_2NiH_4 thin films

Given the 5 orders of magnitude higher resistivity of the hydride phase as compared to the Mg_2Ni alloy, the change in electrical properties is a good indication for the amount of hydride formed [63].

In Fig. 5.1, we plot the film resistivity versus heating power of the H source capillary, which is an analogue for the amount of atomic hydrogen. Each point in the figure represents a fresh 200 nm thick Mg_2NiH_x film deposited at the corresponding heating power. Point 1 indicates the resistivity of a metallic Mg_2Ni film prepared at a background pressure of 2×10^{-7} Pa (vacuum conditions). Under these conditions, films with a resistivity of $\rho = 1.45 \times 10^{-5}$ Ωcm are obtained. This is the resistivity usually measured for metallic Mg_2Ni films [63, 71, 72]. Using hydrogen, i.e. supplying molecular hydrogen at a pressure of 2×10^{-2} Pa through the source without heating the capillary, results in a slightly higher resistivity (point 2 in Fig. 5.1). This means that the film contains a very small amount of hydrogen. Obviously the formation of the hydride phase is impossible by using molecular hydrogen since we operate below the hydrogen equilibrium pressure of 50 Pa at room temperature [72]. Keeping the gas flow rate constant and increasing the amount of atomic hydrogen by increasing the heating power to 128 watt (corresponding to a capillary temperature of 2100 K), we observe an increase of the resistivity to 0.34 Ωcm (point 7 in Fig. 5.1). The increase by 5 orders of magnitude of the resistivity of the exposed film indicates the formation of a semiconducting (or insulating) phase, Mg_2NiH_4 or MgH_2. We show below that the film is optically identified as Mg_2NiH_4. Reducing the deposition rate of the Mg and Ni atoms, to obtain a larger H/M ratio, does not result in a higher resistivity value. Once a 200 nm hydride thin film is grown, we terminate the deposition of Mg and Ni as well as the gas flow and the deposition chamber is pumped down to 2×10^{-7} Pa. Remarkably, the resistivity does not change. Apparently, the hydride is stable and does not loose hydrogen although the pressure is well below the hydrogen equilibrium pressure of Mg_2NiH_4. This means that the dehydrogenation reaction is kinetically blocked.

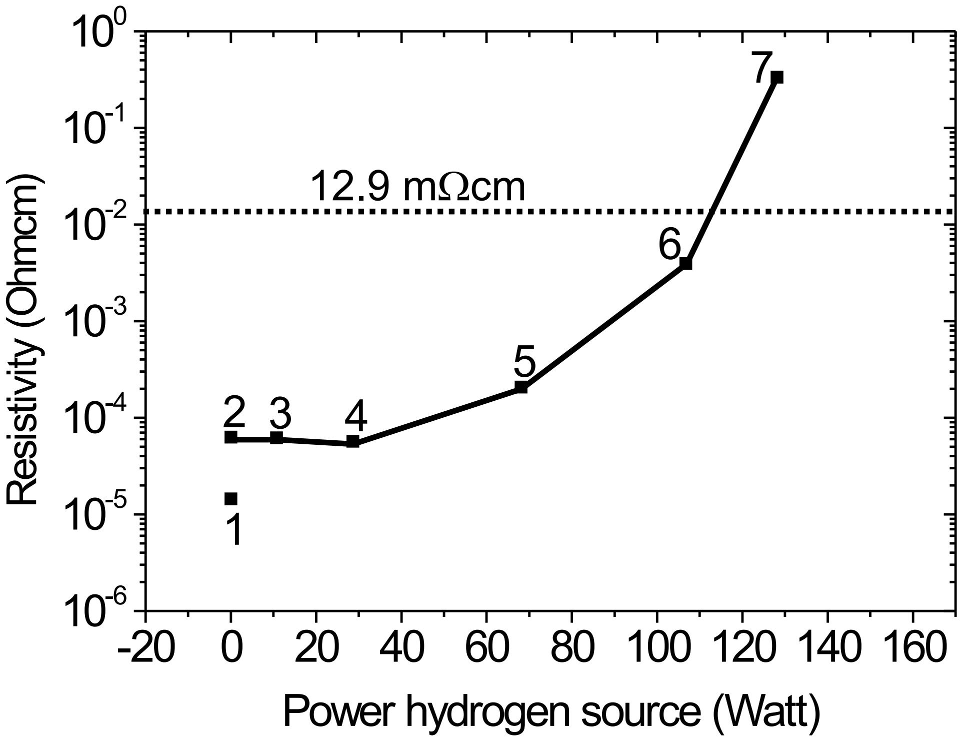

Figure 5.1: *In-situ* resistivity of Mg_2NiH_x thin films prepared by activated reactive evaporation. Each point in the figure represents another 200 nm thick Mg_2NiH_x film deposited at the corresponding capillary heating power (see text). The horizontal line at 12.9 mΩcm indicates the resistivity of an *ex-situ* hydrogenated Mg_2Ni film. Point 1: resistivity of a metallic Mg_2Ni thin film deposited at 5×10^{-7} Pa. Points 2-7: resistivity at an increasing heating power of the atomic hydrogen source capillary. The resistivity increases from 1.45×10^{-5} Ωcm to 0.34 Ωcm.

Enache *et al.* reported a detailed investigation of the electronic transport properties of Mg_2NiH_x thin films (capped with a discontinuous 2 nm Pd layer) [63]. For *ex-situ* hydrided films they found a resistivity of 12.9 mΩcm and concluded that Mg_2NiH_4 behaves as a heavily doped semi-conductor. The resistivity value of an *in-situ* grown Mg_2NiH_4 hydride thin film is 26 times higher than *ex-situ* hydrogenated Mg_2NiH_4 thin films. As we will see later, the grain boundary density of our *in-situ* grown films is much higher than those prepared by *ex-situ* hydrogenation of Mg_2Ni films. This observation may explain the difference between the resistivity value found by Enache *et al.* and our *in-situ* grown films.

In the next sections the optical characterization of the films both during and after deposition substantiates our claim that we indeed form Mg_2NiH_4.

5.4 Identification of the *in-situ* grown Mg_2NiH_4 phase

Figure 5.2 shows the reflection versus thickness of an as-grown Mg_2Ni and a Mg_2NiH_4 as well as the numerical simulation of a Mg_2NiH_4 film at 1.95 eV. The reflection measured during activated reactive evaporation exhibits a well defined interference pattern. This pattern arises from the reflections of the fiber/film and film/vacuum interfaces and indicates the growth of a transparent film. Apart from a small overshoot at the interference maximum and minimum, the measured reflection spectrum is identical to the calculated spectrum for

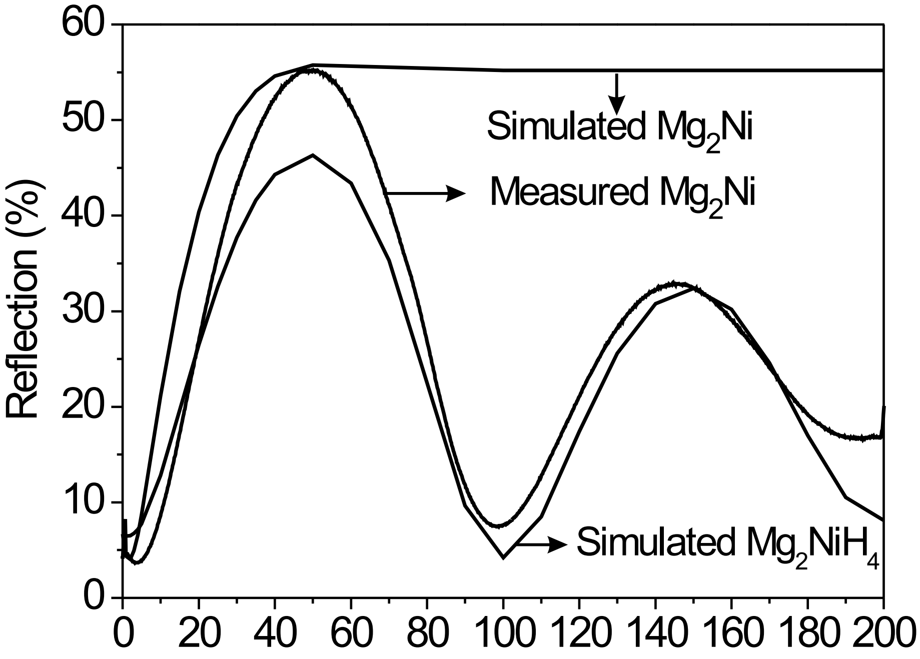

Figure 5.2: Reflection at photon energy 1.95 eV versus deposited Mg_2NiH_4 thickness. The calculated reflection of a Mg_2NiH_4 thin film and of a Mg_2Ni thin film are also shown. The good agreement between the measured and simulated reflection indicates that Mg_2NiH_4 is synthesized *in-situ*.

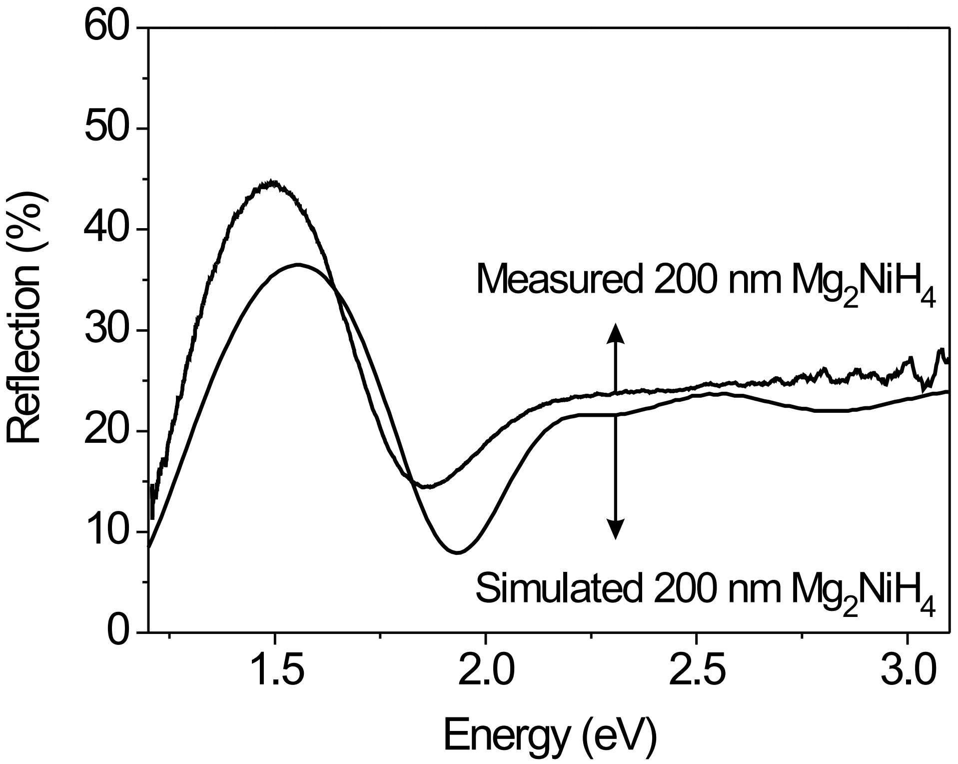

Figure 5.3: Reflection spectrum versus energy for a 200 nm Mg_2NiH_4 thin film. The great similarity with the simulated spectrum of Mg_2NiH_4 indicates that we indeed grow the hydride phase. It is shifted by 0.15 eV as compared with the measured spectrum.

a homogenous Mg_2NiH_4 thin film. This indicates that we indeed grow the Mg_2NiH_4 phase from the individual elements Mg, Ni and H. The reflection measured *in-situ* as a function of energy and the corresponding calculated reflection spectrum are shown in Fig. 5.3. Except for a small red shift in energy of 0.15 eV, the measured and calculated spectra are very similar in shape.

The reflection and transmission spectra of the *in-situ* grown Mg_2NiH_4 film are also measured *ex-situ* using a Bruker spectrometer (see Figs. 5.4 and 5.5). Note that the film remains stable when it is taken out of the vacuum system. The resistivity and optical properties do not change when exposing the *in-situ* grown film to air/oxygen. Even after depositing subsequently a Pd caplayer on the film, once exposed to air the films do not unload anymore at temperatures below 373 K (films capped with Pd directly after deposition can be loaded-

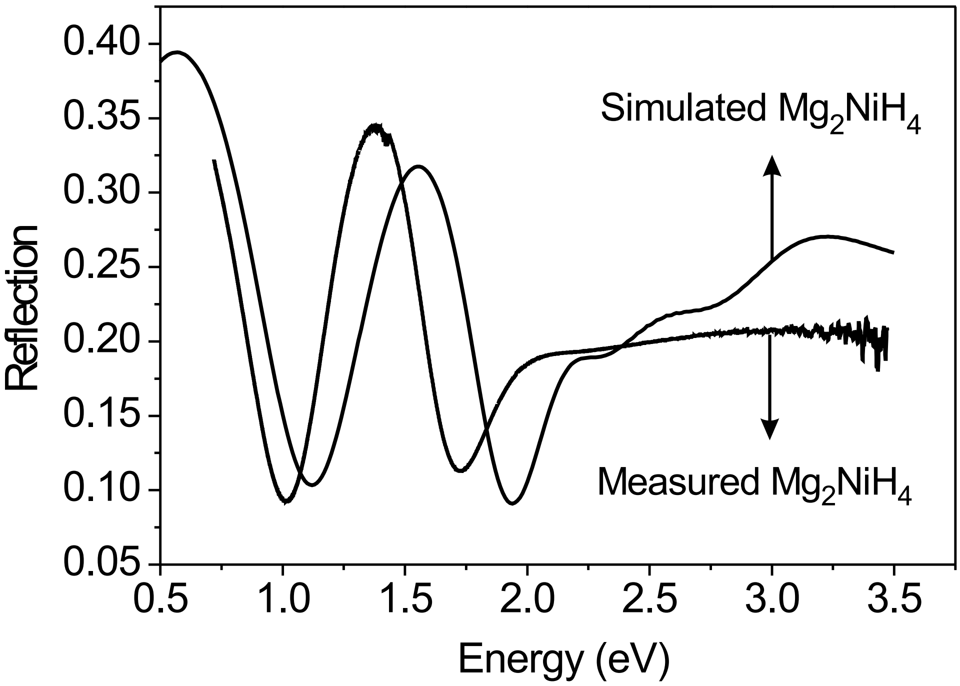

Figure 5.4: *Ex-situ* measured reflection spectrum for an *in-situ* grown 200 nm Mg_2NiH_4 thin film without a Pd caplayer. The spectrum displays a 0.15 eV red shift which is also observed in the *in-situ* measured spectrum. The interference pattern of the simulated reflection is comparable to the interference pattern of the measured reflection.

unloaded at RT). This shows that on exposure to air/oxygen a passivated surface layer forms on top of the hydride. This layer is so thin that it is not detected optically but it blocks the desorption of hydrogen. Probably an oxide skin develops on top of the film which prevents dehydrogenation, but we could not yet identify its nature. The *ex-situ* measured reflection spectrum is very similar to the calculated spectrum (Fig. 5.4) with a small red shift of 0.15 eV (the same as in Fig. 5.3). The transmission spectrum shows a band gap of 1.75 eV (see Fig. 5.5) by extrapolating the top-part of the band gap to zero. This is close to the band gap of an *ex-situ* hydrogenated Mg_2Ni thin film, 1.9 eV [71, 72], which confirms the direct formation of Mg_2NiH_4 by ARE. If MgH_2 had been formed, the band gap should be much higher since the band gap of MgH_2 is 5.6 eV [77]. Furthermore an effective medium approximation with a Ni-MgH_x compound does not reproduce the obtained optical data.

The red-shift from 1.90 to 1.75 eV in the apparent optical band gap might

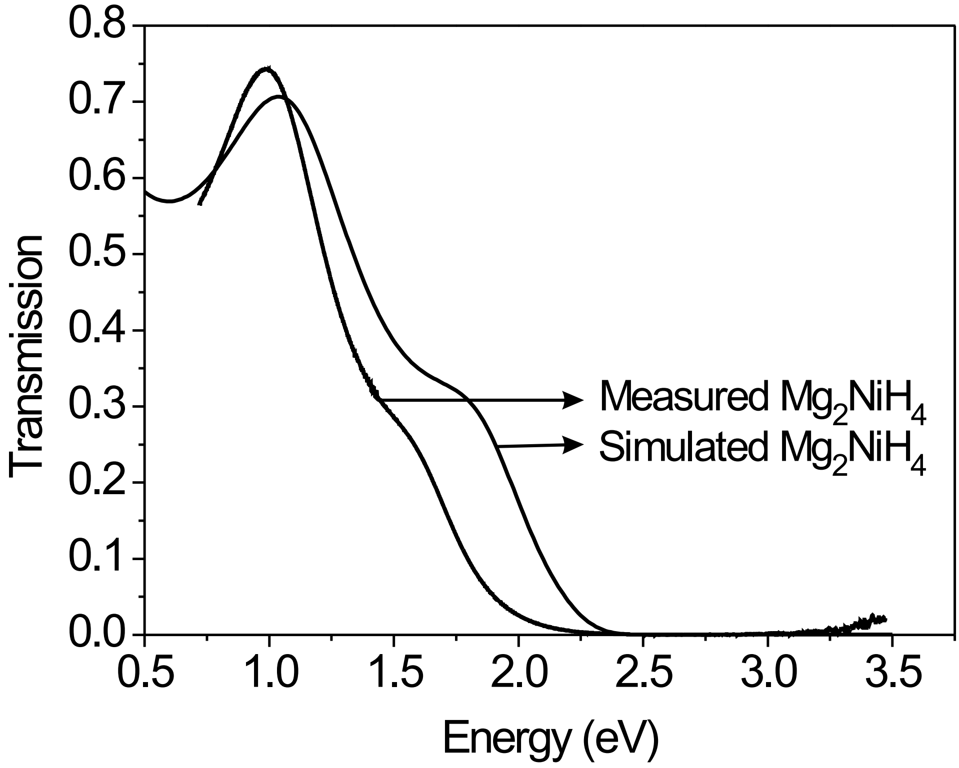

Figure 5.5: *Ex-situ* measured transmission spectrum for an *in-situ* grown 200 nm Mg_2NiH_4 thin film without a Pd caplayer. We observe that the measured transmission has an optical band gap of 1.75 eV and the simulated transmission has an optical band gap of 1.9 eV.

be due to a higher purity of the *in-situ* grown film. As the apparent gap in heavily doped semiconductors decreases with the dopant level, the lower dopant level of our *in-situ* films might explain the observed reduction [112]. The shift of E_g is given by the Burstein-Moss equation:

$$\triangle E_g = \frac{\hbar^2}{2m^*_{eh}}(3\pi^2 N_{opt})^{2/3} \tag{5.1}$$

in which m^*_{eh} is the reduced effective mass, and N_{opt} the optical carrier concentration. The 0.15 eV band gap shift results in $2.64 \times 10^{20}/\mathrm{cm}^3$ charge carriers, which is a factor 5 lower than found by Enache *et al.* [63] for *ex-situ* hydrided Mg_2Ni thin films. This is consistent with the difference in resistivity which is one order of magnitude higher in our *in-situ* grown films as compared to the *ex-situ* hydrided films.

5.5 The optical switching of Mg_2NiH_4 thin films

Before describing the optical behavior of the *in-situ* grown films, we shortly summarize that of an *ex-situ* hydrided Mg_2NiH_4 film for comparison.

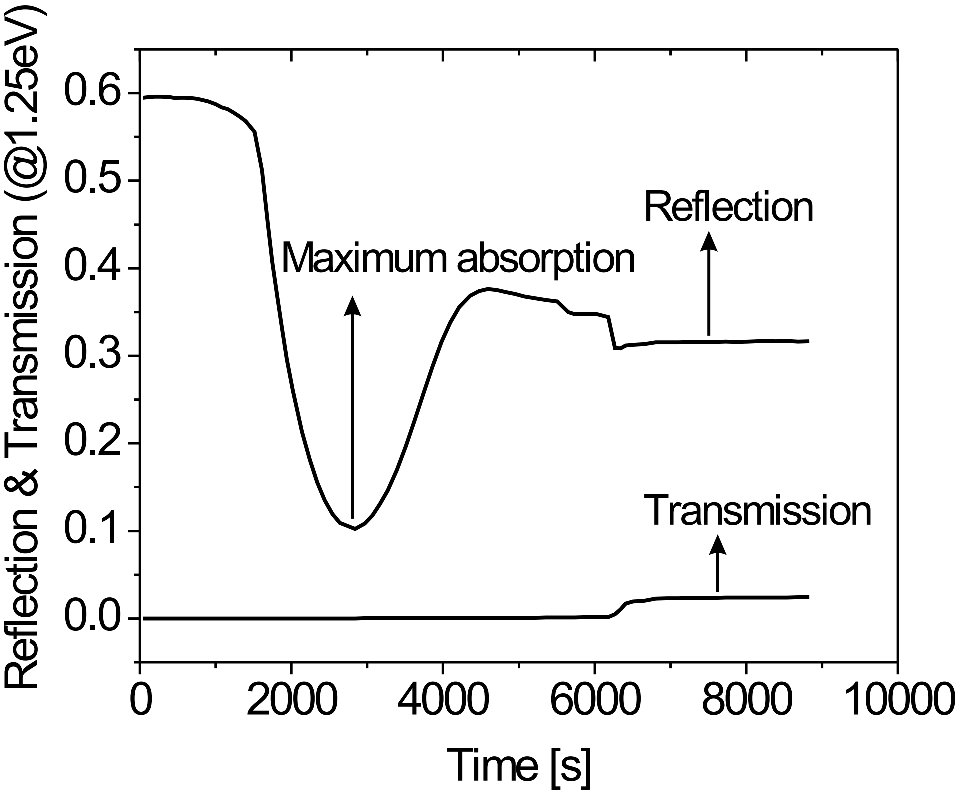

Figure 5.6: Reflection and transmission spectra at photon energy 1.25 eV versus hydrogenation time of an as-prepared Mg_2Ni thin film. At the minimum of the reflection, the transmission is essentially zero, indicating the preferred hydride nucleation at the interface with its maximal absorption.

When a Mg_2Ni film is exposed *ex-situ* to hydrogen the reflection drops to a minimum value at which the transmission is still essentially zero (see Fig. 5.6). Transmission starts to increase after the reflection has recovered from its first minimum value. This results in an intermediate optically black state which is a consequence of the self-organized double layering of these films upon hydrogenation. The hydride preferentially nucleates at the film/substrate interface. Consequently it is not possible to find a single set of n and k values that describe the observed reflection (R) and and transmission (T) spectra

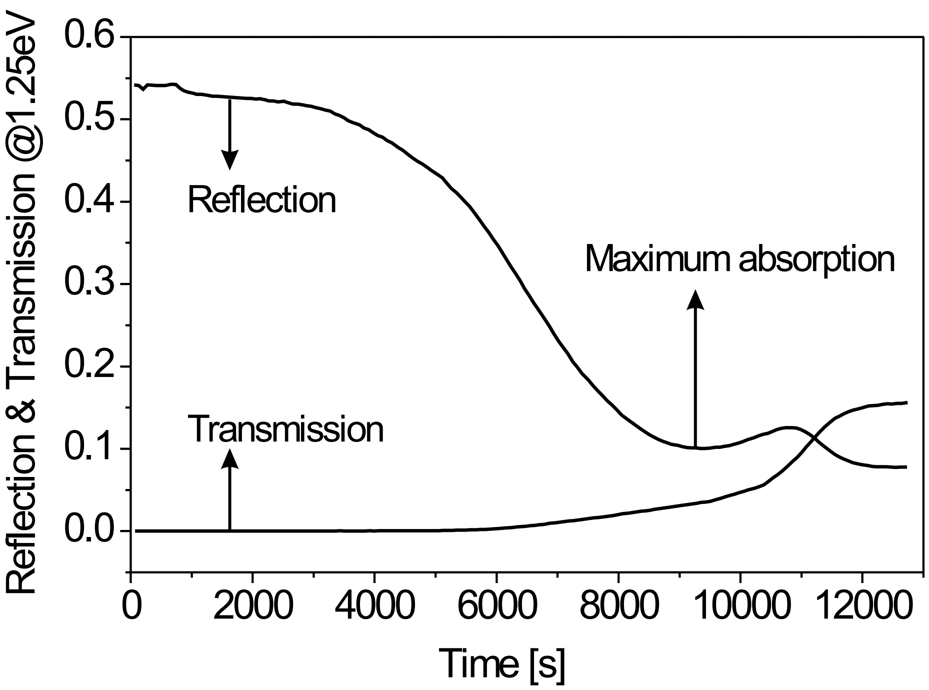

Figure 5.7: Reflection and transmission spectra at photon energy 1.25 eV versus hydrogenation time of a film which is *in-situ* deposited as Mg_2NiH_4 and then dehydrogenated. At the reflection minimum, the transmission has a finite value of 0.04. This finite value of the transmission leads to a crossing of the R and T curves in Fig.5.8.

during the optical black state (maximal absorption) and that one needs to assume a double layer model to explain the optical state [71, 72].

To examine the re-hydriding properties of an *in-situ* grown Mg_2NiH_4 film, we cap the film *in-situ* with 10 nm Pd. This results in the dehydrogenation of the hydride phase and enables us to re-hydrogenate the film. The re-hydrogenation of the *in-situ* grown Mg_2NiH_4 thin films displays a clear difference in hydrogenation behavior (see Fig. 5.7). The minimum in reflection is less pronounced and before the reflection reaches its minimum value, the transmission has already increased to T = 0.035. This means that the hydride nucleates throughout the entire film and that effective n and k values can be found to describe the optical properties of the film. Using a transfer matrix method as described previously we calculate R and T spectra for a dense grid of (n,k) for the Mg_2NiH_x layer. A crossing of R and T indicates a

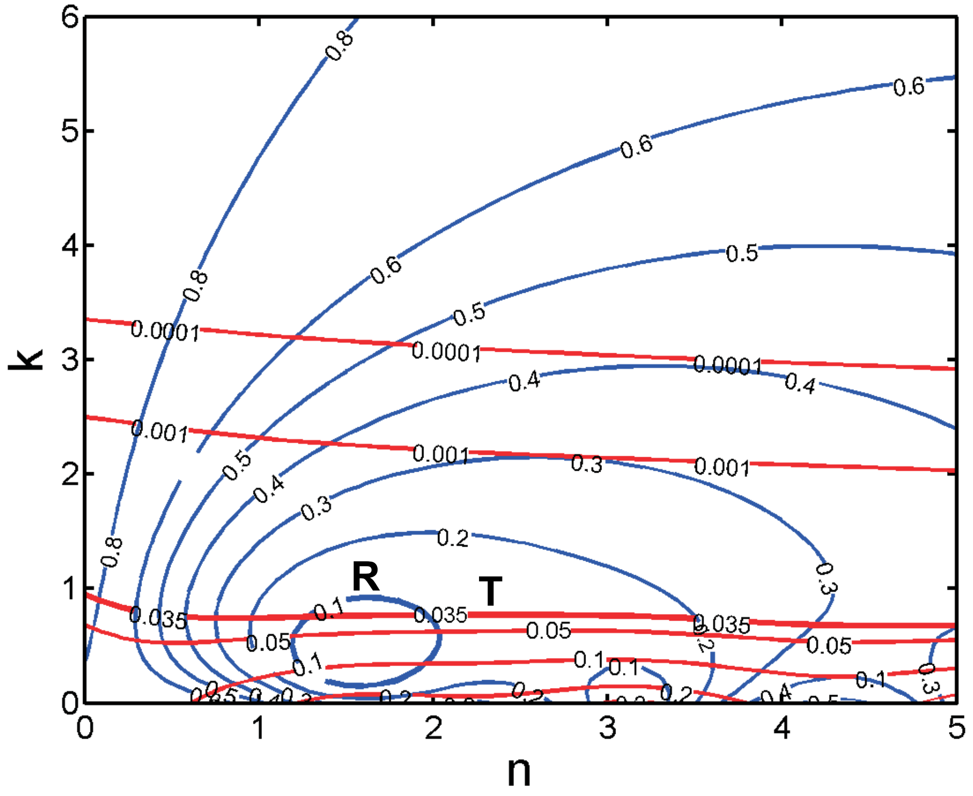

Figure 5.8: Contour maps of the reflection and transmission at 1.25 eV for a 200 nm Mg_2NiH_x thin film capped with 10 nm Pd on quartz. The crossing of the contour plot for transmission at T = 0.035 and the reflection at R = 0.1 (which correspond to the values for a film in the black state) indicates that optically the Mg_2NiH_x film can be modelled as a homogeneous layer.

solution (n,k). For the experimental values R = 0.1 and T = 0.035 we find two sets of effective (n,k) (see Fig.5.8). This implies that the film behaves as a homogeneous layer, and can be described by an effective medium theory. In the next section we show that the microstructure of a dehydrogenated *in-situ* grown Mg_2NiH_4 film is quite different from that of an as-grown Mg_2Ni film. This explains the different optical behavior. Note, that the microstructure is largely determined by the thin film growth conditions.

5.6 Microstructure of *in-situ* grown Mg_2NiH_4 thin films

The surface morphology of the *in-situ* prepared Mg_2NiH_4 thin films is investigated by AFM measurements. A comparison between an as-prepared

Mg_2Ni, an *ex-situ* post-deposition hydrided Mg_2NiH_4 film and an *in-situ* grown Mg_2NiH_4 film is shown in Fig. 5.9. The grains of a 200 nm *ex-situ* hydrided Mg_2NiH_4 film have an average diameter of 75 nm (see Fig. 5.9b) which is comparable to the grain size in an as-deposited Mg_2Ni film (see Fig. 5.9a). The surface microstructure of an *in-situ* prepared Mg_2NiH_4 film has a significantly smaller grain size of 25 nm. Furthermore, the roughness of the *in-situ* deposited Mg_2NiH_4 film surface has decreased and is in the order of 1 nm, whereas a normal 200 nm Mg_2NiH_4 film has a roughness of 20 nm, see Fig. 5.9b.

With AFM we can only probe the film surface. We use SEM measurements on cleaved 200 nm *in-situ* prepared Mg_2NiH_4 films deposited on Si substrates, to investigate the microstructural cross-section of the film. The specific columnar microstructure of Mg_2Ni thin films with the typical small grain structure near the substrate interface has disappeared in the *in-situ* prepared Mg_2NiH_4 films (see Figs. 5.10a and b). The *in-situ* grown thin film consists of a homogeneous phase without any noticeable microstructure and the film microstructure is smaller than or close to the resolution of the SEM apparatus (maximum resolution 1.5-2.0 nm). Preliminary plane view TEM measurements show that these films are almost amorphous and that the crystallites are typically 1 nm in diameter. These measurements imply that there is no microstructural reason for a preferred hydride nucleation in contrast to *ex-situ* hydrided Mg_2NiH_x thin film. This is consistent with the optical measurements where we concluded that the hydride nucleates throughout the whole thin film, and not just at the substrate interface.

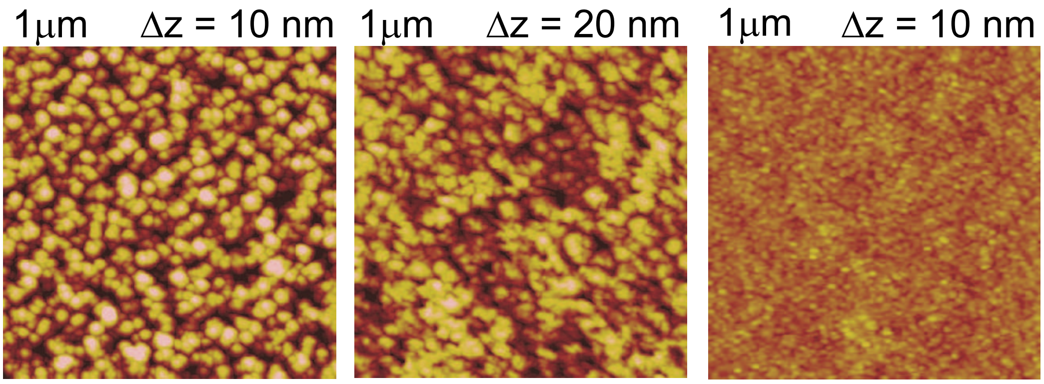

(a) Metallic Mg_2Ni (b) Mg_2NiH_4 *Ex-situ* loaded (c) Mg_2NiH_4 *In-situ* grown

Figure 5.9: AFM measurements on (a) a 200 nm Mg_2Ni thin film covered by 10 nm of Pd (b) a 200 nm Mg_2NiH_4 thin film covered by 10 nm of Pd (c) a 200 nm $Mg_2NiH_{4-\delta}$ thin film prepared by activated reactive deposition. The shown area is 1 μm

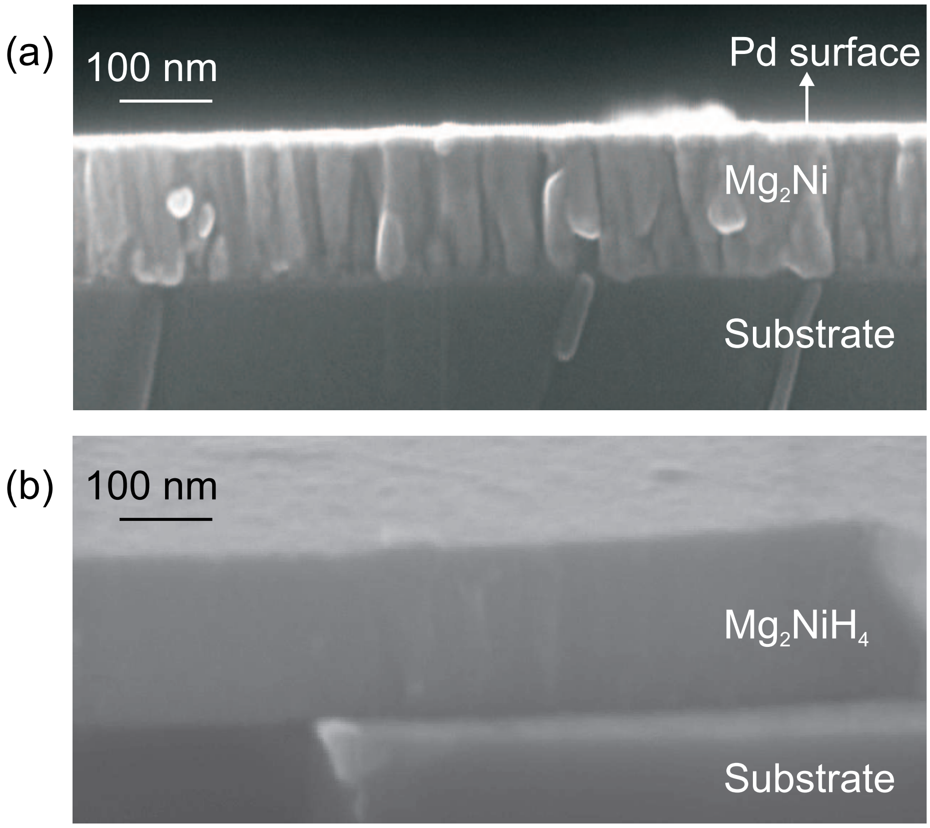

Figure 5.10: (a) SEM image of the cross-section of an as-deposited 200 nm Mg_2Ni film. The film has a clear columnar structure. (b) SEM cross-sectional image of a 200 nm Mg_2NiH_4 thin film prepared by activated reactive deposition. The surface of the film is very flat as compared to the as-deposited Mg_2Ni film.

5.7 The stability of Mg_2NiH_4 and the role of Pd

The atomic hydrogen source allows us to grow *in-situ* Mg_2NiH_4 thin films at an applied hydrogen pressure below the H_2 equilibrium pressure of Mg_2NiH_4 formation. While the atomic hydrogen source is essential for the hydride formation in complex hydride systems, the blocked decomposition reaction stabilizes the hydride formed. Indeed, the *in-situ* grown Mg_2NiH_4 hydride film remains in its metastable state in vacuum (5×10^{-7} Pa) after deposition. The hydrogen desorption from the film without a Pd caplayer is almost negligible on a time scale of hours. This shows that the dehydrogenation process of Mg_2NiH_4 has a high activation barrier and is kinetically blocked. Depositing a Pd caplayer on top of an *in-situ* grown hydride film results in a spontaneous dehydrogenation of the film. This process starts already with a few angström

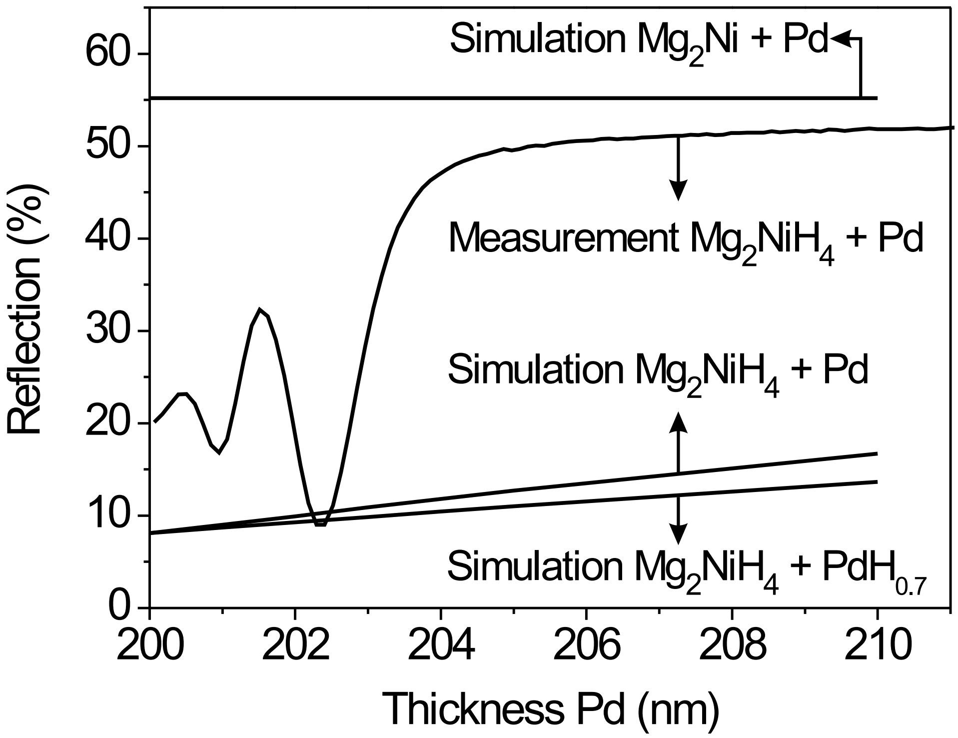

Figure 5.11: Reflection at 1.95 eV as a function of deposited Pd thickness on an *in-situ* grown 200 nm Mg_2NiH_4 hydride film. Simulation of the reflection of a 200 nm Mg_2NiH_4 film capped with Pd and capped with $PdH_{0.7}$ are shown together with a 200 nm metallic Mg_2Ni/Pd film. The developing interference pattern indicates the unloading of the film with the metallic Mg_2Ni phase forming from the Pd surface downwards. The simulations with Pd and $PdH_{0.7}$ indicates that the film really unloads and that the change in reflection is not due to the deposited Pd caplayer.

of Pd, as the oscillations in Fig. 5.11 start immediately. The deposition of a 10 nm Pd caplayer results in a completely unloaded Mg_2Ni metallic film within minutes, under High Vacuum (HV) conditions. After re-hydrogenating this film in the load lock of the vacuum system, the subsequent unloading kinetics slowed down considerably. However, when we subject the film to air, the hydrogen desorption is accelerated and the film unloads to the metallic phase within minutes (see point 3 in Fig. 5.12 and point 4 in Fig. 5.13). The need to activate the dehydrogenation process by O_2 is always observed in *ex-situ* hydrided Pd/Mg_2NiH_4 thin films. It appears as if the hydrogenation of the

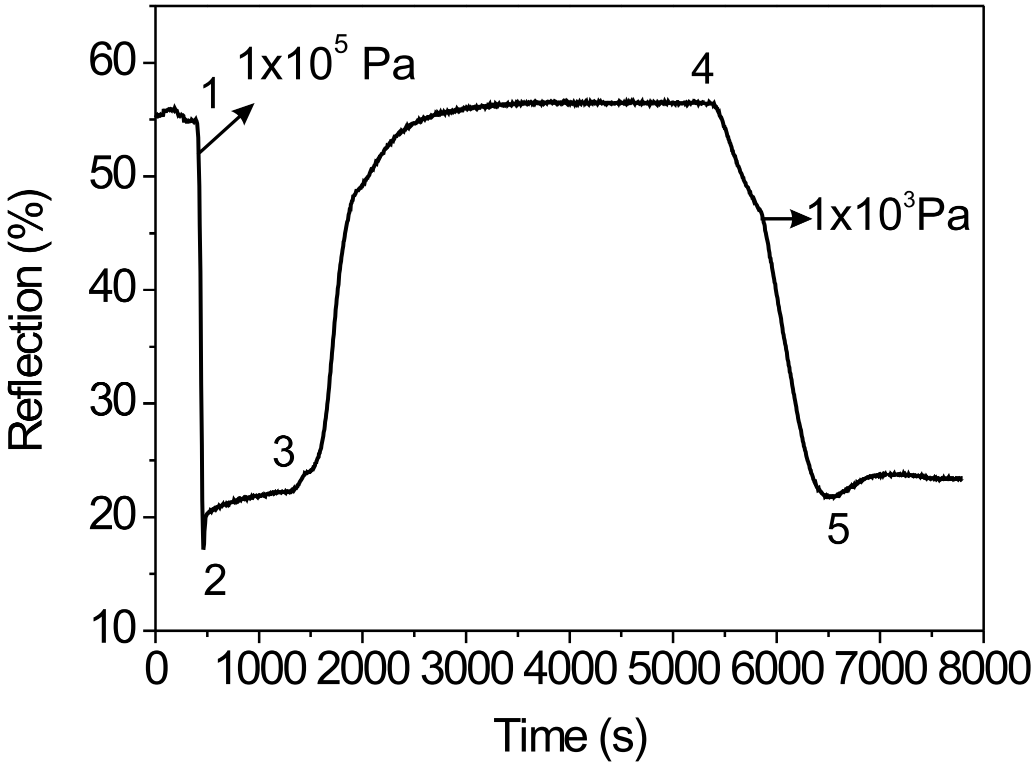

Figure 5.12: Reflection at 1.95 eV during the loading/unloading process at room temperature of an *in-situ* grown Mg_2NiH_4 thin film. (1) Start of the re-hydrogenation at 1×10^5 Pa of an *in-situ* prepared Mg_2NiH_4 film which unloaded during *in-situ* capping with Pd, (2) reduced minimum in reflection, (3) start to unload the thin films in air, (4) start of a re-hydrogenation but now at 1×10^3 Pa, (5) again the reduced minimum in reflection is observed but kinetics is much slower.

Pd-covered metal alloy has a detrimental effect on the activation energy for dehydrogenation.

In the investigation of the surface reaction of palladium hydride in vacuum, air and water, Gräsjö *et al.* found that the activation energy of desorption of hydrogen is lowered by the reaction with oxygen [113]. Furthermore a humid atmosphere catalyzes the reaction between hydrogen and oxygen and increases the release rate of hydrogen by a factor of 100 as compared to desorption in a vacuum system. In a vacuum system the release of hydrogen can only take place by the recombination and desorption process of hydrogen.

It is difficult to understand the difference between the unloading of the *in-situ* grown hydride in vacuum and that of the re-hydrided film, because the dehydrogenation conditions are the same in both cases. Possibly a sulfur contamination of the Pd or the intermixing of Pd with Mg_2NiH_4 plays a role here. Although the hydrogen gas used to re-hydrogenate the film is 99.999 pure its contaminants may also degrade the catalytical properties of the Pd. This is however not plausible since the same hydrogen gas is used in the *in-situ* growth.

Alternatively, Borgschulte *et al.* suggest that the Pd may become covered by the hydride-metal on hydrogenation. This so-called SMSI (strong-metal support interaction) effect is driven by the minimization of the surface energy and plays a large role in the reduced catalytic properties of the Pd caplayer [79, 114].

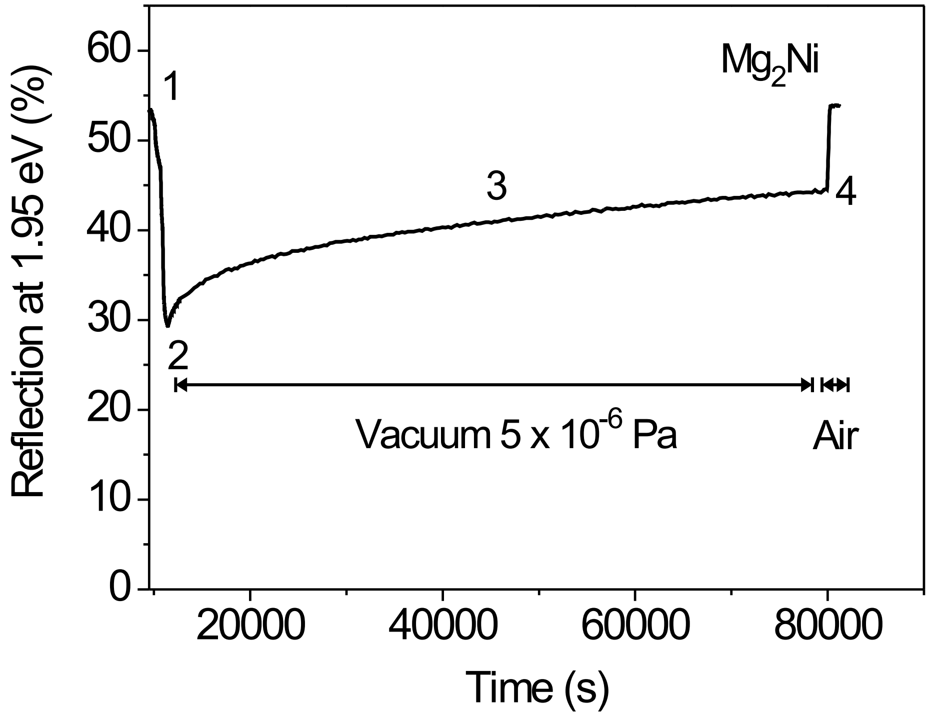

Figure 5.13: Post-deposition hydrogen absorption/desorption cycle of an *in-situ* grown 200 nm Mg_2NiH_4 thin film capped with 10 nm Pd. (1) Unloaded Mg_2Ni phase, (2) reduced interference minimum, (3) hydrogen desorption in vacuum, (4) applied atmospherical air environment. The exposure to an air environment catalyzes the dehydrogenation tremendously.

5.8 Conclusions concerning the *in-situ* growth of Mg_2NiH_4

In-situ fiber spectroscopy and *in-situ* resistivity measurements show that complex metal hydride thin films can be grown by ARE. Mg_2NiH_4 hydride thin films are formed from the constituent elements Mg, Ni and H, where H is provided by an atomic hydrogen source. The hydride films are stable in vacuum. Only after *in-situ* capping with Pd, do the as-grown hydride films transform to the metallic state. The dehydrogenation of a re-hydrided film is much more difficult and requires oxygen. The difference in dehydrogenation behavior of an *in-situ* grown Mg_2NiH_4 thin film and a re-hydrogenated thin film may have its origin in a contamination effect of the Pd catalyst or a microstructural reorganization upon re-hydriding the thin film. Further research has to be done to clarify the origin of this effect. The most plausible explanation is a sulfur contamination of the Pd caplayer.

In-situ resistivity measurements show that the resistivity of an *in-situ* grown Mg_2NiH_4 thin film is 0.34 Ωcm, which is 26 times higher than for a post-deposition hydrided film. This mismatch between *in-situ* and *ex-situ* hydrided films can be attributed to the high density of hydride grain boundaries in *in-situ* prepared hydrides. The shift of the energy band gap indicates a low charge carrier density, which may also contribute to the high resistivity value.

As proposed in chapter 4, here we prove the correlation between the preferred hydride nucleation in Mg_2Ni thin films and their specific microstructure. Thin films grown by activated reactive evaporation consist of a small grained homogeneous layer and since there is no microstructural development throughout the film, there is no preferred hydride nucleation within the film. This is consistent with the absence of an optical black state in these films.

5.9 *In-situ* grown MgH_2 thin films by activated reactive evaporation

The interest in the magnesium-hydrogen system arises from the fact that it can absorb and desorb a large amount of hydrogen. Furthermore, Mg switchable mirrors are color neutral in the fully hydrogenated state which make them very attractive for smart window applications. However, slow reaction kinetics at room temperature (RT) and poor thermodynamic properties limits its practical use. The advantages of Mg as hydride storage material are numerous: Mg is abundant, light weight and its hydride phase contains 7.6 wt% of hydrogen. These attractive properties make it worthwhile to investigate the possibility to improve its hydrogenation behavior. Mg thin films gained attention due to their fascinating change in optical properties upon hydrogenation. These Mg films can be switched from a shiny metallic film to a color neutral transparent semiconductor with an optical band gap of 5.6 eV [77]. Between the metallic reflecting state and the transparent semiconducting state, Giebels *et al.* discovered a third optical state. At intermediate hydrogen concentration a highly absorbing optical state is observed. This optical black state results from a spatial disproportionation in metallic Mg and MgH_2 grains caused by the MgH_2 nucleation throughout the entire sample [77]. The optical and electrical properties of these films were modelled with a Bruggeman effective medium approximation for a Mg-MgH_2 composite [115]. The origin of this optical black state is completely different from that observed in Mg_2Ni thin films [71, 72]. In these films the black state is caused by a self-organized layering of the film upon hydrogenation, originating from the specific thin film microstructure [16].

When an as-prepared Mg film is hydrogenated, the electrical resistivity increases during the transition to the optical black state and reaches a value of 10 mΩcm in the fully loaded transparent state [77, 116]. The hydrogenation kinetics of such a thin film is not straightforward. The formation of a MgH_2 layer beneath the protective Pd forms a hydrogen diffusion barrier preventing hydrogen diffusion and blocks further hydride formation. The growth of the blocking layer can be circumvented by starting at low hydrogenation pressures (10^2 Pa) and higher temperatures (372 K) [117, 118].

The study of the intrinsic physical properties of *ex-situ* loaded Mg films is hampered by the presence of the metallic Pd caplayer. It is thus very attractive to grow the MgH_2 hydride phase by ARE.

Giebels *et al.* show that an as-grown 120 nm thick Mg film capped with 10 nm Pd is fully hydrogenated at 10^7 Pa and 373 K. Therefore, we will use their optical data and resistivity value as reference for our *in-situ* grown Mg hydride films. Furthermore, we use this data to calculate the reflection and transmission spectra of MgH_2 films, thus we use ϵ_1 and ϵ_2 which are obtained by *ex-situ* hydrogenation of an as-grown Mg film. Since we do not know the exact hydrogen concentration in the *in-situ* grown hydride Mg films, we will denote these films as MgH_x. Before we describe the optical properties we start with a section on the electrical properties of these films.

5.10 Resistivity measurements of *in-situ* grown MgH_2 thin films

The resistivity of a film in the MgH_2 phase should be extremely high since it is a wide gap insulator. Indeed we obtained films of which the resistivity was too high to measure ($\rho >$ MΩcm) using various electrical contacts and techniques. The high resistivity value indicates a high measure of quality of the *in-situ* grown MgH_x films. For *ex-situ* hydrogenated Mg thin films, Isidorsson *et al.*

report an electrical resistivity of 630 $\mu\Omega$cm. This rather low resistivity value is due to the metallic Pd caplayer [116]. Giebels *et al.* corrected for this and reported a resistivity 10 mΩcm [77]. This rather low resistivity value suggests that these films have a high impurity level, but the optical data do not give any evidence for that. The high resistivity of our *in-situ* grown MgH_x thin films suggests that they have a higher purity than the *ex-situ* hydrogenated Mg films. This is intriguing since the optical data show that *in-situ* grown films are not at all pure. They still contain some metallic Mg grains.

5.11 *In-situ* reflection measurements during ARE of MgH_2 thin films

With *in-situ* reflection measurements using fiber optics, we identify the nature of the growing hydride phase. In Fig. 5.14 the reflection at 1.95 eV versus deposited MgH_x thickness is shown. The observed reflection shows a well defined interference pattern indicating the formation of a dielectric material. The oscillation in reflection arises from the reflection from the various interfaces involved (fiber/film and film/vacuum interfaces). For an accurate simulation of the reflection data (using the dielectric functions of metallic Mg and insulating

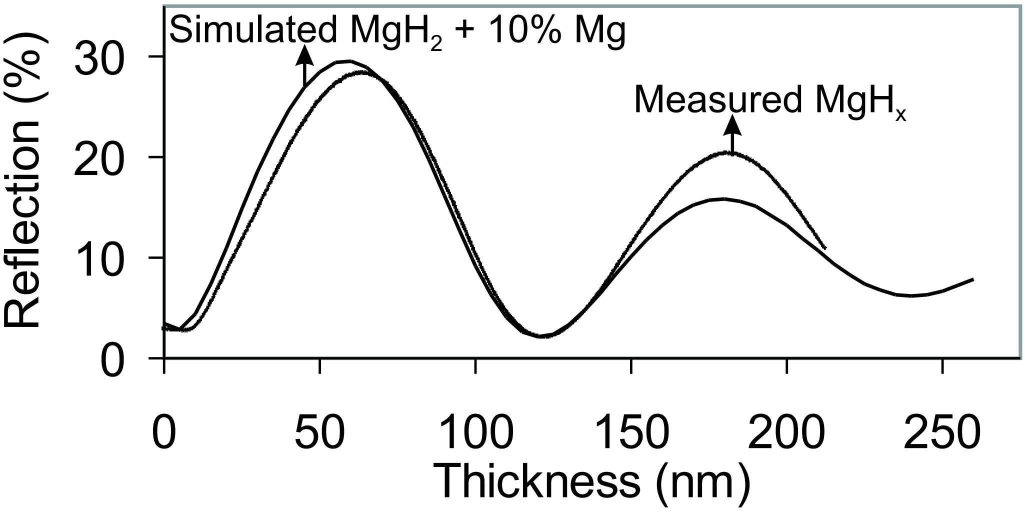

Figure 5.14: *In-situ* measured reflection at 1.95 eV versus deposited MgH_2 thickness. The simulated reflection of a MgH_2 thin film is also shown. The good agreement between the measured reflection and simulated reflection indicates that we indeed grow the MgH_2 hydride phase.

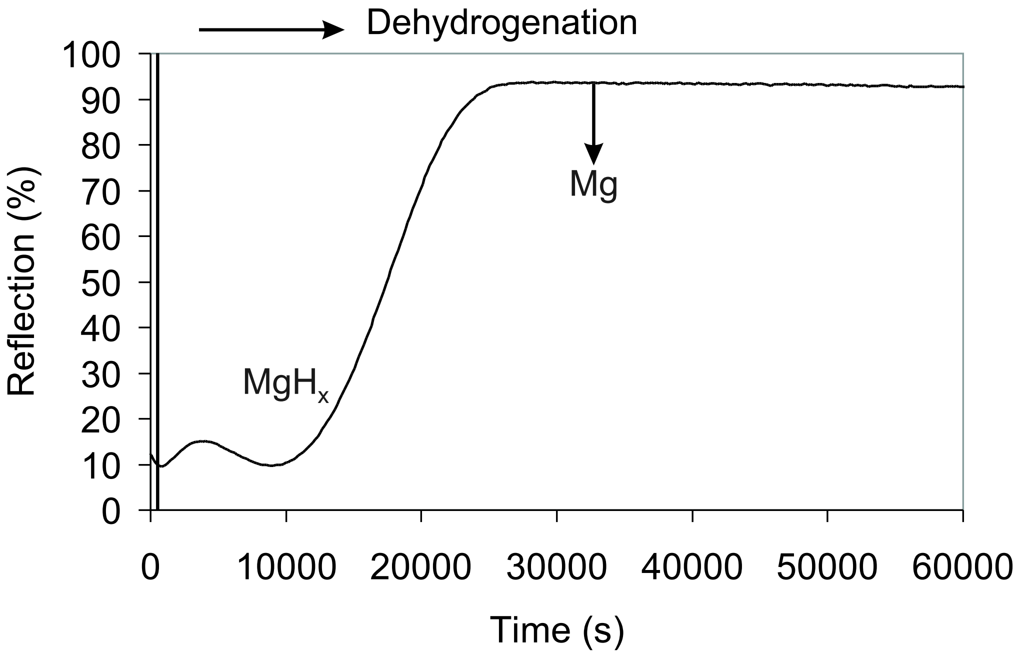

Figure 5.15: Reflection at 1.95 eV of a *in-situ* grown 200 nm MgH_x hydride film during dehydrogenation. During the first 500 s the Pd caplayer is deposited at 0.02 nm/s. The developing interference pattern indicates the layer like unloading of the film. The metallic Mg phase extends from the Pd surface downwards.

MgH_2), we need to assume the presence of 10 vol.% metallic Mg in the form of small grains. This appears to be typical for all *in-situ* grown Mg films, independently of the film thickness. Thus although we supply a surplus of atomic hydrogen, not all Mg atoms react with the atomic hydrogen to form the MgH_2 phase.

We observe that *in-situ* grown MgH_x films remain in their hydrided state in vacuum (5×10^{-7} Pa) when we shut off the atomic hydrogen source after deposition. The hydrogen desorption from the film is negligible as long as we do not deposit a Pd caplayer. This indicates the importance of the catalytical active Pd caplayer. Deposition of a Pd caplayer on the *in-situ* grown MgH_x thin film, immediately results in a spontaneous unloading in vacuum (see Fig. 5.15). When the film has returned to its metallic state after unloading, the film can be re-hydrogenated.

While the atomic hydrogen source is essential for the hydride formation, the blocked decomposition reaction is essential to stabilize the hydride during growth. The dehydrogenation process of MgH_2 has a high activation barrier and is kinetically blocked.

When we compare the results on the *in-situ* growth of MgH_2 with our study on the *in-situ* growth of the complex hydride Mg_2NiH_4 [119], there are some interesting similarities. Also the *in-situ* grown Mg_2NiH_4 hydride film remains in its metastable state in vacuum (5×10^{-7} Pa) after deposition. Furthermore, both types of films start to unload upon capping them with a Pd caplayer. The only difference is that upon Pd deposition the dehydrogenation of MgH_2 is much slower (days) than for Mg_2NiH_4 (hours).

The metastable state of the *in-situ* grown hydride phase allows us to transport these samples outside the protecting vacuum system for further experiments. It is found that the oxide skin, which is probably formed when exposed to air, has negligible influence on the optical properties of the film.

5.12 ***Ex-situ*** optical measurements MgH_2

Due to the stability of the *in-situ* grown Mg hydride films, we can measure *ex-situ* their optical properties. In Fig. 5.16 the reflection and transmission spectra are shown for *in-situ* deposited MgH_x films, grown at different H/Mg ratio's: 19 (film A), 7.3 (film B) and 4.2 (film C). The interference pattern of the reflection spectra is similar to that found for reflection spectra of *ex-situ* hydrogenated Mg thin films [77, 116]. However the transmission spectrum has a completely different shape as compared to the spectrum of an *ex-situ* hydrogenated Mg film (see Fig.5.17 Near 2 eV an optical absorption edge occurs in the *in-situ* grown film, which is absent in *ex-situ* hydrogenated Mg films (see Fig. 5.17). Halfway this absorption edge, at 2 eV, a shoulder is present. The origin of this shoulder is unclear. The transmission remains practically zero until around 4.5 eV it shortly increases again before decreasing finally to zero at approximately 6 eV, which corresponds to the optical band gap of MgH_2.

Lowering the temperature of the capillary (at constant applied hydrogen pressure) and increasing the Mg rate results in a decreasing H/Mg ratio. We find that the H/Mg ratio affects the reflection without any change in the shape of the spectra (see Fig. 5.16a). The transmission as shown in Fig. 5.16b is almost identical for the three films. A small effect is observed for the film with highest H/Mg ratio which has the lowest transmission below 2 eV.

The absorption coefficient α as function of energy is calculated with equation ,

$$\alpha(10^5 cm^{-1} cm) = -\frac{1}{d(cm)} 10^{-5} \frac{T}{1-R} \tag{5.2}$$

From the absorption coefficient, the optical band gap is determined by extrapolating the absorption edge to zero. A small shift of the MgH_2 optical band gap for film A (5.55 eV), film B (5.48 eV) and film C (5.41 eV) is observed. Although the H/Mg ratio for the three films are quite different, the band gaps are very similar and consistent with the band gap of 5.6 eV for MgH_2 found

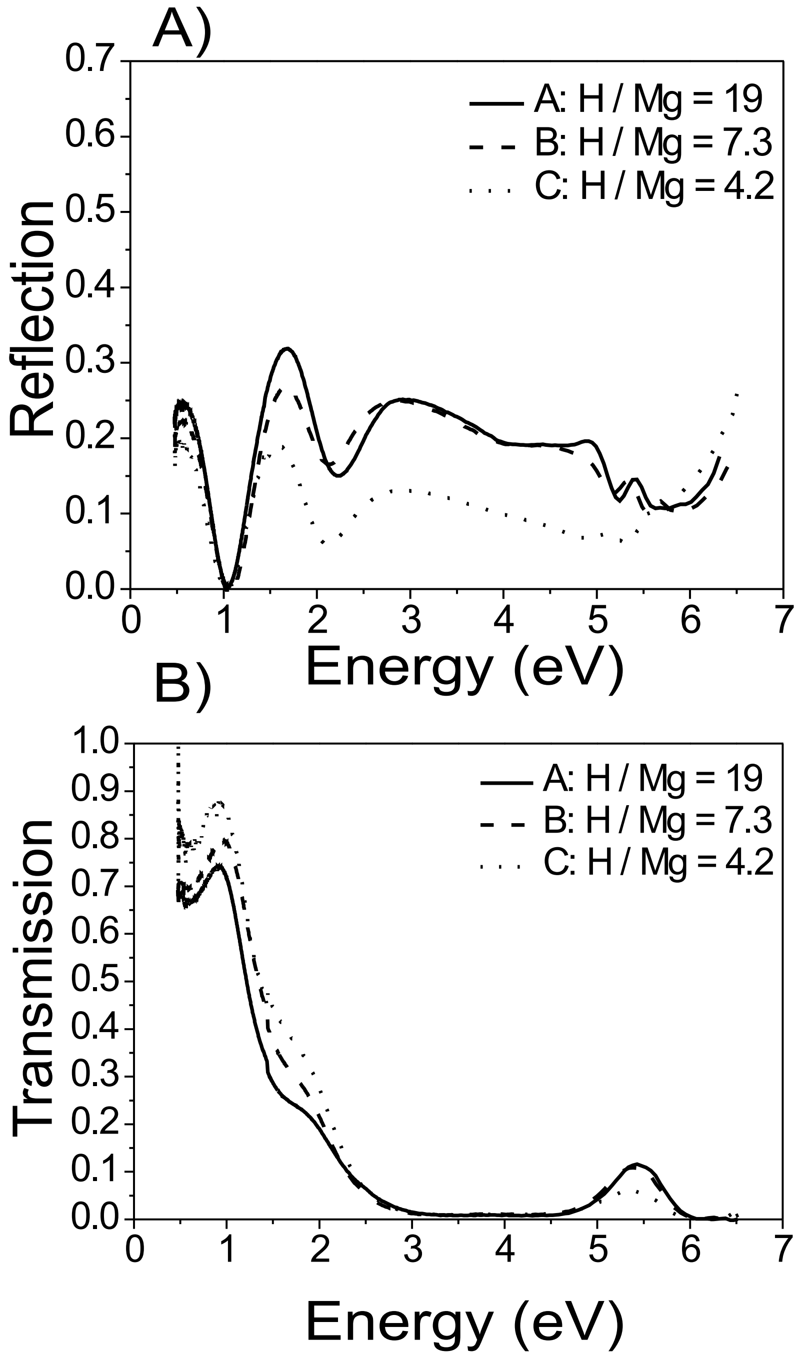

Figure 5.16: *Ex-situ* measured (a) reflection and (b) transmission spectrum versus energy for 200 nm *in-situ* deposited MgH_x thin films grown at a different powers of the atomic hydrogen source and Mg rate.

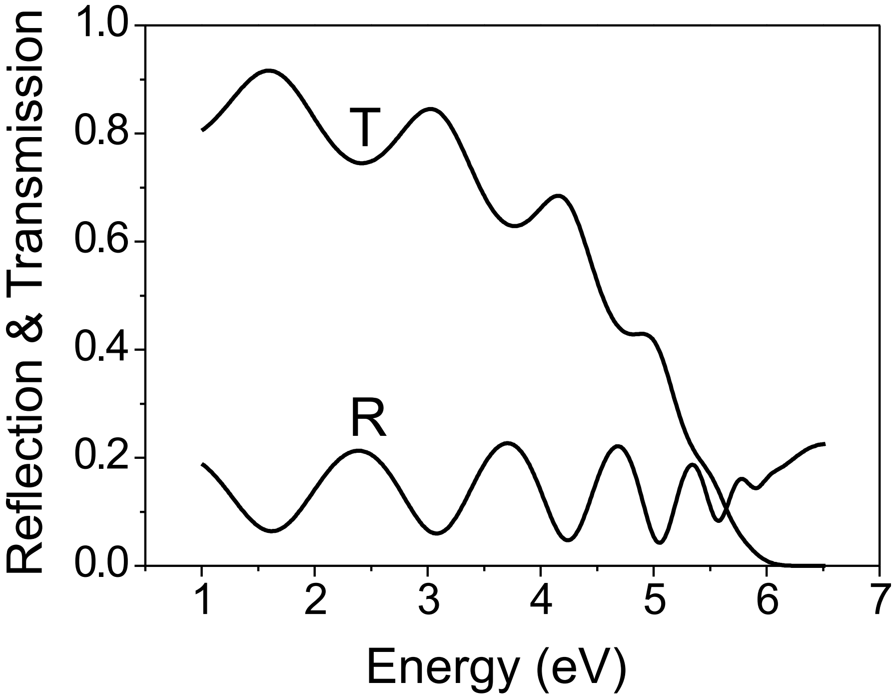

Figure 5.17: Calculation of the reflection and transmission spectrum versus energy for a 200 nm MgH_2 film.

by Giebels *et al.* [77]. The small optical differences between the three films demonstrate the insensitivity of the deposition process on the H/Mg ratio. Although the *in-situ* grown and *ex-situ* hydrogenated Mg hydride films have a different electrical behavior, the optical band gap at 5.6 eV, due to MgH_2, is the same for both types of films.

5.13 Effective medium approximations EMA: Simulating the optical spectra of *in-situ* grown MgH_2

The induced optical absorption edge at 2 eV in the transmission spectra shown in Fig. 5.16b suggests the presence of impurities in the film. Since we deposit a Mg film, metallic Mg grains are most likely the origin of this optical effect. In the Maxwell-Garnett effective medium approximation (EMA), the effective dielectric function $\langle\tilde{\epsilon}\rangle$ is approximated by assuming spherical inclusions of material B (Mg) in a host dielectric background A (MgH_2) The grain size is assumed to be much smaller than the wavelength of light. In this EMA

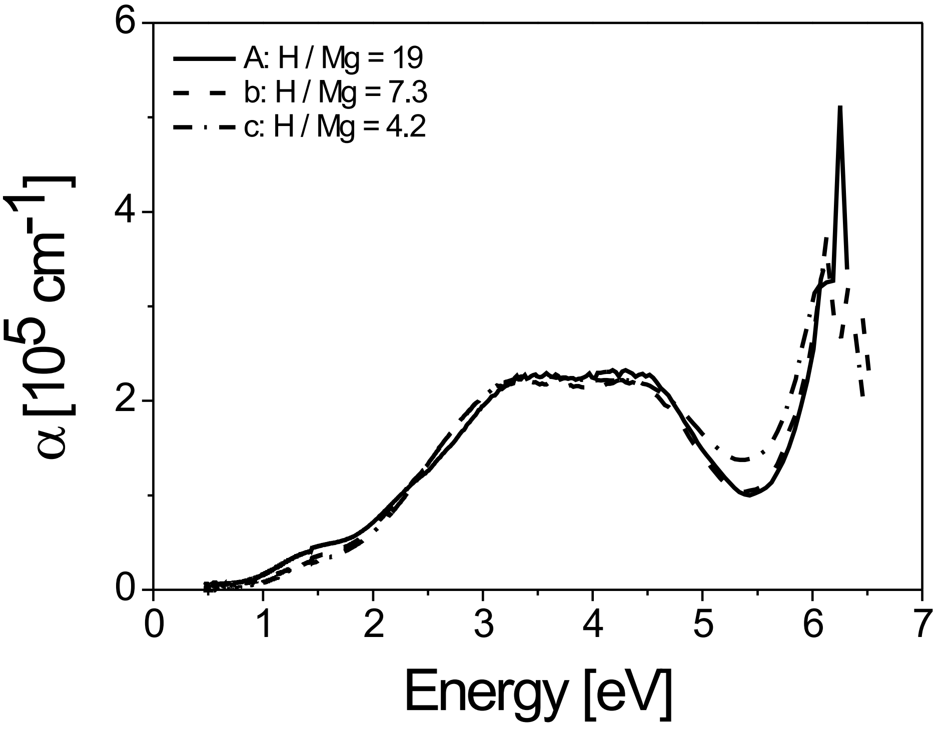

Figure 5.18: Absorption versus energy as derived from Fig.5.16 for a 200 nm *in-situ* deposited MgH_x thin film grown at a different powers of the atomic hydrogen source and Mg rate.

approximation the effective dielectric function $\langle\tilde{\epsilon}\rangle$ is implicity given by

$$\frac{\langle\tilde{\varepsilon}\rangle - \tilde{\varepsilon}_A}{\langle\tilde{\varepsilon}\rangle + 2\tilde{\varepsilon}_A} = \mathrm{f}_B \frac{\tilde{\varepsilon}_B - \tilde{\varepsilon}_A}{\tilde{\varepsilon}_B + 2\tilde{\varepsilon}_A} \tag{5.3}$$

where the volume fraction of B is given by f_B. The solution of this equation is given by:

$$\langle\tilde{\varepsilon}\rangle = \tilde{\varepsilon}_A \frac{2(1-\mathrm{f}_B)\tilde{\varepsilon}_A + (1+2\mathrm{f}_B)\tilde{\varepsilon}_B}{(2+\mathrm{f}_B)\tilde{\varepsilon}_A + (1-\mathrm{f}_B)\tilde{\varepsilon}_B} \tag{5.4}$$

Reflection and transmission spectra for 5, 10, and 20 vol.% of Mg grains in a MgH_2 host dielectric matrix are shown in Figs. 5.19a and b, respectively.

Apart from a small difference in absolute value and a small energy shift, the calculated reflection for 5 and 10 vol.% of metallic Mg is similar to the measured reflection (see Fig. 5.16). From this we conclude that the optical absorption edge is the result of small metallic Mg inclusions. Although shifted with respect to the measured spectra it clearly shows the influence of these metallic grains inside the Mg hydride film. The calculated transmission becomes negligible at 3.25 eV and the width of the dip in transmission is smaller than the experimental spectra. Between 4 eV and 6 eV, the calculated transmission is higher than the experimental observed. The deviations from the experimental behavior might indicate that the inclusions are not perfectly spherical as assumed in the Maxwell-Garnett EMA.

For comparison with the results obtained by the Maxwell-Garnett EMA, we also used the Bruggeman effective medium approximation for the same film configuration and composition [115]. The reflection and transmission are shown in Fig. 5.20a and Fig. 5.20b. It is evident that the calculated reflection resembles quite well the measured reflection, however between 2 and 4.5 eV the calculated transmission deviates strongly from the measured zero transmission. However, the absolute transmission represents better the measured values than in the Maxwell-Garnett EMA. Also the width of the minimum in transmission (between 2.5 and 4.5 eV) is better modelled by the Bruggeman EMA. We conclude that neither effective medium theory represents exactly the measured optical behavior for *in-situ* grown Mg hydride films. The deviation between experiment and theory must be found in grain shape and exact concentration of the Mg grains.

5.14 *Ex-situ* re-hydrogenation of *in-situ* grown Mg hydride films

Capping an *in-situ* grown MgH_x film with Pd results in the dehydrogenation of the film. In Fig. 5.21 the reflection (measured from the substrate side) of an 170 nm dehydrogenated *in-situ* grown MgH_x film is compared with the calculated reflection of an as-deposited Mg film (also capped with 10 nm of Pd) of the same thickness [15]. The reflection of the dehydrogenated film is slightly lower than the calculated spectrum, indicating the presence of some un-desorbed hydrogen.

Note that the presence of some oxygen inside the metallic Mg film cannot be excluded since the partial water pressure during *in-situ* growth is 5×10^{-6} Pa. The minimum in reflection at 0.6 eV is attributed to interband transitions between parallel occupied and unoccupied conduction bands [15, 120, 121]. Fig. 5.22 and 5.23 show the reflection and transmission of an *in-situ* grown 120 nm Mg film, which is re-hydrogenated at 10^5 Pa and 373 K. The measured reflection deviates only slightly from the calculated reflection for a fully hydrogenated MgH_2 film. The transmission, however, deviates from the simulated transmission by roughly 20 %, which is probably due to an incomplete hydro-

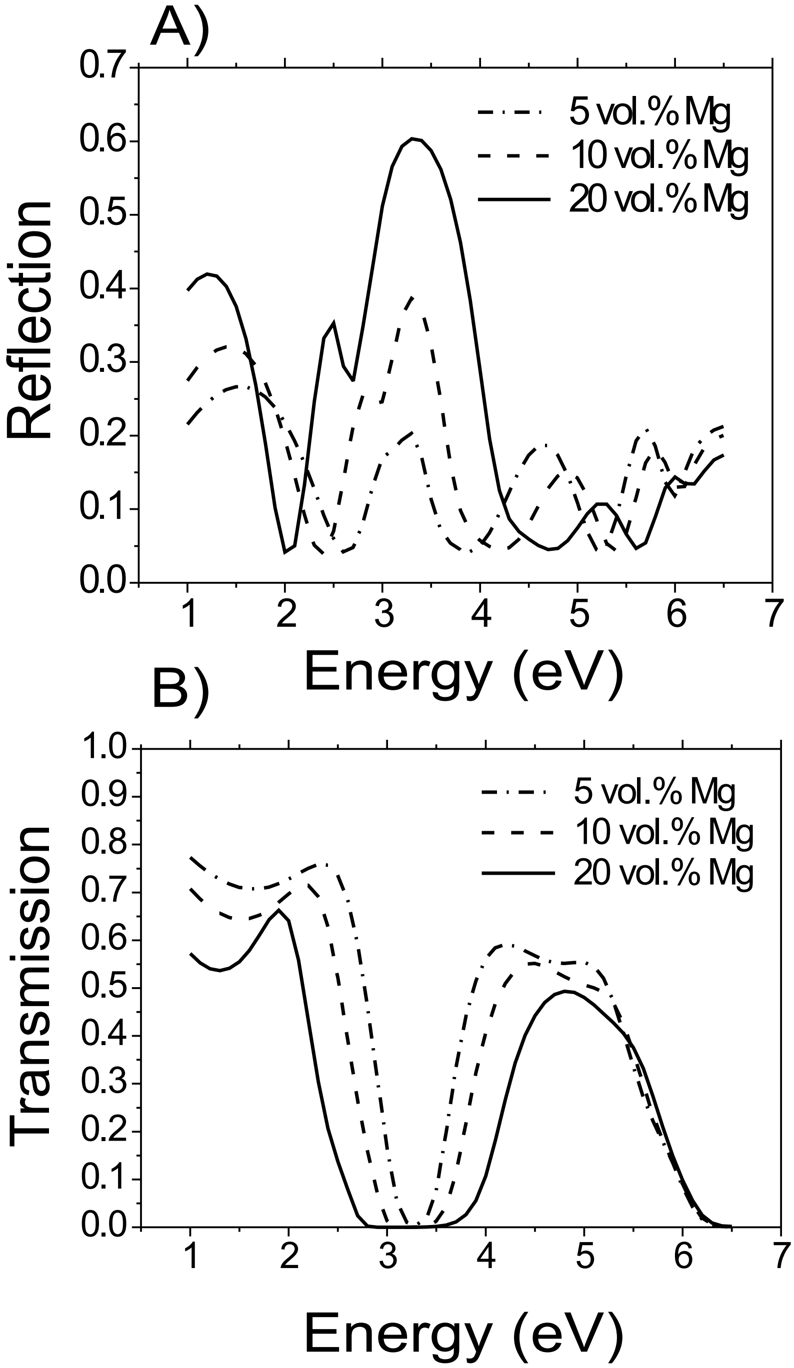

Figure 5.19: (a) Reflection and (b) transmission spectra for a 200 nm MgH_2 film with 5, 10 and 20 vol.% of metallic Mg grains using a Maxwell-Garnett effective medium approximation.

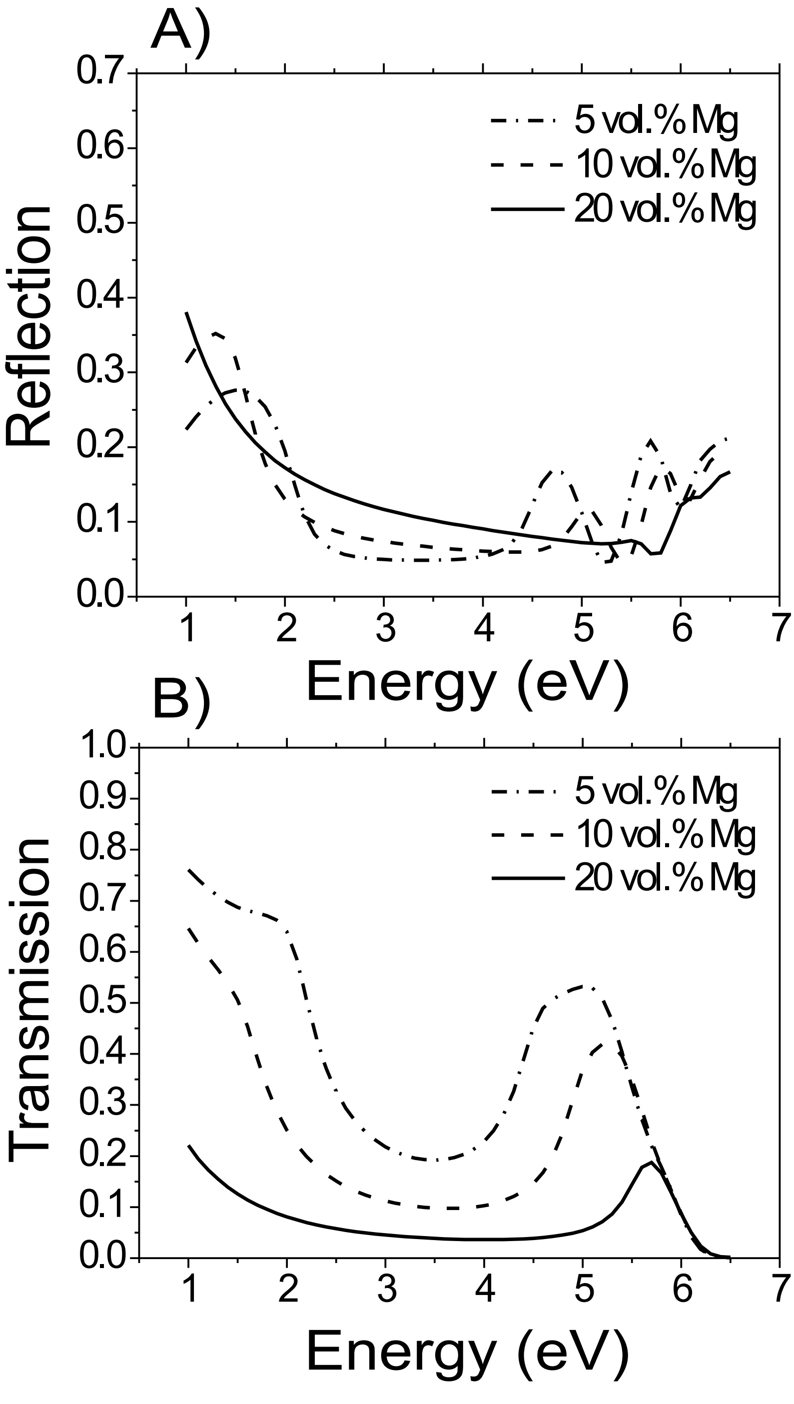

Figure 5.20: (a) Reflection and (b) transmission spectra for a 200 nm MgH_x film with 5, 10 and 20 vol.% of metallic Mg grains using a Bruggeman effective medium approximation.

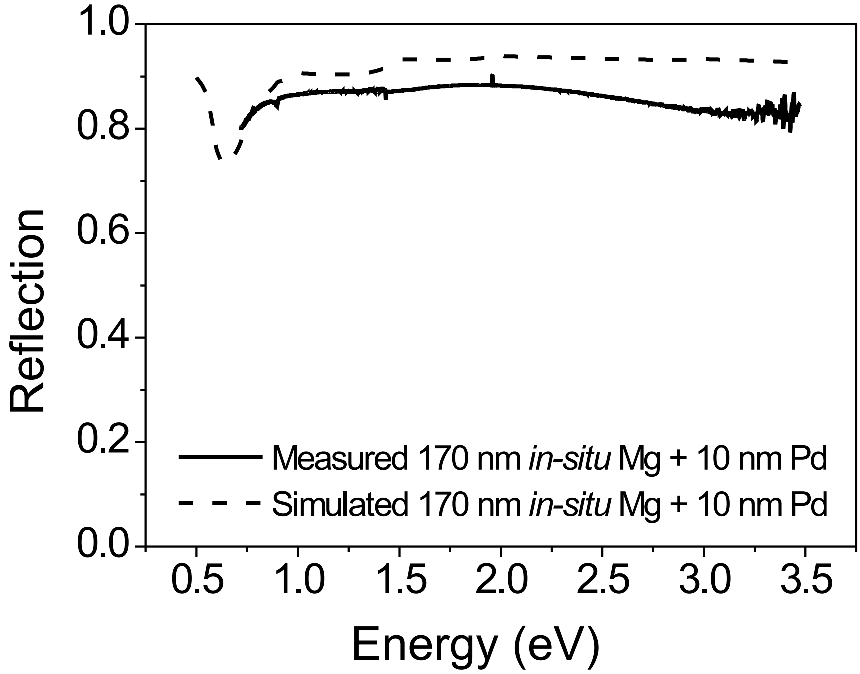

Figure 5.21: Reflection measurement of a Mg film after de-hydrogenation of an *in-situ* grown 170 nm MgH_x thin film covered with 10 nm Pd.

genation of the film. Remarkably, the absorption edge at 2 eV, observed *in-situ* grown MgH_x film, disappears in the re-hydrogenated state. This indicates that the microstructure of the *in-situ* film changes drastically on re-hydrogenation.

The same effect is seen in the electrical resistivity. When an *in-situ* film is re-hydrogenated we find a value of the same order of magnitude as the resistivity of an *ex-situ* hydrogenated as-grown Mg film. This indicates that there is now an electrical percolation throughout these films which was not the case for the *in-situ* grown Mg hydride film.

5.15 Microtopography of *in-situ* grown MgH_2

The surface morphology of the *in-situ* grown Mg hydride thin films is investigated with atomic force microscopy (AFM). AFM micrographs of a 175 nm *in-situ* grown film are shown in Fig. 5.24. Figure 5.24 show the MgH_x film surface at scan ranges of 10, 5 and 1 μm, respectively. In Fig. 5.24d an AFM micrograph of an 80 nm as-deposited metallic Mg film is shown for comparison. Figs. 5.24a - c show that the film surface consists of grains with sizes ranging from 10 to 75 nm, whereas the average diameter is in de order of 20 nm. The

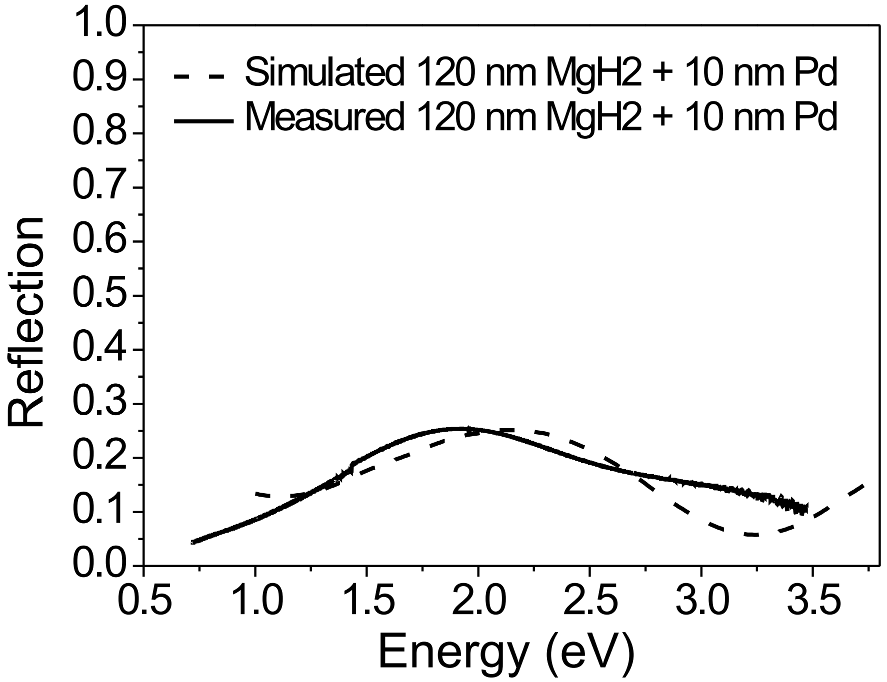

Figure 5.22: Reflection spectrum of a re-hydrogenated 120 nm *in-situ* grown MgH_x thin film capped with 10 nm of Pd. A simulation of a 120 nm MgH_2 film capped with 10 nm Pd is shown as reference. The difference between the two spectra is due to the presence of some metallic Mg in the re-hydrogenated film.

as-deposited Mg film surface, Fig. 5.24d, is characterized by stacked hexagonal crystals which mimics the hexagonal unit cell of metallic Mg. The average size of these hexagonal structures is approximately 0.4 μm. The surface morphology of an *in-situ* deposited MgH_2 film has a smaller grain size. Although we cannot identify individual Mg-grains, their size will be of the same order as assumed by the effective medium approximations.

5.16 Discussion

It is well-known that when crystals of any material are scaled down in size, their optical properties change. First and foremost there is a change in the perceived color as the crystal is made smaller than the wavelengths of visible light, which occurs for particle sizes from 500 nm to around 10 nm (classical size effect). The geometrically induced change in optical properties can be explained with Mie theory [122]. Quantum size effects take place for thin

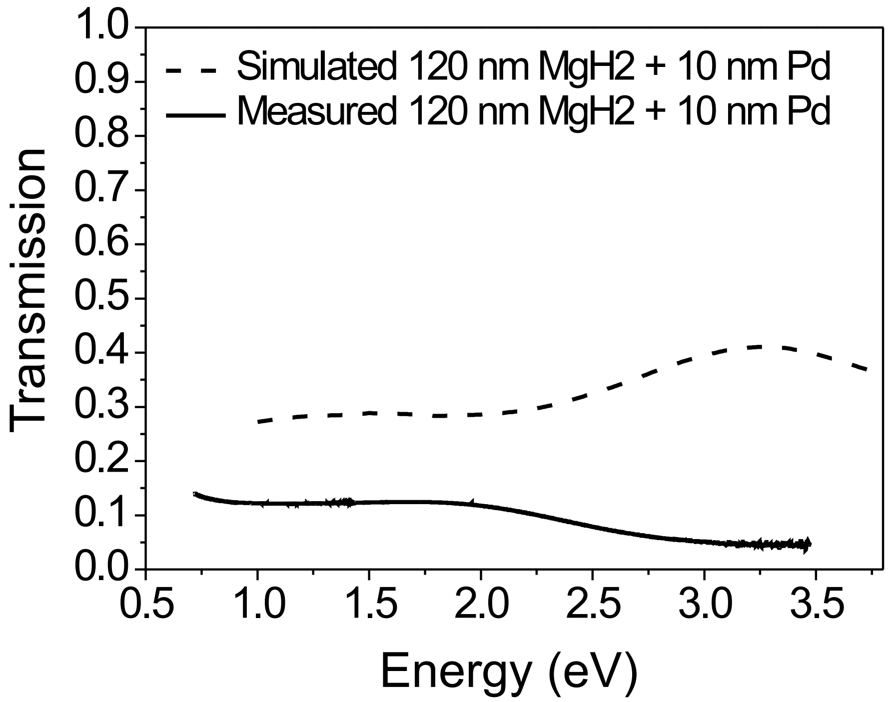

Figure 5.23: Transmission spectrum of a re-hydrogenated 120 nm *in-situ* grown MgH_x thin film capped with 10 nm of Pd. A simulation of a 120 nm MgH_2 film capped with 10 nm Pd is shown as reference.

continuous metal (conducting) films with a thickness up to 10 nm, thus when the Fermi wavelength of the free carriers is comparable to the film thickness. The limited film thickness results in discrete energy levels and the quantum size effect manifest itself in the transmission, reflection, and absorption spectra in the form of well defined peaks. For larger film thicknesses the quantum size effects and the classical size effect converge. We conclude that the observed absorption width in our case cannot be explained by quantum size effects and is due to classical size effects [123, 124, 125].

The absorption induced by a particle size effect is reported in several papers [126, 127]. An explanation of this effect is given by Marton *et al.* [128] and Mulvaney *et al.* [129]. The origin of the change in optical properties is due to the change in dynamics of the conduction electrons. For particles much smaller than the wavelength of light, the electrons in the particle move in phase and thus the electrons can be considered to generate a giant dipole under the influence of the incident radiation. Electron motion leads to the generation of surface polarization charges on each side of the particle, which act as a restoring force on the conduction electrons, and this leads to a resonance

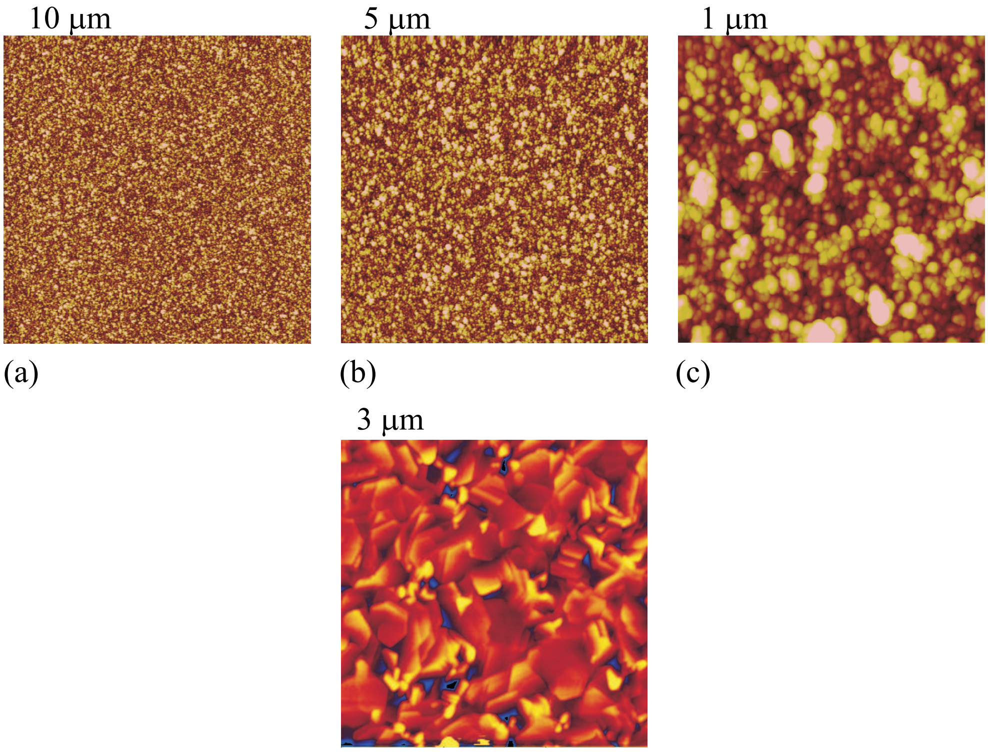

10 μm

5 μm

1 μm

(a)

(b)

(c)

3 μm

(d) 80 nm, Δz = 30 nm

Figure 5.24: AFM measurements on a 175 nm *in-situ* grown Mg hydride film at scan ranges 10 μm, 5 μm and 1 μm respectively with a Δz of 30 nm. In (d) an AFM micrograph of an as-prepared 80 nm Mg film is shown for comparison.

frequency in the absorption spectrum (a surface plasmon absorption). If the particle increases in size, the electrons run out of phase and the restoring force decreases with the result that the absorption band broadens. In this context it is interesting to note that Mulvaney *et al.* report that the optical properties are determined by the single nanocrystals as the particle spacing is at least 2 radii. This corresponds to a metallic volume fraction of 10 vol.% [129]. Hence, we conclude that the absorption effect we observe is due to the presence of Mg-clusters and is of a similar nature.

The *in-situ* grown MgH_x films reveal several other unexpected properties. The most surprising observation is that although the H/Mg ratio during deposition is always sufficiently high to form the Mg hydride phase, still 10 vol.% of metallic Mg is found in the film. This implies the existence of a mechanism which induces both phases to form simultaneously (see Fig. 5.25). During growth the film surface is covered by Mg atoms, H atoms and H_2 molecules. This enables several reactions to occur and a competition between the different reactions develops. Mg atoms can react with molecular hydrogen to form the hydride phase $Mg + H_2 \rightarrow MgH_2$, however this reaction is rather slow due to the high activation barrier for hydrogen dissociation on metallic Mg (Nørskov *et al.* found 0.5 eV and Bird *et al.* found 0.4 eV for this activation barrier [130, 131]). The second reaction Mg + H + H → MgH_2 does not suffer from this barrier, however this process requires a 3 atom collision, which is less likely to occur. The Mg + Mg → Mg_2 reaction is a fast process since only two Mg atoms are required. As a result a substantial fraction of Mg-nuclei may form.

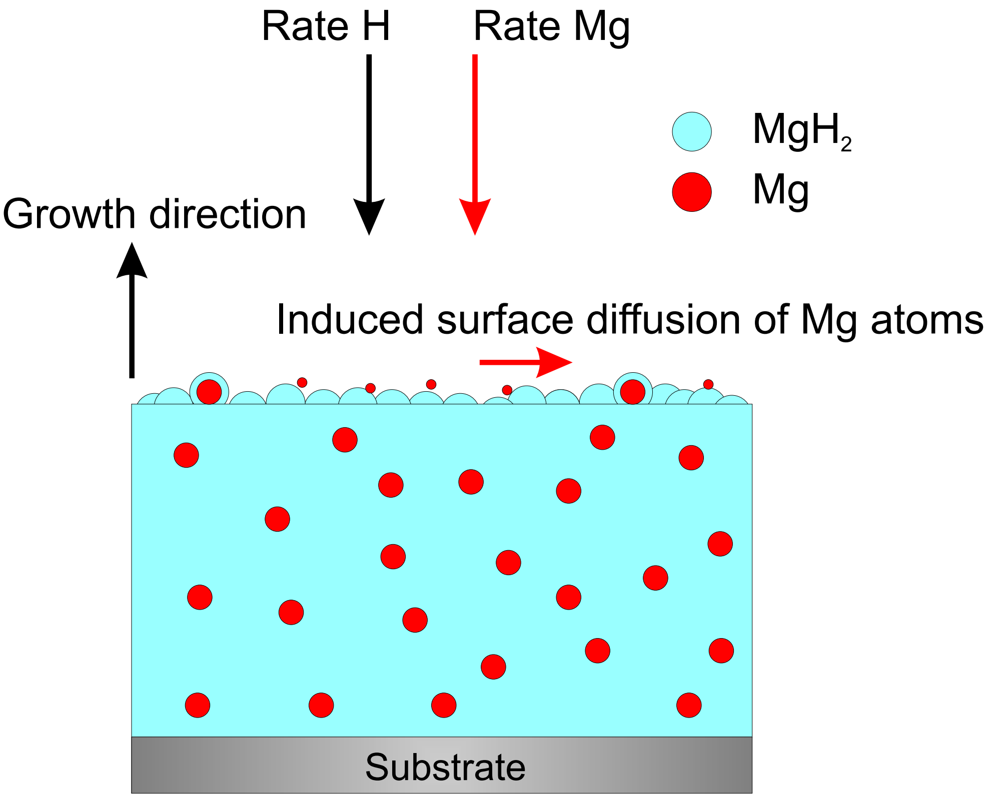

Figure 5.25: Schematic representation of the induced surface diffusion by the atomic hydrogen beam. The surface diffusion of the Mg adatoms is increased by the presence of an hydrogen beam. This results in the segregation of Mg grains in the MgH_2 host hydride phase.

Also the fact that metallic Mg has a low surface energy as compared to that of MgH_2 favors the nucleation of Mg clusters. For the surface energy of Mg we find in the literature: 3.14×10^{14} - 3.99×10^{14} eV/cm^2 [132, 133, 134]. For the hydride we have not found any data, but the oxide should be comparable. A higher surface energy is expected for materials, with a high cohesive energy and a high melting point. The surface energy of MgO is found to be: 7.43×10^{14} - 8.11×10^{14} eV/cm^2 [135, 136, 137]. Hence, the nucleation barrier for MgH_2 is expected to be higher than for Mg. Wagemans *et al.* calculated both the Mg and MgH_2 energies (using DFT calculations) as function of the number of Mg atoms in the cluster. When going down in number of atoms the energy of the clusters become less negative, which indicates a destabilization of the small particles. Upon decreasing the cluster size the surface to volume ratio increases. The surface atoms have a lower coordination and thus the average number of bonds is lower for smaller clusters. For the metallic clusters a similar trend in desorption energy vs cluster size is found. However the MgH_2 clusters are more strongly destabilized than the corresponding Mg clusters upon decreasing the cluster size below 19 Mg atoms. Furthermore the hydrogen desorption energy decreases as the number of Mg atoms decreases. For the smallest possible cluster, MgH_2, the desorption energy drops even to negative values, which means that the magnesium hydride molecule is not stable [138, 139]. Although the MgH_2 clusters have a lower total energy than the Mg clusters, we conclude that the nucleation of Mg clusters is favored over the formation of MgH_2 clusters.

In addition, the hydrogen flux may provide an increased surface mobility, thus enhancing the chance of forming a minority phase. Mg is thermally evaporated around 673 K and the atoms reach the substrate surface with an energy of kT = 0.058 eV (k Boltzmann constant, T temperature in K). Upon condensation these Mg atoms loose their energy within a few diffusion steps. However, the hydrogen flux increases the surface mobility of adatoms (Mg atoms) as hydrogen is used to improve the crystalline quality of thin films during growth. Gerbi *et al.* e.g. showed that microcrystalline silicon is deposited when a large quantity of molecular hydrogen is added to the process gas such that a large flux of atomic hydrogen impinges on the growing film surface [140]. Hydrogen leaving the hydrogen source reaches the film surface with an energy of 0.18 eV. These energetic hydrogen atoms increase the surface diffusivity of the Mg atoms and thus will facilitate the Mg clustering. This may explain why an increase in the atomic hydrogen flux does not result in a fully hydrided film. One merely increases the Mg diffusion at the growing film surface and the competition between the hydride growth and Mg clustering reaches an equilibrium at 10 vol.% of metallic Mg grains at these deposition conditions (see Fig. 5.16).

Comparing the ARE MgH_x films with the *ex-situ* hydrogenated Mg films, we see that the *in-situ* grown films consist of a collection of grains which are unequal both in size and composition. Since there is no mixing between these types of grains, due to the fact that there is no solubility, these composite films are stable. The existence of isolated Mg particles in an MgH_2 matrix (see Fig. 5.25) is consistent with the observation that the resistivity of these *in-situ* films is beyond the limit of the measuring setup. The question then arises why upon rehydrogenation of such a film, the resistivity reduces to 10 mΩcm. This points to an increase or redistribution of conductive material (i.e. Mg). On the other hand the Mg-related feature disappears from the optical spectrum on rehydrogenation. We propose that the increase in conductivity is related

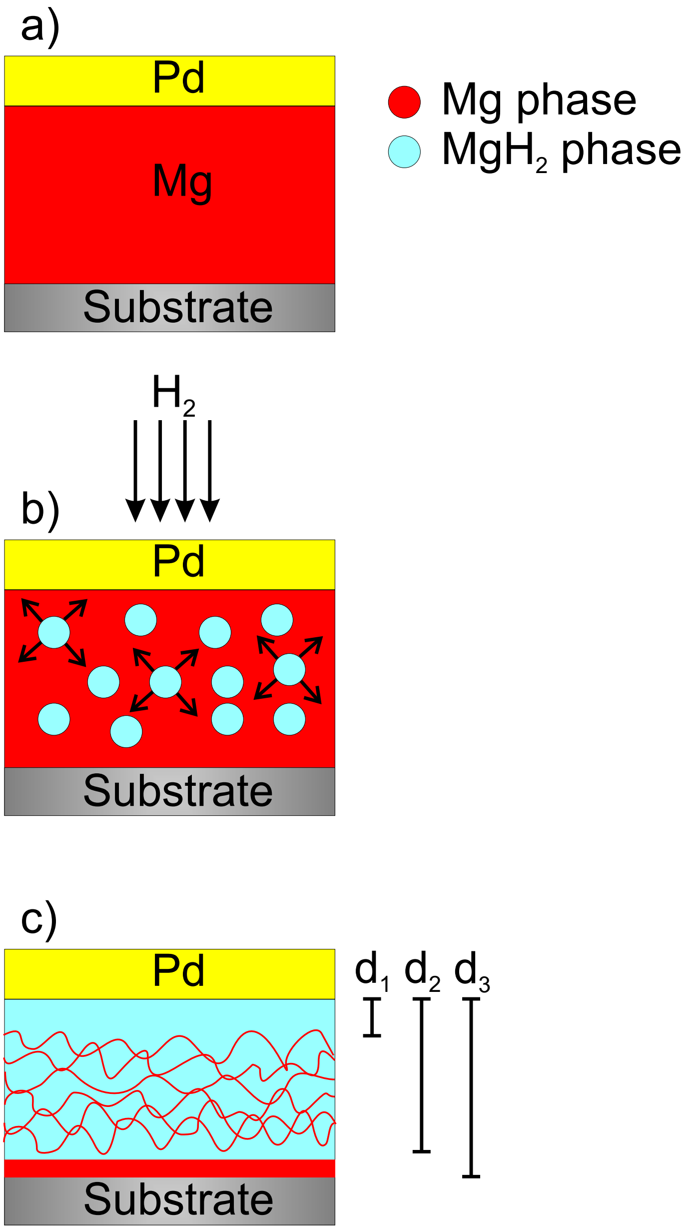

Figure 5.26: Schematic representation of the formation of the electrical percolation network in a hydrogenated MgH_2 film. (a) A Mg film capped with a Pd caplayer, (b) random hydride nucleation throughout the Mg film, (c) the nucleating hydride grains increased in size until the film is hydrogenated leaving a electrical percolation network of grain boundaries. In the fully hydrogenated state, the top of the Mg layer forms a hydrogen blocking layer, d_1. For films thicker than the critical thickness for rehydrogenation, $d_3 > d_2$, the film does not hydrogenate completely.

to the formation of a percolative conductive network. This network forms during the solid state transformation of Mg to MgH_2. Its nature is apparently independent from the pre-existing microstructure since the conductivity of the sample does not appear to depend on the way the sample was grown. The microstructure of *in-situ* films is quite distinct from that of *ex-situ* films.

Giebels *et al.* investigated the electrical percolation through a Mg-MgH_2 composite film. Intuitively one expects that the percolation threshold depends on the exact particle shape. To make a simulation on hydriding a Mg film, they have calculated the resistivity for a 90-nm-thick Mg-MgH_2 composite capped with 20 nm Pd-Mg layer. It is found that the resistivity increases strongly above 65 vol.% of MgH_2 (35 vol.% of Mg) indicating that the electrical percolation disappears. This is consistent with our *in-situ* resistivity measurements in which the resistivity of a 90 vol.% MgH_2 - 10 vol.% Mg film is very high.

Nevertheless the conductivities after rehydrogenation and the critical thickness for rehydrogenation (d_2 in Fig. 5.26) are quite similar. The nucleation of MgH_2 in Mg occurs more or less randomly throughout the thin film for films < 100 nm [77, 116]. As soon as MgH_2 grains form they will hinder the diffusion of hydrogen to the remaining parts of the film, due to the poor diffusivity of hydrogen through MgH_2 [77, 116, 118]. This will make it difficult to transform all the Mg, especially at the boundaries between the MgH_2 grains. Upon prolonged hydrogen exposure the boundaries at the top of the film may fill up, but this makes the full loading of the underlying areas even more difficult. This would then result in a microstructure as shown in Fig. 5.26.

This electrical percolation network (see Fig. 5.26) appears to be quite robust and persists even after hydrogenation at 10^7 Pa and 373 K [77, 116]. The origin of this behavior can be due to stress effects, a limited diffusion or a possible lattice mismatch. Note that, in contrast to Mg_2NiH_4, no shift in the upper optical band gap is observed. This suggest that this is the intrinsic optical band gap of MgH_2.

Many scientists are interested in metallic particles surrounded by an insulating material, because of their varying physical (optical) properties. As a possible application of obtaining metallic grains in an insulating matrix, the ARE technique has shown to be a very useful method to produce and study these kind of composite systems [129].

5.17 Conclusions

In-situ fiber spectroscopy and *in-situ* resistivity measurements show that MgH_2 + 10 vol.% Mg thin films can be grown by activated reactive evaporation. These hydride films can be grown from the atomic constituents Mg and H, where the atomic hydrogen is provided by an atomic hydrogen source. These Mg hydride films appear to be stable in vacuum and air. The as-grown hydride films only transform back into the metallic state, after the film is *in-situ* capped with Pd.

Although optical measurements indicate the existence of metallic Mg grains in the *in-situ* grown hydride film, the resistivity is higher than $\rho >$ MΩcm. The re-hydrogenation of these *in-situ* grown Mg films indicates that the growth of coalescence of metallic Mg and MgH_2 grains is not reversible. In contrast to the *in-situ* grown Mg hydride films, the *ex-situ* (re-)hydrogenation of Mg films results in an electrical percolation network throughout the MgH_2 film.

The optical absorption edge observed at 2.0 eV is attributed to the interaction between the applied field and the small Mg grains. This absorption edge disappears upon re-hydrogenation (and thus the metallic Mg grains). The optical band gap at 5.6 eV is attributed to the band gap of MgH_2 and indeed confirms the growth of the MgH_2 phase by ARE.

Chapter 6

Catalysis

6.1 Abstract

The optical properties, switching kinetics and lifetime of hydrogen switchable mirrors based on Mg-Ni alloys are studied as a function of composition of the optically active metal hydride layer and the thickness of the catalytic capping layer. The hydrogenation is correlated to the surface structure of Pd on $\mathrm{Mg}_y\mathrm{Ni}_{1-y}$ as investigated by Scanning Tunneling Microscopy. The results are consistent with a strong metal-support interaction (SMSI), characterized by a complete encapsulation of the capping layer clusters by oxidized species originating from the active hydride. The SMSI-effect becomes less important when increasing the Pd-layer thickness, and is suppressed by a good wetting of the Pd-clusters on the optically active film. This explains the critical thickness for the catalyzed hydrogen-uptake observed in many switchable mirror systems. The degradation of the kinetics during cycling is found to depend on the Pd-layer thickness and on the gas environment. The SMSI-effect is partly reversible: after changing the gas environment from hydrogen to oxygen, the oxide on the Pd-clusters can be partly removed.

Furthermore, we show in this chapter the importance of contaminations and the number of active sites of the Pd caplayer. From *in-situ* hydrogenation experiments we conclude that the presence of a small amount of sulfur on the Pd caplayer surface has disastrous consequences for the hydrogen desorption. After sputtering this Pd caplayer with argon ions, the fresh Pd surface regains its original catalytical properties. The same result is obtained for depositing a new and fresh Pd layer.

6.2 Introduction

The *in-situ* growth of hydrides showed that the catalytical properties of the surface are very important for the hydrogenation process. Reversible hydrogenation occurs only when covered with a catalyst such as Pd.

The adsorption of hydrogen can be described in terms of a simplified one-dimensional potential energy curves for an H_2 molecule and for two H atoms on a clean metal surface (see Fig. 6.1). Far away from the surface the two curves are separated by the heat of dissociation, E_D = 218 kJ/mol H. The flat minimum in the "H_2 + M"-curve corresponds to physisorbed H_2, $E_P \approx 10$ kJ/mol H. The deep minimum in the "2H + M"-curve describes chemisorbed, dissociated H, $\Delta H_{chem} \approx 50$ kJ/mol H for Pd. If the two curves intersect *above* the zero energy level, chemisorption requires an activation energy E_{diss}. The chemisorbed H atoms dissolve exothermically or endothermically in the bulk where a hydride phase may nucleate and grow [141]. According to diffusion data, hydrogen transport inside metals or metal hydrides is fast enough to provide high hydrogen absorption and desorption rates at room temperature. However, in most systems only slow rates are observed, which indicates that the *surface properties* of the metal grains determine their H sorption kinetics, i.e. the dissociation of the hydrogen molecule [79, 141]. Borgschulte *et al.* concluded that for a high catalytic activity, materials are needed that combine a small dissociation barrier E_{diss} with a small and negative heat of solution without exceeding the heat of formation/solution of the hydride forming metal host [142].

Although Pd is the perfect catalyst in this framework, all switchable mirrors degrade using this caplayer (see e.g. Refs. [143, 144]). The main reason for this is, that the capping layer reacts in various ways with the hydriding film [71, 72, 77].

Several groups found that the switching kinetics of an yttrium switchable mirror - and consequently its hydrogen uptake rate - is mainly determined by the thickness of the catalytic Pd cap layer [145, 146, 147]. In particular, it was observed that a minimum Pd thickness is required for a sufficient hydrogen uptake. The effect was explained by an encapsulation of the Pd clusters by a reduced yttrium oxide layer after exposure to hydrogen [79]. The catalytically active surface of the Pd-clusters is gradually covered and their catalytic effect is reduced. The degree of encapsulation decreases with increasing Pd thickness. Small clusters are completely covered with yttrium oxide (-hydroxide), which explains the minimum thickness required for a fast hydrogen-uptake kinetics of these systems. This behavior is well known by the catalysis community, which coined the expression strong-metal support interaction (SMSI) [148, 149]. The driving force behind the SMSI effect is the minimization of the surface energy. Borgschulte *et al.* indicate some favorable surface species may form on top of the Pd and that the Pd surface energy is replaced by an "oxide" surface + interface energy. Due to the SMSI effect a minimum amount of Pd-catalyst is required on switchable mirrors.

Here, we demonstrate that the SMSI-effect is responsible also for the degradation of Mg-Ni based switchable mirrors. We study the SMSI-effect using a

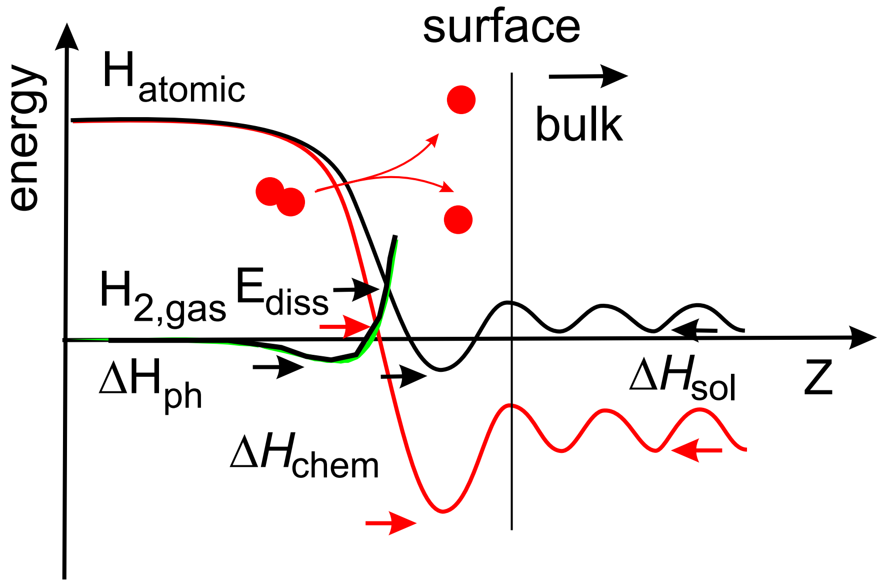

Figure 6.1: Characteristic solid-gas interaction steps pictured by the dependence of the potential energy on distance z from surface for two different metals with a positive (black line), and negative (red line) heat of solution ΔH_{sol}. Intuitively, one expects a correlation between the heat of solution and the barrier height of dissociation E_{diss}, i.e. a high negative heat of solution corresponds to a small dissociation barrier E_{diss}. This is indeed empirically found within a similar group of materials (Brønsted-Evans-Polanyi (BEP)-relation).

gradient alloy film and the novel indicator method described in Refs. [150, 151, 152]. Our thin film approach allows us to monitor the hydrogen uptake as a function of alloy composition of the optically active layer and the Pd-catalyst layer thickness. To shed light on the physical origin of the hydrogen uptake kinetics, we study the morphology of Pd-capped Mg-Ni films by scanning tunnelling microscopy (STM). Furthermore, we investigate how the quality of the Pd-surface effects the dehydrogenation process. We find that also the surface properties of the Pd itself (surface roughness, sulfur contamination) determine its catalytic properties.

6.3 Experiment

Polycrystalline Mg, Ni, and Pd are deposited on glass substrates using DC sputter sources. The argon pressure is 1 Pa, the background pressure less than 10^{-6} Pa. Pd is deposited directly on Mg-Ni-alloy films without any intermediate oxidation step. A chemical compositional gradient is produced by adjusting the angle of both Mg and Ni sources relative to the sample surface.

The composition of the films is determined by Rutherford Backscattering Spectrometry (RBS). The surface composition of the gradient film is determined by Auger Electron Spectroscopy (AES). AES measurements are recorded in the first derivative mode, dN/dE, where the intensity is measured from the peak-to peak height.

STM images are taken with an Omicron UHV scanning probe microscope in constant current mode for the topography images. The STM data are collected using an electrochemically etched W tip.

The hydrogen loading behavior of the samples is monitored by exposing the whole sample to 10^5 Pa of hydrogen gas in an optical setup. Technical details are described elsewhere [152]. A charge coupled device camera and a PC are used to sequentially capture images. The manual H_2 gas loading introduces an overall uncertainty in the absolute switching time ($\simeq$ 2 s). Recording of the optical changes has a time resolution of about 0.1 s. The time between the opening of the H_2 valve and the maximum slope of the transmission-time function (corresponding to the formation of an insulating MgH_2 or Mg_2NiH_4 phase) is defined as the switching time of the film.

6.4 Results and discussion

6.4.1 Critical thickness of Pd on Mg_yNi_{1-y}

To determine the minimum Pd-thickness required to catalyze the hydrogenation of Mg_yNi_{1-y} film, we probe a Mg_yNi_{1-y} gradient sample capped with a Pd thickness gradient perpendicular to the compositional gradient in y. In this way a number of different composition/thickness combinations are obtained on a single substrate. By loading the whole wafer with hydrogen we can simultaneously study the switching behavior of the various layer combinations using an optical camera. Apart from being very efficient, this method eliminates errors due to spread in preparation parameters as we prepare all samples in a single run.

Figure 6.2 shows the optical transmission images of a 200 nm Mg_yNi gradient film at different hydrogenation states. The Mg_yNi_{1-y} compositional gradient ranges from $y = 0.55$ to $y = 0.95$ and is covered by a perpendicular Pd thickness gradient ranging from 1-8 nm. The film is loaded in 10^5 Pa hydrogen at room temperature for 1 h ('fully loaded'). The optical properties of MgH_2 and Mg_2NiH_4 are different due to a band gap of 5.6 eV and 1.8 eV, respectively, and different absorption coefficients [71, 72]. As a result we have different colours, bright regions in transmission images representing MgH_2 and Mg_2NiH_4. Region (i) in Fig. 6.2 is attributed to a mixture of transparent Mg_2NiH_4 and metallic $(Mg_2)Ni$, regions (ii) and (iii) to a mixture of transparent Mg_2NiH_4 and transparent MgH_2. The borderline between region (ii) and (iii) is believed to be related to the eutectoid of the phases Mg and Mg_2Ni

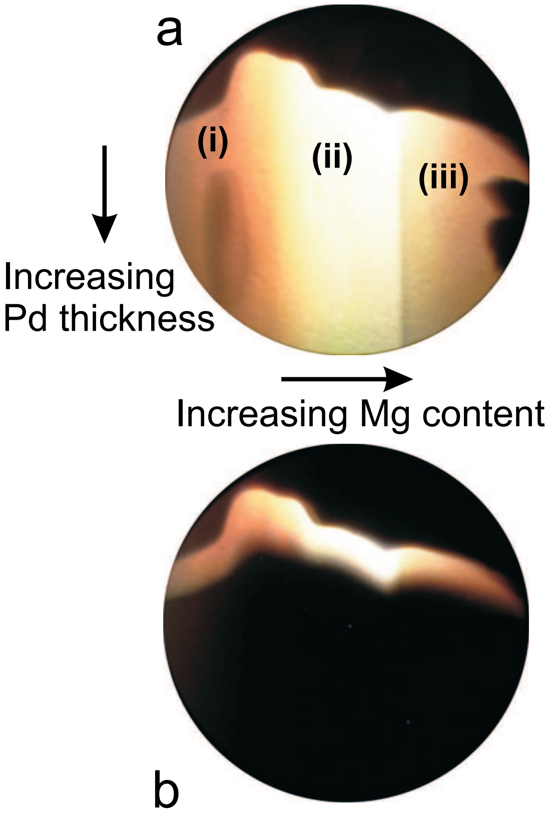

Figure 6.2: Optical transmission images of a 120 nm Mg_yNi_{1-y} gradient film at different hydrogenation states. The compositional gradient is covered by a Pd thickness gradient ranging from 1-8 nm. The film is loaded in 10^5 Pa hydrogen at room temperature for 1 h ('fully loaded', picture (a). The different band gaps of MgH_2 and Mg_2NiH_4 (1.8 and 5.6 eV) lead to a different coloration of regions (i), (ii) and (iii). The pure metallic Mg_yNi_{1-y} alloys and $MgH_{\sim 0}$ and $Mg_2NiH_{0.3}$ have essentially zero transmission. The borderline of the opaque region in the fully loaded state (black region at the top of the four photographs) corresponds to the minimum Pd thickness. This thickness depends on the underlying Mg/Ni ratio. After unloading in air (b), a small region around this thickness remains, evidencing the SMSI-effect. For a second loading (c), a thicker Pd layer is needed for H-uptake as evidenced by several black regions, which do not absorb hydrogen. After the 2^{nd} unloading (d), the inactivated region has considerably broadened. The white squares indicate regions, which are probed by STM.

[153]. The borderline towards non-zero transmission in the fully loaded state displays the minimum Pd thickness needed for a sufficient hydrogen uptake rate. From the figure it is clear that this thickness depends on the Mg/Ni ratio. After unloading in air for several days, a small region around this thickness still remains transparent (see Fig. 6.2b). Additionally, we show the transmis-

sion image of the wafer re-loaded at 10^5 Pa hydrogen after unloading in air in Fig. 6.2c and the subsequent unloading in air Fig. 6.2d. These observations can be easily explained by the SMSI-effect. First of all, partially covered Mg_2Ni areas will have oxidized in air. Secondly, during hydrogen exposure the *smallest* Pd clusters become fully encapsulated by reduced (hydrogenated) oxide (hydroxide) that blocks hydrogen uptake. The corresponding region (below the critical thickness) shows no transmission. *Slightly thicker* clusters retain enough free metal surface to the Mg-Ni film during the first hydrogen exposure. However, unloading (the reversed process) is not possible any longer, since the clusters have become fully encapsulated during the loading process. This effect continues to play a role. The amount of Pd needed for H-uptake increases as is evidenced by the moving of the borderline towards thicker Pd (compare Fig. 6.2b with Fig. 6.2d). We conclude that the SMSI-effect is a dynamical effect leading to a broadening of the inactivated region. It therefore might be responsible for the degradation observed more or less in all switchable mirror systems [144]. A closed Pd film extends the SMSI-free time period, but does not maintain it. While the films capped with 15 nm Pd showed nearly no changes in the maximum transmission after repeated cycling, we find that after approximately 200 cycles, [147] deterioration sets in again. Although we do not completely understand the mechanism, this implies substantial diffusion of the species involved. In the next section we concentrate on the effect of the Mg/Ni ration on the critical Pd-thickness.

6.4.2 Microscopic structure of Pd on Mg_yNi_{1-y}

Figure 6.2 indicates that the critical Pd thickness depends on the Mg/Ni roughness, which depends in turn on the Mg/Ni ratio. Using STM, we investigate the morphology of representative Pd-covered Mg_yNi_{1-y} films in order to find a reason for this dependence. In Fig. 6.3 we show two representative UHV STM scans for two prominent compositions. One is performed at $Mg_{70}Ni_{30}$, i.e. near the peritectic point of the binary alloy system [154], and one is performed at $Mg_{93}Ni_7$, i.e. near the eutectoid of Mg-Mg_2Ni. Due to peritectic segregation during solidification within the sputtering process, the films near the peritectic point display very disordered structures probably consisting of Mg_2Ni and $MgNi_2$ grains. Accordingly, the surface is very rough. The crystallization process of Mg-rich Mg_2Ni-films leads to larger and more ordered structures, resulting in smoother films (see Fig. 6.3).

The films are covered by Pd-grains. As the radius of curvature of the STM tip is of the same order of magnitude as the Pd grains, it is impossible to observe directly whether the Pd-grains form a closed film or not. As AES-measurements shows only a Pd signal for this thickness, the Pd layer is probably more or less continuous. To separate the roughness of the two layers, we measured STM-scans on a 100 × 100 nm^2 square for both films. The im-

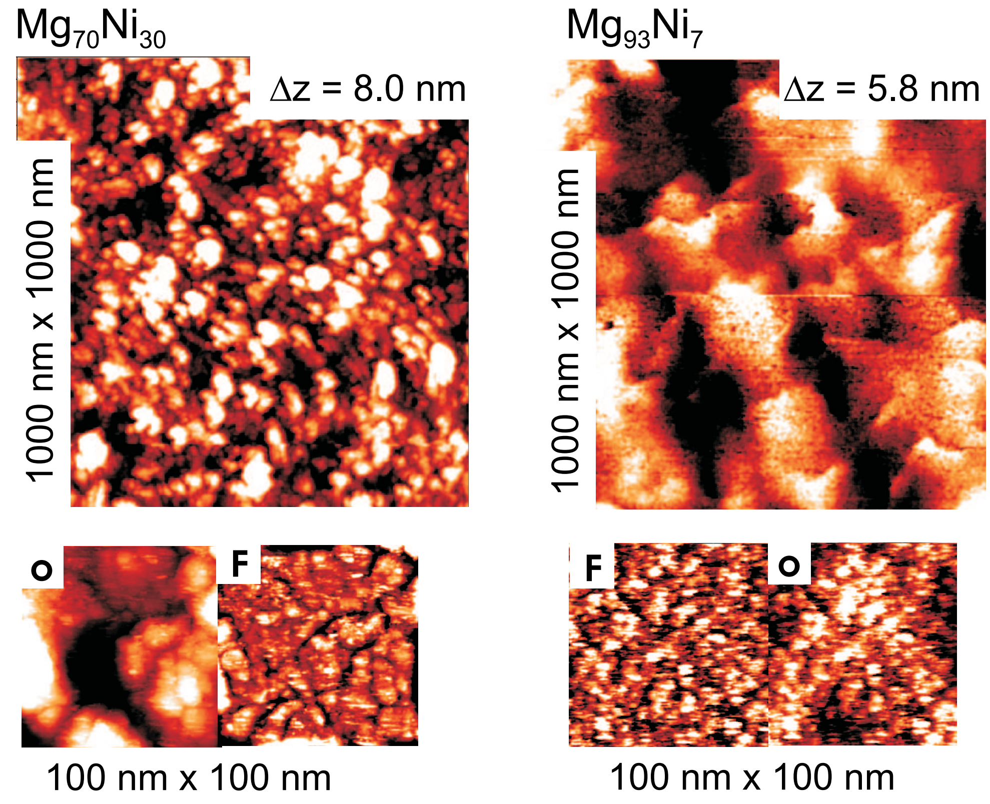

Figure 6.3: UHV STM scan of the coverage of a 200 nm thick Mg_2Ni film by 8 nm of Pd, acquired at $U_{gap} = 2$ V, $I = 0.5$ nA. Small grains associated with the Pd cap layer are typically 10 nm in diameter. The Mg_2Ni substructure has a corrugation of 10 nm. The small images (o) are enlargements of the corresponding top images to show the microscopic fine structure. Pictures assigned with (f) are fourier filtered to visualize the Pd-grains.

ages are Fourier-transformed and the lower frequencies were removed using a low-pass filter. Subsequently, the images were back-Fourier transformed. With this method, we filter the coarse surface structures (Mg_yNi_{1-x}) and extract the fine structure. Despite the different underlying Mg_yNi_{1-x} structure. Surprisingly, the roughest surface with composition $Mg_{70}Ni_{30}$ shows the smoothest and continuous fine structure (see Fig. 6.3f for $Mg_{70}Ni_{30}$).

For a quantitative analysis, we compare the surface structure measured on a mesoscopic scale (1000 nm) with that on a microscopic scale (100 nm) as a function of composition. The small images (o) are enlargements to show the microscopic fine structure. Pictures assigned with (f) are fourier filtered to visualize the Pd-grains. From these images we calculate the rms-roughness (root-mean square). The roughness analysis on the two different length-scale, 1000 and 100 nm, is used to quantify the structure of the Mg_yNi_{1-y} and Pd-

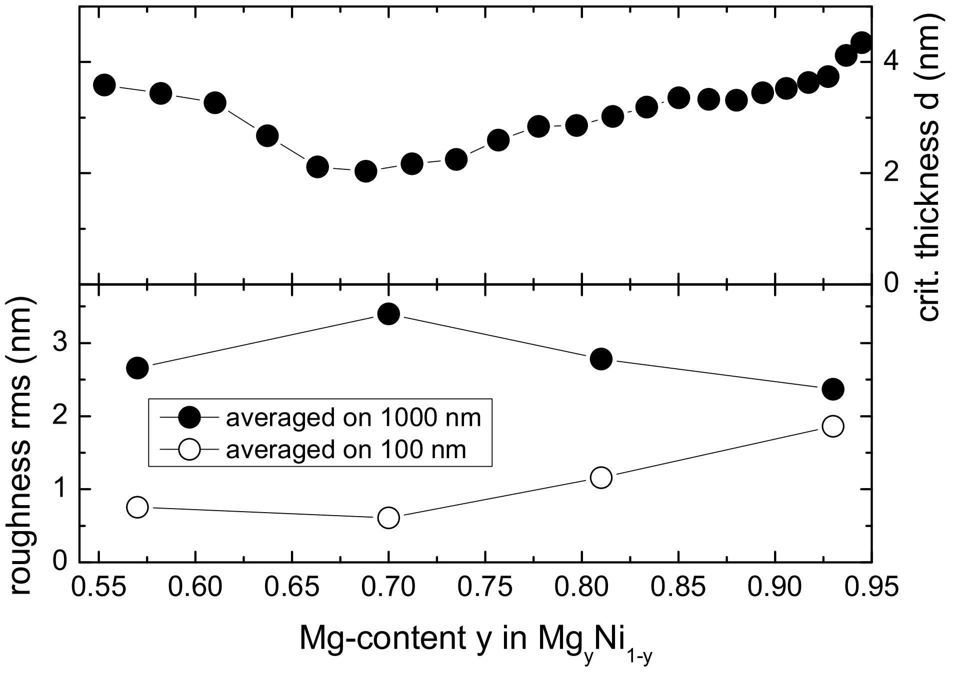

Figure 6.4: Top: Critical thickness of Pd-capped Mg_yNi_{1-y} films as measured optically (analysis of Fig. 6.2) as a function of the Mg-content y. Bottom: Roughness analysis of UHV-STM images (root mean square), averaged on 1 × 1 μm^2 and 100 × 100 nm^2 for various compositions.

grains. Figure 6.4 displays the roughness as a function of the composition. At high Mg-concentration, the roughness is mainly determined by the Pd-substructure. At $Mg_{70}Ni_{30}$, the roughness originates mainly from the alloy substructure. Here, Pd appears to be relatively smooth and the critical Pd-thickness determined by optical measurements (see Fig. 6.2) has its minimum. Comparing the 'Pd'-roughness with the critical Pd thickness as a function of the Mg_yNi_{1-y}-composition we conclude that the wetting (and consequently the roughness) of the Pd on the active hydride is the crucial parameter determining the catalytic activity of the capping layer. This makes sense, since flat, smooth grains are more difficult to encapsulate than small grains.

6.4.3 Hydrogen sorption kinetics of Mg_yNi_{1-y} films

Here we will study the SMSI effect during repeated hydrogenation cycles. Figure 6.5 shows switching cycles of 200 nm thick Mg_2Ni films, covered with a

Pd layer of variable thickness. The whole film is alternatingly exposed to 10^5 Pa hydrogen and to "vacuum" (< 10 Pa) at room temperature. These pressures are much above and below the dissociation pressure of Mg_2NiH_4, respectively ($p_{Mg_2NiH_4} \simeq 50$ Pa at room temperature, from Ref. [72]). The optical transmission T is measured as a function of time t and location and therefore of the capping layer thickness. For the present discussion, we set the precise correlation between optical properties of the thin film and its hydrogen content aside adopt the following convention: minimum transmission = zero H-content, maximum transmission = $4H/Mg_2Ni$ (for a more precise analysis we refer to Ref. [72]) and consider the maximum slope of the optical changes as a measure of the absorption kinetics of the switchable mirror.

Due to the high optical absorption of metallic Pd, Mg_2Ni films covered with the thickest Pd layer exhibit the lowest transmission in the fully hydrided state (see Fig. 6.5, top). To compare different thicknesses, the maximum slopes dT/dt are normalized and d(lnT)/dt are plotted as a function of the cycle number in Fig. 6.5, (bottom). Maximum changes occur after the first cycle (counted after the initial loading). The kinetics of films capped with less than 7 nm Pd slows down by nearly 40%, while for the film capped with 15 nm Pd the kinetics actually improves somewhat. The second cycle does not affect kinetics as much as the previous one, an effect which continues on further cycling [6]. The 15 nm capped film starts to deteriorate after approximately 200 cycles [147]. The deterioration in switching speed is strongly dependent on the Pd thickness. This suggests that it originates from the SMSI-effect. The cycling dependence is probably due to the diffusion time of the oxide species to cover the Pd and subsequently inactivate the catalytic properties upon repeated hydrogenation.

A possible application of switchable mirrors is the use as hydrogen sensors. In this case, the films have to withstand exposure to air. One might expect that changing the gas environment from hydrogen to oxygen enhances the accumulation of oxides on the Pd-surface. However, exposing the sample to air appears to *restore* the sample surface. The switching kinetics of the first hydrogenation after air exposure is faster than that before air exposure - except for the 15 nm capped film (see Fig. 6.5(b)). The deterioration is again highest after this first cycle, after which the deterioration slows down.

An important consequence of the SMSI in composite catalysts is the partial reversibility of the effect. After changing the gas environment from hydrogen to oxygen, the oxide on the Pd-clusters is partly removed [148, 155]. The process depends on the exact composition of the used gas, in particular its water content [155]. Moreover, the process is strongly time and therefore thickness dependent, which is not surprising as a relatively large amount of matter is transported during the process. Consequently thin caplayers are more sensitive to deterioration but are also more easily regenerated. This is strong evidence for the the important role of the SMSI-effect and not of

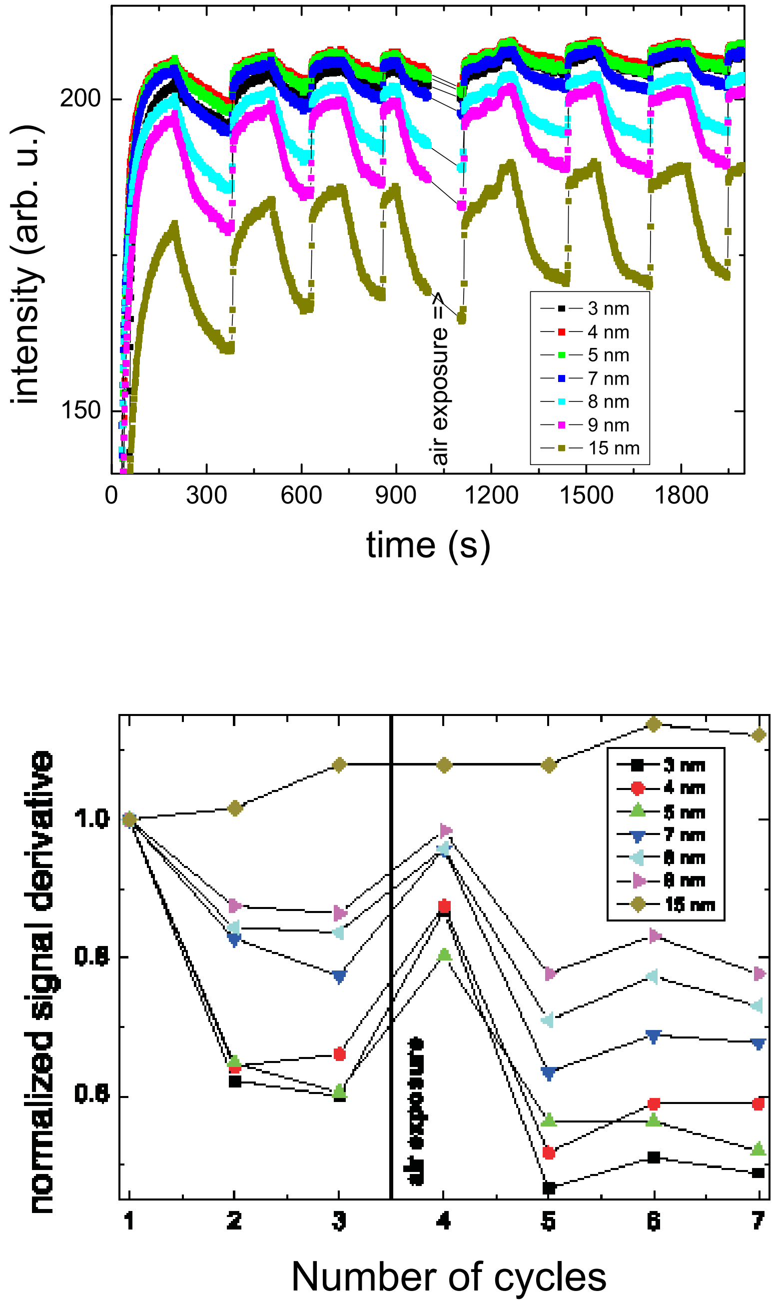

(a)

(b)

Figure 6.5: Top: Optical transmission of a 200 nm Mg_2Ni film during loading with a Pd thickness ranging from 3 to 15 nm. Bottom: Maxima of the normalized derivative as a function of the cycle number.

chemisorption of oxygen/water etc. ('deactivation' of the surface [156]).

6.4.4 Oxygen impurities on Pd covered Mg_yNi_{1-y}-films

The conclusions of the optical measurements are substantiated by Auger measurements. The Auger spectra between 200 and 900 eV of a sample similar to that used for the optical measurements are shown in Fig. 6.6. For a sample that has been cycled once, there are three main transitions visible: Pd-MNN (triplet around 300 eV), O-KLL (around 500 eV), Ni-LMM (triplet between 700-900 eV). With increasing Pd thickness the Ni-peaks rapidly disappear. Extrapolating this result we conclude that 5 nm Pd completely covers the Mg_2Ni-film. With increasing Pd thickness, the oxygen signal decreases but does not vanish completely. Since only the surface of Mg_2Ni films oxidizes, the Auger oxygen signal should decrease when the Mg_2Ni surface is more and more covered by Pd. However, as we show in Fig. 6.6 one needs more than 10 nm Pd before "O" reduce to zero. This observation suggests that Mg diffuses to the Pd surface and oxidizes there. The poor wetting of the Pd layer contribute to this effect. This is a hint that the concept of a (strong) metal (Pd)-support interaction is valid also for completely covered Pd-surfaces.

Originally, the SMSI was proposed for metal clusters deposited on an oxide, which creeps up and eventually covers these clusters. Figure 6.6 demonstrates that this explanation can also be applied to all-metal systems. The only difference is that the oxides are introduced by impurities in the hydrogen gas and/or exposure to air during the switching process. The crucial consequence of the SMSI, i.e. the coverage of catalytically active clusters by oxides after hydrogen exposure, remains the same [157].

There might be various ways to reduce the negative impact of the SMSI-effect in switchable mirrors. One way is to use buffer layers, which prevent interdiffusion as successfully realized with Al_2O_3 [146] and Nb_2O_5 [8].

6.4.5 Sulfur impurities on Pd

From the previous sections it is obvious that the SMSI effect plays an important role in the cycling stability of switchable mirrors. However, there are other mechanisms/processes effecting the H-sorption process. We find that the *in-situ* grown films immediately unload in vacuum when covered only with a few angströms of Pd. After re-hydrogenation these films do not unload in vacuum anymore and behave just like *ex-situ* hydrogenated films. We believe that the reduced catalytic activity, as compared to freshly deposited Pd, has its origin in a poisoning effect of the Pd layer.

In literature it is reported that a sulfur contamination of the Pd surface is very effective to block hydrogen absorption. Burke *et al.* showed that the hydrogen coverage of the Pd surface linearly decreases with increasing sulfur

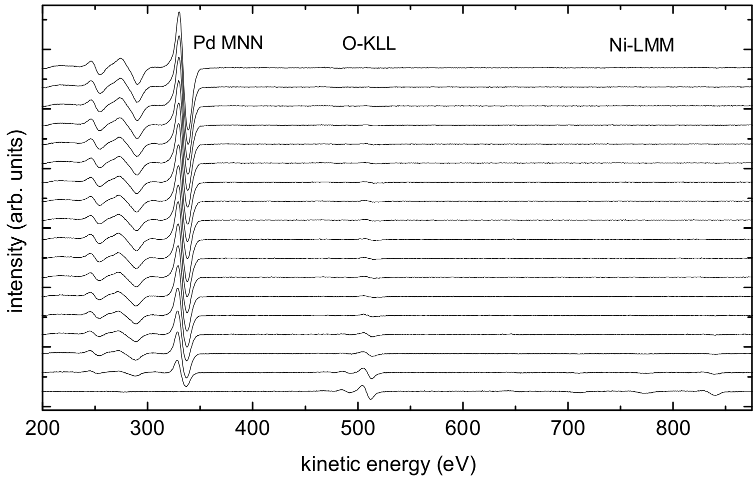

(a)

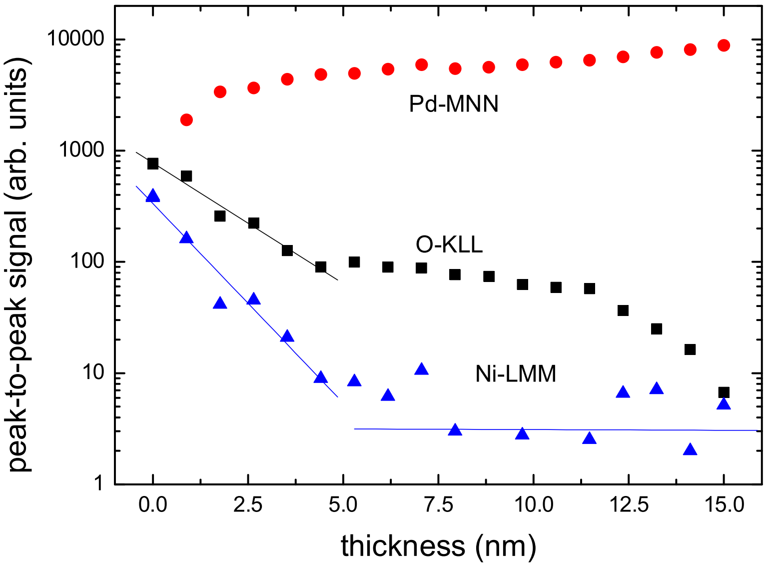

(b)

Figure 6.6: (a) Auger electron spectra of Pd on Mg_2Ni as a function of the Pd-thickness. (b) Intensity of the Auger transitions extracted from the spectra of (a). The background noise is around $I \simeq 5$ (compare Ni LMM signal). After one hydrogenation cycle, the sample has been transported through air before measurement.

coverage due to site blocking [158]. Rendulic *et al.* reported that adsorption of sulfur on Ni(110) and Pd(100) preferentially blocks the non-activated path leading to predominantly activated adsorption. The same observation is made by Wilke *et al.* who showed that the poisoning effect of sulfur originates from the formation of energy barriers hindering the dissociation of H_2 [159, 160].

Not many results are reported on the role of sulfur during the dehydrogenation process. Castro *et al.* show that sulfur poisoning induces a delay on hydrogen desorption kinetics and that the effect increases for samples with a greater surface-to-volume ratio [161]. Burke *et al.* showed that for a sulfur coverage above $\Theta = 0.28$ no hydrogen dissociation on Pd(100) is possible. Furthermore, they observe that the activation energy for hydrogen desorption with a sulfur coated Pd layer is reduced. This is at first sight curious since one would expect that a low activation energy enhances kinetics [158]. However, these authors measure the desorption of surface adsorbed hydrogen. The blockage of surface sites by sulfur hinders the adsorption and lowers the activation energy for desorption. Castro *et al.* report that for a sulfur covered Pd surface the activation energy for hydrogen desorption from the bulk indeed increases [161]. However, as shown by Borschulte *et al.*, apparent activation energies often describe both the surface adsorption and the ensuing specific diffusion process and therefore they are not necessarily an intrinsic surface property of the catalyst.

To investigate the blocked dehydrogenation we examine the chemical surface composition with X-ray photoelectron spectroscopy (XPS). We measured a 100 nm thick Pd film in the as-grown, hydrogenated (10^5 Pa, room temperature) and annealed state (at 815 K in UHV). We find that on hydrogenation, the sulfur concentration of the Pd surface increases considerably, as indicated by the sulfur $2p_{3/2}$ peak in Fig. 6.7. This means that the hydrogenation process induces a segregation in which the sulfur diffuses towards the Pd surface. Annealing the hydrogenated Pd film results in a decrease of the sulfur signal. Probably part of the sulfur has dissolved again in the Pd or it has evaporated to the vacuum.

From XPS measurements we know that roughly the first 20 monolayers of Pd contains 2.3% of sulfur which increases to 2.9% upon hydrogenation and decreases to 1.28% upon annealing. This means that not the complete Pd surface is covered by sulfur. However, as we have discussed before, sulfur also has a blocking effect on neighboring sites. From RBS measurements we found that there is some sulfur throughout the Pd with a maximum of a few percent.

If sulfur is indeed responsible for the decreased dehydrogenation, the catalytic properties should be recovered once the sulfur has been removed from the film surface (see Fig. 6.10). Unfortunately, at 815 K Pd strongly reacts with Mg-compounds and thus we cannot use the annealed sample to test this idea. Therefore, we tried to remove the sulfur by sputtering the surface with argon ions. A 200 nm Mg_2Ni film is grown on a fiber and is subsequently cov-

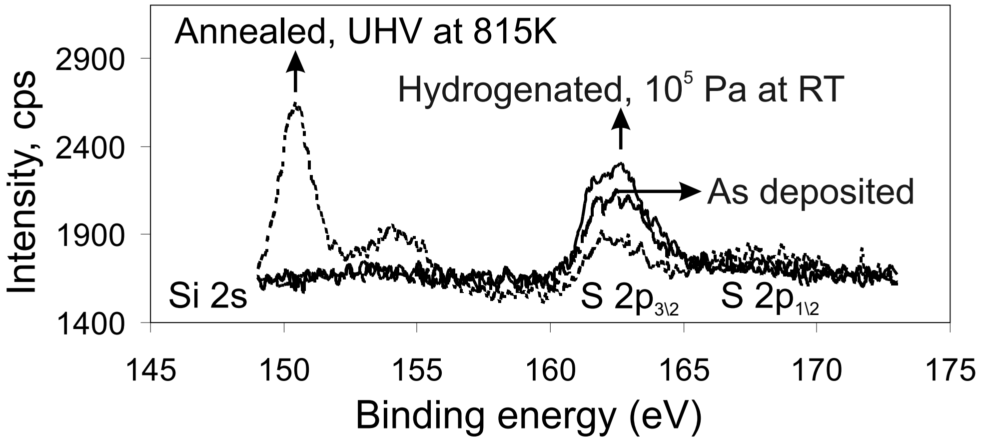

Figure 6.7: XPS measurement on a 100 nm thick Pd sample. A measurement of the as-prepared state is shown. Subsequently the film is hydrogenated at 10^5 Pa at RT which increases the surface sulfur content considerably. Annealing under UHV conditions of this film results in a decrease of the surface sulfur.

ered with 10 nm Pd (see Fig. 6.8). After deposition, the fiber is transported under UHV conditions to a hydrogenation chamber where it is loaded at a hydrogen pressure of 10^5 Pa at room temperature. The dip in reflection is due to the fact that we go through the optical black state. After hydrogenation, the chamber is pumped down to 10^{-5} Pa starting at point (f). As a result the reflection decreases slowly due to the dehydrogenation of the film. Then (g) the Pd is sputtered with argon ions at 1 keV. This results in an increased dehydrogenation rate and a rapid decrease of the reflection. Due to this bombardment some Pd atoms together with the adsorbates (sulfur) are removed from the surface leaving a clean Pd surface (equivalent with a freshly deposited Pd surface). When the bombardment is stopped the dehydrogenation slows down as indicated by point (h) in Fig. 6.8. Starting the sputtering process again the dehydrogenation rate increases. Note, that between i and j the reflection goes through a minimum again, due to the fact that during unloading we again pass through the black state, now in the opposite way. Although the film is still under an argon bombardment at point (l), the dehydrogenation has essentially stopped here, which is due to the fact that the complete Pd caplayer is sputtered away. The fact that argon sputtering influences the hydrogenation was also found by Gdowski *et al.* who investigated the effect of the surface temperature on the hydrogen sorption by Pd(111) [162]. They report that sputtering the Pd(111) surface causes an increase in the hydrogen absorption rate at 115 K. Our experiment reveals that 1) as long as the film is covered by a "fresh" Pd caplayer the dehydrogenation (hydrogenation) rate is fast and 2) the catalytic properties of the Pd layer degrade when exposed

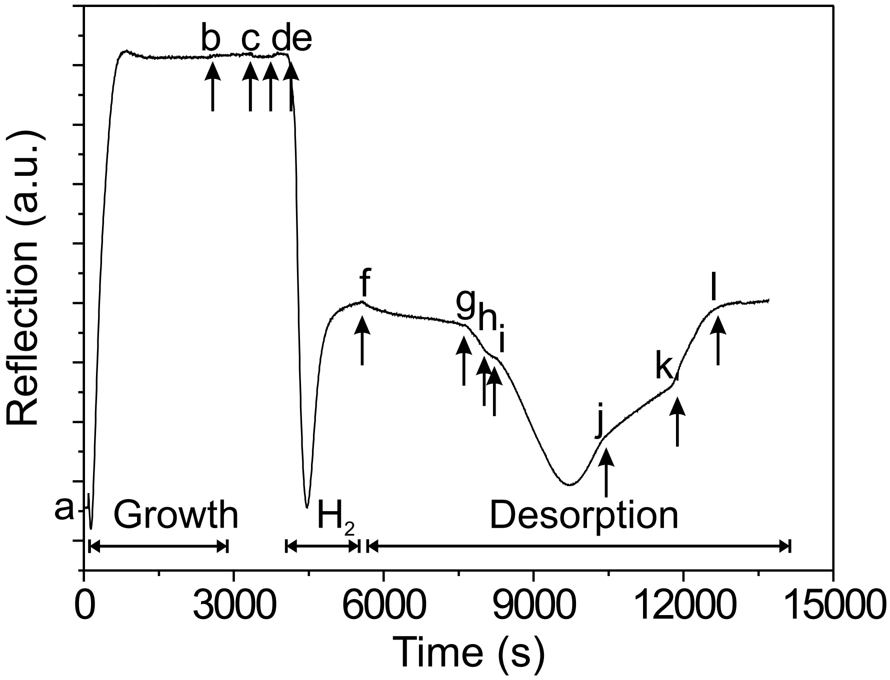

Figure 6.8: Determining the surface properties of a Pd caplayer upon sputtering with argon ions. First, between point a (0 s) and b (2580 s) a 200 nm Mg_2Ni film is grown on a fiber. This film is subsequently covered with a 10 nm Pd layer, point c - d (3385-3820 s). At point e (4080 s) the hydrogenation of the sample starts (at 10^5 Pa and room temperature) until point f (5580 s) whereafter the system is pumped down to 10^{-5} Pa. From this point the reflection decreases only modest. At point g (7110 s), i (8250) and k (11400 s) the sample is bombarded with argon ions which induces an increase in the dehydrogenation rate. When the argon beam is switched off, the rate decreases again, point h (8004 s) and j (10320 s). After point l (13125 s) the dehydrogenation decreases strongly due to the fact that the catalytic Pd layer is sputtered away. The minimum in reflection between point e - f and point i - j corresponds to the black state of the Mg-Ni film.

to vacuum and hydrogenation cycles. An important observation is that the dehydrogenation rate decreases as soon as the sputtering is stopped, indicating the fast degradation of the catalytic properties of the Pd layer.

The same result is obtained upon depositing a new Pd layer on the blocked Pd caplayer. In Fig. 6.9 the film is hydrogenated until 2100 s after which the system is pumped vacuum. It is obvious that the film does not unload. However upon depositing 5 nm of Pd at 3800 s, the film spontaneously starts to unload reaching its initial unloaded state at around 5400 s.

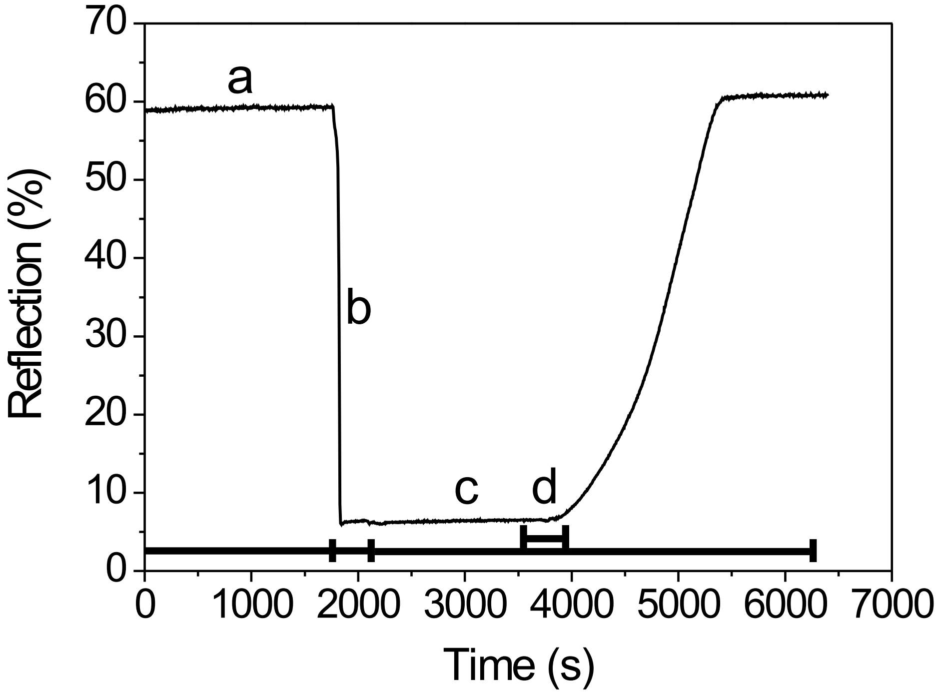

Figure 6.9: Dehydrogenation in vacuum of a hydrided film upon depositing a new and fresh 5 nm Pd layer. The colored blocks indicate time interval of a certain action. At (a) we start with a 200 nm metallic film. (b) The film is hydrogenated till 2100 sat room temperature and a hydrogen pressure of 10^5 Pa. At (c) the system is pumped vacuum (10^{-5} Pa). At 3800 s (d) an additional 5 nm Pd cap layer is deposited after which the film spontaneously unloads.

Summarizing, we find that the dehydrogenation of *in-situ* grown and as-deposited films depends strongly on the physical conditions. 1) The desorption of hydrogen is in most cases impaired. At room temperature one has to apply an air/oxygen atmosphere to the Pd surface to obtain a sizeable desorption. 2) In *vacuum* ($< 10^{-5}$ Pa) dehydrogenation is only possible from a clean or freshly deposited Pd caplayer. During Pd deposition or argon sputtering, the Pd surface is not in an equilibrium state and may contain non-equilibrium sites and/or a transient lattice spacing, which may have a large influence on the hydrogenation kinetics. After some time in vacuum, the Pd surface reaches an equilibrium state under the influence of minimizing of the surface energy and so reducing the amount of non-equilibrium sites for hydrogenation. In a tentative model to explain our results, desorption only takes place from special step-edge sites and such sites can be easily blocked by the presence of a few sulfur adatoms (see Fig. 6.10). New step-edge sites can be created by sputtering, which result in a higher desorption rate. When the sputtering is stopped these edges disappear due to the rearrangement of the Pd surface and/or can be blocked by the sulfur. Note, that desorption in air is always fast. In this case a surface reaction occurs which results in the formation and desorption of water. This reaction apparently depends not on specific sites and is therefore insensitive to the Pd-surface properties.

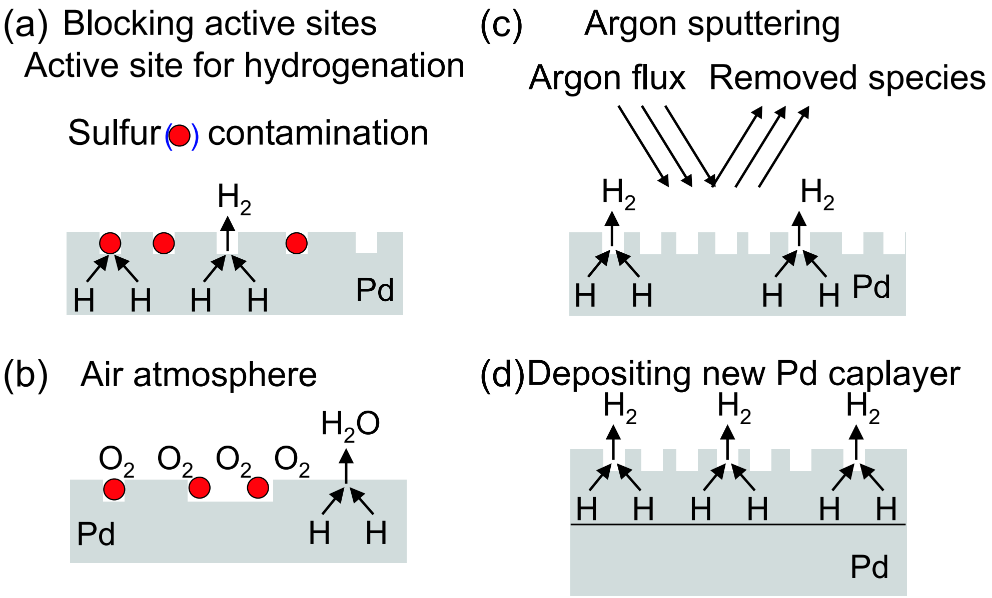

Figure 6.10: Schematic representation of processes involved in hydrogen desorption. (a) Active sites for hydrogen desorption are blocked by a sulfur atom. (b) In an air atmosphere, hydrogen desorption can occur at less favorable sites. The creation of a clean and fresh Pd surface with active sites for hydrogen desorption can be obtained by argon sputtering of the Pd surface (c) or by deposition of a new Pd layer (d).

The idea that there are different types of sites (or defects) which have different energies for hydrogenation is supported by findings of Wilke *et al.* and Behm *et al.* [159, 163]. They show that there is a difference in the hydrogen adsorption energy between the surface hollow sites and other adsorption positions and as a result the hollow sites are first occupied. Okuyama *et al.* shows that hydrogen absorption occurs only at surface defects on Pd(100) and that no absorption via terrace sites is observed [164]. In this context it is interesting to note that Behm *et al.* shows that for Pd(100) (24.5 kcal/mole), Pd(111) (20.8 kcal/mole) and Pd(110) (24.4 kcal/mole) the strength of the metal-hydrogen bond is only very little affected by the crystallographic orientation of the surface [165]. Furthermore, deposition and sputtering can result in a transient lattice spacing, which can improve the dehydrogenation.

Future experiments needs to be done to determine if the sulfur or the lack of special surface sites is responsible for the activated dehydrogenation. Because our Pd is of purity 99.95, a plausible way to examine this problem is to work with Pd of higher purity. On the other hand due to prolonged exposure to air Pd may pick up sulfur from air contaminations as well. Castro *et al.* indicated that the sulfur contamination has its origin in a stainless-steel component [161]. During sample hydriding, gaseous hydrogen reacts with the sulfur and forms H_2S, which subsequently pollutes the sample surface. There it decomposes and the sulfur covers the Pd surface. Comparable results with CS_2 on the desorption of hydrogen is found by Bucur *et al.* [166]. However as we do not observe a S or H_2S contamination in the UHV chamber during deposition by partial pressure measurements, this is not a very convincing mechanism to obtain the sulfur contamination.

6.5 Conclusions

The impact of the microscopic structure on the kinetics and stability of Mg-Ni switchable mirrors has been investigated by means of a high-throughput method and various surface science techniques. The strongest limiting factor in mirror switching kinetics is the deterioration by oxidation of the optically active hydride layer. The oxidation is only partially prevented by a Pd-capping layer. During the hydrogenation process part of the catalytic Pd caplayer is covered by an inactive oxide layer limiting the kinetics of this layer. We studied the behavior of this layer as a function of the capping layer thickness and Mg-Ni thin film composition. The microstructure of the Mg-Ni thin film system is related to its composition and determines the critical Pd-thickness required for hydrogen uptake. We find that the strong metal-support interaction (SMSI) plays a major role. The interaction depends on the applied gas atmosphere, which changes during hydrogenation cycles from H_2 to O_2 in Ar. The loading cycles lead to a rearrangement of the capping layer and eventually the deterioration of the whole thin film system. Originally, the SMSI was proposed for metal clusters deposited on oxide supports. We demonstrate that this explanation can also be applied to all-metal systems, in particular to the Pd/Mg_2Ni system. One way to minimize the consequences of the SMSI-effect is the use of very thick Pd capping layers. However a complete coverage of the film with Pd is not enough to suppress the effect completely. Another possibility is the reinforcement of the interface by surface oxidation of the hydride layer or by the growth of an intermediate buffer layer, to prevent interdiffusion.

Furthermore we show by means of XPS measurements that the presence of sulfur on the outermost Pd surface limits the dehydrogenation process in vacuum tremendously. Removing this contaminated Pd skin by argon sputtering results in an increase in the dehydrogenation properties of the catalytic Pd layer. The same result is obtained by depositing a new Pd layer on top of the blocked Pd layer.

References

[1] T. Graham, Philos. Trans. Roy. Soc. London **156**, 399 (1866).

[2] J. N. Huiberts, R. Griessen, J. H. Rector, R. J. Wijngaarden, J. P. Decker, D. G. de Groot, and N. J. Koeman, *Yttrium and lanthanum hydride films with switchable optical properties*, Nature **380**, 231 (1996).

[3] D. R. Rosseinsky and R. J. Mortimer, *Electrochromic systems and the prospects for devices*, Adv. Mater. **13**, 783 (2001).

[4] A. Remhof, S. J. van der Molen, A. Antosik, A. Dobrowolska, N. J. Koeman, and R. Griessen, *Switchable mirrors for visualization and control of hydrogen diffusion in transition metals*, Phys. Rev. B **66**, 020101 (2002).

[5] D. Iannuzzi, M. Lisanti, and F. Capasso, *Effect of hydrogen-switchable mirrors on the Casimir force*, Proceedings of the National Academy of Sciences of the USA **101**, 4019 (2004).

[6] M. Slaman, B. Dam, M. Pasturel, D. Borsa, H. Schreuders, J. H. Rector, and R. Griesen, *Fiber optic hydrogen detectors containing Mg-based metal hydrides*, Accepted by Sensors and Actuators B, chemical (2006).

[7] P. van der Sluis, M. Ouwerkerk, and P. A. Duine, *Optical switches based on magnesium lanthanide alloy hydrides*, Appl. Phys. Lett. **70**, 3356 (1997).

[8] T. J. Richardson, J. L. Slack, R. D. Armitage, R. Kostecki, B. Farangis, and M. D. Rubin, *Switchable mirrors based on nickel-magnesium films*, Appl. Phys. Lett. **78**, 3047 (2001).

[9] T. J. Richardson, J. L. Slack, B. Farangis, and M. D. Rubin, *Mixed metal films with switchable optical properties*, Appl. Phys. Lett. **80**, 1349 (2002).

[10] J. L. M. van Mechelen, B. Noheda, W. Lohstroh, R. J. Westerwaal, J. H. Rector, B. Dam, and R. Griessen, *Mg-Ni-H film as selective coatings: Tunable reflectance by layered hydrogenation*, Appl. Phys. Lett. **84**, 3651 (2004).

[11] E. P. T. M. Suurmeijer and J. Verhoeven, *Vacuümtechniek*, Nederlandse Vacuüm Vereninging, 1989.

[12] L. J. van der Pauw, *A method of measuring specific resistivity and Hall-effect of discs of arbitrary shape*, Philips Res. Repts. **13**, 1 (1958).

[13] O. S. Heavens, *Optical Properties of Thin Sollid Films*, Dover, New York, 1965.

[14] A. T. M. van Gogh, *Probing the metal-insulator transition in rare-earth based switchable mirrors*, Vrije Univeristeit, Amsterdam, 2001.

[15] E. D. Palik, *Handbook of Optical Constants of Solids*, Academic Press, San Diego, 1998.

[16] R. J. Westerwaal, A. Borgschulte, W. Lohstroh, B. Dam, B. Kooi, G. ten Brink, M. J. P. Hopstaken, and P. H. L. Notten, *The growth induced microstructural origin of the optical black state of* Mg_2NiH_x *thin films*, J. Alloys Compd. **416**, 2 (2006).

[17] N. R. Y. Caranto, S. C. Kaddu, J. Szajman, M. M. Murphy, S. F. Collins, and D. J. Booth, *An optical-fiber thin-film thickness monitor*, Meas. Sci. Technol. **4**, 865 (1993).

[18] C. M. Emmerson, T.-H. Shen, S. D. Evans, and H. Allinson, *Temperature dependence of magnetoresistance and Hall-effect in* Mg_2NiH_x *films*, J. Appl. Lett. **68**, 3740 (1996).

[19] F. Wouten, *Optical properties of solids*, Academic Press, New York and London, 1972.

[20] M. A. Butler and R. J. Buss, *Kinetics of the micromirror chemical sensor*, Sensors and Actuators B **11**, 161 (1993).

[21] M. A. Butler, *Micromirror optical-fiber hydrogen sensor*, Sensors and Actuators B **22** (1994).

[22] K. G. Tschersich and V. von Bonin, *Formation of an atomic hydrogen beam by a hot capillary*, J. Appl. Phys. **84**, 4065 (1998).

[23] K. G. Tschersich, *Intensity of a source of atomic hydrogen based on a hot capillary*, J. Appl. Phys. **87**, 2565 (2000).

[24] J. J. Reilly and R. H. Wiswall, *The reaction of hydrogen with alloys of magnesium and nickel and the formation of* Mg_2NiH_4, Inorg. Chem. **7**, 2254 (1968).

[25] J. L. Soubeyroux, D. Fruchart, A. Mikou, M. Pezat, and B. Darriet, *Structural study of the system* Mg_2Ni*-*H_2*. III. Monoclinic variety of* Mg_2NiH_4, Mater. Res. Bull. **19**, 1119 (1984).

[26] J. Schefer, P. Fischer, W. Hälg, F. Stucki, L. Schlappbach, J. J. Didisheim, K. Yvon, and A. F. Andresen, *New structure results for hydrides and deuterides of the hydrogen storage material* Mg_2Ni, J. Less-Common Met. **74**, 65 (1980).

[27] P. Zolliker, K. Yvon, J. D. Jørgensen, and F. J. Rotella, *Structural studies of the hydrogen storage material* Mg_2NiH_4*. 2. Monoclinic low temperature structure*, Inorg. Chem. **25**, 3590 (1986).

[28] Z. Gavra, M. H. Mintz, G. Kimmel, and Z. Hadari, *Allotropic transitions of* Mg_2NiH_4, Inorg. Chem. **18**, 3595 (1979).

[29] J. Genossar and P. S. Rudman, *Structural transformation in* Mg_2NiH_4, J. Phys. Chem. Solids **42**, 611 (1981).

[30] W. Hume-Rothery, *The Structure of Metals and Alloys*, Institute of Metals Monographs and Report Series, London, 3rd ed. edition, 1954.

[31] T. Massalski, P. S. H. Okamoto, and L. Kacprzak, *Binary Alloy Phase Diagrams*, American Society for Metals, Metals Park OH, 1990.

[32] J. L. Corkill and M. L. Cohen, *Structural, bonding, and electronic properties of IIA-IV antifluorite compounds*, Phys. Rev. B **48**, 17138 (1993).

[33] P. Baranek, J. Schamps, and I. Noiret, *Ab initio studies of electronic structure, phonon modes, and elastic properties of* Mg_2Si, J. Phys. Chem. B **101**, 9147 (1997).

[34] G. N. García, J. P. Abriata, and J. O. Sofo, *Calculation of the electronic and structural properties of cubic* Mg_2NiH_4, Phys. Rev. B **59**, 11746 (1999).

[35] J. Tejeda and M. Cardona, *Valence bands of the* Mg_2X *(X=Si, Ge, Sn) semiconducting compounds*, Phys. Rev. B **14**, 2559 (1976).

[36] P. M. T. M. van Attekum, G. K. Wertheim, G. Crecelius, and J. H. Wernick, *Electronic properties of some* CaF_2*-structure intermetallic compounds*, Phys. Rev. B **22**, 3998 (1980).

[37] D. Mingos and J. Hawes, *Structure and Bonding*, volume 63, Springer, Berlin, 1986.

[38] M. Gupta, *Electronic structure of intermetallic hydrides:* Mg_2FeH_6 *and* Ca_2RuH_6, J. Less-Common Met. **103**, 325 (1984).

[39] M. Gupta, E. Belin, and L. Schlapbach, *Density of occupied states of intermetallic hydride* $NiMg_2H_4$, J. Less-Common Met. **103**, 389 (1984).

[40] W. R. Myers, L.-W. Wang, T. J. Richardson, and M. D. Rubin, *Calculation of thermodynamic, electronic, and optical properites of monoclinic* Mg_2NiH_4, J. Appl. Phys. **91**, 4879 (2002).

[41] G. N. García, J. P. Abriata, and J. O. Sofo, *Hydrogen movement in cubic* Mg_2NiH_4, Phys. Rev. B **65**, 064306 (2002).

[42] P. Zolliker, K. Yvon, P. Fischer, and J. Schefer, *Dimagnesium cobalt(I) pentahydride,* Mg_2CoH_5*, containing square-pyramidal* CoH_5^{4-} *anions*, Inorg. Chem. **24**, 4177 (1985).

[43] R. Černý, F. Bonhomme, K. Yvon, P. Fischer, P. Zolliker, D. E. Cox, and A. Hewat, *Hexamagnesium dicobalt undecadeuteride* $Mg_6Co_2D_{11}$*: containing* $[CoD_4]^{5-}$ *and* $[CoD_5]^{4-}$ *complex anions conforming to the 18-electron rule*, J. Alloys Compd. **187**, 233 (1998).

[44] J.-J. Didisheim, P. Zolliker, K. Yvon, P. Fischer, J. Schefer, M. Gubelmann, and A. F. Williams, *Dimagnesium Iron(II)Hydride,* Mg_2FeH_6*, Containing Octahedral* FeH_6^{4-} *anions*, Inorg. Chem. **23**, 1953 (1984).

[45] M. Bortz, B. Bertheville, K. Yvon, E. A. Movlaev, V. N. Verbetsky, and F. Fauth, Mg_3MnH_7 *containing the first known hexahydridomanganese(I) complex*, J. Alloys Compd. **279**, 8 (1998).

[46] E. Orgaz and M. Gupta, *Electronic structure of the new manganese ternary hydride* Mg_3MnH_7, J. Alloys Compd. **330**, 323 (2002).

[47] M. Y. Song, *Phase separation of* Mg_2Ni *by hydriding-dehydriding cycling*, J. Less-Common Met. **282**, 297 (1999).

[48] H. Zabel and A. Weidinger, Comments Cond. Mat. Phys. **17**, 239 (1995).

[49] V. Leiner, H. Zabel, J. Birch, and B. Hjörvarsson, *Deuterium in 001-oriented* $Mo_{0.5}V_{0.5}/V$*: Density profile on the atomic level*, Phys. Rev. B **66**, 235413 (2002).

[50] S. Olsson, B. Hjörvarsson, E. B. Svedberg, and K. Umezawa, *H-H interactions in Nb/W(110) superlattices*, Phys. Rev. B **66**, 155433 (2002).

[51] D. Noréus and P.-E. Werner, Acta Chem. Scand. **36**, 847 (1982).

[52] M. H. Mints, Z. Gavra, G. Kimmel, and z. Hadari, *The reaction of hydrogen with magnesium alloys and magnesium intermetallic compounds*, J. Less-Common Met. **74**, 263 (1980).

[53] H. Buchner, O. Bernauer, and W. Straub, *T.N. Veziroglu, W. Seifritz (eds.) Proceedings of the World Hydrogen Energy Conference, Zürich*, Pergamon, Oxford **3**, 1677 (1978).

[54] E. Akiba, K. Nomura, S. Ono, and S. Suda, *Kinetics of the reaction between Mg-Ni alloys and* H_2, Int. J. Hydrogen Energy **7**, 787 (1982).

[55] M. L. Post, J. J. Murray, and J. B. Taylor, *Metal hydride studies at the National Research Council of Canada*, Int. J. Hydrogen Energy **9**, 137 (1984).

[56] K. Zeng, T. Klassen, W. Oelerich, and R. Borman, *Thermodynamic analysis of the hydriding process of Mg-Ni alloys*, J. Alloys Compd. **283**, 213 (1999).

[57] J. Isidorsson, I. A. M. E. Giebels, R. Griessen, and M. D. Vece, *Tunable reflectance Mg-Ni-H films*, Appl. Phys. Lett. **80**, 2305 (2002).

[58] M. D. Vece, A. M. J. van der Eerden, D. Grandjean, R. Westerwaal, W. Lohstroh, S. G. Nikitenko, J. J. Kelly, and D. C. Koningsberger, *Structure of the* Mg_2Ni *switchable mirror: an EXAFS investigation*, 2005.

[59] B. Farangis, P. Nachimuthu, T. J. Richardson, J. L. Slack, R. C. C. Perera, E. M. Gullikson, D. W. Lindle, and M. Rubin, *In-situ x-ray absorption spectroscopy study of hydrogen absorption by nickel-magnesium thin films*, Phys. Rev. B **67**, 085106 (2003).

[60] H. Blomqvist, *Competing stabilisation mechanisms in* Mg_2NiH_4, J. Alloys Compd. **330-332**, 268 (2002).

[61] H. Blomqvist, *Mechanically reversible conductorinsulator transition in* Mg_2NiH_4, J. Appl. Phys. **91**, 5141 (2002).

[62] D. Noréus and L. G. Olsson, *The structure and dynamics of hydrogen in* Mg_2NiH_4 *studied by elastic and inelastic neutron scattering*, J. Chem. Phys. **78**, 2419 (1983).

[63] S. Enache, W. Lohstroh, and R. Griessen, *Temperature dependence of Magnetoresistance and Hall-effect in* Mg_2NiH_x *films*, Phys. Rev. B **69**, 115326 (2004).

[64] W. M. Mueller, L. L. Tay, J. Yang, and G. G. Libowitz, *Metal Hydrides*, Academic Press, New York, 1968.

[65] D. Lupu, R. Sârbu, and A. Biriş, *Microstructure and surface scaling in ballistic deposition at oblique incidence*, Int. J. Hydrogen Energy **12**, 425 (1987).

[66] P. Selvam, B. Viswanathan, and V. Srinivasan, *X-ray photoelectron spectroscopic, electrical and magnetic studies on* Mg_2NiH_4, J. Electron Spectrosc. Relat. Phenom. **46**, 357 (1988).

[67] Y. Fujita, M. Yamaguchi, and I. Yamamoto, *Electrical and optical properties of* Mg_2NiH_4 *films*, Z. Phys. Chem. Neue Folge **163**, 633 (2003).

[68] U. Häussermann, H. Blomqvist, and D. Noréus, *Bonding and stability of the hydrogen storage material* Mg_2NiH_4, Inorg. Chem **41**, 3684 (2002).

[69] T. C. Paulik, *Inversion of normal-incidence (R,T) measurements to obtain n+ik for thin films*, Appl. Opt. **25**, 562 (1986).

[70] G. A. Niklasson and C. G. Granqvist, *Optical properties and solar selectivity of coevaporated* Co-Al_2O_3 *composite films*, J. Appl. Phys. **55**, 3382 (1984).

[71] W. Lohstroh, R. J. Westerwaal, B. Noheda, S. Enache, I. A. M. E. Giebels, B. Dam, and R. Griessen, *Self-organized layered hydrogenation in black* Mg_2NiH_x *switchable mirrors*, Phys. Rev. Lett. **93**, 197404 (2004).

[72] W. Lohstroh, R. J. Westerwaal, J. L. M. van Mechelen, C. Chacon, E. Johansson, B. Dam, and R. Griessen, *Structural and optical properties of* Mg_2NiH_x *switchable mirrors upon hydrogen loading*, Phys. Rev. B **70**, 165411 (2004).

[73] W. Lohstroh, R. J. Westerwaal, A. Lokhorst, J. L. M. van Mechelen, B. Dam, and R. Griessen, *Double layer formation in Mg-TM switchable mirrors (TM: Ni, Co, Fe)*, J. Alloys Compd. **404**, 490 (2005).

[74] D. M. Borsa, W. Lohstroh, R. Gremaud, J. H. Rector, B. Dam, R. J. Wijngaarden, and R. Griessen, *Critical composition dependence of the hydrogenation of* $Mg_{2d}Ni$ *thin films*, J. Alloys Compd. , In Press (2006).

[75] A. C. Lokhorst, *Reflections on switchable mirror devices*, Vrije Universiteit, Amsterdam, 2006.

[76] W. Lohstroh, R. J. Westerwaal, J. L. M. van Mechelen, H. Schreuders, B. Dam, and R. Griessen, *The dielectric function of* Mg_yNiH_x *thin films* $(2 \leq y \leq 10)$, J. Alloys Compd. , In Press (2006).

[77] I. A. M. E. Giebels, J. Isidorsson, and R. Griessen, *Highly absorbing, black Mg and rare-earth-Mg switchable mirrors*, Phys. Rev. B **69**, 205111 (2004).

[78] R. Armitage, M. Rubin, T. Richardson, N. O'Brien, and YongChen, *Solid-state gadolinium-magnesium hydride optical switch*, Appl. Phys. Lett. **75**, 1863 (1999).

[79] A. Borgschulte, R. J. Westerwaal, J. H. Rector, B. Dam, R. Griessen, and J. Schoenes, *Effect of the strong metal-support interaction on hydrogen sorption kinetics of Pd-capped switchable mirrors*, Phys. Rev. B **70**, 155414 (2004).

[80] J. Isidorsson, I. A. M. E. Giebels, E. S. Kooij, N. J. Koeman, J. H. Rector, A. T. M. van Gogh, and R. Griessen, *Structural, optical and electronic properties of* $LaMgH_x$ *switchable mirrors*, Electrochim. Acta **46**, 2179 (2001).

[81] M. Ouwerkerk, A. M. Janner, P. van der Sluis, and V. M. M. Mercier, *Optical switching device*, United States Patent application 20030227667 (1998).

[82] R. Griessen and T. Riesterer, *Topics in Applied Physics: Hydrogen in Intermetallic Compounds I*, page 219, Springer Verlag, Berlin Heidelberg, 1988.

[83] S. Orimo and H. Fujii, *Materials science of Mg-Ni-based new hydrides*, Appl. Phys. A **78**, 167 (2001).

[84] P. G. Shewmon, *Diffusion in solids*, McGraw-Hill Book Company, Inc., New York, 1963.

[85] C. G. Granqvist and V. Wittwer, *Materials for solar energy conversion: An overview*, Solar Energy Materials and Solar Cells **54**, 3948 (1998).

[86] M. Born and E. Wolf, *Principles of Optics*, University Press, Cambridge, 1980.

[87] A. Schüler, I. R. Videnovic, P. Oelhafen, and S. Brunold, *Titanium-containing amorphous hydrogenated silicon carbon films (a-Si:C:H/Ti) for durable solar absorber coatings*, Solar Energy Materials and Solar Cells **69**, 271 (2001).

[88] X. Bévenot, A. Troullet, C. Veillas, H. Gagnaire, and M. Clément, *Surface plasmon resonance hydrogen sensor using an optical fibre*, Measurement Science and Technology **13**, 118 (2002).

[89] R. D. Smith(II), P. Liu, S. H. Lee, C. E. Tracy, and J. R. Pitts, *Low-cost fiber optic hydrogen sensors*, Fuel Chemistry Division Preprints **47(2)**, 825 (2002).

[90] M. Ohring, *The materials science of thin films*, Academic Press, 1991.

[91] P. Ramanlal and L. M. Sander, *Theory of ballistic aggregation*, Phys. Rev. Lett. **54**, 1828 (1985).

[92] I. Petrov, P. B. Barna, L. Hultman, and J. E. Greene, *Microstructural evolution during film growth*, J. Vac. Sci. Technol. **21**, 117 (2003).

[93] G. H. Gilmer, H. Huang, T. D. de la Rubia, J. D. Torre, and F. Baumann, *Lattice Monte Carlo models of thin film deposition*, Thin Solid Films **365**, 189 (2000).

[94] A. Mazor, D. J. Srolovitz, P. S. Hagan, and B. G. Bukiet, *Columnar growth in thin films*, Phys. Rev. Lett. **60**, 424 (1988).

[95] Z. Czigány and G. Radnóczi, *Columnar growth structure and evolution of wavy interface morphology in amorphous and polycrystalline multilayered thin films*, Thin Solid Films **347**, 133 (1999).

[96] J. Krug and P. Meakin, *Microstructure and surface scaling in balistic deposition at oblique incidence*, Phys. Rev. A **40**, 2064 (1989).

[97] C. Tang, S. Alexander, and R. Bruinsma, *Scaling theory for the growth of amorphous films*, Phys. Rev. Lett. **64**, 772 (1990).

[98] S. M. Paik, S. Kim, and I. K. Schuller, *Surface kinetics and roughness on microstructure formation in thin films*, Phys. Rev. B **43**, 1843 (1991).

[99] A. G. Dirks and H. J. Leamy, *Columnar microstructure in vapour-deposited thin films*, Thin Solid Films **47**, 219 (1977).

[100] L. Zaluski, A. Zaluska, and J. O. Ström-Olsen, *Nanocrystalline metal hydrides*, J. Alloys Comp. **253-254**, 70 (1997).

[101] T. Spassov and U. Köster, *Hydrogenation of amorphous and nanocrystalline Mg-based alloys*, J. Alloys Compd. **287**, 243 (1999).

[102] C. Iwakura, S. Nohara, S. G. Zhang, and H. Inoue, *Hydriding and dehydriding characteristics of an amorphous* Mg_2Ni*-Ni composite*, J. Alloys Compd. **285**, 246 (1999).

[103] S. Orimo, K. Ikeda, H. Fujii, Y. Fujikawa, Y. Kitano, and K. yamamoto, *Structural and hydriding properties of the Mg-Ni-H system with nano- and/or amorphous structures*, Acta. Mater. **45**, 2271 (1997).

[104] Y. Ben-Eliyahu, M. Brill, and M. H. Mintz, *Hydride nucleation and formation of hydride growth centers on oxidized metallic surfaceskinetic theory*, J. Chem. Phys. **111**, 6053 (1999).

[105] R. Arkush, A. Venkert, M. Aizenshtein, S. Zalkind, D. Moreno, M. Brill, M. H. Mintz, and N. Shamir, *Site related nucleation and growth of hydrides on uranium surfaces*, J. Alloys Compd. **244**, 197 (1996).

[106] M. Brill, J. Bloch, and H. Mintz, *Experimental verification of the formal nucleation and growth rate equations-initial UH_3 development on uranium surface*, J. Alloys Compd. **266**, 180 (1998).

[107] T. T. Ueda, M. Tsukahara, Y. Kamiya, and S. Kikuchi, *Preparation and hydrogen storage properties of Mg-Ni-Mg_2Ni laminate composites*, J. Alloys Compd. **386**, 253 (2005).

[108] N. Cui, J. L. Luo, and K. T. Chuang, *Study of hydrogen diffusion in α- and β-phase hydrides of Mg_2Ni alloy by microelectrode technique*, J. Electroanalytical Chem. **503**, 92 (2001).

[109] F. Feng and D. O. Northwood, *Hydrogen diffusion in the anode of Ni/MH secondary batteries*, J. of Power Sources **136**, 346 (2004).

[110] J. Schoenes, M. Rode, H. Schröter, D. Zur, and A. Borgschulte, *Optical properties of YH_x ($0 \leq x \leq 2.1$) thin films*, J. Alloys Compd. **404-406**, 453 (2005).

[111] J. Hayoz, T. Pillo, M. Bovet, A. Züttel, S. Guthria, G. Pastore, L. Schlapbach, and P. Aebi, *Preparation and characterization of clean, single-crystalline YH_x films ($0 \leq x \leq 2.9$) on W(110)*, J. Vac. Sci. Technol. **18**, 2417 (2000).

[112] H. Fujiwara and M. Kondo, *Effects of carrier concentration on the dielectric function of ZnO:Ga and In_2O_3:Sn studied by spectroscopic ellipsometry: Analysis of free-carrier and band-edge absorption*, Phys. Rev. B. **71**, 075109 (2005).

[113] L. Gråsjö, G. Hultquist, K. L. Tan, and M. Seo, *Surface reactions on palladium hydride in vacuum, air and water studied in situ with mass spectrometry*, Appl. Surf. Sci. **89**, 21 (1995).

[114] A. Borgschulte, R. Gremaud, S. de Man, R. J. Westerwaal, J. H. Rector, B. Dam, and R. Griessen, *High-throughput concept for tailoring switchable mirrors*, Appl. Surf. Sci. **253**, 1417 (2006).

[115] D. A. G. Bruggeman, *Berechnung verschiedener physikalischer Konstanten von heterogene Substanzen - I. Dielektrizitätskonstanten und Leitfähigkeiten der Mischkörper aus isotropen Substanzen*, Ann. Phys. (Leipzig) **24**, 636 (1936).

[116] J. Isidorsson, I. A. M. E. Giebels, H. Arwin, and R. Griessen, *Optical properties of MgH_2 measured in $-$ situ by ellipsometry and spectrophotometry*, Phys. Rev. B **68**, 115112 (2003).

[117] A. Krozer, A. Fischer, and L. Schlapbach, *Experimental study of the valence band region of Mg-Pd and Ba-Pd interface with and without hydrogen and of the Mg and Ba hydrides*, Phys. Rev. B **53**, 13808 (1996).

[118] J. Rydén, B. Hjörvarsson, T. Ericsson, E. Karlsson, A. Krozer, and B. Kasemo, *Unusual kinetics of hydride formation in Mg-Pd sandwiches, studies by hydrogen profiling and quartz crystal microbalance measurements*, J. Less-Common Met. **152**, 295 (1989).

[119] R. J. Westerwaal, M. Slaman, A. Borgschulte, C. P. Broedersz, D. M. Borsa, W. Lohstroh, B. Kooi, G. ten Brink, K. G. Tschersich, H. P. Fleischhauer, B. Dam, and R. Griessen, *Optical, structural, and electrical properties of Mg_2NiH_4 thin films in $-$ situ grown by activated reactive evaporation*, J. Appl. Phys. **100**, 063518 (2006).

[120] A. P. Lenham and D. M. Treherne, *Optical constants of single crystals of Mg, Zn, Cd, Al, Ga, In, and white Sn*, J. Opt. Soc. Am. **56**, 752 (1966).

[121] R. H. W. Graves and A. P. Lenham, *Interband absorption in single crystals of Mg, Zn, and Cd at 295 K and 82 K*, J. Opt. Soc. Am. **58**, 126 (1968).

[122] M. Kerker, *The Scattering of Light and Other Electromagnetic Radiation*, Academic Press, New York, 1969.

[123] J. Dryzek and A. Czapla, *Quantum size effect in optical spectra of thin metallic films*, Phys. Rev. Lett. **58**, 721 (1987).

[124] E. V. Alieva, L. A. Kuzik, F. A. Pudonin, and V. A. Yakovlev, *Manifestation of quantum size effects in optics of ultrathin niobium films*, Optics and Spectroscopy **90**, 106 (2000).

[125] M. Eto and K. Kawamura, *Quantum size effect on optical absorption in a small spherical shell*, Phys. Rev. B **51**, 10119 (1995).

[126] J. I. Gittleman and B. Abeles, *Comparison of the effective medium and the Maxwell-Garnett predictions for the dielectric constants of granular metals*, Phys. Rev. B **15**, 3273 (1977).

[127] R. W. Cohen, G. D. Cody, M. D. Coutts, and B. Abeles, *Optical properties of granular silver and gold films*, Phys. Rev. B **8**, 3689 (1973).

[128] J. P. Marton and J. R. Lemon, *Optical properties of aggregated metal systems. I. theory*, Phys. Rev. B **4**, 271 (1971).

[129] P. Mulvaney, *Not all that's gold does glitter*, MRS Bulletin (2001).

[130] J. K. Norskov, A. Houmøller, P. K. Johansson, and B. I. Lundquist, *Adsorption and dissociation of H_2 on Mg surfaces*, Phys. Rev. Lett. **46**, 257 (1981).

[131] D. M. Bird, L. J. Clarcke, M. C. Payne, and I. Stich, *Dissociation of H_2 on Mg(0001)*, Chem. Phys. Lett. **212**, 518 (1993).

[132] N. D. Lang and W. Kohn, *Theory of metal surfaces: charge density and surface energy*, Phys. Rev. B **1**, 4555 (1970).

[133] B. E. Hayden, E. Schweitzer, R. Kötz, and A. M. Bradshaw, *The early stages of oxidation of magnesium single crystal surfaces*, Surf. Sci. **111**, 26 (1981).

[134] E. Wachowicz and A. Kiejna, *Bulk and surface properties of hexagonal-close-packede Be and Mg*, J. Phys.: Condens. Matter **13**, 10767 (2001).

[135] J. J. Gilman, *Direct measurements of the surface energies of crystals*, J. Appl. Phys. **31**, 2208 (1960).

[136] A. Wander, I. J. Bush, and N. M. Harrison, *Stability of rocksalt polar surfaces: an ab initio study of MgO (111) and NiO(111)*, Phys. Rev. B **68**, 233405 (2003).

[137] P. L. Gutshall and G. E. Gross, *Cleavage surface energy of NaCl and MgO in vacuum*, J. Appl. Phys. **36**, 2459 (1965).

[138] R. Wagemans, *Magnesium for Hydrogen Storage - From Micrometer to Nanometer*, Universiteit Utrecht, Utrecht, 2006.

[139] R. Wagemans, J. H. van Lenthe, P. E. de Jong, A. J. van Dillen, and K. P. de Jong, *Hydrogen storage in magnesium clusters: Quantum chemical study*, J. Am. Chem. Soc. (2005).

[140] J. E. Gerbi and J. R. Abelson, *Deposition of microcrystalline silicon: Direct evidence for hydrogen-induced surface mobility of Si adspecies*, J. Appl. Phys. **89**, 1463 (2001).

[141] L. Schlappbach, *Surface Properties and Activation, Hydrogen in Intermetallic Compounds vol. II*, Springer, Berlin, 1992.

[142] A. Borgschulte, W. Lohstroh, R. J. Westerwaal, H. Schreuders, J. H. Rector, B. Dam, and R. Griessen, *Combinatorial method for the development of a catalyst promoting hydrogen uptake*, J. Alloys Compd. **404**, 699 (2005).

[143] J. L. Slack, J. C. W. Locke, S. W. Song, J. Ona, and T. J. Richardson, Solar Energy Materials and Solar Cells , In Press (2005).

[144] P. H. L. Notten, Current opinion in solid state and materials science **4**, 5 (1999).

[145] S. J. van der Molen, J. W. J. Kerssemakers, J. H. Rector, N. J. Koeman, B. Dam, and R. Griessen, *Hydriding kinetics of Pd capped YH_x switchable mirrors*, J. Appl. Phys. **86**, 6107 (1999).

[146] A. T. M. van Gogh, S. J. van der Molen, J. W. J. Kerssemakers, N. J. Koeman, and R. Griessen, *Performance enhancement of metal-hydride switchable mirrors using Pd/AlO_x composite cap layers*, Appl. Phys. Lett. **77**, 815 (2000).

[147] K. von Rottkay, M. Rubin, F. Michalak, R. Armitage, T. J. Richardson, J. Slack, and P. Duine, *Effect of hydrogen insertion on the optical properties of Pd-coated magnesium lanthanides*, Electrochimica Acta **44**, 3093 (1999).

[148] S. J. Tauster, S. C. Fung, R. T. K. Baker, and J. A. Horsley, *Strong interactions in supported-metal atalysts*, Science **211**, 1121 (1981).

[149] O. Dulub, W. Hebenstreit, and U. Diebold, *Imaging cluster surfaces with atomic resolution: the strong metal-support interaction state of Pt supported on TiO_2(110)*, Phys. Rev. Lett. **84**, 3646 (2000).

[150] A. Borgschulte, R. J. Westerwaal, J. H. Rector, B. Dam, and R. Griessen, *Hydrogen sorption mechanism of oxidized nickel clusters*, Appl. Phys. Lett. **85**, 4884 (2004).

[151] A. Remhof, J. L. M. van Mechelen, N. J. Koeman, J. H. Rector, R. J. Wijngaarden, and R. Griessen, *Generation and detection of H electrodiffusion waves*, Rev. Sci. Instrum. **74**, 445 (2003).

[152] A. Borgschulte, R. J. Westerwaal, J. H. Rector, H. Schreuders, B. Dam, and R. Griessen, *Catalytic activity of noble metals promoting hydrogen uptake*, J. of Catalysis **239**, 263 (2005).

[153] R. Gremaud, Submitted to J. Phys.: Condens. Matt. (2005).

[154] T. B. Massalski, *Binary Alloy Phase Diagrams*, ASM International, NY 1990, 1990.

[155] A. R. Gonzales-Elipe, P. Malet, J. P. Espinos, A. Caballero, and G. Munera, *in Structure and Reactivity of Surfaces*, ed. by C. Morterra, A. Zecchina, and G. Costa , 427 (1989).

[156] H. Amandusson, L.-G. Ekedahl, and H. Dannetun, *Hydrogen permeation through surface modified Pd and PdAg membranes*, J. Membr. Sci. **193**, 35 (2001).

[157] A. J. A. Borgschulte, M. Rode and J. Schoenes, *Alloy formation of Y with Pd investigated by photoemission and electron diffraction*, J. Appl. Phys. **90**, 1147 (2001).

[158] M. L. Burke and R. J. Madix, *Hydrogen on Pd(100)-S: the effect of sulfur on precursor mediated adsorption and desorption*, Surf. Sci. **237**, 1 (1990).

[159] S. Wilke and M. Scheffler, *Mechanism of poisoning the catalytic activity of Pd(100) by a sulfur adlayer*, Phys. Rev. Lett. **76**, 3380 (1996).

[160] K. D. Rendulic, G. Anger, and A. Winkler, *Wide range nozzle beam adsorption data for the systems H_2/nickel and H_2/Pd(100)*, Surf. Sci. **208**, 404 (1989).

[161] F. J. Castro, G. Meyer, and G. Zampieri, *Effects of sulfur poisoning on hydrogen desorption from palladium*, J. Alloys Compd. **330-332**, 612 (2002).

[162] G. E. Gdowski, T. E. Felter, and R. H. Stulen, *Effect of surface temperature on the sorption of hydrogen by Pd(111)*, Surf. Sci. **181**, 147 (1987).

[163] R. J. Behm, K. Christmann, and G. Ertl, *Adsorption of hydrogen on Pd(100)*, Surf. Sci. **99**, 320 (1980).

[164] H. Okuyama, W. Siga, N. Takagi, M. Nishijima, and T. Aruga, *Path and mechanism of hydrogen absorption at Pd(100)*, Surf. Sci. **401**, 344 (1998).

[165] H. Conrad, G. Ertl, and E. E. Latta, *Adsorption of hydrogen on palladium single crystal surfaces*, Surf. Sci. **41**, 435 (1974).

[166] R. V. Bucur, *Inhibition of hydrogen desorption from a thin palladium layer by surface poisoning*, J. of Catalysis **70**, 92 (1981).

Samenvatting

Groei, microstructuur en waterstof-absorptie door Pd-gekatalyseerde, complexe metaal hydride dunne films

Schakelbare spiegels

Het onderzoek dat in dit proefschrift gepresenteerd wordt is gebaseerd op experimenten met een bepaald type schakelbare spiegels. Huiberts e.a. toonde het schakelbare effect van dunne metaal lagen voor het eerst aan in 1995 aan de Vrije Universiteit Amsterdam. Een schakelbare spiegel bestaat uit een dunne metaal film die is aangebracht op een glasplaatje, het substraat. De eerste schakelbare spiegels bestonden uit de metalen lanthaan (La) en yttrium (Y). Het andere element dat nodig is voor het functioneren van een schakelbare spiegel is waterstof (H_2). Een waterstof molecuul bestaat uit twee waterstof atomen en wanneer deze moleculen gesplitst worden kunnen de waterstof atomen opgenomen worden door de metaal laag. Op deze metaal laag wordt doorgaans een palladium (Pd) laag aangebracht die de film beschermt tegen oxidatie en de waterstof opname katalyseert. De waterstof atomen, die tussen de metaal atomen door diffunderen kunnen dan met de metaal atomen een hydride fase vormen. Wanneer dit gebeurt dan verandert de film van een spiegelende metaal film naar een transparante isolator (vergelijkbaar met een normale ruit). Het bijzondere van deze reactie is dat deze omkeerbaar is door het waterstof te verwijderen wordt de transparante film weer een metaal film.

Schakelbare spiegels die volledig uit zeldzame aarden bestaan worden gerekend tot de eerste generatie schakelbare spiegels. Philips research ontdekte in 1997 dat een legering tussen magnesium (Mg) en zeldzame aarden (tweede generatie) resulteert in een schakelbare spiegel die neutraal in kleur is in de transparante toestand. Vanzelfsprekend is dit voor een toepassing van een schakelbare spiegel als "smart window" zeer interessant. Het blijkt echter dat deze schakelbare spiegels naast de reflecterende en transparante toestand nog een derde optische toestand bezitten namelijk een optisch zwarte toestand. Het opvallende licht wordt geabsorbeerd en dit resulteert in een zwarte toestand. Dit fysische verschijnsel maakt deze schakelbare spiegels zeer interessant voor een temperatuur regelende functie in bijvoorbeeld zonnecollectoren. De volgende (derde) generatie schakelbare spiegels werd gentroduceerd door Richardson e.a. Zij ontdekten dat schakelbare spiegels die bestaan uit een legering tussen magnesium en overgangs metalen (TM = Ni, Co, Fe etc.) ook schakelen van een reflecterende metaal fase naar een transparante toestand. Dit brengt ons bij het onderwerp van dit proefschrift.

De zwarte toestand in Mg_2Ni-H dunne films

Na intensief onderzoek aan Mg-Ni schakelbare spiegels hebben wij aangetoond dat ook deze schakelbare spiegels een zwarte toestand vertonen. Echter, het mechanisme dat leidt tot deze zwarte toestand is volledig verschillend van de fasescheiding die de zwarte toestand in Mg-zeldzame aarden schakelbare spiegels veroorzaakt. De oorsprong van de zwarte toestand in Mg-TM schakelbare spiegels was lange tijd onduidelijk. Dit is dan ook een van de centrale vragen in mijn proefschrift. We zullen laten zien dat de zwarte toestand in Mg-TM schakelbare spiegels een oorsprong heeft in het ontstaan van een metaal - hydride dubbellaag in de film gedurende de waterstof opname. Dit mechanisme wordt beschreven in hoofdstuk 3 samen met de optische, thermodynamische en structurele eigenschappen van Mg-Ni films.

Overzicht van kenmerkende eigenschappen van Mg-Ni schakelbare spiegels

De optische zwarte toestand in Mg-Ni films is het gevolg van het samenspel tussen de optische eigenschappen van de verschillende fases en de ontwikkeling van een dubbellaag in de film gedurende waterstof opname. Uit het modelleren van de optische data met behulp van de dielectrische constanten $\tilde{\epsilon}_{Mg_2Ni}$ en $\tilde{\epsilon}_{Mg_2NiH_4}$ blijkt dat de hydride nucleatie bij voorkeur aan het film/substraat interface plaatsvindt. Dit is een zeer opvallend resultaat aangezien je verwacht dat de hydride nucleatie begint waar het atomaire waterstof de film binnenkomt, namelijk aan de Pd kant. Dat deze voorkeurs-hydride groei inderdaad optreedt laten we zien door middel van X-ray diffractie metingen en de film dikte afhankelijkheid van de waterstof concentratie (gemeten met de resonant nucleaire reactie ^{1}H(^{15}N, $\alpha\gamma$)^{12}C) gedurende waterstof opname.

Wanneer we de druk-compositie isothermen van deze films vergelijken met die van bulk samples, zien we dat de hydride groei aan het substraat interface een lokaal kinetisch effect kan zijn. Echter ook een thermodynamische oorspong is niet uit te sluiten. Omdat je verwacht dat de waterstof concentratie het hoogst is aan de Pd kant en afneemt naarmate je dichter bij het substraat komt, hebben we ook de waterstof diffusie door de film onderzocht. Dit model voor Mg_2Ni films laat inderdaad zien dat het mogelijk is een verhoogde waterstof concentratie aan het substraat interface te hebben.

De oorzaak van de voorkeurs-nucleatie aan het interface wordt onderzocht in hoofdstuk 4.

Structurele eigenschappen van Mg-Ni films

De voorkeurs-nucleatie aan het substraat interface kan grofweg twee oorzaken hebben. Ten eerste is het mogelijk dat zich gedurende de depositie van de film zich een gradiënt ontwikkeld in de chemische samenstelling van de film. Een tweede mogelijkheid is dat de specifieke hydride groei gestuurd wordt door de microstructuur van de film. De chemische homogeniteit van de film hebben we onderzocht met RBS en SIMS metingen. Hieruit blijkt dat er geen gradiënt in compositie is die de zwarte toestand zou kunnen verklaren. We concluderen dat de zwarte toestand een structurele oorspong heeft. We hebben de microstructuur geanalyseerd met behulp van STM, TEM and SEM metingen. Het blijkt dat tot een dikte van 50 nm de film bestaat uit een zeer fijne korrel structuur. Bij films dikker dan deze 50 nm ontwikkelt zich een kolom structuur bovenop deze fijn-korrelige laag. Deze kolom structuur heeft een hogere dichtheid dan de initiele laag. De nucleatie van de hydride fase vindt dus plaats in de laag die uit kleine korrels bestaat. Wij nemen aan dat de nucleatie vergemakkelijkt wordt door deze kleine korrels, waarna de hydride verder door de kolomstructuur kan aangroeien. Uit de SEM metingen blijkt verder dat er een "tunnel" structuur bestaat tussen de grensvlakken van de verschillende kolommen. Deze faciliteren mogelijkerwijs de waterstof diffusie naar het substraat. Om dit model te toetsen hebben we getracht de microstructuur te veranderen en zodoende de zwarte tostand te onderdrukken. Dit lukte niet door een verandering van de substraat temperatuur tijdens de groei. Een andere mogelijkheid die we onderzocht hebben is om de hydride fase *in-situ* te groeien.

In-situ groei van hydrides

In hoofdstuk 5 laten we zien dat we *in-situ* de Mg_2NiH_4 en de MgH_2 hydride fases direct kunnen groeien met behulp van een geactiveerde reactive depositie (ARE) in een MBE systeem. Om dit te bereiken maken we gebruik van een atomaire waterstof bron.

De groei van de hydride fase kunnen we volgen door gedurende de depositie *in-situ* de weerstand te meten. Om een idee te krijgen van de kwaliteit van de gegroeide fase meten we ook *in-situ* de reflectie met behulp van fiber optica en een spectrometer. *Ex-situ* reflectie en transmissie metingen wijzen uit dat *in-situ* gegroeide Mg_2NiH_4 films bij opnieuw beladen geen zwarte toestand vertonen en er dus geen initiële hydride nucleatie aan het substraat interface plaatsvindt. SEM metingen laten duidelijk zien dat de microstructuur van een *in-situ* gegroeide Mg_2NiH_4 film uit een zeer homogene korrelstructuur van kleine korrels bestaat over de hele dikte van de film. Dit heeft tot gevolg dat de hydride nucleatie willekeurig plaatsvindt door de hele film. *In-situ* gegroeide Mg_2NiH_4 films hebben een optische band kloof van 1.75 eV. Deze is vergelijkbaar met de band kloof of *ex-situ* geformde Mg_2NiH_4 films.

Deze *in-situ* groei experimenten leveren nog veel meer interessante gegevens op. Zowel de *in-situ* gegroeide Mg_2NiH_4 als de MgH_2 fase zijn stabiel in vacuum en dit laat zien dat het ontladen kinetisch geblokkeerd is. De *in-situ* gegroeide hydride films ontladen alleen wanneer er een (katalytische) Pd laag op gegroeid wordt.

Het is opmerkelijk dat de *in-situ* gegroeide MgH_2 fase een zeer hoge elektrische weerstand heeft, maar dat optisch blijkt dat deze films nog 10 vol.% Mg bevatten. Dit geeft aan dat deze metallische Mg korrels volledig geisoleerd zijn van elkaar. Deze Mg deeltjes hebben een grote invloed op het optische gedrag van deze films, ze creëren namelijk een absorptie band bij 2.0 eV, waardoor deze films roodachtig zijn in transmissie. Met de ARE depositie techniek zijn we in staat om dikke MgH_2 films te groeien zonder dat de waterstof diffusie blokkerende MgH_2 laag ontstaat. Echter wanneer we deze films bedekken met een Pd laag om vervolgen weer te beladen, dan gedragen deze films zich als normale metallisch gegroeide Mg films. Ook is dan de absorptie band bij 2.0 eV verdwenen. Gedurende deze experimenten hebben we ondervonden dat de katalytische eigenschappen van de Pd laag zeer belangrijk zijn en veranderen gedurende waterstof-absorptie en -desorptie.

Katalyse

In hoofdstuk 6 zullen we de katalytische werking van Pd bespreken en wat de invloed van het SMSI effect op het beladen is. Het SMSI effect houdt in dat onder invloed van waterstof-absorptie en -desorptie de katalytische Pd clusters bedekt worden door oxides die hun oorsprong hebben in de actieve laag. We onderzoeken de optische en kinetische eigenschappen alsmede de schakelstabiliteit van Mg-Ni films als funktie van Mg-Ni compositie en Pd dikte. Met STM metingen relateren we de oppervlakte structuur van de Pd laag aan de beladingseigenschappen van de schakelbare spiegel en we laten de invloed van het SMSI effect zien op de schakel-eigenschappen van de film.

Het teruglopen van de katalytische eigenschappen van Pd ten gevolge van het SMSI effect is tegen te gaan door de Pd laag dikker te maken. Ook wordt het SMSI effect onderdrukt naarmate de bedekking van de Mg-Ni film door het Pd beter is. Dit verklaart ook waarom er een kritieke Pd dikte is voor de gekatalyseerde waterstofopname door schakelbare spiegels. Wanneer de Pd laag te dun is wordt deze snel bedekt door oxides en verliest het zijn katalytische eigenschappen. De teruglopende katalytische eigenschappen hangen dus af van de Pd dikte en de gas atmosfeer.

Uit de *in-situ* beladings experimenten blijkt duidelijk dat een H_2 gas-beladen film niet meer ontlaat in vacuum. Dit effect is echter niet toe te schrijven aan het SMSI effect. Daarom moet de geblokkeerde desorptie veroorzaakt worden door een contaminatie van het Pd oppervlak of een reductie van het aantal actieve sites voor waterstof desorptie. *In-situ* beladings experimenten tonen de desastreuze gevolgen aan voor desorptie wanneer er zich een kleine hoeveelheid zwavel op het Pd oppervlak bevind. Deze films ontladen niet, ook niet in ultra-hoog vacuum. Wij vinden dat waterstof het beste desorbeert (bij kamertemperatuur) als het Pd oppervlak vers opgedampt is, vrij van zwavel is of met Ar-ionen gebombardeerd wordt. Dit zwavel diffundeert onder invloed van het beladen naar het Pd oppervlak. Echter na sputteren met argon ionen verkrijgt het verse Pd oppervlak weer zijn oorspronkelijke katalytische eigenschappen. Wij vinden dan ook dat een vers en schoon Pd oppervlak vereist is voor een snelle desorptie in vacuum.

Conclusie

In dit proefschrift laten we zien dat de microstructuur een elementaire rol speelt in het beladingsgedrag van een metaalhydride. De nucleatie van een hydride in een metaal wordt daardoor niet altijd door het diffusieveld bepaald. Als gevolg hiervan treedt er in Mg_2Ni films een intermediare zwarte (licht absorberende) fase op.

List of publications

- *Mg-Ni-H films as selective coatings: Tunable reflectance by layered hydrogenation*
  J. L. M. van Mechelen, B. Noheda, W. Lohstroh, R. J. Westerwaal, J.H. Rector, B. Dam, and R. Griessen, Appl. Phys. Lett. **84**, 3651-3653 (2004)

- *Effect of hydrogen uptake and substrate orientation on the flux penetration in* NbH_x *thin films*
  M. S. Welling, C. M. Aegerter, R. J. Westerwaal, S. Enache, R. J. Wijngaarden, and R. Griessen, Physica C **406**, 100 (2004)

- *Huge compact flux avalanches in superconducting Nb thin films*
  M. S. Welling, R. J. Westerwaal, W. Lohstroh, and R. J. Wijngaarden, Physica C **411**, 11 (2004)

- *Structure of the* Mg_2 *Ni switchable mirror: an EXAFS investigation*
  M. Di Vece, A. M. J. van der Eerden, D. Grandjean, R. J. Westerwaal, W. Lohstroh, S. G. Nikitenko, J. J. Kelly, D. C. Koningsberger, Mat. Chem. and Phys. **91**, 1-9 (2005)

- *Self-organized layered hydrogenation in black* Mg_2NiH_x *switchable mirrors*
  W. Lohstroh, R. J. Westerwaal, B. Noheda, S. Enache, I. A. M. E. Giebels, B. Dam, and R. Griessen, Phys. Rev. Lett. **93**, 197404 (2004)

- *Structural and optical properties of* Mg_2NiH_x *switchable mirrors upon hydrogen loading*
  W. Lohstroh, R. J. Westerwaal, J. L. M. van Mechelen, C. Chacon, E. Johansson, B. Dam, and R. Griessen, Phys. Phys. Rev. B. **70**, 165411 (2004)

- *Effect of the strong metal-support interaction on hydrogen sorption kinetics of Pd-capped switchable mirrors*
  A. Borgschulte, R. J. Westerwaal, J. H. Rector, B. Dam, R. Griessen, and J. Schoenes, Phys. Rev. B. **70**, 155414 (2004)

- *Hydrogen sorption mechanism of oxidized nickel clusters*
  A. Borgschulte, R. J. Westerwaal, J. H. Rector, B. Dam, and R. Griessen, Appl. Phys. Lett. **85**, 4884 (2004)

- *Combinatorial method for the development of a catalyst promoting hydrogen uptake*
  A. Borgschulte, W. Lohstroh, R. J. Westerwaal, H. Schreuders, J. H. Rector, B. Dam, and R. Griessen, J. Alloys Compd. **404**, 699-705 (2005)

- *Double layer formation in Mg-TM switchable mirrors (TM: Ni, Co, Fe)*
  W. Lohstroh, R. J. Westerwaal, A. C. Lokhorst, J. L. M. van Mechelen, B. Dam, and R. Griessen, J. Alloys Compd. **404**, 490-493 (2005)

- *Microstructural origin of the black state in* Mg_2NiH_x *thin films*
  R. J. Westerwaal, A. Borgschulte, W. Lohstroh, B. Dam, and R. Griessen, J. Alloys Compd. **404-406**, 481-484 (2005)

- *The growth induced microstructural origin of the black state of* Mg_2NiH_x *thin films*
  R. J. Westerwaal, A. Borgschulte, W. Lohstroh, B. Dam, B. Kooi, G. ten Brink, M. J. P. Hopstaken, and P. H. L. Notten, J. Alloys Compd. **416**, 2-10 (2006)

- *Optical, structural and electrical properties of* Mg_2NiH_4 *thin films in-situ grown by activated reactive evaporation*
  R. J. Westerwaal, M. Slaman, A. Borgschulte, C. P. Broedersz, D. M. Borsa, W. Lohstroh, B. Kooi, G. ten Brink, K. G. Tschersich, H. P. Fleischhauer, B. Dam, and R. Griessen, J. Appl. Phys. **100**, 063518 (2006)

- *Distortion of the fcc lattice in superstoichiometric* β-YH_{2+d} *and cubic* YH_{3-h} *thin films*
  A. -M. Carsteanu, M. Rode, D. Zur, J. Schoenes, A. Borgschulte, R. J. Westerwaal, J. Alloys Compd. **404-406**, 82-84 (2005)

- *Catalytic activity of noble metals promoting hydrogen uptake*
  A. Borgschulte, R. J. Westerwaal, J. H. Rector, H. Schreuders, B. Dam, and R. Griessen, J. of Catalysis **239**, 263-271 (2006)

- *High-throughput concept for tailoring switchable mirrors*
  A. Borgschulte, R. Gremaud, S de Man, R. J. Westerwaal, J. H. Rector, B. Dam, and R. Griessen, Appl. Surf. Sci. **253**, 1417-1423 (2006)

- *The dielectric function of* Mg_yNiH_x *thin films* $(2 \leq y \leq 10)$
  W. Lohstroh, R. J. Westerwaal, J. L. M. van Mechelen, H. Schreuders B. Dam, and R. Griessen, Accepted for J. Alloys Compd. (2006)

- *Tuning the electrical, structural and optical properties of in-situ grown MgH_2 thin films by activated reactive evaporation*
  R. J. Westerwaal, C. P. Broedersz, R. Gremaud, M. Slaman, A. Borgschulte, W. Lohstroh, K. G. Tschersich, H. P. Fleischhauer, B. Dam, R. Griessen, Submitted to Thin Solid Films (2006)

- *Determining in-situ the change in catalytical properties of the Pd caplayer upon hydrogenation*
  R. J. Westerwaal, E. Batyrev, M. Slaman, A. Borgschulte, W. Lohstroh K. G. Tschersich, H. P. Fleischhauer, B. Dam, R. Griessen, To be submitted (2006)

Dankwoord

Gedurende de afgelopen vier en een half jaar heb ik met veel plezier gewerkt in de groep vaste-stoffysica aan de Vrije Universiteit te Amsterdam. Hiervoor wil ik de volgende mensen bedanken die de afgelopen jaren hebben bijgedragen aan het tot stand komen van dit proefschrift en hebben bijgedragen aan mijn promotieonderzoek.

Allereerst wil ik Ronald Griessen bedanken voor zijn steun, enthousiasme en de mogelijkheid die hij me geboden heeft om naar verschillende (internationale) conferenties en workshops te gaan. Hiertoe behoren o.a. de TMR workshops op IJsland (Fludir) en Spanje (Palma de Mallorca). Ook mocht ik naar de MH2002 en MH2004 conferenties in Frankrijk (Annecy) en Polen (Krakow) om mijn onderzoek te tonen. Verder heb ik mijn werk kunnen presenteren op een MRS conferentie in Boston (MRS: Materials Research Society). Verder wil ik ook graag Bernard Dam bedanken voor zijn begeleiding gedurende mijn promotie. Altijd positief en motiverend over nieuwe resultaten en onderzoeken, Bernard bedankt!

Gedurende mijn promotieonderzoek, wat veel experimenteel werk inhield, was technische ondersteuning onmisbaar. Allereerst wil ik Nico Koeman bedanken voor het uitleggen van het MBE systeem en mij bekend te maken met de UHV-wereld. Kier Heeck voor de ideeën, adviezen en ondersteuning op electronicagebied (en de koffie). Jan Rector voor de RBS-metingen en zijn (praktische) hulp bij het oplossen van problemen en het onderhouden van het MBE systeem. Herman Schreuders wil ik bedanken voor zijn hulp en ondersteuning in het algemeen. Martin Slaman voor de samenwerking, discussies en het opbouwen van de fiber opstelling om *in-situ* optische spectra te meten. Ook de mensen van de mechanische en elektronische werkplaats voor de altijd snelle ondersteuning en oplossingen.

Veel dank ben ik ook verschuldigd aan Wiebke Lohstroh voor de samenwerking gedurende de afgelopen jaren. De discussies, overleg en samenwerking heb ik als zeer prettig ervaren. Natuurlijk wil ik ook Andreas Borgschulte ('as you know') bedanken voor de fijne samenwerking en het overleg gedurende mijn promotie. Jouw manier van experimenten uitvoeren werkt soms heel verfrissend en motiverend! In hoofdstuk 4 en 6 zul je vast wel enige resultaten herkennen. Naast het serieuze onderzoek hebben we ook veel gelachen in de kelder. Ook wil ik Ingrid Giebels bedanken voor de begeleiding tijdens mijn afstudeerproject. Ik kon altijd bij je terecht voor vragen over van alles en nog wat en je maakte altijd tijd voor mij.

Natuurlijk wil ik ook alle andere groepsleden bedanken voor de discussies, goede sfeer, samenwerking en groeps-activiteiten: Rinke Wijngaarden, Marco Welling (samenwerking, discussies), Annemarie Lokhorst (overleg, discussies), Arndt Remhof, Erdny Batyrev, Beatriz Noheda, Mariella Menghini, Dana Borsa (discussies, overleg, hulp bij schrijven van proefschrift), Robin Gremaud (optische metingen), Sonia May, Marta Gonzalez, Jan Isidorsson, Stănică Enache, Christof Aegerter, Mathieu Pasturel, Kinga Lorincz, Diana Gheorge, Philip Mauron, Davide Iannuzzi, Andrea Baldi (kamergenoot), Dook van Mechelen, Sven de Man, Chase Broedersz (overleg, berekeningen), Kirsten Smith and Iris Crassee.

Ook wil ik Bart Kooi bedanken voor het mogelijk maken van de vele TEM en SEM metingen aan mijn samples en Gert ten Brink voor het uitvoeren van deze metingen.

Tot slot wil ik mijn vader en moeder bedanken voor de steun en het vertrouwen die ik heb ontvangen gedurende mijn promotie periode. Verder wil ik ook mijn familie en vrienden niet vergeten en bedanken voor hun interesse gedurende de afgelopen jaren.

Curriculum Vitae

Ruud Westerwaal werd geboren op 16 oktober 1976 te Alkmaar. Van 1990 tot 1996 volgde hij het VWO op het Bernardus Alfrink College te Schagen. Hierna studeerde hij natuurkunde van 1996 to 2002 aan de Vrije Universiteit te Amsterdam. Daar verrichtte hij zijn afstudeerproject in de vaste-stoffysica groep van Ronald Griessen aan de Vrije Universiteit. Gedurende dit project onderzocht hij de optimale omstandigheden en parameters om Mg schakelbare spiegels te laten schakelen door waterstof opname. Van 2002 tot 2006 verrichtte hij zijn promotieonderzoek aan zeldzame-aarden-vrije schakelbare spiegels in dezelfde groep. Gedurende deze periode nam hij deel aan diverse workshops en conferenties over metaal-waterstof systemen in binnen- en buitenland. Verder gaf hij werkcolleges aan studenten van de studierichting medische natuurwetenschappen. Gedurende dit promotieonderzoek slaagde hij erin om metaal-hydrides *in-situ* te groeien met behulp van een atomaire waterstof bron. Dit type onderzoek is uniek in de wereld en resulteerde in deelname aan het project: Optische Fiber Waterstof Sensoren.

Ruud Westerwaal was born on 16 October 1976 in Alkmaar, The Netherlands. From 1990 till 1996 he followed high school at the Bernardus Alfrink College in Schagen. He studied physics from 1996 till 2002 at the Vrije Universiteit. He performed his graduation project in the solid state physics group of Ronald Griessen at the Vrije Universiteit. There he investigated how to optimize Mg based switchable mirrors. From 2002 till 2006 he performed his Ph.D project called: Rare-earth-free switchable metal-hydrides in the same group. During this period he attended many workshops and conferences on metal-hydride systems in The Netherlands and abroad. Furthermore, he gave tutorials to undergraduate students in medical natural science. During his Ph.D period he succeeded in growing *in-situ* metal-hydride thin films by using an atomic hydrogen source. This research is unique in the world and this research resulted in the participation on the project: Optical Fiber Hydrogen Sensors.